Copyright Warning & Restrictions

The copyright law of the United States (Title 17, United States Code) governs the making of photocopies or other reproductions of copyrighted material.

Under certain conditions specified in the law, libraries and archives are authorized to furnish a photocopy or other reproduction. One of these specified conditions is that the photocopy or reproduction is not to be "used for any purpose other than private study, scholarship, or research." If a, user makes a request for, or later uses, a photocopy or reproduction for purposes in excess of "fair use" that user may be liable for copyright infringement,

This institution reserves the right to refuse to accept a copying order if, in its judgment, fulfillment of the order would involve violation of copyright law.

Please Note: The author retains the copyright while the New Jersey Institute of Technology reserves the right to distribute this thesis or dissertation

Printing note: If you do not wish to print this page, then select "Pages from: first page # to: last page #" on the print dialog screen

NJIT New Jersey's Science & Technology University

The Van Houten library has removed some of the personal information and all signatures from the approval page and biographical sketches of theses and dissertations in order to protect the identity of NJIT graduates and faculty.

ABSTRACT

SHALE SOFTENING BASED ON PORE NETWORK AND LABORATORY INVESTIGATIONS

by
Di Zhang

This dissertation consists of two major parts: Firstly, experimental investigation of four major shale softening mechanisms and quantifications of structural parameters. Secondly, numerical simulations of nano-scale flow behaviors using the previous experiments determined parameters based on modified pore network modeling.

Hydraulic fracturing is widely applied to economical gas production from shale reservoirs. Still, the gradual swelling of the clay micro/nano-pores due to retained fluid from hydraulic fracturing causes a gradual reduction of gas production. Four different gas-bearing shale samples are investigated to quantify the expected shale swelling due to hydraulic fracturing. These shale samples are subject to heated deionized (DI) water at 100°C temperature and 8.2 MPa pressure in a laboratory reactor for 72 hours to simulate shale softening. The micro and nano-pore structures change during shale swelling, and the porosity decreases after shale treatment. The porosity decreases by 4% for clayey shale, while for well-cemented shale, the porosity only decreases by 0.52%. The findings show that the initial mineralogical composition of shale plays a significant role in the swelling of micro and nano-pores and the pore structure alteration due to retained fluid from hydraulic fracturing.

Secondly, the permeability of shale is of significance in the gas extraction process. The shale gas permeability is usually obtained based on Darcy flow using standard

laboratory permeability tests that do not account for different transport mechanisms and anisotropic effects in shale due to nano-scale pore structure. However, this method cannot reflect the variations in transport mechanisms and anisotropic effect in shale due to additional nano-scale pore structure into consideration. In this study, the permeability of shale is simulated by a pore network model. Pore structure characteristics can be described by specific parameters, including porosity, pore size, pore throat distribution, and coordination number. The anisotropy is incorporated into the model using a coordination number ratio, and an algorithm is developed for connections of the pores in the shale formation. The proposed three-dimensional pore network model is verified by predicting hydraulic connectivity and comparing it with several high-pressure permeability tests. Results show that the prediction of the anisotropic model is closer to the test results than that of the isotropic model. The predicted permeability calculated by numerical simulation is consistent with the measured permeability.

Finally, the production rate with time for three formations and the negative effect of shale softening on gas production is analyzed, respectively. Then the historical production data from Eagle Ford Shale, Haynesville Shale, and Longmaxi shale are compared. A modified PNW model is developed to simulate each shale formations' flow properties using realistic reservoir parameters. The simulation results have a similar decline rate compared to actual historical production data, and the effect of softening of shale matrix is also incorporated. These results can predict how shale softening impacts the production rate of different conditions and provide a clear picture of how reservoir properties influence the overall production rate within nano-scale.

SHALE SOFTENING BASED ON PORE NETWORK AND LABORATORY INVESTIGATIONS

by
Di Zhang

A Dissertation
Submitted to the Faculty of
New Jersey Institute of Technology
in Partial Fulfillment of the Requirements for the Degree of
Doctor of Philosophy in Civil Engineering

John A. Reif, Jr. Department of Civil and Environmental Engineering

August 2021

Copyright © 2021 by Di Zhang

ALL RIGHTS RESERVED

APPROVAL PAGE

SHALE SOFTENING BASED ON PORE NETWORK AND LABORATORY INVESTIGATIONS

Di Zhang

Dr. Jay N. Meegoda, Dissertation Advisor — Date
Professor of Civil and Environmental Engineering, NJIT

Dr. Bruno Gonçalves da Silva, Committee Member — Date
Assistant Professor of Civil and Environmental Engineering, NJIT

Dr. Liming Hu, Committee Member — Date
Professor of Department of Hydraulic Engineering, Tsinghua University, Beijing, China

---

Dr. Matthew J. Bandelt, Committee Member — Date
Assistant Professor of Civil and Environmental Engineering, NJIT

Dr. David W. Washington, Committee Member — Date
Associate Professor of Engineering Technology, NJIT

BIOGRAPHICAL SKETCH

Author: Di Zhang

Degree: Doctor of Philosophy

Date: August 2021

Undergraduate and Graduate Education:

- Doctor of Philosophy in Civil Engineering,
  New Jersey Institute of Technology, Newark, NJ, 2021

- Master of Science in Civil Engineering
  New Jersey Institute of Technology, Newark, NJ, 2016

- Bachelor of Science in Civil Engineering,
  China Agriculture University, Beijing, China, 2013

Major: Civil Engineering

Presentations and Publications:

Zhang, D., Meegoda, J. N., Gonçalves da Silva, B. M., and Hu, L., Impact of hydraulic fracturing on the production rate of unconventional gas reservoirs based on a pore network model [Manuscript under Preparation for possible publication]

Zhang, D., Meegoda, J. N., Gonçalves da Silva, B. M., and Hu, L., Impact of hydraulic fracturing on change in mineralogy, micro and nano porosities and permeability of shales, Manuscript submitted to Scientific Reports for review and possible publication.

Zhang, D., Zhang, X., Guo, H., Lin, D., Meegoda, J. N., and Hu, L., An anisotropic pore-network model to estimate the shale gas permeability. Sci Rep 11, 7902 (2021). https://doi.org/10.1038/s41598-021-86829-4

Zhang, D, Zhang, X., Meegoda, J. N, Hu, L., and Goncalves da Silva, B. M., Impact of shale softening on permeability, American Geophysical Union Fall Meeting 2020, Retrieved from: https:agu2020fallmeeting-agu.ipostersessions.com Access date : July 16 ,2021.

Zhang, D., Guo, H., Meegoda, J. N, Hu, L., and Zhang, P., A pore-network model to estimate the shale gas permeability. IS-Atlanta 2018 Geo-Mechanics from Micro to Macro in Research and Practice. Atlanta, Georgia, 2018.

Guo, H., Hu, L., Meegoda, J. N, Yan, D., and Zhang, D., An improved pore-network model for porous geo-materials IS-Atlanta 2018 Geo-Mechanics from Micro to Macro in Research and Practice. Atlanta, Georgia, 2018

This dissertation is dedicated to my mother, Jia Rong, and my father, Zhang Xiaohui. Their support, encouragement, and constant love have sustained me throughout my life.

ACKNOWLEDGMENT

First and foremost, I would like to express my sincere gratitude to my advisor, Dr. Jay Meegoda. Without his assistance and dedicated involvement in every step throughout the process, this paper would have never been accomplished. I would like to thank you very much for your support and understanding over these past five years. Dr. Meegoda motivated me to be a better researcher, lecturer, scholar, and educator. Research under the guidance of Dr. Jay Meegoda was a worthwhile experience.

I would also like to express my gratitude to my committee, including Dr. Liming Hu, Dr. Bruno M. Goncalves da Silva, Dr. Matthew J. Bandelt, and Dr. David W. Washington, for their kindly participation and valuable ideas in the dissertation. I am thankful to Dr. Methi Wecharatana for accepting me into the NJIT Ph.D. program, which provided me with an excellent doctoral platform. I would also like to express my gratitude to Dr. Liming Hu, Co-advisor at Tsinghua University, for his involvement and his helpful remarks on different research projects during the research. Also, I would express my gratitude to Dr. Bruno M. Goncalves da Silva for his help and instruction during the program. I would also like to thank the scholarship provided by the Department of Civil and Environmental Engineering (CEE) at the New Jersey Institute of Technology (NJIT) for the doctoral study.

I want to thank Stephen J. George and Nasser M. Channaoui for their support, notably in manufacturing several test settings and providing technical instructions. I especially like to mention the department chair, Dr. Taha F. Marhaba, and the staff member, Ms. Dallas Link and Ms. Sylvana Brito, for giving assistance and encouragement during

my Ph.D. Also, I would thank Dr. Jeong Seop Shim for his kind guidance and support at the York Center, NJIT, with C.T. analysis, XRD, and BET equipment learning.

I cannot begin to express my gratitude and appreciation for their friendship during my Ph.D. program. I want to express my gratitude to my friends, including Jin Fan, Anuruddha Jayasuriya, Mandeep Pokhrel, Gayani Gunarathna, Aluthgun Hewage Shaini, Jitendra Kewalramani, Catarina Baptista Pereira, and Bezerra de Souza Bruno. I must also thank several colleagues at Tsinghua University, Pengwei Zhang, Haohao Guo, Xinghao Zhang, and Dantong Lin, for their support in my numerical modeling process.

Most importantly, none of this could have happened without my family: my mother, Jiarong, who offered her encouragement through phone calls every week. My father, Dr.Xiaohui Zhang, has been kind and supportive to me. Without my family, this work can never be achieved.

TABLE OF CONTENTS

TABLE OF CONTENTS

(Continued)

Chapter **Page**

TABLE OF CONTENTS

(Continued)

Chapter **Page**

TABLE OF CONTENTS

(Continued)

Chapter **Page**

TABLE OF CONTENTS

(Continued)

Chapter **Page**

TABLE OF CONTENTS

(Continued)

LIST OF TABLES

LIST OF TABLES

(Continued)

LIST OF FIGURES

LIST OF FIGURES

(Continued)

LIST OF FIGURES

(Continued)

LIST OF FIGURES

(Continued)

LIST OF FIGURES

(Continued)

LIST OF FIGURES

(Continued)

LIST OF FIGURES

(Continued)

LIST OF FIGURES

(Continued)

LIST OF FIGURES

(Continued)

CHAPTER 1

INTRODUCTION

1.1 Background Information

World Energy needs have risen and will rise even further in the future. The expectance of a high standard of living, recent technology development, and population growth in the world are the three main reasons for higher energy demands [1]. Extracting natural gas from shale in the United States (USA) is one of the landmark events of the 21st century. Horizontal drilling combined with hydraulic fracturing has allowed the extraction of large amounts of natural gas from low permeability shale formations previously considered impossible or uneconomical to exploit.

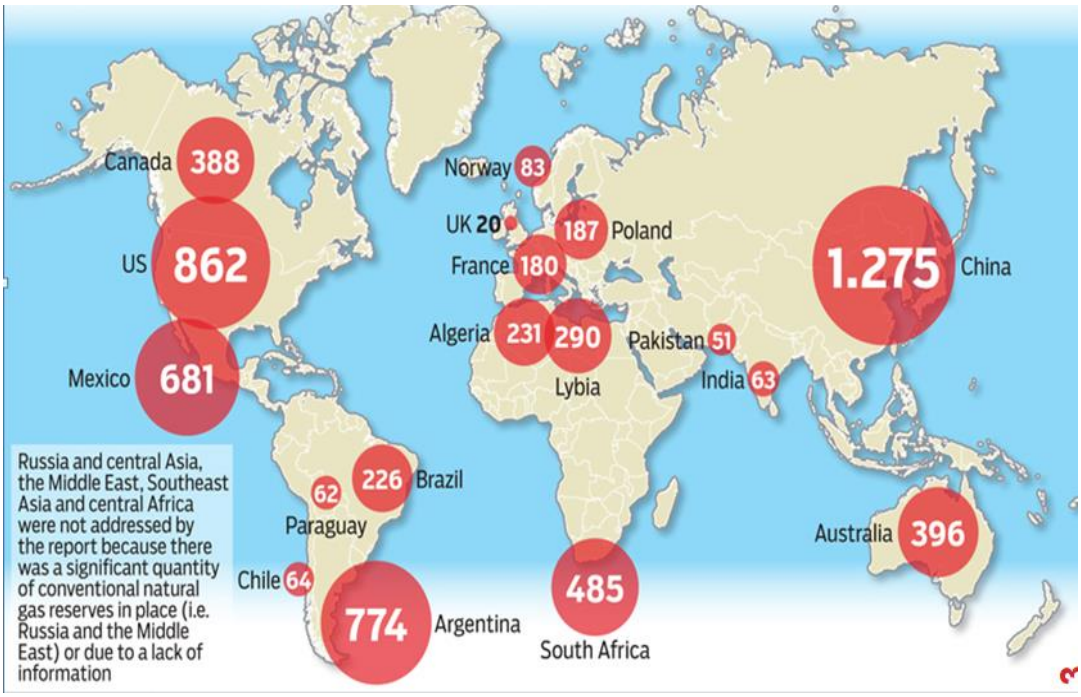

Figure 1.1 World Shale Gas Reserves. Units: trillion cubic feet.

Source: [2].

Figure 1.1 shows the world shale gas reserves. Many of those countries with shale gas reserves are trying to cope with growing energy demand while reducing their dependence on imported fossil fuels. Most notably, China is the world's largest energy consumer and one of the world's largest shale gas resource holders. China has increased shale gas production from nearly zero in 2012 to 6.5 billion cubic meters per year in 2015 and will be exploiting 8-10 billion cubic meters by 2020, accounting for a quarter of their total gas consumption [3]. It is speculated that shale gas will play an essential role in meeting global energy needs and will be an indispensable part of the energy policy in most countries of the world [4]. The exploration and transformation of shale gas have attracted the interest of many countries and have experienced rapid development [5]. Shale gas is a mature and highly profitable industry [6]. In 2018, EIA reported an average dry natural gas production of 80.4 billion cubic feet per day (Bcf/d), increasing 9% from 2017 levels[7]. Hence, it is of great importance to thoroughly study the extraction of shale gas from shale formations and the interaction of fracturing fluid on shale formations.

1.2 Problem Statement

In typical gas production wells, the gas production rate declines rapidly within the first few months of initial extraction. For example, Valkó and Lee compiled monthly production data from selected Barnett shale wells and shown in Figure 1.2, and the newer wells have higher initial production. Still, the production rates declined rapidly, as indicated in the graph. Several other researchers observed this phenomenon, and a similar decline in gas production rate can be seen in different shale gas reservoirs, as shown in Figure 1.3. This

early decline of gas production raises several questions regarding hydraulic fracturing, including gas wells instability and decreasing permeability of the formation.

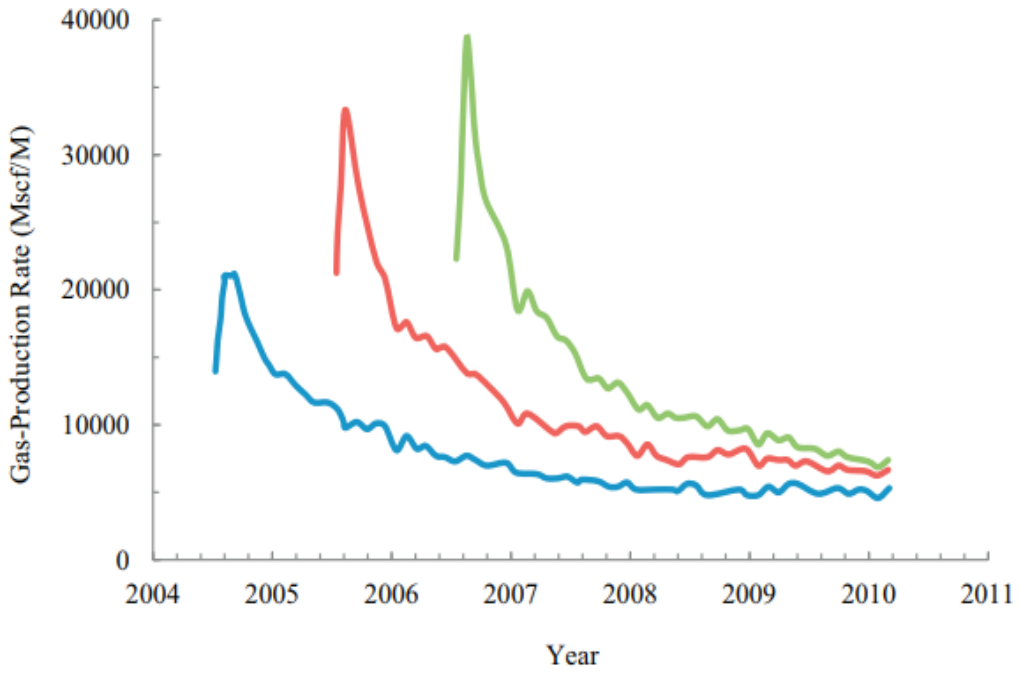

Figure 1.2 The variation of the average gas production rate of three selected Barnett shale wells with production time.

Source: [8].

This rapid decline in production rate could be due to the depletion of methane or the decline in fracture conductivity between the reservoirs and wellbores. Researchers who have been studying this decline have concluded that the shale-water reactions under high temperature and pressure may be the main reason for the loss of fracture conductivity. The fracture conductivity between the reservoirs and wellbores is critical for gas production. Therefore, the loss of fracture conductivity within a few months seems to be the main reason for the steep decline in gas production and causing a significant decrease in long-

term production. To achieve an economical production rate, gas permeability within the whole matrix must remain at a certain level. Therefore, the depletion of gas production rate within initial production remains a potential problem for the shale gas industry.

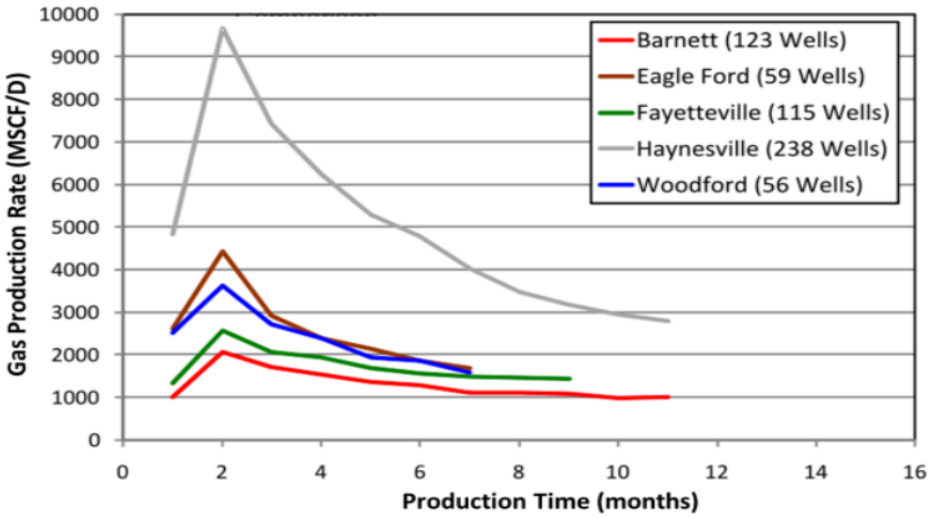

Figure 1. 3 Gas production rate in different shale gas basins.

Source: [9].

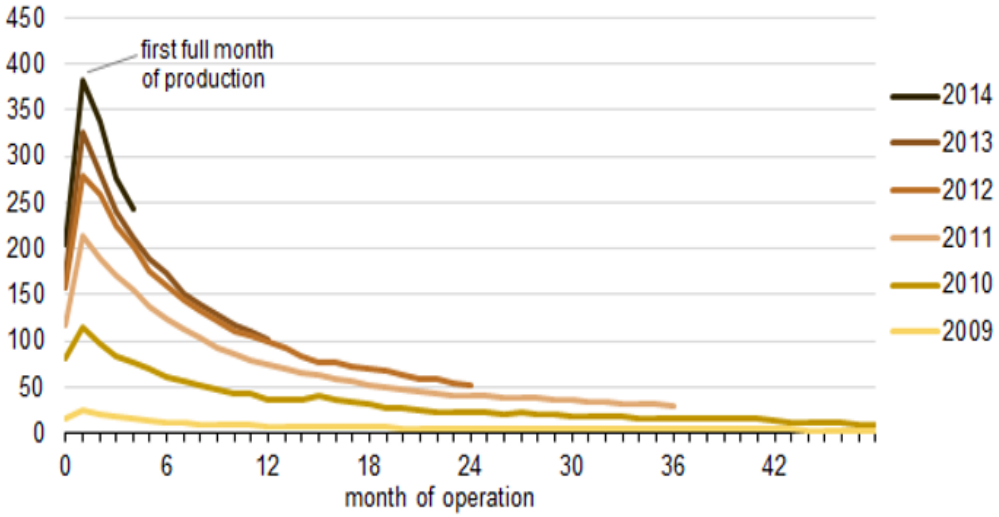

Figure 1. 4 New Eagle Ford wells gas production rate during the first 48 months.

Source: [10].

Figure 1.3 shows the average gas production rate per well in different shale basins across the United States. Figure 1.4 shows that the gas production rate increased, and the rate of declination also increased both with the time of installation.

1.3 Objectives

The shale gas extraction using horizontal drilling and hydraulic fracturing technologies have enabled the production of hydrocarbons from tight shale formations. However, rapid depletion of shale gas production rate with time due to shale softening and constrain in the interconnectivity of pores of shale formations remain two major concerns during drilling and completion of wellbores in unconventional shale reservoirs. Both issues are primarily due to shale-fluid interactions. Understanding the interactions of organic-rich shale with water-based fluids is the first step towards quantifying the problems. Hence, the main objective of this study is to investigate the interactions of organic-rich shale with water-based fluids and the impact of that on shale permeability. A series of tests will be performed to determine specific surface area, pore size distribution, total porosity. The combined N_2 and CO_2 gas sorption test, along with micro-computerized tomography measurements of several shale samples (Sichuan formation and Eagle Ford formation), will also be performed. Changes in shale properties will be measured before and after shale samples encountered water-based fluids. This research will evaluate the changes in pore structure, namely: porosity, pore size distribution, and pore connectivity before and after shale in contact with water-based fluids used during hydraulic fracturing.

The experimentally obtained pore structure of shale will then be used to develop a pore network model for virgin shale and shale contact with fracturing fluids. First, the developed pore network model will be modified to include anisotropy. The modified pore network will predict the variation in shale permeability with the difference in pressure between inlet and outlet. The predicted permeability values will then be compared with the measured values reported in the literature. Then, the variation of pore structure between pre-treated shale and treated shale will be compared, and the above anisotropic pore network model will be used to predict the permeability variances of shale samples before and after treatment with the pressure difference between inlet and outlet to quantify the impact of shale permeability due to shale softening.

Though fracturing enhances the shale gas production of tight gas-bearing shale, the water-based fracturing fluids contribute to shale softening and hence swelling of pores to rapidly decline the gas production rate with time. Hence, this research attempts to present a mechanistic explanation for the decline in shale gas production with time. The research goals are elaborated in Figure 1.5, and specific tasks are listed below.

Task 1 Experimentally investigation of virgin and treated shale to determine the pore structure and the softening process effect (see Chapter 3)

Task 2 Details of the pore network model and the modification to simulate anisotropic shale (see Chapter 4)

Task 3 Evaluations of experimental data and developments of representative pore structure for both virgin and treated shale (see Chapter 5)

Task 4 Prediction of virgin and treated shale permeability using the modified pore network model with experimentally determined pore structure to quantify the degradation of gas production rate with time. (see Chapters 6)

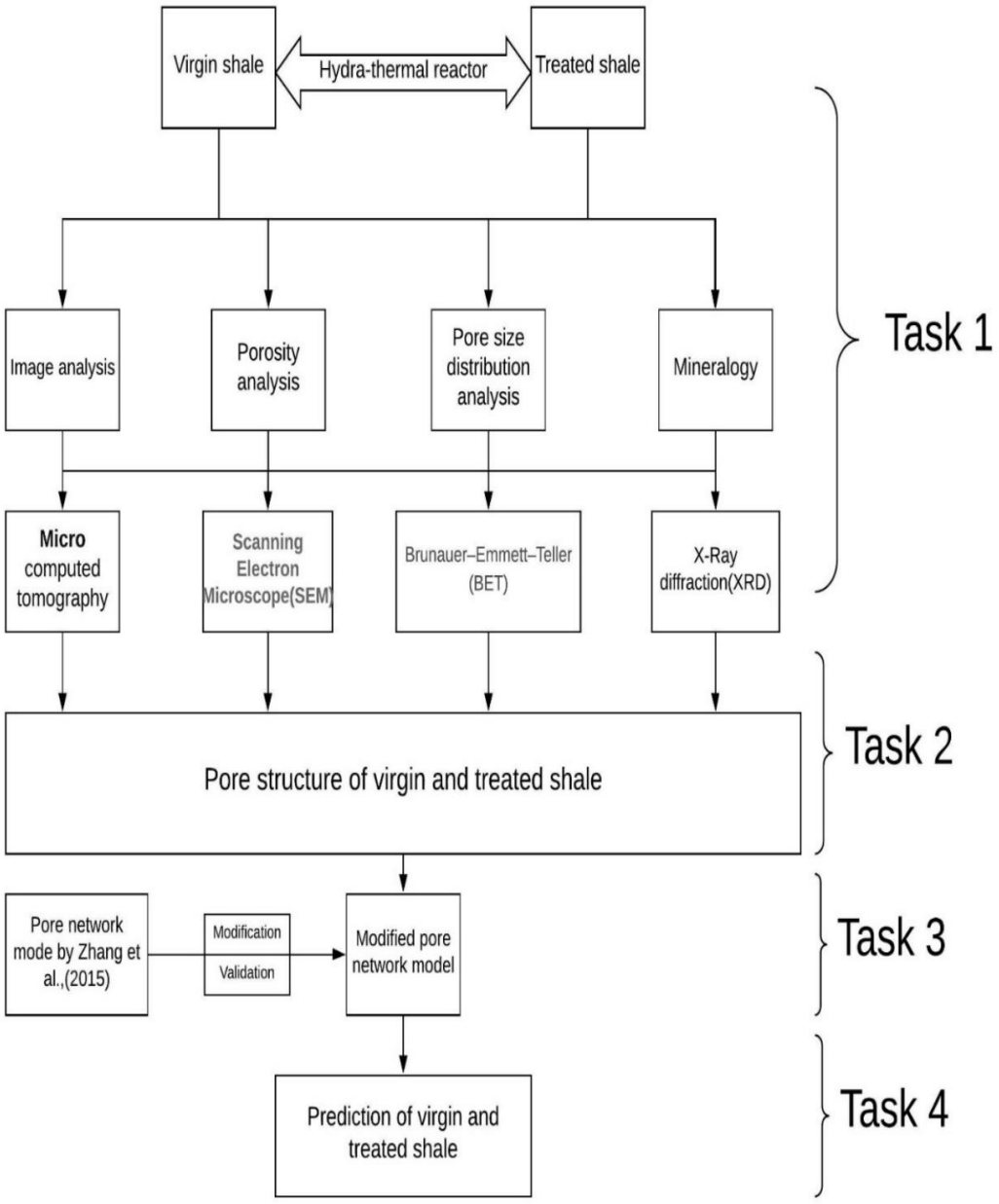

Figure 1. 5 Research goals.

CHAPTER 2

LITERATURE REVIEW

2.1 Shale Softening

Shale formations are different from conventional gas reservoirs; shale gas is stored in nano-pores connected by nano fractures and natural microcracks. Two technological innovations contributed to the rapid rise in shale gas extraction, namely horizontal drilling, and hydraulic fracturing. Figure 2.1 depicts both.

Hydraulic fracturing has experienced tremendous technological development since its early days. The hydraulic fracturing technique has been transformed from a low-volume, low-rate operation to a highly complex, engineering-driven procedure in the subsurface [11]. Hydraulic fracturing is known as the alteration of the reservoir rock by fracturing the structure around the wellbores and adding sand or other granular material in those fractures to support the opening into the wellbore. The extraction of oil and natural gas in areas in which traditional methods have proved inefficient is feasible by hydraulic fracking. Recent reports have estimated that hydraulic drilling would be necessary for up to 95% of natural gas wells boiled in the next decade. A highly automated, designed and monitored technique that uses specifically chosen chemical types and quantities to increase the performance of hydraulic fracturing. Usually, these additives constitute less than 1% of fluid drilling. However, experience and ongoing experiments have increased the process's efficiency and allowed the application of reduced chemical quantities and environmentally sound chemical products.

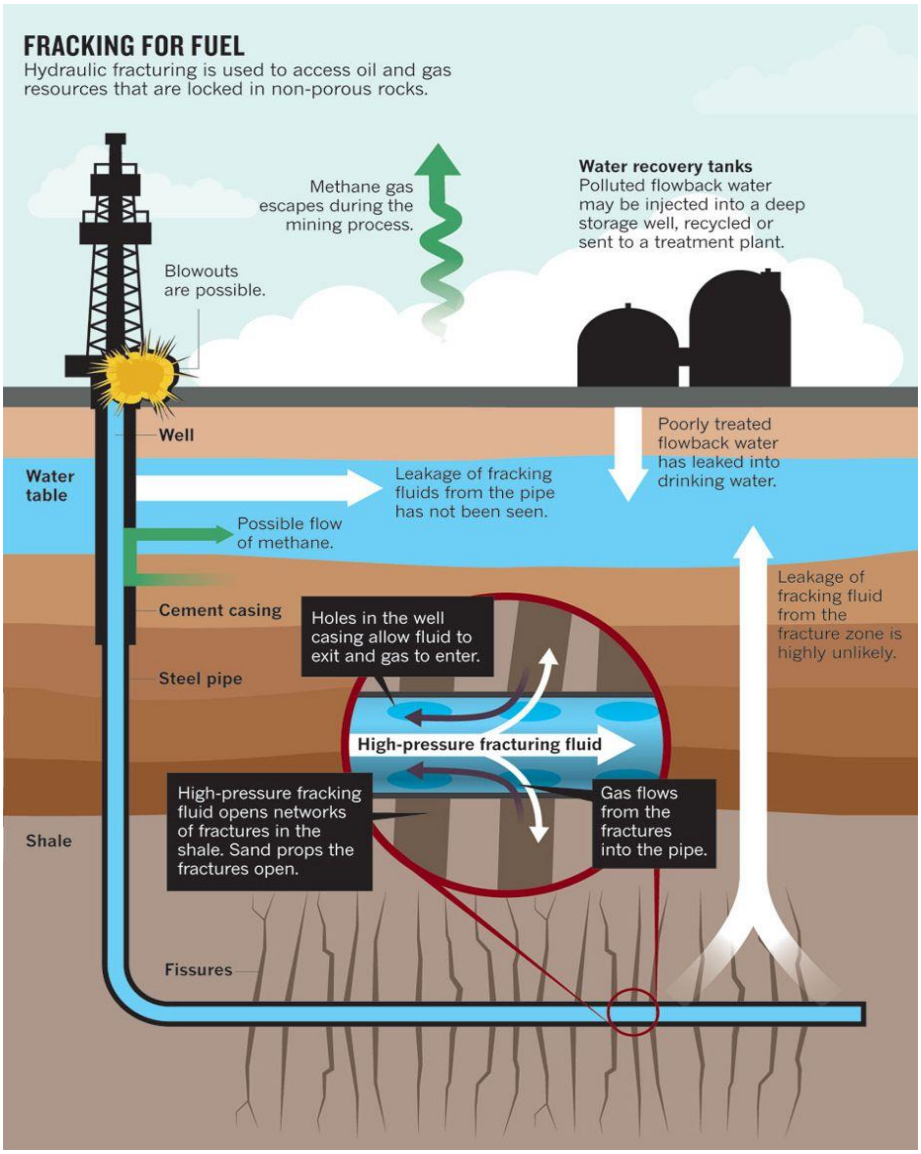

Figure 2. 1 Horizontal drilling and hydraulic fracture.

Source: [12].

Like horizontal drilling, the primary purpose of hydraulic fracturing is to create an additional area of contact in the reservoir so that hydrocarbons can flow in the shale formations. Multiple hydraulic fractures can be created in stages on the same horizontal wellbore, enabling the well productivity to be increased many times [13,14]. Academic and

industrial research efforts have been focused on issues such as geomechanics and formation damage due to shale-fluid interactions.

Upon exposure to the aqueous fracturing fluids at high temperatures and high pressures, the mechanical properties of shales such as elasticity, hardness, and strength usually deteriorate due to a phenomenon called "shale softening," which occurs within the shale matrixes [15]. It is generally agreed that shale softening significantly impacts the design and operation of shale gas exploration and long-term gas production. This reactivity between water-based fracturing fluids and shale formations can be attributed to the water-sensitive clay minerals and acid-sensitive carbonate minerals in shale rocks [16,17]. When shale matrix encounters water-based drilling and fracturing fluids, shale swelling and softening can occur. As a result, the flow of shale gas can be significantly reduced. In other words, the pore structure of the shale would change with the interaction of fracturing fluids. Hence, the petroleum industry will benefit tremendously if the sensitivity of shale to water-based fluids can be quantified. The change in permeability of each type of shale gas well can be predicted.

To investigate the factors contributing to changes in shale matrix due to water-based fluids, shale-fluid interactions have been studied extensively to understand the various mechanisms involved in phenomena such as shale swelling [18–20]. However, there is limited research on how clay-water interaction and acid-carbonate integrations affect the pore structure of the shale matrix. After shale softening, the predictions of gas production rate will be critical to both designs of fracturing fluids and gas well planning.

2.2 Water-based Fracturing Fluid on Pore Structure

Shale is defined as fine-grained classic sedimentary rocks. It is formed by the compaction of clay and silt, or mud [21]. Due to their small grain size, the porosity of shales is generally below 10% [22], and their permeability is typically in the range of 1,000 nano-Darcy to 10 nano-Darcy [23]. In terms of mineralogical composition, shale typically consists of different types of clay, fine-size quartz, and feldspars. In addition, carbonates (calcite), sulfides, iron oxides, and organic carbon compounds also exist in shales [24]. The uniqueness of the mineralogy of shale reservoirs, compared with conventional reservoir systems, is the organic matter, and organic matter adds complexity to the characteristics of shales. Therefore, the proper characterization of the physical properties of shale is essential in the success of resource evaluation and estimation of the permeability. Hence, in this study, several physical properties of shale will be measured and compared. Those critical parameters included: porosity, pore size, coordination number, and pore throat size of shale matrix.

2.3 Clay-water Reactions and Carbonate-acid Reactions

Figure 2.2 shows the mineralogical compositions of different shale reservoirs, where typically less than 50% could be clays. Less than 60% would be quartz and carbonate, where carbonate concentration would range from 0 to nearly 90%. There is a wide range of mineralogy of gas shale with clay and carbonate contents currently used to produce hydrocarbons or are being evaluated for production in the United States. The mineralogy of shales is vital because it is related to other physiochemical and microstructural properties, such as the potential for water-clay reaction and acid-carbonate reaction, both directly

contributing to shale softening. These shale properties will facilitate drilling and fracturing activities to get the target shale gas production rate from shale reservoirs.

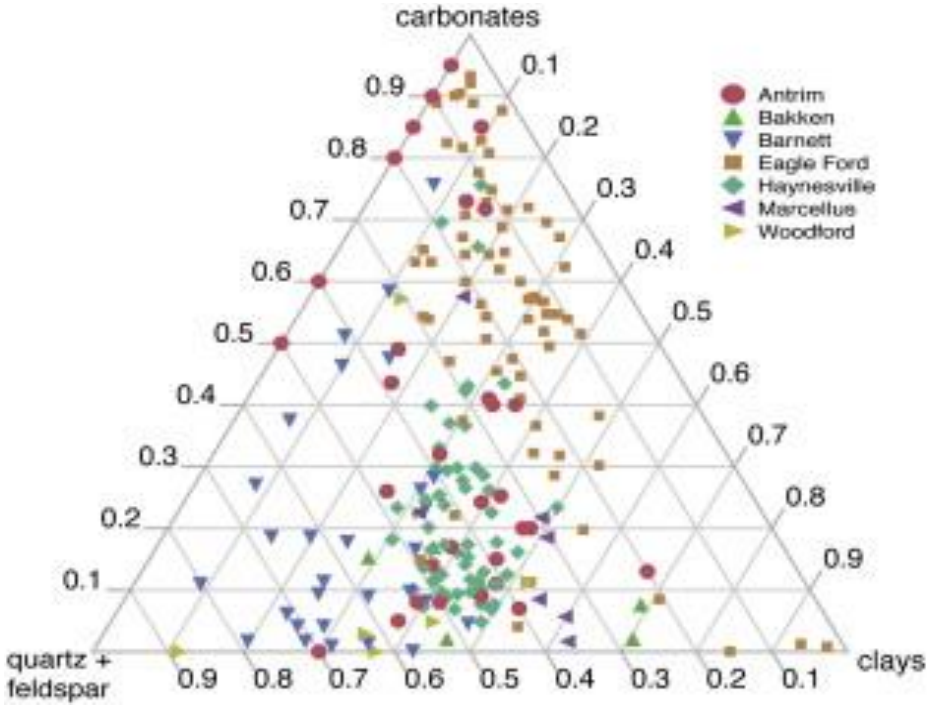

Figure 2. 2 Quartz and feldspar, carbonate, and clay content for different shale formations.

Source: [25].

Wu and Sharma showed that the change in shale's microstructure would strongly depend on mineral composition [26]. Clay minerals are naturally formed by the weathering and decomposition of igneous rocks or inherited from fine-grained sedimentary rocks [27]. Due to the excessive negative charges on the surface of clay particles and the distribution of ions in the electrolyte between clay particles, an electrical double layer (EDL) or diffused double layer (DDL) is formed [28]. Hence, when a clay particle is in contact with fracturing fluid, an aqueous electrolyte, a double layer repulsive potential is developed,

resulting in pore structure changes and swelling of pores. Sun et al. [29] studied the impact of slickwater fracturing fluid on the mineralogical composition of pre-treated and treated samples, as shown in Table 2.1.

Table 2. 1 Mineral Compositions of the Pre-treated and Post-treated Shale Samples

Source: [29].

Samples	Quartz	Calcite	Dolomite	Pyrite	Plagioclase	Clay
Pre-treated shale	36	36	7	2	4	16
Treated shale	37	32	5	2	5	19

The clay minerals in the pre-treated shale sample mainly consisted of a mixed layer of illite and smectite (I/S) (97%) and a small amount of chlorite (3%). After the fracturing fluid treatment, the content of clay minerals increased from 16% to 19%. The slickwater in fracturing fluid is water-based, clays can absorb the water in shale during fracturing, and the adsorbed water may change the pore structure of the shale matrix [30]. Wu and Sharma [26] showed that slickwater is often a mild acid solution with a pH ranging from 5.6-6.8. Carbonate-acid reactions could be another reason for the micro structural change of pore structure fracturing water injected into the shale formations.

Figure 2.3 shows the loss of four major minerals (dolomite, calcite, quartz, and clay) in shale that reacted with slickwater. The weight loss of carbonate (calcite and dolomite) contributed to almost 15% of total weight loss. This dissolution of carbonate may also lead to a change in porosity and pore size distribution.

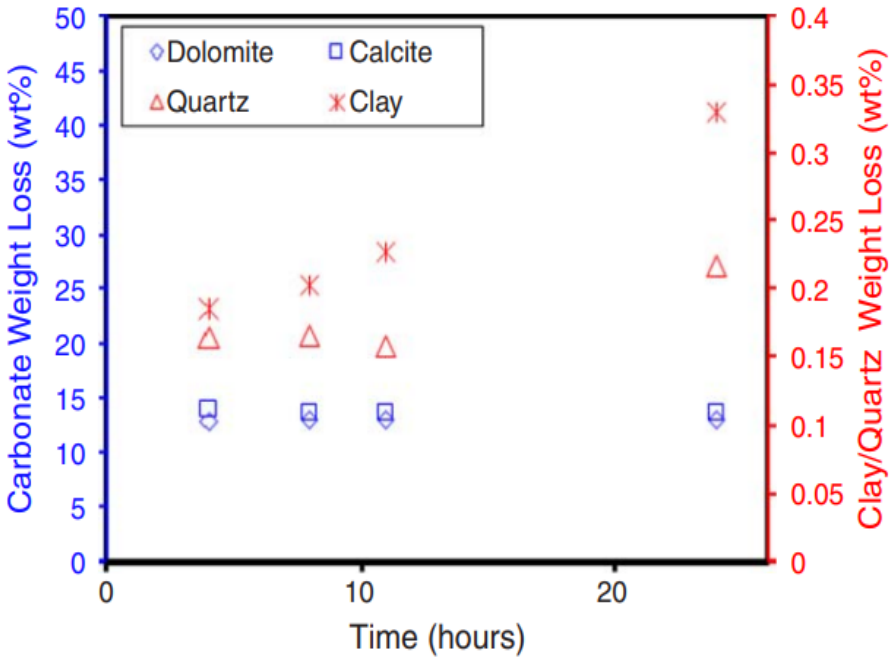

Figure 2. 3 Weight loss of minerals from Bakken shale in slickwater over 24 hours.

Source: [26].

2.4 Impact of Slick Water on Changes in Pore Size Distribution

Figures 2.4 and 2.5 show comparisons of pore size distributions of two different formations before and after exposure to slickwater. It is evident that the pore size distribution of formations is altered after treatment. Hence, the shale matrix parameters such as porosity, coordination number, average pore size, and pore throat are also changed. Therefore, the permeability of each shale reservoir would also change.

Figure 2.4 shows the change in the number of nano-pores, leading to a completely different pore structure. The experimental results suggest that after slickwater fracturing fluid treatment, the carbonate minerals were reduced by dissolution, resulting in a large number of dissolution pores measuring 2–5 μm in diameter. By combining these

observations with both BET and C.T. analysis, it became clear that the reduction of total pore volume and specific area of nano-pores might be the two controlling factors:

(1) the carbonate minerals dissolution transformed the nano-pores into pores with diameters up to 2 μm.

(2) the clay minerals in the shale mainly composed of I/S and the smectite in the I/S mixed layer had a positive correlation with water activity, which could cause the clay swelling and reduce the specific surface area and pore volume of shale samples after reaction due to shale softening.

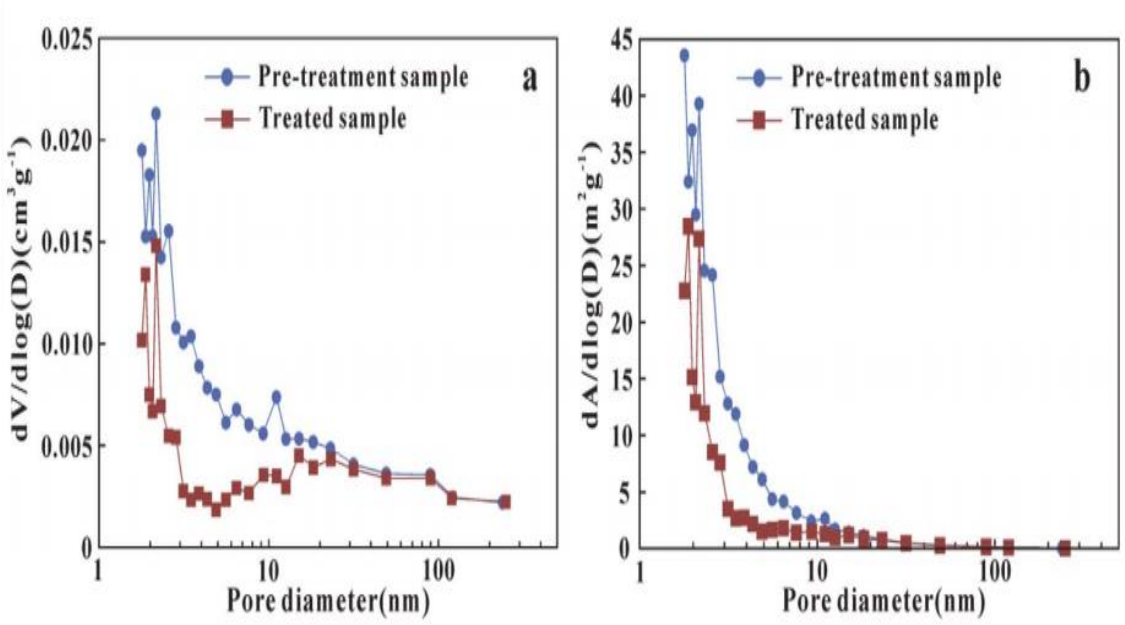

Figure 2. 4 Sichuan Longmaxi samples pore size distribution for treated and pre-treated by mild acid slick fracturing water. a: (pore volume), b: (Specific surface area).

Source: [29].

However, other researchers have suggested that acid fracturing creates many macrospores with diameters up to 120 μm, which will increase the gas permeability of shale. As shown in Figure 2.5, there is a significant increase of macrospores ranging from

500nm-3000nm. Based on N_2 gas adsorption method, the microspores are also increasing from 10nm to 120nm, which are quite different from previous results.

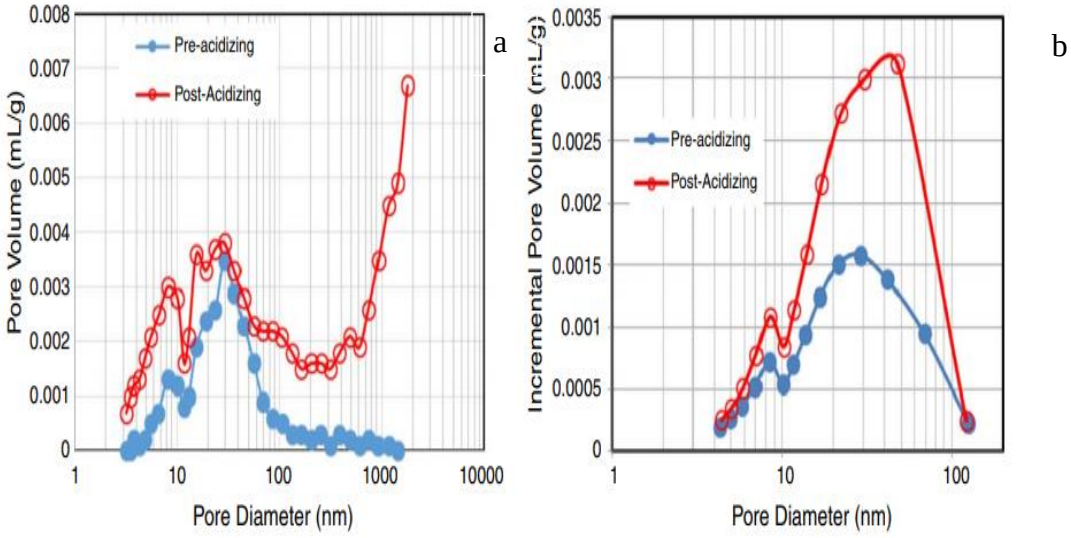

Figure 2. 5 Pore size distribution measured by MIP (a) and N_2 adsorption (b) for both treated and pre-treated Bakken samples.

Source: [31].

Based on the above discussion, two competing reactions contribute to shale softening due to the injection of slickwater during fracturing. The first one is the clay-water reaction that causes swelling of pores and pore throats. The second would be the dissolution of carbonates that increase the size of pores and pore throats. The dissolution of carbonates would increase the shale gas permeability, while the swelling of clays would reduce the permeability of the shale matrix. The literature shows that shale gas-bearing formations have more extensive clay contents compared to carbonate. Hence, the clay swelling will dominate during the slickwater reactions; therefore, reducing pore sizes will be expected.

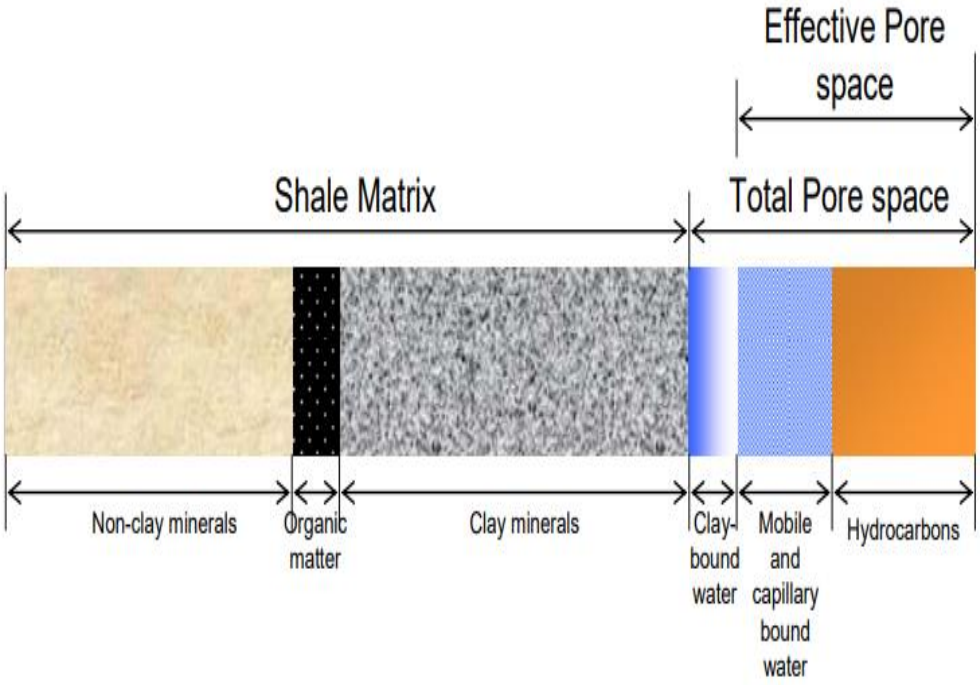

Figure 2. 6 Schematic of a typical gas production shale rock-solid.

Source: [32,33].

Figure 2.6 shows the average mineralogical content of gas-bearing shales of the United States. There is a higher percentage of clay minerals ranging from 20%-60% of total mass, directly controlling the fluid-clay reaction [32,33]. Zhang et al. [34] reported that the clay content in shale rocks is the fundamental cause for the significant reduction of shale fracture conductivity after fracturing. However, the chemical interactions between shale and fracturing fluid have not been thoroughly elucidated [35]. The interactions between these minerals and fracturing fluid would affect the pore structure and permeability of the shale. Sanaei et al. [36] reported that the composition and content of clay minerals determined the clay swelling and the size of the diffused double layer. They investigated the production loss due to clay swelling in a realistic, complex hydraulic fracture network. However, the impact of fracturing fluid on the permeability in shale was

not quantified. Quantifying the influence of fracturing fluids on pore structures and predicting the production rate of shale gas reservoirs could improve shale gas extraction.

2.5 Pore Network Model

It is well known that some nano-scale gas transport processes may be difficult to predict or explain unless there is a well-defined experiment used to study the phenomenon accurately. The pore network model can bridge the gap between laboratory simulation and the prediction of shale gas transport. Although a pore network is challenging to obtain with traditional experimental studies, a detailed pore network makes it possible for researchers to study nano-scale gas transport properties.

The equivalent pore network model is a simplified model of the pore structure of the geo-media. The model simplifies the complex flow path (pores, throats, etc.) in the geo-media into regular geometric shapes, such as spheres and cylinders. The rules are developed so that the model has a similar seepage performance as the actual geo-media. Fatt [37] first proposed the two-dimensional equivalent pore network model. The methodology gradually evolved from two-dimensional to three-dimensional and now developed into equivalent pore network models suitable for simulation of various geo-media.

The equivalent pore network model consists of pores and throats. The pores represent the larger part of the cavity in the geo-media. The pores are connected by the throat, where fluid migration occurs. The radii of the pores are all variable, but their positions are regularly arranged on grid points; that is, the distance between adjacent pores is a constant value, the purpose of which is to simplify the calculation. The shape of the throat is a

cylinder whose radius is calculated according to the BACON key formula to ensure that the seepage property is like the actual structure[38,39]. A pore can be connected to the surrounding 26 pores with pore throats[40]. The average number of surrounding pores varies according to the geomaterial. The average number of active connections is called the "coordination number." By adjusting the size of the pore radius, pore throat radius, and pore coordination number, a pore network model can be developed to simulate the seepage characteristics of geo-media.

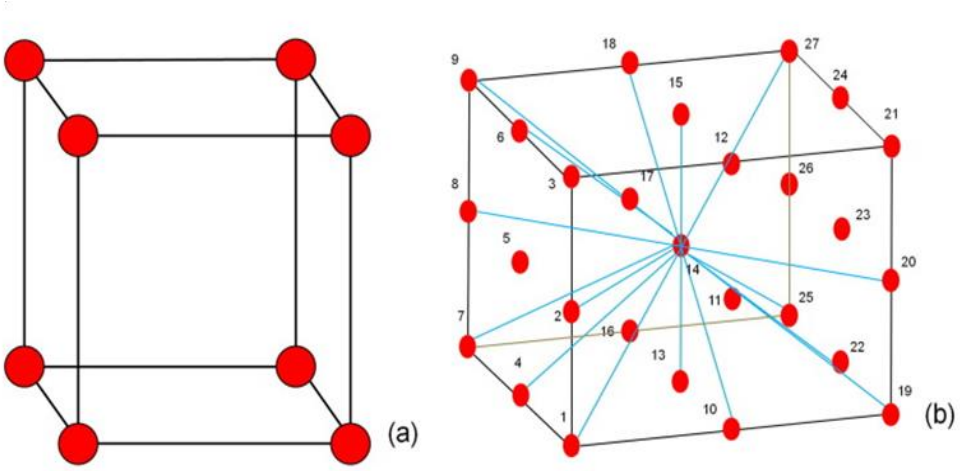

Figure 2.7 (a) Cubic lattice with a constant coordination number of six (b) cubic lattice with 26 pore coordination number.

Pore network model developed by Zhang et al.[41] will be used in this research. The above model is an isotropic one. However, shale is an anisotropic material. Hence, the above model will be first modified to be used for actual shale. This modified model will be validated using actual measured permeability data. This validated model with experimentally determined pore structure of virgin shale and pre-treated shale will be used to predict the permeability of virgin shale and pre-treated shale to quantify the impact of fracturing fluids on the deterioration of shale gas production with time. Also, the softening

process of water-clay interaction will be incorporated by changing the geometry of pore network modeling to predict shale gas production with time.

CHAPTER 3

SHALE SOFTENING AND ITS IMPACT ON NANO-SCALE PROPERTIES

3.1 Introduction

Hydraulic fracturing involves the injection of high-pressure fracturing fluid into the shale formation to produce a complex fracture network, facilitating the extraction of adsorbed or stored shale gas stored in micro and nanopores. Though approximately 50% of the fracturing fluid is recovered after hydraulic fracturing, the balance is retained in the shale formation. These trapped fracturing fluids interact with the shale formation and reduce the permeability and hence, the gas productivity of the shale formation [42].

Although the current hydraulic fracturing technology for shale gas production has been widely used, the geochemical reactions and physical changes due to the shale-hydraulic fracturing fluid reaction and the factors contributing to those reactions are not well understood. Several studies have shown shale swelling due to the interaction of retained and fracturing fluid with clays in shale. Johnston and Beeson [43] analyzed the permeability of more than 1,200 oil sand samples from 107 wells in 43 zones. They showed that approximately 70% of the sands showed significant and distinct permeability change due to injected freshwater. Morris et al. [44], based on flood tests designed to measure steady flow rate on reservoir cores containing 8% swelling clays, showed that the average permeability decreased by 92.5%. Goldenberg et al. [45] showed a reduction in porosity due to a logarithmic decrease in the overall connectivity of highly reactive smectite minerals.

Due to retained fluid from hydraulic fracturing, exchangeable cations between clay layers of shale formations are hydrated, and the space between clay layers is increased.

Fink et al. [46], Krishna Mohan et al., [47], Norrish [48], Zhang, and Low [49] showed that the two active pathways of clay swelling, namely crystalline and osmotic swelling, and hence potential porosity reduction. Wilson et al. [50] showed the swelling of North Sea sandstone formation due to clay content. Davy et al. [51] showed that for poorly connected sedimentary rocks with low porosities ranging from 1% to 5%, fractures heal when in contact with fracturing fluids.

Clay swelling hinders gas flow and reduces the effective permeability of shale [51,52]. Simultaneously, hydration weakens the binding of mineral particles, thereby further decreasing fracture aperture and hydraulic conductivity. Although laboratory-scale water-clay interaction experiments provide valuable preliminary data on the physical and chemical interactions between shale and fracturing fluid, most of these absorption experiments were performed at low temperatures and low pressures [44,45]. Field shale reservoirs are usually at high temperatures and subject to high pressures. Several researchers have performed high temperatures and high-pressure laboratory shale softening studies to simulate the processes that occur in reservoirs. Du et al. [15] used deionized water for 48 hours without heating or applying pressure to soften the shale and degradation of mechanical properties after treatment. However, water-clay interaction will be different for actual natural gas reservoirs subjected to high temperature and pressure. Wu and Sharma [26] showed that carbonate-acid reactions could be another reason for the porosity change for the interaction of shale formations with slickwater containing a mild acid solution of pH ranging from 5.6-6.8. Sun et al. [29] used simulated slick water with a 1% clay-control agent at 100°C and 50 MPa for 72h to simulate site conditions. The typical composition of slickwater is not freely available and is a trade secret in the fracturing

industry. Hence, it is not easy to quantify and standardize additives to simulate actual site conditions for shale softening experiments. Therefore, clay control agents, along with pH controllers, should be eliminated to simplify the measurements. Therefore, deionized water was used in this research to investigate the clay-swelling. The primary objective of this research is to identify the impact of mineralogy on the change in micro and nano porosity of shale during hydraulic fracturing of shale.

The clay-water reaction is complex, with several factors controlling, leading to variable test outcomes. As a result, several high-temperature and high-pressure shale immersion tests were performed to determine the impact of water-based drilling fluid on the physical properties of gas-bearing formations. Subsequently, low-pressure nitrogen absorption-desorption (BET) experiments, porosity, and density tests were performed on four different shales to measure the change in the distribution of pore sizes and the change in porosity. The final purpose of this measurement is to estimate the decline in shale gas production over time by quantifying the shift in pore structure and reducing the permeability of shale due to the interaction of shale with drilling fluid resulting in shale softening. The pore network model will then be used to simulate the decline in permeability decline with a softened shale structure.

Therefore, several experiments will be performed to obtain the physical parameters of shale before and after softening to quantify the shale softening. The required parameters for the pore network model are porosity, pore size, pore throat, and specific surface area of the virgin and treated shale, along with C.T. and SEM images. The details of the experimental methodology, including sample preparation, experiment condition, special treatment of the sample, data processing, and initial results, is shown below.

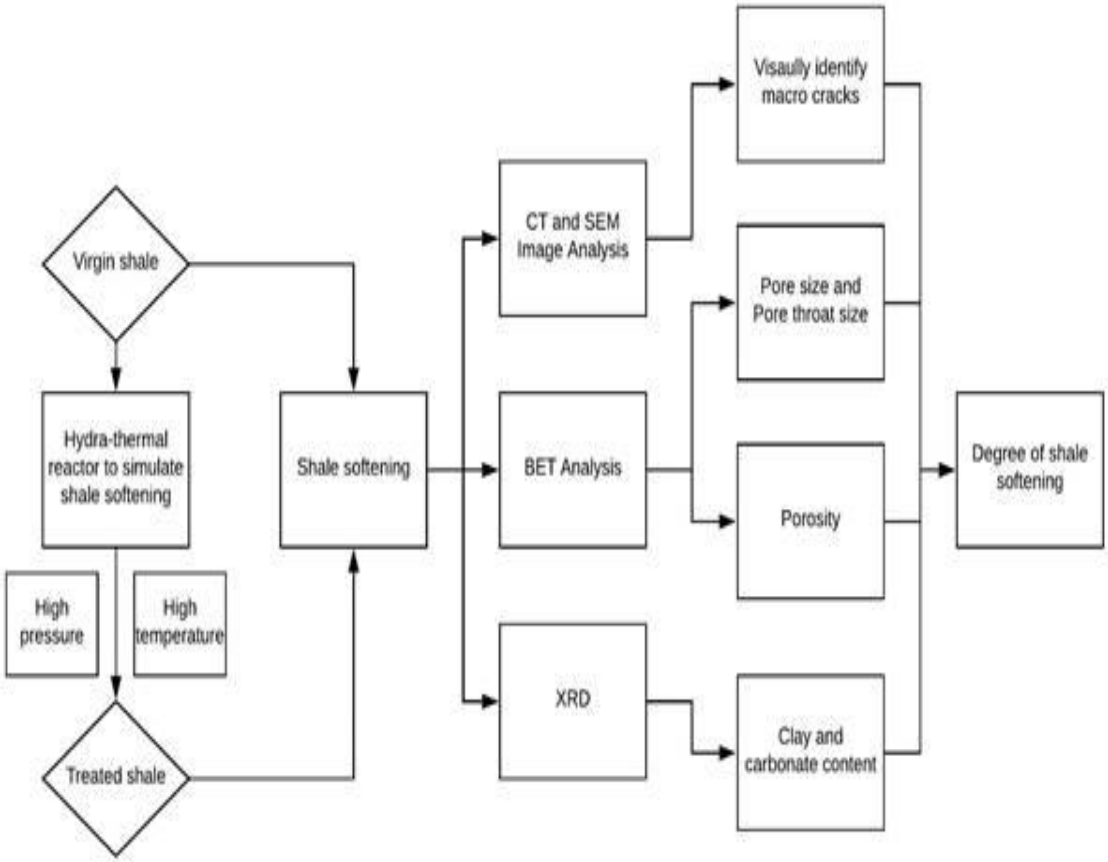

Figure 3.1 Flow chart of the whole tests.

3.2 Sample Preparation

The clay-rich shale is extremely sensitive to water due to its tendency to react with moisture. Drying and cracking of a shale sample are encountered if in contact with the moisture in the environment. Hence, cores samples used in this research were carefully stored in containers to provide a moisture-free and constant-pressure environment before the softening experiments [53].

Shale samples of Hayneville, Longmaxi, Eagle Ford, and Opalinus formations were cut into smaller pieces using a low-speed precision cutter, as shown in Figure 3.2 (model

type–minitom manufactured by Struers). This machine allows producing accurate $1cm^3$ cubic shale samples, as shown in Figure 3.3. Pure ethanol is used as a cooling fluid to cool the cutter instead of water to prevent water interaction with the shale before the treatment. To fit the hydrothermal reactor (shale treatment reactor), the shale sample size must be smaller than 1cm*1cm*1cm. Several powder samples were also prepared before the treatment from four shale samples. The powder samples were prepared using a grinding machine shown in Figure 3.4 (model type Brinkman manufactured by Restsch), which allows a sufficient amount of 80-100 mesh size for BET tests.

Figure 3.2 Low-speed precision cutter.

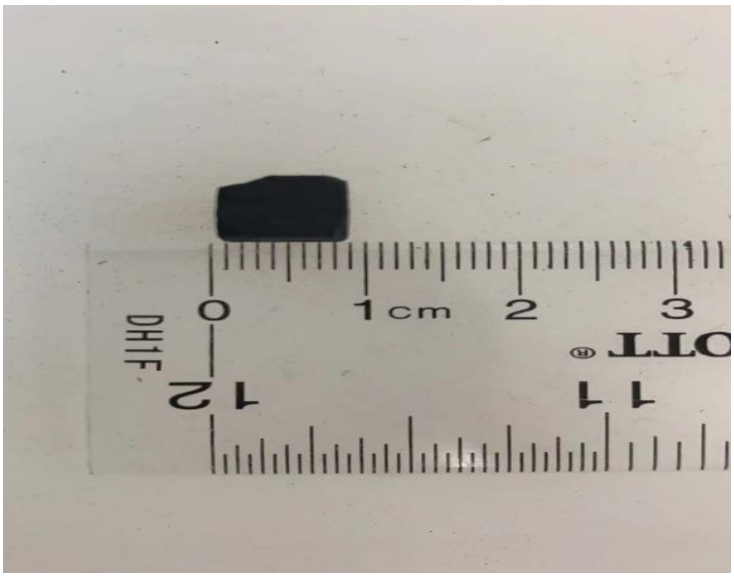

Figure 3.3 Sample size.

Figure 3.4 The Grinding machine.

There are two sizes of the sample that need to be prepared before the softening, one type is powder samples, and another is cubic samples. The powder sample will be used for

XRD and BET tests. The cubic sample will be used during Water-treatment, CT, and SEM tests.

3.3 Shale Treatment

The shale treatment experiments were performed using a specially designed test setup. The main component of the test setup consists of a hydrothermal reactor. High pressure was supplied using inner liquid nitrogen gas for this core treatment chamber. The hydrothermal reactor was immersed in a constant temperature water bath. This treatment chamber simulated high-temperature and high-pressure fluid-rock interaction. Before the treatment test, the setup connections were checked because each shale sample must be inside the chamber for three days to achieve the softening. Nitters et al. [54] provided the typical breakdown of fracturing fluid, as shown in Table 3.1. Wu and Sharma [26] and Sun et al. [29] suggested that using mild acids can accelerate the shale softening.

Table 3.1 Accepted Level for Water-based Fracturing Fluids

Source: [54].

Item	Value
pH	6 to 8
Iron	< 10 ppm
Oxidizing agents	None
Reducing agents	None
Carbonate*	< 300 ppm
Bicarbonate*	< 300 ppm
Bacteria	None
Cleanliness	Reasonable

*Higher carbonate/bicarbonate content requires further pilot testing on gel break and crosslinking.

This device is called a hydra-thermal reactor (CIT-XHTC400-V25B manufactured by Columbia international) with a chamber volume of 25 ml. This reactor was connected to a

high-pressure gas cylinder and heating device with pressure and temperature measuring devices. The maximum operating temperature and pressure are 400 °C and 30 MPa, respectively. Barbot et al. [55] suggested that the fracturing fluid injected into the typical formation is around 48-68Mpa. Also, Shaffer et al., [56] and Estrada and Bhamidimarri, [57] indicated in their research that the temperature of slickwater is usually around 65 ℃ to 100 ℃.

Furthermore, before the tests, the whole setup was checked for leaks to ensure it is fully sealed. The treatment chamber was filled with DI water, and the original cubic shale was fully immersed in the simulated fracturing fluid. A 1200 psi pressure was applied to the hydrothermal reactor, and the reactor was kept at a 100℃ constant temperature water bath for 72 hours to simulate the actual field conditions [58–60].

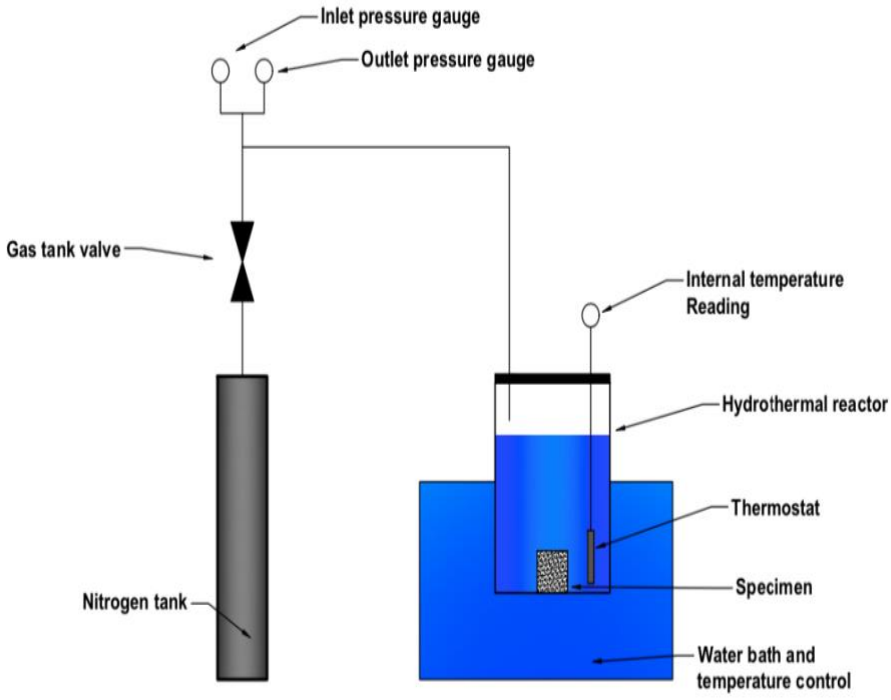

Figure 3.5 Schematic shale treatment setup.

In order to prevent the water evaporation from the water bath, it was covered using a plastic tarp during the test. After the test, the shale sample was placed inside an oven at 70°C under controlled humidity and moisture for 24 hours before the BET analysis. In this research, shale samples were subject to deionized water at 1200 psi and 100℃ for 72 hours to simulate shale softening. There were five main reasons for the use of deionized water, which are summarized below:

1. The concentration of electrolytes in water can reduce the potential swelling by reducing the diffuse double layer (DDL)[61].

2. The high salt concentration in slickwater can affect the physical properties of clay by causing fine particles to bind together to aggregates or flocculate. Flocking can reduce surface area and decrease free swell and swell pressure [62].

3. The swell potential can decrease with cation exchange between water and clay and prevent water entry between the layers [63]. In addition, the DDL thickness decreases with salt concentrations leading to the collapse of the clay structure and reducing swelling potential [64].

4. Also, high sodium ion concentration can cause divalent ions such as calcium, which appear to lower DDL in water samples, to be replaced. Therefore, the swell potential decreases with an increased sodium concentration in the slickwater [65].

5. The high temperature and pressure have a significant impact on shale-fluid interactions, which control shale treatment. The addition of chemicals will also increase the mineral dissolution rate, intensified by high temperatures, leading to the breakdown of the integrity of the shale structure.

Hence, chemicals should be excluded when investigating the pure clay interactions in shale formations. The following is a table for the testing conditions for four core samples.

Table 3.2 Condition of softening experiment

Sample	Sample size	Pressure	Temperature	Fluid	Duration
Haynesville	1cm^3 cubic	1200 psi	100℃	DI water	72 hours
Eagle Ford	1cm^3 cubic	1200 psi	100℃	DI water	72 hours
Longmaxi	1cm^3 cubic	1200 psi	100℃	DI water	72 hours
Opalinus	1cm^3 cubic	1200 psi	100℃	DI water	72 hours

Figure 3.6 Softening setup.

The actual setup was shown in Figure 3.6, including a hydra-thermal reactor, a Nitrogen tank, a constant water bathing device, and thermal-pressure gauges. Figure 3.7 shows the positioning of the shale sample and thermal reactor.

Figure 3.7 Combination of the water bath and hydrothermal reactor.

3.4 XRD Analysis

The X-ray diffraction (XRD) data from four shale samples were used to determine the mineralogy. The mineralogical study is critical to explain the shale softening mechanism based on the clay content of shale. With higher clay contents in a shale formation, a more significant clay-water reaction is expected [46,48]. Also, clay content varies over a wide range in different formations; hence the determination of clay content is essential to quantify the degree of shale softening. The carbonates may also contribute to shale softening. Therefore, the mineralogy study included the quantification of both clay and carbonate contents using XRD tests. Thus, XRD was performed before and after the treatment tests for all shales.

The original and treated shale samples were cleaned, dried, and grounded to a size smaller than 120 μm to be used for mineralogical analysis. The same procedure was followed for the treated shale. A copper source of 40kV and 40mA was used for the XRD, and the shale powders before and after treatment were subjected to diffraction angles (2θ) between 5° and 60° at a scan rate 1°/min [66].

X-ray diffraction (XRD) is a modern technology used to detect the mineralogy and elements in shale samples. The mineralogy study is critical to observe shale softening mechanisms based on the clay content of shale. The higher the clay contents in a shale formation, the greater the clay-water reaction. Also, clay content varies within a wide range, so the determination of the clay content is essential to quantify the degree of shale softening. The carbonate may also contribute to shale softening. Hence mineralogy of both clay and carbonate content will be quantified using laboratory tests. Thus, XRD will be performed before and after the softening tests for all shales.

Figure 3.8 XRD powder sample.

The detailed XRD preparation procedure is summarized below. The powder sample shown in Figure 3.8 must be kept away from moisture. To make reasonable comparisons,

the same amount of sample powder was used for the XRD test. The sample preparation must be followed as exactly described below to keep the data consistent. There are several essential steps for the XRD experiment as following.

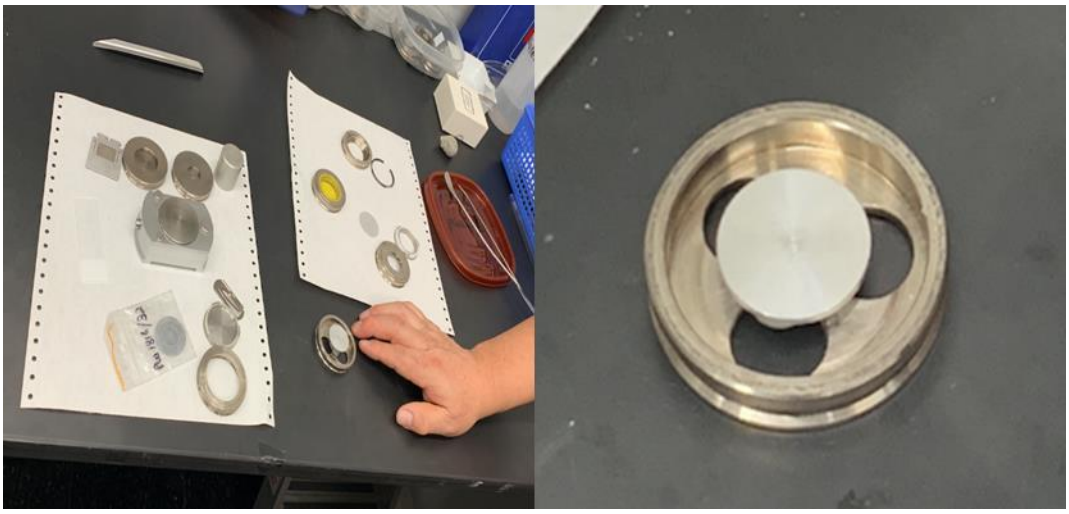

Figure 3.9 Accessories for sample preparation, powder sample preparation, and installation.

Figure 3.9 shows the accessories and holders of the powder samples. The powder sample has different holders, and handling the powder sample requires much more attention than a solid sample. To keep everything consistent, the following steps were followed, as shown in Figures 3.10 and 3.11.

After sample preparation, the sample stage was selected for the spinning stage. The mounting of powder and selection of suitable slits was based on the sample size and accuracy. In our case, the shale powder holder was 16 mm, and the mask size was 10 mm based on the starting angle of 5 degrees, as shown in Figure 3.12. The Soller silt and divergence silt must be changed manually, shown in Figure 3.13.

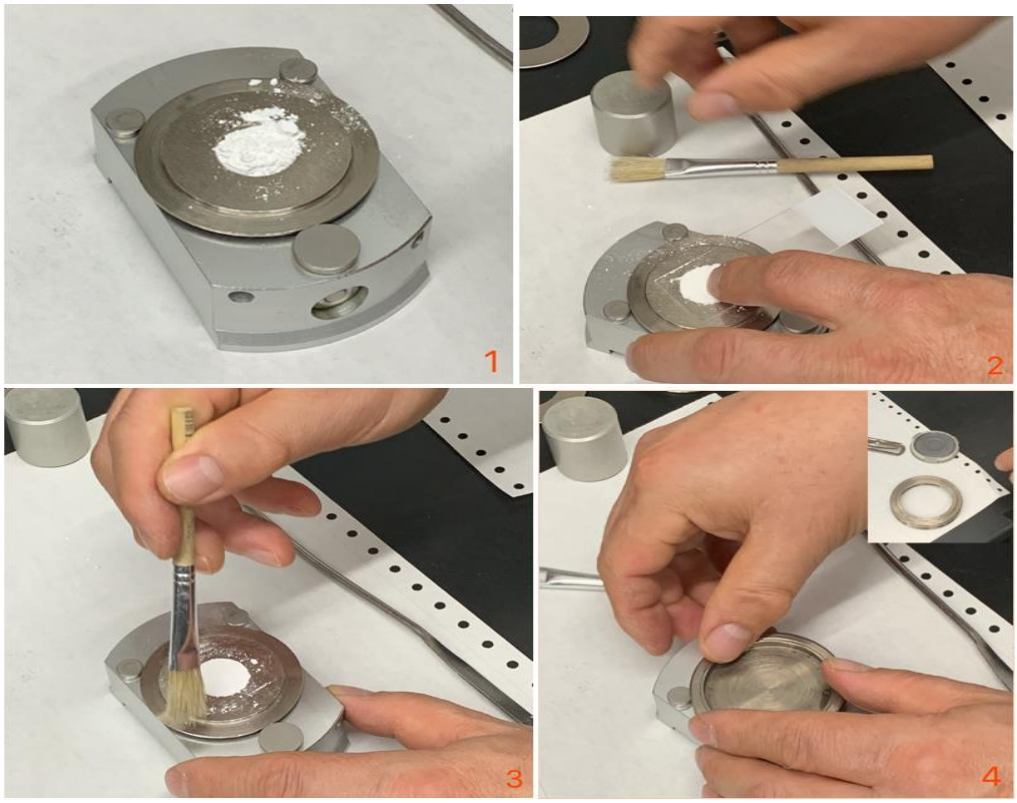

Figure 3.10 Powder sample preparation. 1) powder sample after filled into the groove; 2) sample compact using glass slide; 3) sample remains cleaning; 4) sample covered using lids after wiping.

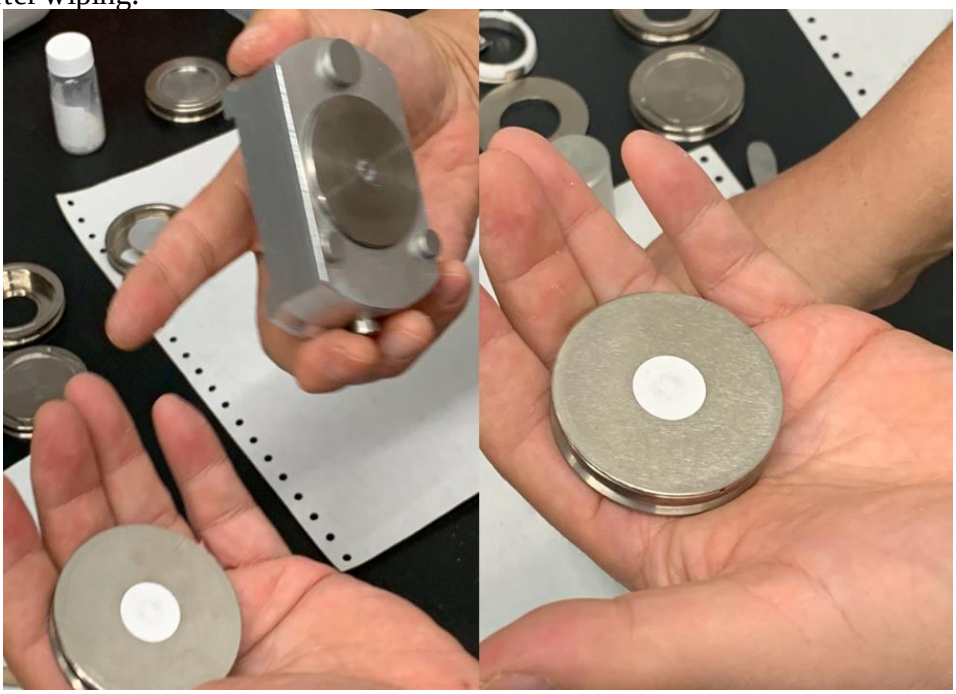

Figure 3.11 Alignment of the sample.

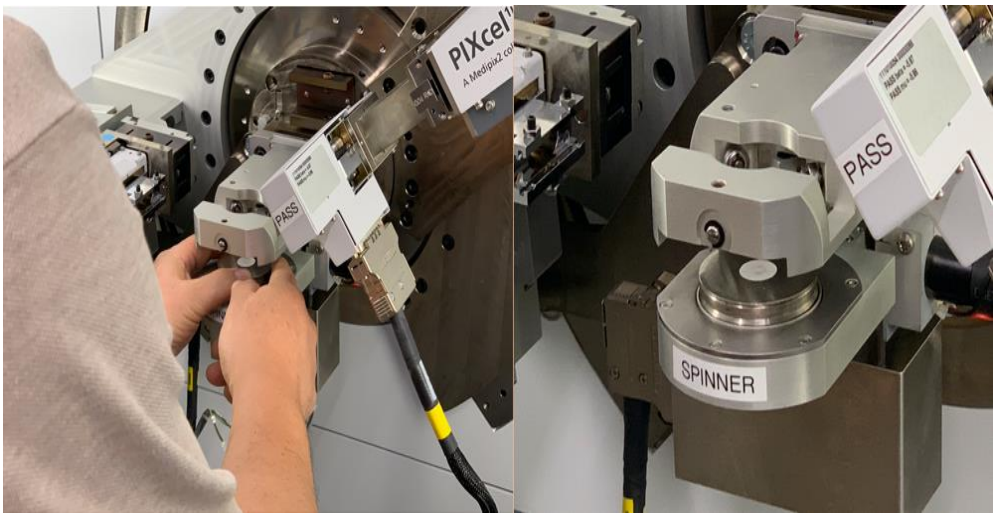

Figure 3.12 Sample mounting. 1) Placing the sample; 2) Sample position and placement.

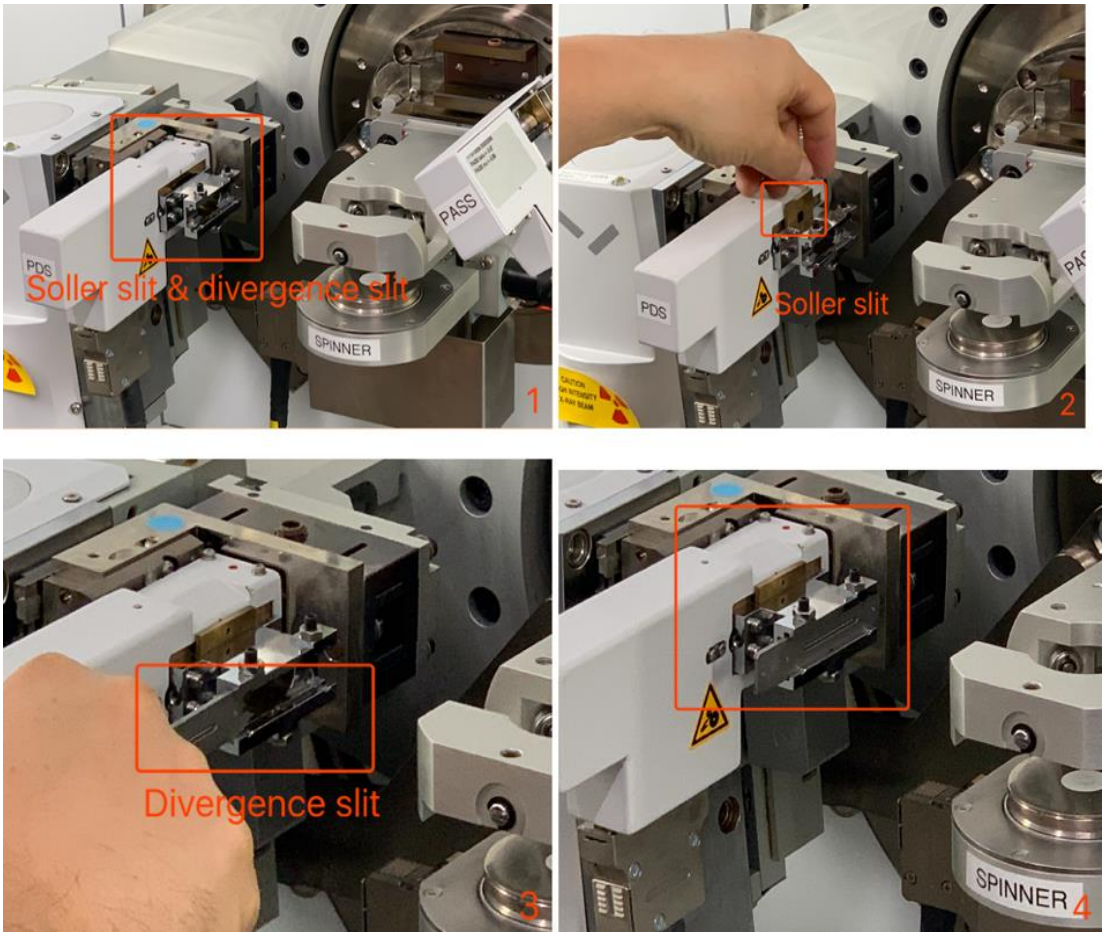

Figure 3.13 Installation of Soller slit and divergence slit. 1) uninstalled unit; 2) installation of Soller slit; 3) installation of divergence slit; 4) complete installation.

3.41 XRD data analysis

The XRD results are the peak value of each crystalline over the scanning angles. Thus, by matching the database of known crystalline patterns, one can quantify the mineralogy of a particular powder or solid using the Rietveld method.

Table 3.3 Parameter of XRD Scanning of Original Shale Powder

Raw Data Origin	XRD measurement
Start Position [°2Th.]	5.0117
End Position [°2Th.]	69.9857
Step Size [°2Th.]	0.013
Scan Step Time [s]	8.67
PSD Length [°2Th.]	3.35
Offset [°2Th.]	0
Divergence Slit Type	Fixed
Divergence Slit Size [°]	0.125
Specimen Length [mm]	10
Measurement Temperature [°C]	25
K-Alpha1 [Å]	1.5406
K-Alpha2 [Å]	1.54443
K-Beta [Å]	1.39225
K-A2 / K-A1 Ratio	0.5
Generator Settings	40 mA, 45 kV
Diffractometer Type	11131886
Diffractometer Number	0
Goniometer Radius [mm]	240

Using high-score-plus, which is the advanced XRD data handling software, the quantification of mineralogy can be summarized into a detailed peak list. The same procedure was followed when scanning the powder of softened shale, and the same mineralogy was applied to quantify the change in mineralogy.

Table 3.4 Peak List of Original Shale Powder

Pos. [°2Th.]	Height [cts]	FWHM Left [°2Th.]	d-spacing [Å]	Rel. Int. [%]
5.1265	16.62	0.0384	17.23827	0.98
5.2682	1.22	0.0640	16.77498	0.07
5.7362	19.21	0.0384	15.40728	1.13
5.8195	21.20	0.0640	15.18702	1.25
6.0190	20.89	0.0384	14.68405	1.23
6.2782	26.15	0.0512	14.07838	1.54
6.7515	39.34	0.0512	13.09243	2.32
8.8489	147.00	0.0512	9.99346	8.68
9.3031	16.47	0.0384	9.50649	0.97
9.9445	8.53	0.0384	8.89477	0.50
10.0445	19.93	0.0384	8.80645	1.18
10.7920	6.64	0.6140	8.19810	0.39
11.6627	14.96	0.2047	7.58791	0.88
11.9454	35.34	0.0640	7.40895	2.09
12.0853	34.75	0.0256	7.32352	2.05
12.5148	83.31	0.1023	7.07312	4.92
13.3334	16.00	0.0512	6.64064	0.94
14.2691	22.74	0.0384	6.20722	1.34

Table 3.5 Continued

14.4131	23.58	0.0384	6.14552	1.39
15.1278	12.14	0.0768	5.85677	0.72
15.3845	8.44	0.0384	5.75963	0.50
15.5413	16.55	0.0768	5.70187	0.98
16.0981	14.32	0.0512	5.50586	0.85
16.4153	20.77	0.0384	5.40017	1.23
17.3610	21.19	0.0384	5.10810	1.25
17.7605	25.39	0.1535	4.99408	1.50
18.1226	30.37	0.0384	4.89510	1.79
18.8198	10.29	0.1535	4.71532	0.61
18.9371	14.96	0.0384	4.68636	0.88
19.0815	4.15	0.0768	4.65124	0.24
19.7903	82.10	0.0768	4.48622	4.85
20.8452	305.54	0.0512	4.26151	18.03
21.3090	12.38	0.0384	4.16979	0.73
21.4785	3.29	0.0384	4.13726	0.19
21.6154	20.13	0.0384	4.11136	1.19
22.0120	29.36	0.1279	4.03819	1.73
22.6119	4.68	0.0640	3.93238	0.28
23.0827	40.49	0.0768	3.85324	2.39
23.5532	24.52	0.1023	3.77732	1.45
24.2576	20.35	0.2047	3.66920	1.20
25.1406	40.12	0.1279	3.54230	2.37
26.6294	1694.17	0.0512	3.34754	100.00

Table 3.6	**Continued**			
27.9295	87.97	0.0768	3.19461	5.19
29.4039	251.72	0.0768	3.03768	14.86
30.8000	10.14	0.1535	2.90310	0.60
31.2201	8.88	0.1535	2.86500	0.52
31.8737	5.73	0.3070	2.80771	0.34
33.0072	29.55	0.1791	2.71384	1.74
33.9240	7.52	0.1023	2.64257	0.44
35.0076	47.82	0.3070	2.56322	2.82

3.42 Minerology of Shale

The XRD results show the peak value for each crystalline material over the scanning angles. By matching the database of known crystalline patterns, one can quantify the mineralogy of a particular powder or solid using the Rietveld method [31,67–69]. Figure 3.14 shows the XRD results for the Haynesville shale. Using high-score-plus, the advanced XRD data handling software, the quantification of mineralogy can be summarized into a pie chart for Haynesville shale, as shown in Figure 3.15. Figure 3.15 shows that the average mineralogy of Hayesville shale was as follows: 24.1% Quartz, 43.2% Illite, 0.9% Kaolinite, 0.6% Chlorite, 2.5% Pyrite, 17.9% Pyrite, and 3.0% Dolomite.

Although there were minor differences between the measured and the reported, the measured results are comparable to those reported [70,71]. Table 3.5 summarizes the results of all the shales used in this study.

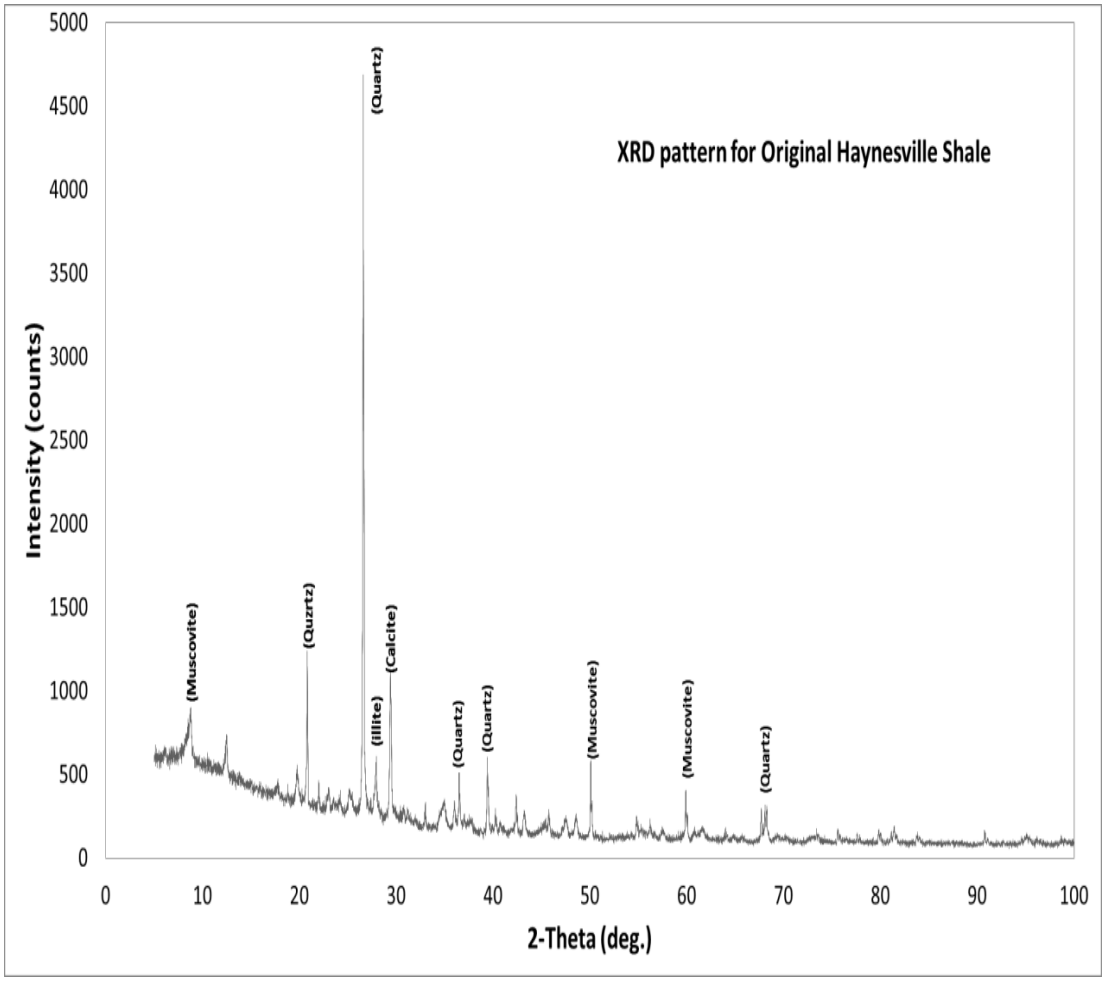

Figure 3.14 XRD pattern of original Haynesville shale

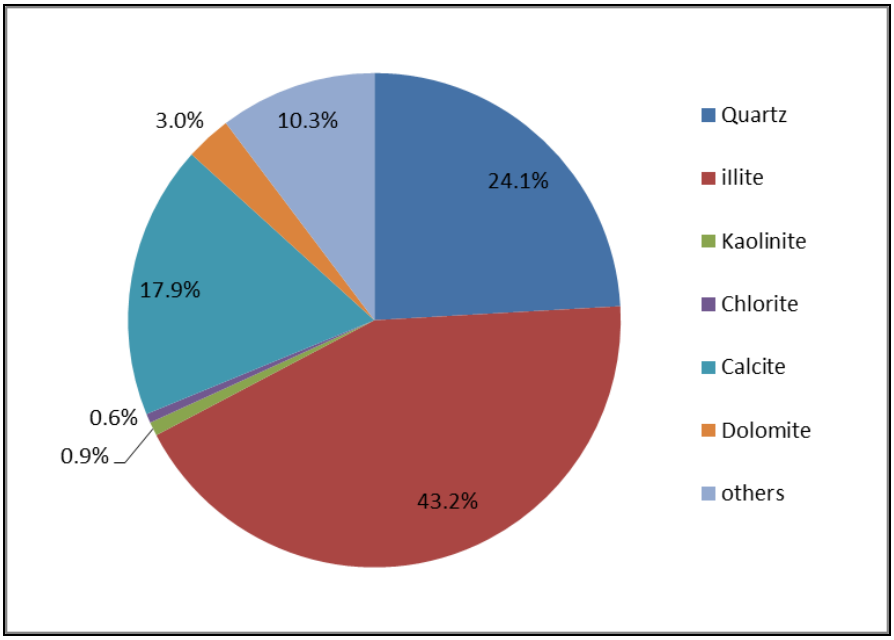

Figure 3.15 Mineralogy chart of Haynesville shale.

Table 3.7 Mineralogical Composition of Four Shales (%)

Shale	Quartz	illite	Kaolinite	Chlorite	Total clay	Calcite	Siderite	Dolomite	Total Carbonate
Opalinus	13.5	44.2	18.1	3.4	65.7	12.8	0.7	1.3	14.1
Haynesville	24.1	43.2	0.9	0.6	44.7	17.9	0	3	20.9
Longmaxi	36.3	35.6	0.8	0	36.4	2	0	10.3	12.3
Eagle Ford	20	3.4	2.2	0	5.6	60	0	4	64

3.5 BET Measurements

Before the treatment test, the density in g/cm3 of each shale was determined, and they were 2.29 for Opalinus, 2.53 for Haynesville, 2.58 for Longmaxi, and 2.43 for Eagle Ford.

The BET analysis aims to determine the absorption and desorption patterns of powder samples, in this case, shale before and after treatment, using the Autosorb machine (model

type Autosrob-iQ manufactured by Quantachrome Instruments). All test samples were first dried in a vacuum for 12 hours under a constant temperature of 150°C before BET tests. The pore volume was determined using the Density Functional Theory (DFT) model [72–74].

After 12 hours of degassing and a full isotherm gas sorption test, both sample powder before and after shale treatment were tested under the same conditions, including degassing pressure and temperature, loading condition, and same liquid N_2. Finally, based on the raw data, the porous media-absorption and desorption graphs for four shale samples before and after treatment were obtained.

After 12 hours of degassing and 24 hours of full isotherm gas sorption test, both sample powder before and after shale softening will be tested under the same parameters, including degassing pressure and temperature and loading condition for the same partial pressures of N_2. To ensure that the test was comparable, the same weight of the test sample was also used to ensure that the weight does not affect the test. Finally, the classic porous media-absorption and desorption graph was obtained based on the raw data, as shown in section 3.61.

Figure 3.16 Autosorb iQ manufactured by The Bruker.

There are major peak changes in the absorption and desorption patterns between the original and softened samples. After softened, shale absorbed more volume of gas per gram than original shale. Most importantly, based on the absorption and desorption patterns and DFT method, the pore size distribution of both original and treated shale can be generated, as shown in the next section.

The experiment is designed to obtain the pore size distribution (PSD) for the same sample but with different treatment conditions. The major peak changes during the shale softening indicate that softening impacts the structural parameter of shale. The peak of softened shale decreases after shale treatment, and this peak change proved that clay swelling is the primary interaction during hydraulic fracturing.

3.51 Pore Size Distribution of Original and Treated Shale

Based on density functional theory (DFT) [75], the BET results can be converted to pore size distribution, as shown in Figures 3.17. The pore size distributions in Figure 3.17 show subtle differences between the untreated and treated shale samples. However, the maximum amount of N_2 adsorbed at the highest pressure changed.

The pore size distribution can be used to quantify the changes in the pore structure of shale samples. The pore size distributions of the four shales indicated that the shale pore structure is multimodal, where at least two significant peaks can be found in all pore sizes. The pore volumes of four shales reduced from pore sizes of 1nm to 5nm. However, after treatment, pore volumes of the Eagle Ford shale significantly reduced compared to the untreated samples, indicating a substantial change in micropores during treatment. Figure 3.17 shows that the peaks for the four shales are around 1 nm and 7 nm based on the half pore width. The pore size distribution of the original four shales was altered after softening treatment.

Figure 3.17(b) shows a significant change in peak volumes for Eagle Ford shale from 2nm to 6nm. In this case, a large amount of inner Illite/Smectite (I/S) layer structure contributed to a substantial change in pore sizes with clay swelling. Also, it was observed that after treatment from Figures 3.17(a), (c), and (d), the pore volumes of Haynesville, Longmaxi, and Opalinus shale have slightly reduced from pore sizes 0.7nm to 2.1nm.

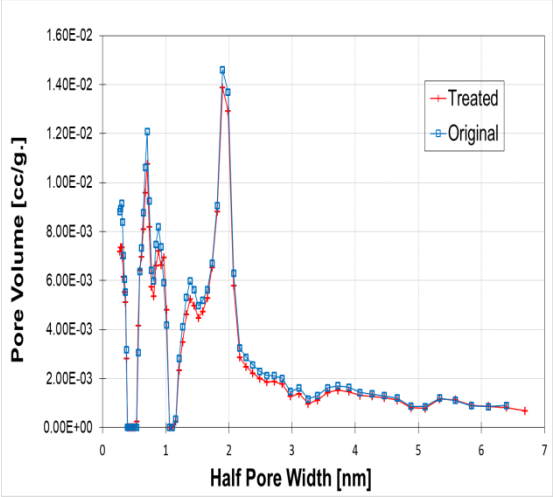

(a) Haynesville Shale

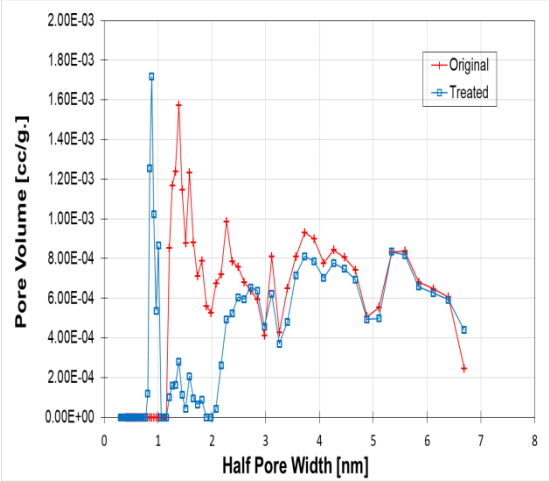

(b) Eagle Ford Shale

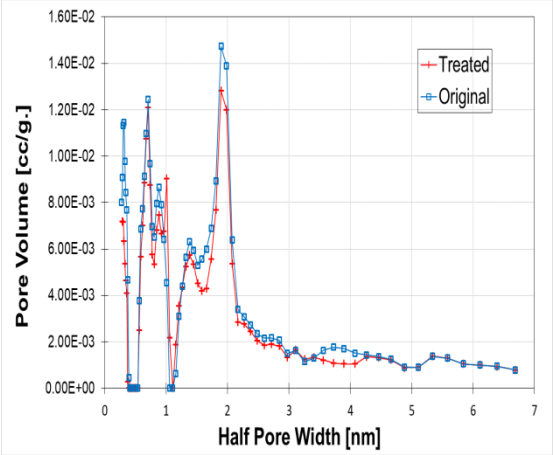

(c) Longmaxi Shale

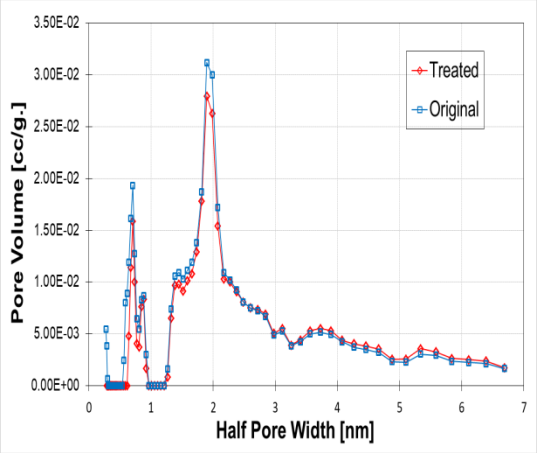

(d) Opalinus Shale

Figure 3.17 Pore size distribution comparison before and after treatment.

After integration, the cumulative volume of the four shales was calculated and is reported in Table 3.4. Before each BET test, the dry weight of powder samples was measured using a highly sensitive scale. Hence, the porosity can be calculated by knowing the density of each shale. The volumetric density of each original and treated shale was

obtained from BET analysis, and powder mass was used to calculate porosity. It should be noted that the possible mass loss after the heating and degassing was neglected.

Table 3.8 Variation in Porosity between Original and Treated Shale

Sample	Volume/mass (Original)	Volume/mass (Treated)	Porosity(original)	Porosity (Treated)
Longmaxi	0.0177 cc/g	0.0164 cc/g	1.58%	1.06%
Eagle Ford	0.0168 cc/g	0.0148 cc/g	4.40%	3.80%
Haynesville	0.0401 cc/g	0.0322 cc/g	2.94%	1.84%
Opalinus	0.0368 cc/g	0.0346 cc/g	7.80%	3.80%

From Figure 3.17, the major peak of Haynesville, Longmaxi, and Opalinus shale is around 2 nm, while that for Eagle Ford shale was around 1 nm. It was also observed that the major peak of Eagle Ford shale shifted to 2nm after treatment, indicating the pore structure was altered due to the clay-water reaction. While Figure 3.17 (a), (c), and (d) show no evidence of shifting of peaks, the I/S layer would be the primary reason for such changes. However, after treatment, the PSDs of all four shales decreased.

The clay content of tested shale varies from 65.7% (Opalinus shale) to 5.6% (Eagle Ford). The porosity comparison of four original and treated shale and the calculated loss in shale porosity were plotted with the total clay content shown in Figures 3.18. A linear correlation between clay content of four shales and porosity reduction rate after softening was obtained with the following relationship:

$$\mathbf{Y = 0.6239x + 10.042,\ R^2 = 0.9995.}$$

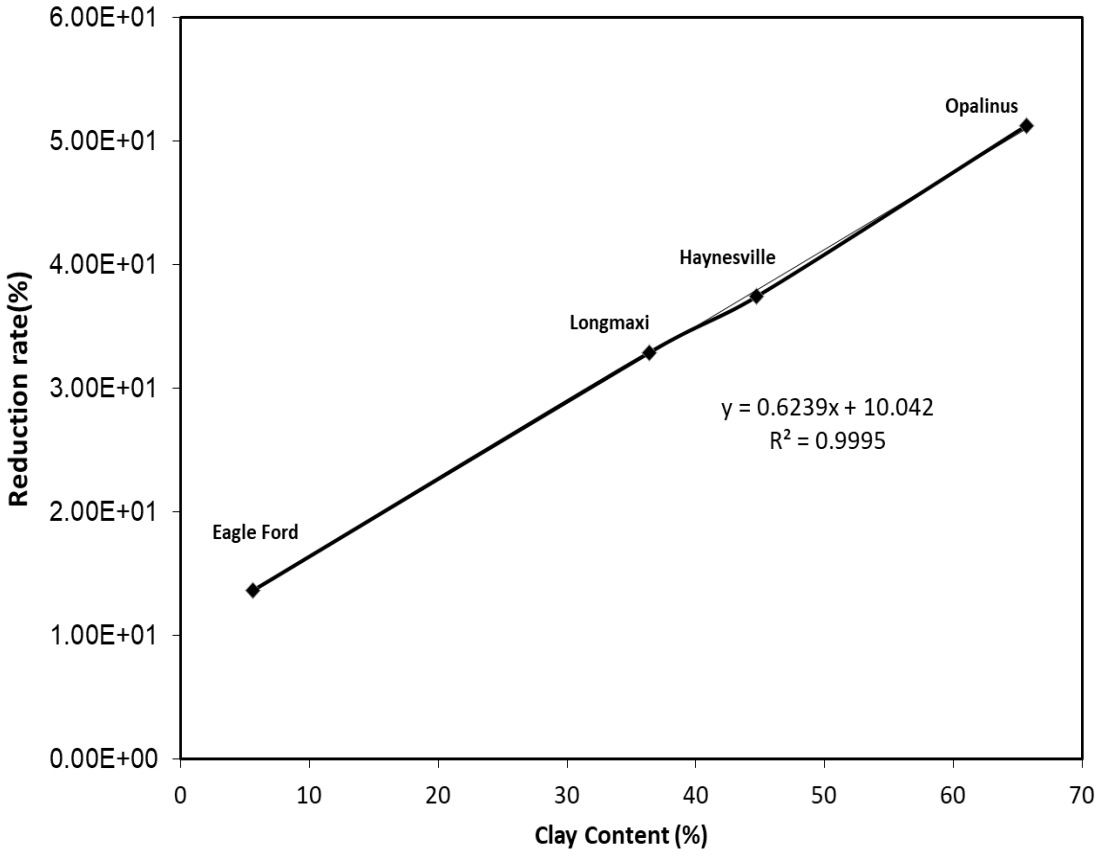

Figure 3.18 Correlation between clay content and porosity loss.

3.52 Absorption-Desorption Curves

The shape and hysteresis of low-temperature N_2 adsorption-desorption isotherms can effectively characterize the pore morphology of shale [76]. According to the International Union of Pure and Applied Chemistry (IUPAC) classification, isotherms can be divided into six types (I to VI), and their hysteresis modes are designated as Type A to Type D [77–79]. Figure 3.19(a) shows the N_2 adsorption-desorption isotherms Haynesville shale before and after treatment. According to the IUPAC classification, the N_2 adsorption isotherms and hysteresis modes of all tested shale samples can be classified into Type IV isotherms [80]. At a lower relative pressure ($P/P_0 < 0.01$), the amount of adsorbed gas in

all tested shale samples was low, while at a higher relative pressure (P/P_0 >0.9), the amount of adsorbed gas sharply increased. This phenomenon indicates that micropores and mesopores with few large pores (larger than 50nm) contribute to the total porosity of samples. Figure 3.19 (b) shows the isotherm comparison for Eagle Ford shale, described as the Type III hysteresis. The Eagle Ford hysteresis loops are type C, demonstrating that in the Eagle Ford shales, slit-formed pores are the primary pores. Previous studies have shown the relation of plate-like pores in clay minerals [81,82].

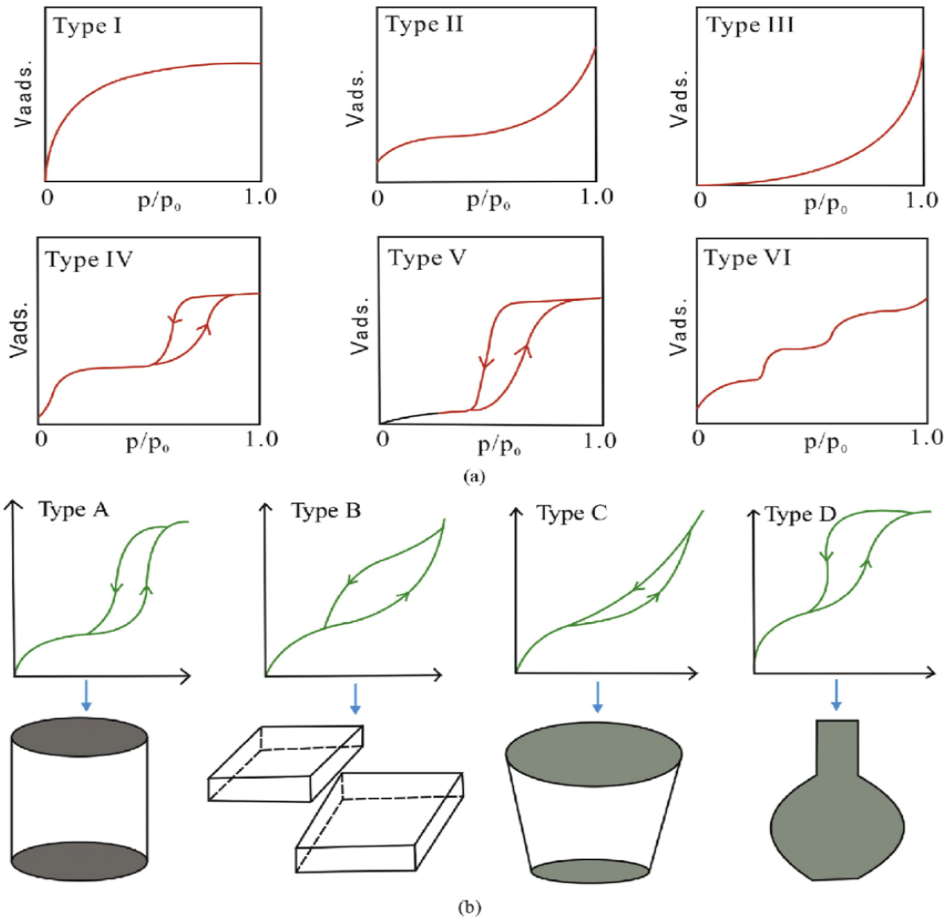

Figure 3.19 Adsorption isotherm types (a) and classification of hysteresis loops and their related pore shapes (b).

Source: [83,84].

The different compositions of clay minerals can cause variations in hysteresis loops types of Type III and Type IV [85]. The type D hysteresis loops of the remaining three shale samples indicate that the pore shape of these shale samples may be bottle-shaped pores (with narrow necks and large pore bodies)[86].

For the Opalinus shale, the N_2 adsorption capacity decreased from 0.0368 cc/g to 0.0346 cc/g by comparing the peak values from the isotherm graphs. The volumetric density was performed using the BET equation: both total volume and mass of the sample were treated to reflect the decrease in the N_2 adsorption capacity of shale after treatment. Similarly, the maximum N_2 adsorption capacity of Longmaxi, Eagle Ford, and Haynesville shales decreased from 0.0168 cc/g to 0.0148 cc/g, 0.04 cc/g to 0.032 cc/g, and 0.0177 cc/g to 0.0164 cc/g, respectively, indicating that the N_2 adsorption capacity of all shale samples decreased after treatment. The adsorption capacity is mainly related to the number of micropores and mesopores. Therefore, the change in the N_2 adsorption capacity of four shale samples is attributed to the change in the pore structure.

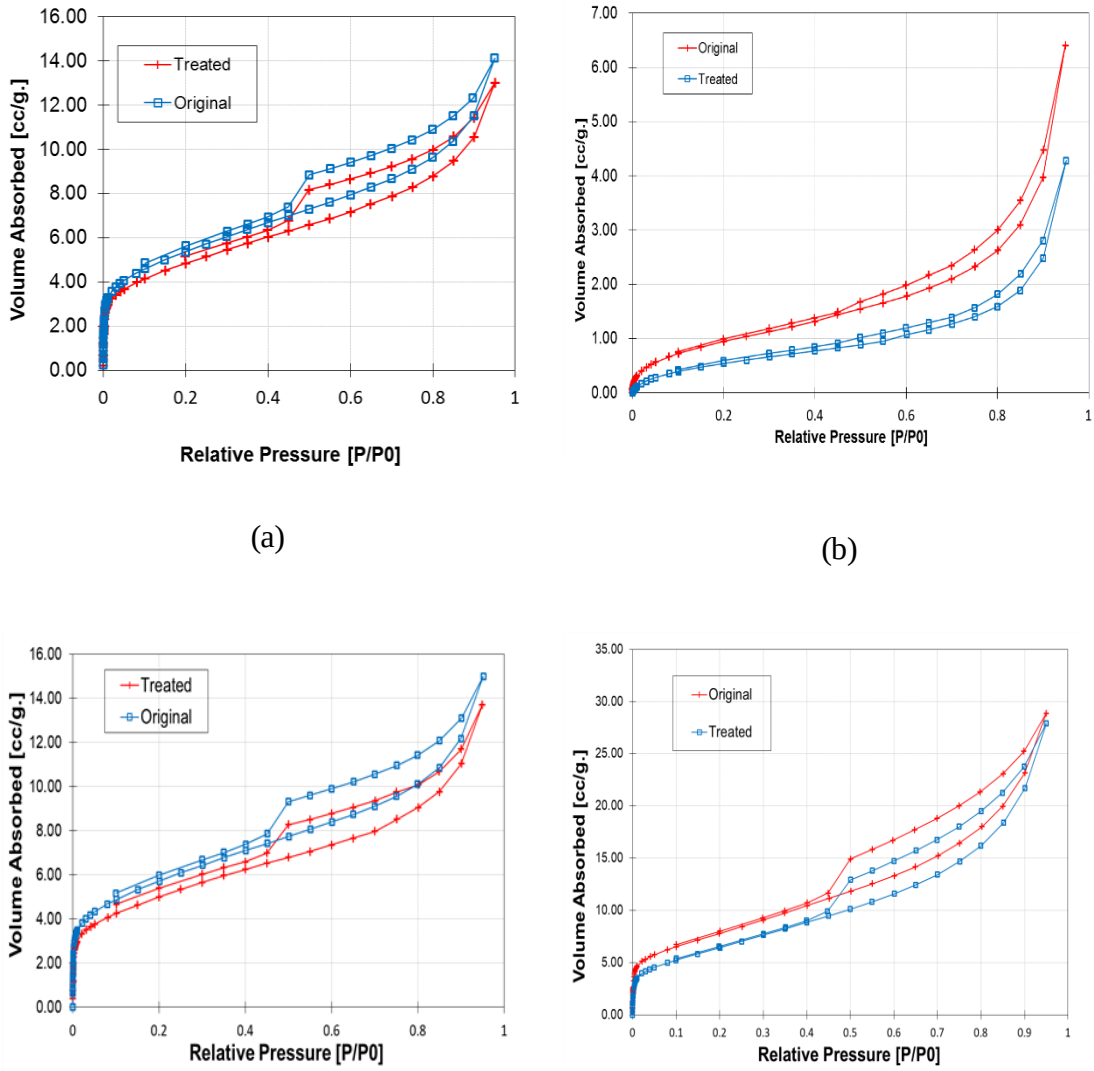

Figure 3.20 Isotherm Comparison for four shales tested (a) Haynesville, (b) Eagle Ford Shale, (c) Longmaxi Shale, and (d) Opalinus Shale.

3.6 CT Analysis

Micro-CT scans of FOUR SHALE samples were performed at NJIT, York Center using Skyscan-1275, manufactured by Bruker. By cutting the shale sample into 1cm×1cm×1cm, a resolution of 2 μm can be reached to detect the micropore swelling due to shale softening.

This would allow shale samples to be scanned at a higher resolution at the expense of sample volume. Scanning resolution ranged from 2-10 microns per voxel. Table 3.5 shows the scan settings for higher resolution images. The same sample was scanned using the same setup before and after the softening test, and series of image analyses were performed to quantify the change during the clay swelling. However, before the accurate images were required, series of data adjustments must be done, including reconstruction of the raw images, the volume of interest selection, artificial effect, and greyscale selection.

Table 3.9 Scanning Settings for High-resolution Images.

Exposure time (ms)	276
Rotation step (deg)	0.4
X-ray Voltage (KV)	100
X-ray current (uA)	65

3.61 Scanning Parameters

To compare the results before and after the C.T. scanning, the exact position of scanning must be maintained by using the same copper rod of 6mm, as shown in Figure 3.21. Most

importantly, the same Z position (height of scanning) must be ensured by adjusting the scanning parameters.

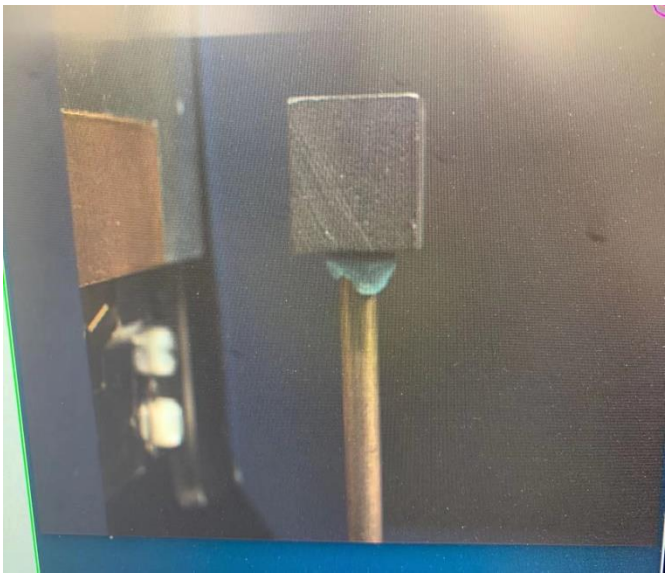

Figure 3.21 Ensure the same copper rod and the same height of scanning.

3.62 Volume of Interest Selection

To control imaging accuracy, the total digital volume to be analyzed was normalized across each sample. Due to the variability of noise and other C.T. scanner parameters such as ring artifacts reduction and beam-hardening correction, the entire sample volume cannot be used for image analysis. To compare the C.T. images, the same data set has to be determined before any quantification analysis. Therefore, the volume of interest must be the same before and after the test. In terms of images, the same total number of images and same pixel size must be the same to get the same resolution images.

Table 3.10 Volume of Interest Selection of Sample after Softening

C.T. Analyzer **Version: 1.17.7.2**

Dataset name	Sample after softening test	
File postfix length	8	
File type	TIF	
Data window	0	65535
Image size (W/H)	1944	1944
Total number of images	1162	
Total Z-position range	209	1370
Number of images inside VOI	583	
Z-position range of VOI	615	1197
Z spacing	1	
Pixel size (um)	10.0001	

Table 3.11 Volume of Interest Selection of Sample before the Test

C.T. Analyzer **Version: 1.17.7.2**

Dataset name	Before test	
File postfix length	8	
File type	TIF	
Data window	0	65535
Image size (W/H)	1944	1944
Total number of images	1162	
Total Z-position range	209	1370
Number of images inside VOI	583	
Z-position range of VOI	633	1215
Z spacing	1	
Pixel size (um)	10.0001	

Based on the bottom layer of the measurement, as shown in Figure 3.22, the right volume of interest for both sets of scans can be determined.

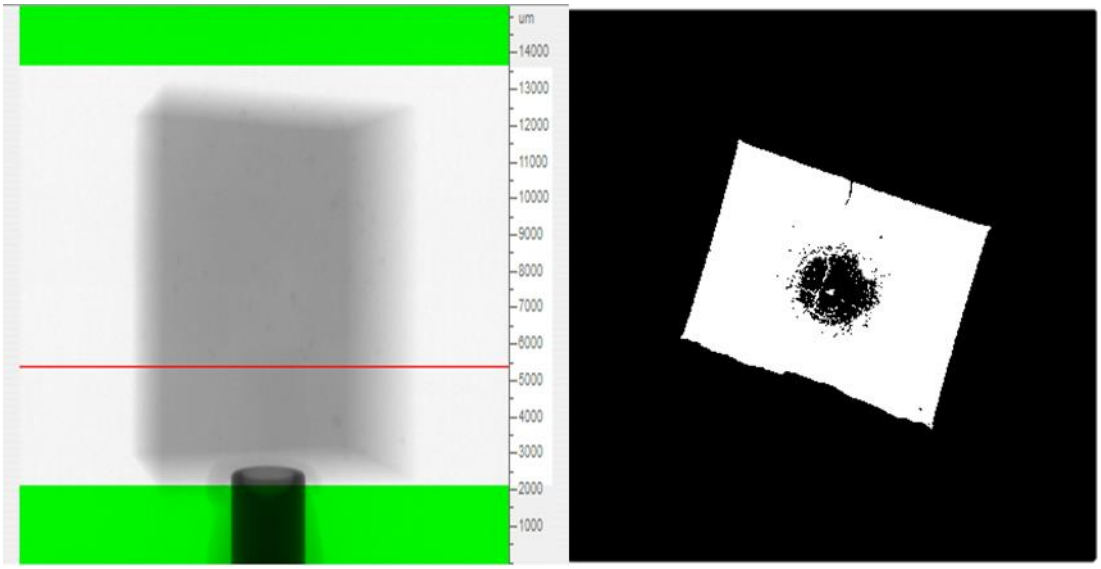

Figure 3.22 Bottom of the volume of interest.

3.63 Reconstruction of Raw Images

After finishing the scanning, the raw images from micro-CT vary in quality, and they must always be post-processed using Nrecon reconstruction software (provided by Bruker). In this study, the post-processing steps followed the same procedures for all samples. The processing parameters of the raw images are shown in Table 3.8. Therefore, using macropores present in the raw data, the actual macropore size distribution can be analyzed based on the filtered images. The raw images of Haynesville shale and the reconstructed image are shown in Figure 3.23.

Table 3.12 Parameters for Reconstruction

Smoothing	Degree of 2
Misalignment compensation	2.5
Ring artifacts reduction	9
Beam hardening correction	54%

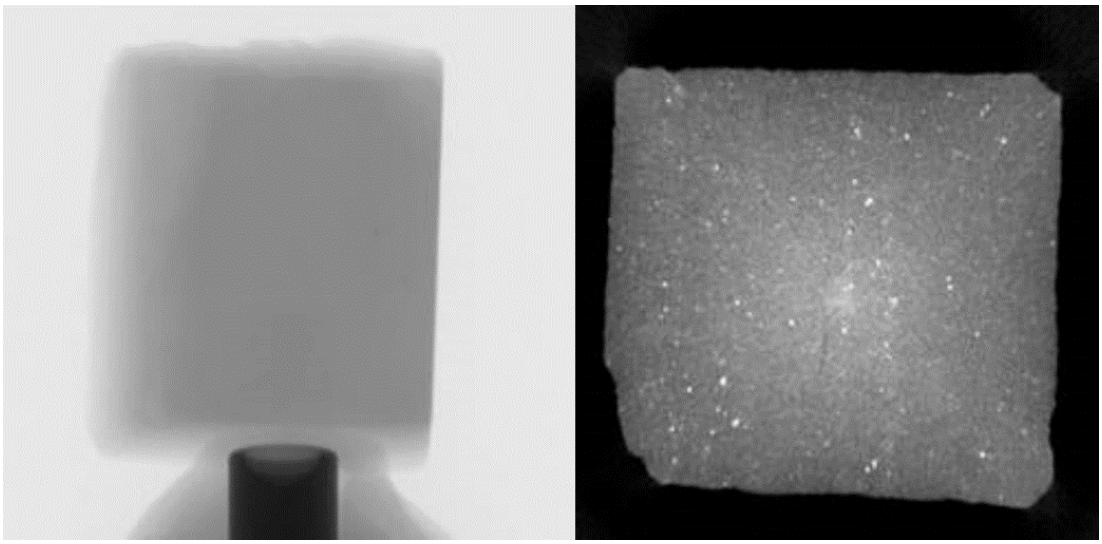

Figure 3.23 Raw images and after reconstruction.

3.64 Binarization

To do quantification analysis of reconstructions images before and after softening shale sample, the binarization processing must be done correctly. It is essential to select the threshold range based on the histogram of each of the images, as shown in Figure 3.24. The prominent peak must be fully covered to get the full spectrum of the greyscale. In this case, the threshold is ranging from 50 to 132.

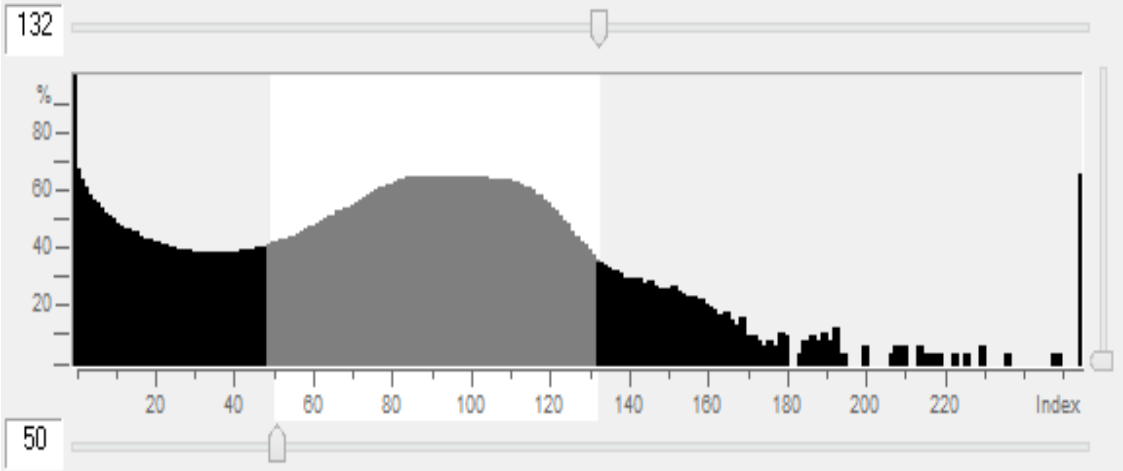

Figure 3.24 Greyscale of reconstruction image.

3.65 Image Comparisons

Firstly, identification of the same sets of image layers must be made. Then bottom and top layers were chosen to clarify the volume of interest before the binarization of C.T. scanning. Figure 3.25 shows the comparisons between the top and bottom layers for original shale and treated shale samples.

3.66 2D Analysis

The advanced C.T. analyzer is a powerful tool for quantifying essential parameters for the image's analysis. For example, by comparing some critical parameters, including Total VOI volume, objects per slice, closed porosity, one can tell how shale properties are changing and how shale softening will affect the shale structures. Also, the specific and exact position of the layer can be drawn out and compared using 2D analysis.

In combination with 3D image analysis, X-micro-tomography is a powerful method for analyzing particle size. 2D Particle Analysis is the most versatile way of collecting quantitative information on particle size, form, and arrangement. Furthermore, the analysis of 2D images may lead to important properties. For example, for uniformly shaped particles,

it is possible to calculate the recorded 2D apparent size distribution into a genuine stereological distribution (model-based assumptions are often required). In addition, 2D processes are less computational and can handle larger datasets.

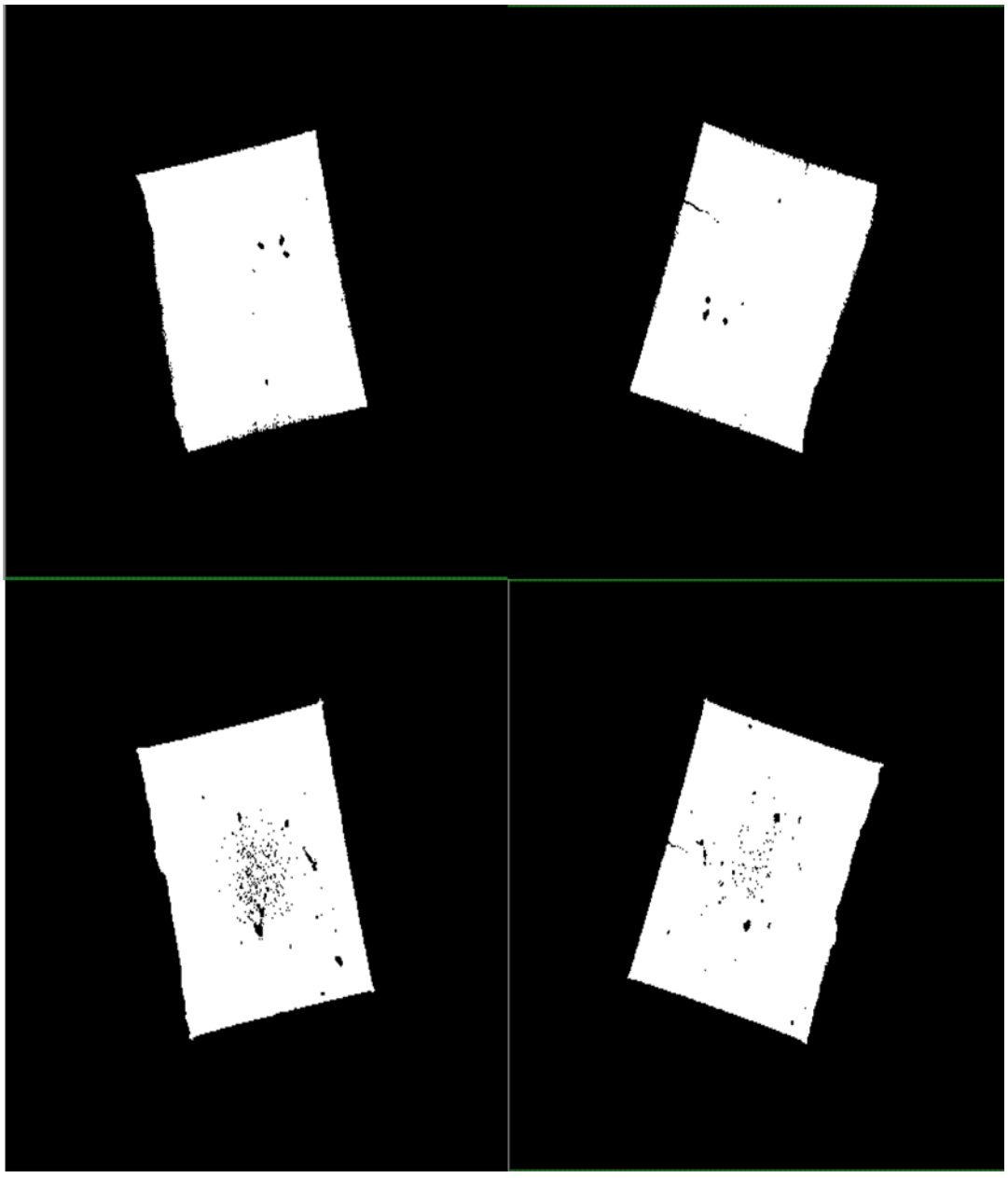

Figure 3.25 The featured images of shale softening comparison. (Left side: original, right side: softened sample).

Now, the identical layers were chosen and analyzed for Eagle Ford shale. The following tables are presents to show the structural parameters based on 2D analysis.

Table 3.13 Eagle Ford Parameters Summary of 2D Analysis after Softening.

Summary 2D data	*After swelling*		
Total VOI volume	TV	4.06785E+11	um^3
Object volume	Obj.V	3.91408E+11	um^3
Percent object volume	Obj.V/TV	96.21985	%
Total VOI surface	TS	351553620.3	um^2
Object surface	Obj.S	642388622	um^2
Peripheral object surface	Obj.S(per)	390103438.8	um^2
Mean total cross-sectional ROI area	T.Ar	70773708	um^2
Mean total cross-sectional ROI perimeter	T.Pm	36364.33693	um
Mean total cross sectional object area	Obj.Ar	67136157.06	um^2
Mean total cross sectional object perimeter	Obj.Pm	66912.44216	um
Mean number of objects per slice	Obj.N	2.44082	
Average object area per slice	Av.Obj.Ar	39278727.07	um^2
Average object area-equivalent circle diameter per slice	Av.Obj.ECDa	6793.48438	um
Mean eccentricity	Ecc	0.66808	
Closed porosity (percent)	Po(cl)	0.77932	%

The advantages of 2D analysis are that every layer can be calculated based on the binarization graph, but this 2D graph also limits the porosity analysis. In addition, since only closed pores can be detected during the analysis, these results cannot yield accurate information because large spatial pores in the shale formation are open in 3D but closed in 2D. So, the closed porosity in the 2D analysis is smaller than that in actual formation.

The Mean total cross-sectional ROI area is based on every slice of the sample, and the result shows that the closed porosity is 1.44644% before softening and 0.77932% after swelling, indicating the shale has swelled.

Table 3.14 Eagle Ford Parameters Summary of 2D Analysis before Softening.

Summary 2D data	*Before swelling*		
Total VOI volume	TV	4.04E+11	um^3
Object volume	Obj.V	3.88E+11	um^3
Percent object volume	Obj.V/TV	95.92287	%
Total VOI surface	T.S.	3.5E+08	um^2
Object surface	Obj.S	9.3E+08	um^2
Mean total cross-sectional ROI area	T.Ar	69347620	um^2
Mean total cross-sectional ROI perimeter	T.Pm	35830.76	um
Mean total cross-sectional object area	Obj.Ar	66520228	um^2
Mean total cross sectional object perimeter	Obj.Pm	98334.81	um

Mean number of objects per slice	Obj.N	3.64666	
Average object area per slice	Av.Obj.Ar	26282987	um^2
Average object area-equivalent circle diameter per slice	Av.Obj.ECDa	5505.211	um
Mean eccentricity	Ecc	0.66992	
Closed porosity (percent)	Po(cl)	1.44644	%

3.67 3D Analysis

The 3D analysis is based on rendering the VOI and structural parameters of 3D analysis to provide more accurate information. After handling the dataset and performing a series of advanced image smoothing, the summarized results of the structural parameters can be seen in the tables below.

Table 3.15 Eagle Ford 3D parameters of shale after softening

Total VOI volume	**TV**	**4.06709E+11**	**um^3**
Object volume	Obj.V	3.91315E+11	um^3
Percent object volume	Obj.V/TV	96.21496	%
Total VOI surface	TS	351329823.7	um^2
Object surface	Obj.S	571434863.7	um^2
Number of objects	Obj.N	65	
Number of closed pores	Po.N(cl)	18258	
The volume of closed pores	Po. V(cl)	2910515231	um^3
Surface of closed pores	Po.S(cl)	197579826.9	um^2
Closed porosity (percent)	Po(cl)	0.73829	%
The volume of open pore space	Po. V(op)	12483585579	um^3
Open porosity (percent)	Po(op)	3.06941	%
The total volume of pore space	Po. V(tot)	15394100810	um^3
Total porosity (percent)	Po(tot)	3.78504	%
Connectivity	Conn	886	
Degree of anisotropy	DA	1.33312 (0.24988)	

Also, the pore size distribution based on the 3D analysis can be drawn out as summarized in table 3.12 for shale after swelling.

Finally, the pore size distribution can be summarized using the information of the 3D analysis. Based on the volume percentage, the range of micro pores of shale after softening can be seen in Figure 3.26. The same procedures were applied to the shale data before softening to get the 2D and 3D results.

Table 3.16 Eagle Ford Pore Size Distribution after Shale Swelling

RANGE	MID-RANGE	VOLUME	PERCENT VOLUME IN RANGE
UM	um	um^3	%
10.00 - <30.00	20	839374181	5.4191
30.00 - <50.00	40	1510584317	9.7525
50.00 - <70.00	60	1100448013	7.1046
70.00 - <90.00	80	790795723.6	5.1055
90.00 - <110.00	100	474548236.3	3.0637
110.00 - <130.00	120	507989239.5	3.2796
130.00 - <150.00	140	919125573.5	5.934
150.00 - <170.00	160	1020556616	6.5888
170.00 - <190.00	180	838838164.9	5.4156
190.00 - <210.00	200	832415972.2	5.3742
210.00 - <230.00	220	834065021.7	5.3848
230.00 - <250.00	240	659209776.1	4.2559
250.00 - <270.00	260	571630148.7	3.6905
270.00 - <290.00	280	580277408.1	3.7463
290.00 - <310.00	300	519734591.9	3.3555
310.00 - <330.00	320	586195585.7	3.7845

330.00 - <350.00	340	705450163.3	4.5545
350.00 - <370.00	360	510032300.8	3.2928
370.00 - <390.00	380	415439463.1	2.6821
390.00 - <410.00	400	264506935.1	1.7077
410.00 - <430.00	420	246223386.6	1.5896
430.00 - <450.00	440	220298608.9	1.4223
450.00 - <470.00	460	302303069	1.9517
470.00 - <490.00	480	239142174.2	1.5439

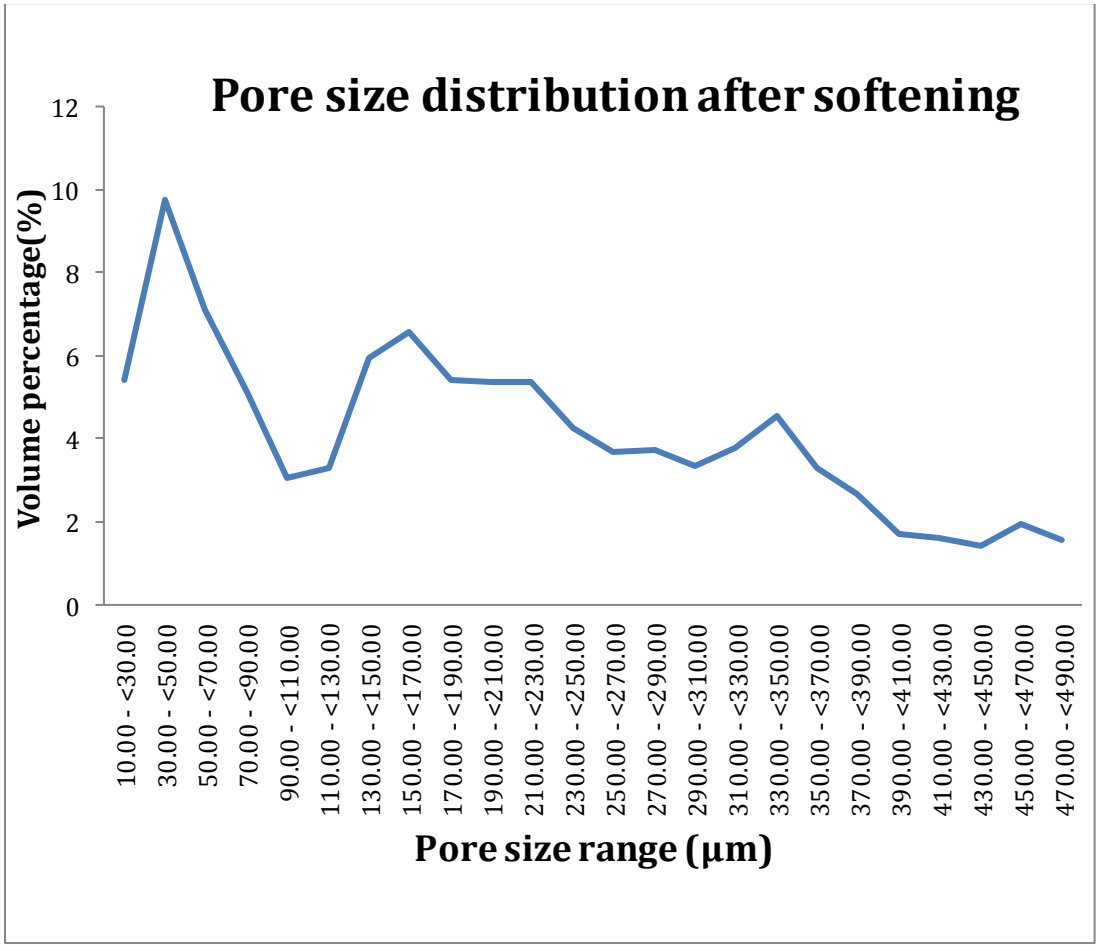

Figure 3.26 Eagle Ford Pore size distribution after softening based on 3D analysis.

Table 3. 17 Eagle Ford 3D Parameters of Shale before Softening.

Total VOI volume	*TV*	*4.04E+11*	*um^3*
Object volume	Obj.V	3.88E+11	um^3
Percent object volume	Obj.V/TV	95.91323	%
Total VOI surface	T.S.	3.48E+08	um^2
Object surface	Obj.S	8.03E+08	um^2
Intersection surface	i.S	1.94E+08	um^2
Number of objects	Obj.N	101	
Number of closed pores	Po.N(cl)	24491	
Volume of closed pores	Po.V(cl)	3.02E+09	um^3
Surface of closed pores	Po.S(cl)	2.76E+08	um^2
Closed porosity (percent)	Po(cl)	0.77364	%
Volume of open pore space	Po.V(op)	1.35E+10	um^3
Open porosity (percent)	Po(op)	3.33896	%
Total volume of pore space	Po.V(tot)	1.65E+10	um^3
Total porosity (percent)	Po(tot)	4.08677	%
Connectivity	Conn	3940	
Connectivity density	Conn.Dn	0.00001	1/um^3
Degree of anisotropy	DA	1.38592 (0.27846)	

Pore size distribution of softened shale can be drawn out using the 3D C.T. scanning, and the following is the table of information.

Table 3.18 Pore Size Distribution before Eagle Ford Shale Swelling

RANGE	MID-RANGE	VOLUME	PERCENT VOLUME IN RANGE
UM	um	um^3	%
10.00 - <30.00	20	1.22E+09	7.3063
30.00 - <50.00	40	2.51E+09	15.0209
50.00 - <70.00	60	1.75E+09	10.4579
70.00 - <90.00	80	1.63E+09	9.733
90.00 - <110.00	100	1.54E+09	9.1902
110.00 - <130.00	120	1.39E+09	8.3273
130.00 - <150.00	140	1.54E+09	9.2079
150.00 - <170.00	160	1.3E+09	7.7542
170.00 - <190.00	180	1.11E+09	6.6383
190.00 - <210.00	200	9.17E+08	5.4896
210.00 - <230.00	220	6.35E+08	3.8024
230.00 - <250.00	240	4.41E+08	2.6393
250.00 - <270.00	260	2.54E+08	1.5179
270.00 - <290.00	280	1.91E+08	1.1453
290.00 - <310.00	300	1.12E+08	0.6699
310.00 - <330.00	320	48310449	0.2891
330.00 - <350.00	340	38832165	0.2324
350.00 - <370.00	360	35345060	0.2115
370.00 - <390.00	380	20765623	0.1243
390.00 - <410.00	400	40486215	0.2423

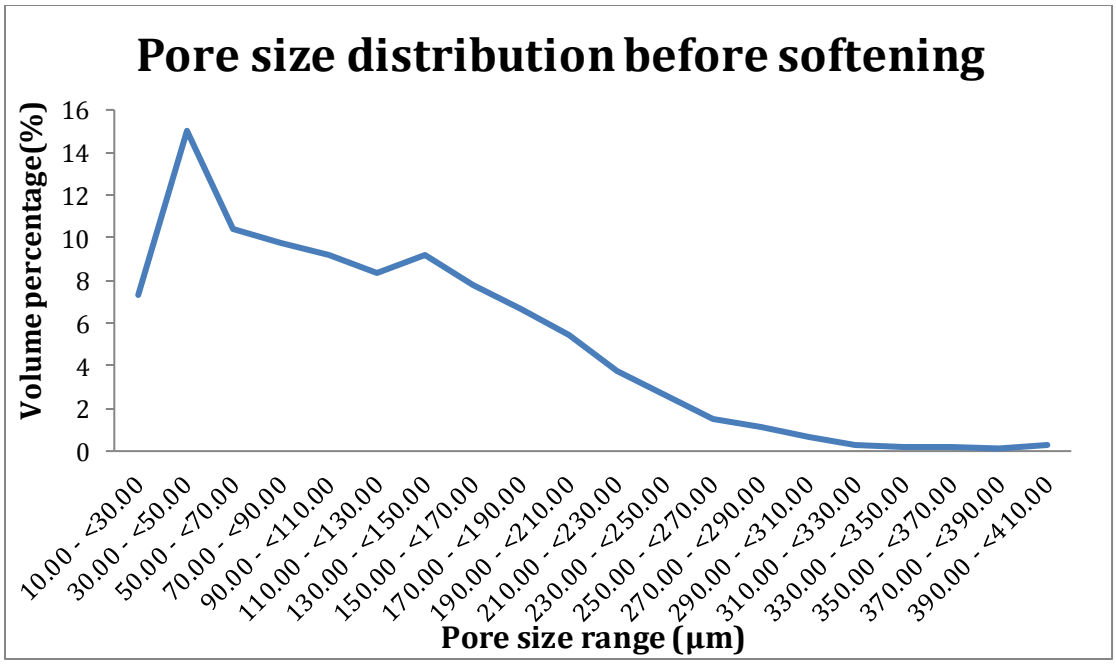

Figure 3.27 Eagle Ford Pore size distribution before softening based on 3D analysis.

Based on the two-pore size distributions of the same sample, the original and treated sample peaks can be compared.

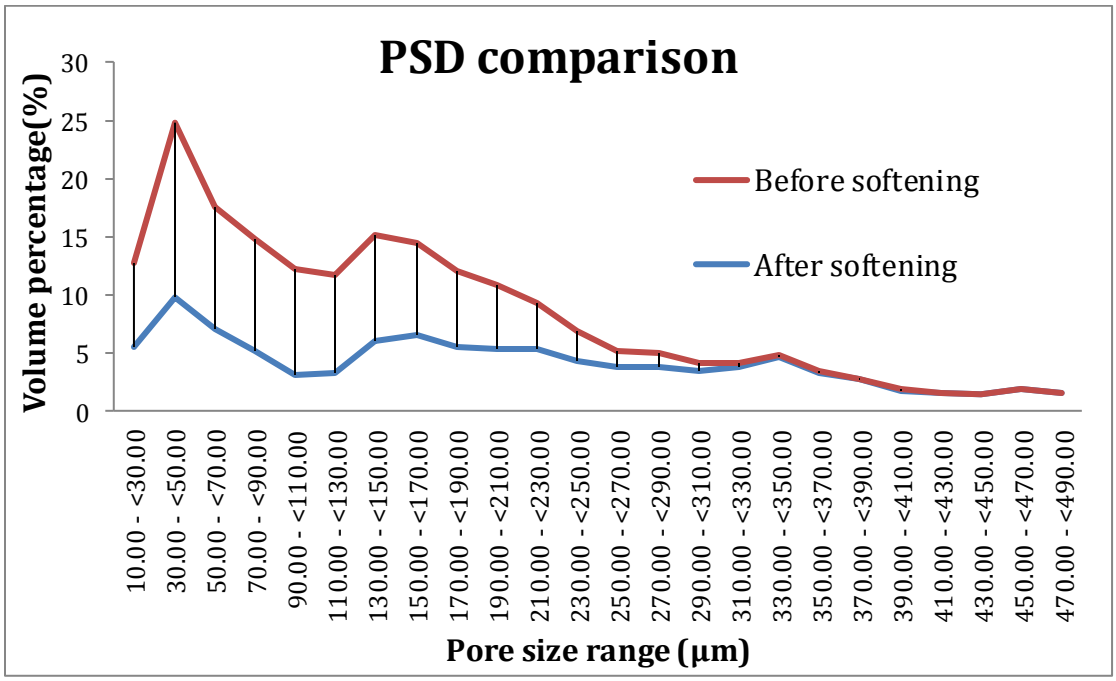

Figure 3.28 Eagle Ford Pore size distributions comparison.

Based on the comparison, the reduction in the volume of pores ranging from 10μm to 300 μm is obvious after the shale softened. The results indicate that pores of shale within the micron range are under the great influence of softening. This softening mechanism will impact the structural parameters, including the number of objects and the number of closed pores. The number of closed pores decreased dramatically from 24491 to 18258. The volume of closed pores and the surface of closed pores declined by 3.1% and 28%, respectively. Also, closed porosity and open porosity decreased by 4.5% and 8%. The total porosity of the original sample was 4.088%, and the softened sample porosity was 3.78%.

In conclusion, the C.T. image amylases yield good results when dealing with swelling and softening of the micro pore. Thus, the results are a good match to those reported in the literature reports, but additional tests should be conducted before firm conclusions.

3.7 Discussion of Test Results

After two series of four diverse shale softening and treatment tests, several observations were made to describe the features of the clay-porosity correlations. The isothermal diagrams modification between initial and treatment can be inferred. Eagle Ford shale contains many I/S layers, contributing to significant swelling of 1.1%. Longmaxi, Haynesville, and Opalinus shale have the same isotherm pattern Type IV, and eagle Ford shale exhibited Type III pattern. The PSD of these four shales was also carried out after treatment; peak changes can be used to calculate the porosity changes.

The clay minerals are essential components that can store oil and natural gas in the source and reservoir rocks. The presence of clay minerals can also strongly affect shale's unconventional physical and chemical properties [87]. Regionally, clay minerals can

explain basin evolution, such as structure, sedimentation, burial, and cementation history, etc. Also, clay minerals in gas-bearing rocks are an essential component to evaluate the quality of hydrocarbon generation, discharge, and migration.

Their presence has an important impact on reservoir properties (such as porosity and permeability). Geologists use clay mineral information to determine the buried diagenesis process and reveal pore types and pore evolution. The clay content is generally considered detrimental to the gas extraction from the reservoir because it can reduce or block pore throats after hydraulic fracturing due to the retained injection fluid. During diagenesis, sediment porosity is substantially reduced for sediments with high clay contents but forms micro and nanopores and prevents cementation of quartz covered with chlorite. Therefore, it is natural to associate reducing the porosity of gas-bearing shale with high clay contents after hydraulic fracturing [88]. When clay minerals become unstable and react with injection fluids to transform into more stable minerals, these will precipitate on the surface of the matrix particles and expand the shale skeleton[89]. These stable clay minerals can block pores, reduce the connectivity between the pores, and increase the flow resistance[90]. Water-based fracturing fluid can significantly reduce the porosity and permeability of the reservoir through the swelling of clay minerals. As demonstrated in this research, the pore throats of high clay content shale gradually swell or block under the influence of high temperature and pressure, reducing the shale gas production with time [91]. This transformation of hard rock into mudstone or soft shale is usually called shale softening.

3.8 Summary and Conclusions

Four shale samples with different mineral compositions were used to study the influence of initial shale mineralogy on change in pore structure evolution during hydraulic fracturing. Using XRD, low-temperature N_2 adsorption, Mirco-CT scanning, and porosity measurements, the changes in the mineral composition and pore structure of four shale samples were measured. The conclusions of this study are summarized as follows:

(1) In the clay-rich Opalinus shale (clay content of 65.7%), the clay softened after immersed in DI water at high temperature and pressure. The expansion of illite in Opalinus shale caused swelling of nanopores and led to a significant decrease in total pore volume (shale porosity decreased from 7.8% to 3.8%).

(2) In the clay-poor Eagle Ford shale (clay content of 5.6%), the clay is cemented with other non-water reaction minerals. The cementation of clay may occur at a slow rate, which the standard softening experiment cannot detect. However, the cementation of clay blocked the majority of the pore throats. As a result, the porosity of the shale matrix reduced from 1.06% to 0.52%.

(3) The change in shale porosity with different mineral compositions during hydraulic fracturing may be related to the clay content of shale. Shales with low clay content have a low softening capacity, resulting in lower porosity loss during treatment. However, clay-rich shales have a high softening capacity. The test results show that during hydraulic fracturing, the initial mineral composition of the shale may affect the pore structure. Hence, the fracturing fluid should be adjusted according to the shale mineralogy to avoid damage to the intact shale.

(4) The knowledge of the structural parameters of shale can help identify shale softening stages.

(5) A linear relationship between clay content and porosity reduction indicated that clay-rich shale would be water damaged and perform worst during hydraulic fracturing. Therefore, softening mostly impacts the clay-rich shale and, in this study: the Opalins shale.

(6) Micro-CT image analysis proved to be an efficient way to detect micro-sized porosity changes during hydraulic fracturing. Both 2D and 3D images were obtained and compared to show that number of pores reduced after the fracturing process, indicating that the softening would harm the inner structural parameters.

CHAPTER 4

THE PORE NETWORK THEORY AND MODEL

4.1 Introduction

To predict the permeability of virgin and treated shale and quantify the reduction of shale permeability due to shale softening, the pore network model for the single-phase flow model proposed by Zhang et al. [41] was modified. In this chapter, the theory and require model parameters are first discussed. Next, the estimation of nano-scale flow rates is discussed, and then the modification to the model proposed by Zhang et al. [41] is described. Finally, the construction methodology and comparison between treated shale and virgin shale are presented.

The morphology of porous media plays a crucial role in determining the flow properties. The morphology of a porous medium is determined by its geometrical properties (the shape and volume of its pores) and its topological properties, i.e., how the pores are connected. It is not easy to obtain detailed information about these properties [92]. The pore morphology of natural porous media is quite complex, and measurement of such in natural porous media is another difficulty. Therefore, many simplifications of the pore morphology are employed in pore network models. For example, pore throats are often assumed to be straight tubes or simple constricted tubes with a regular cross-sectional shape [93], as shown in Figure 4-1. The pore network model attempts to describe the multiphase flow properties of porous media using realistic geologic parameters that are further simplified without significantly deviating from the average. Hence, by applying appropriate boundary conditions and governing equations, the pore network can simulate

various physical and chemical processes, including phase exchange, non-Newtonian displacement, non-Darcy flow, reactive transport, and thermodynamically consistent mixture flow [94].

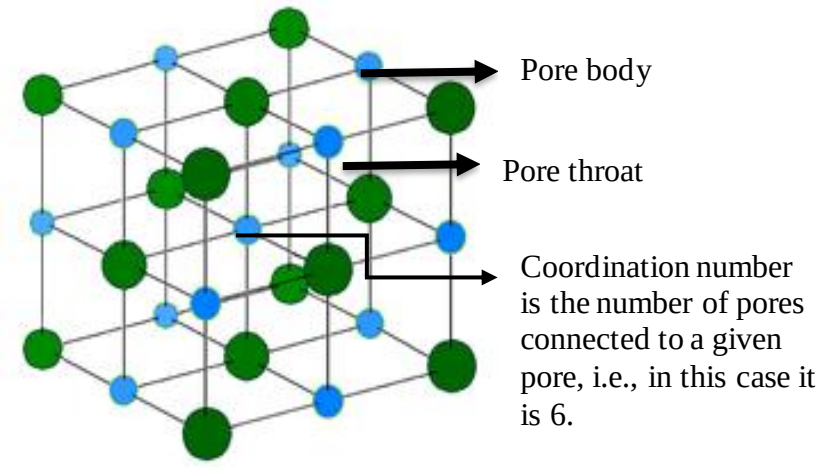

Figure 4.1 Illustration for Pore body and pore throat.

The pore network model is a tool to understand and predict the permeability of the porous media and, in this research, the gas-bearing shale. Specific parameters that describe the characteristics of the pore structure of geo-materials are porosity, pore size distribution, pore throat size distribution, and coordination number. Zhang et al. [41] reviewed the previous research on gas percolation in porous media and proposed a theoretical 3D gas simulation model. This 3D pore-network model can consider the connectivity and porosity of different geo-materials. In this research, the kinetic gas flow theory for different gas flow regimes is used in the pore network model. As described previously, the most critical aspect of characterizing the porous medium is identifying the geometrical and topological properties of the porous medium voids within the porous media.

4.2 Equivalent Pore Network

The equivalent pore network model represents the structural information of the geological media, including porosity, pore size distribution, pore throat size distribution, and distribution of coordination number. After obtaining the pore structure information of a geological media, based on the pore size distribution, the total pore volume in the sample can be constructed. The pore spacing in the pore network, i.e., the length of the coordination bond, is then calculated based on the measured porosity and the total pore volume. The calculated pore spacing determines the spatial coordinates of each pore. The initial pore coordination is set up according to the representative units of pore connectivity [95], as shown in Figure 4-2, where each pore is connected to the adjacent pore through 26 coordination bonds. The topology number of the node is set from bottom to top and front to side. N is the center point pore node number, and the number of layers in the X, Y, and Z direction pore structure models are N_i, N_j, and N_k, respectively, $N_{jk} = N_j \times N_k$. Hence, a fully connected pore network with 26 coordination bonds per pore can be established. The cubic pore network model has six boundary surfaces, and special processing is needed at the boundary surface. The coordination bonds at the boundary surface pointing to the outside of the model are eliminated. Considering seepage in the actual geotechnical medium, there is no plane flow at the boundary surface due to the pressure gradient to the outside. Therefore, the model is modified to reject the coordination bonds between the pores at the entry and exit boundaries. Also, isolated pores present during such construction need to be eliminated too.

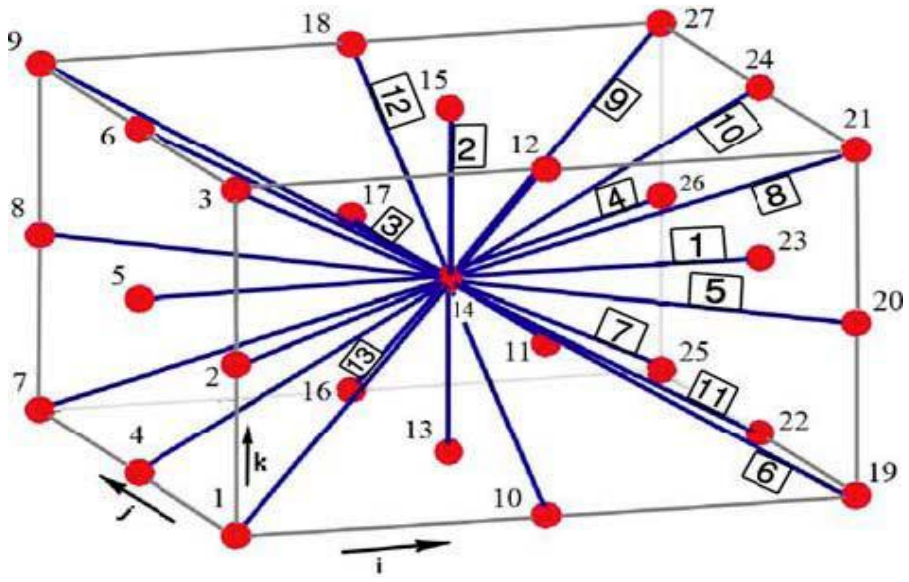

Figure 4.2 Representative units of pore connectivity.

After the pore network is established, it is necessary to include a function to search the main skeleton of pores contributing to the fluid flow and eliminate the isolated pores and pore throats [96]. The main geometric and topological parameters that can be considered in the network include the total number of pores in the network, average pore size, maximum and minimum pore size, pore spacing, and average coordination number. All these parameters can be obtained as described in chapter 3. As stated before, the pore size distribution and throat size distribution with the connectivity define the pore morphology of porous media. Hence, using these parameters, one can develop a pore network to represent the basic morphology of the pores.

4.3 Parameters of the Proposed Pore Network and Their Relationship

A method for creating an equivalent pore network model with variable coordination numbers that can accommodate different pore-sizes, pore-throats, pore connections, and

porosities, with a variable coordination number, is developed with the mathematical method of describing the pore network of shale in combination with data from the actual pore structure.

Via a regular three-dimensional lattice of pores connected by throats, the network model represents the void space of the rock. Each pore throat pore or pore body is presumed as cylindrical and spherical, respectively, in a regularly spaced grid [97,98]. This assumption is the primary basis for developing a predictive model to characterize the porous network of actual geomaterials [99]. This model simplifies the complex seepage channels (pores, throats) geomaterials into regular geometric shapes, such as spheres, cylinders, etc., and arranges them regularly in a lattice grid.

To construct the equivalent pore network as described above, the following six key model parameters are required:

1. Pore body radius (Rp) and its distribution: The pore body radius represents the size of the pores that are large cavities throughout the geological media.

2. Pore throat radius (Rth) and its distribution: The pore throat radius represents the size of the seepage channel between the pore bodies. Since any migration of fluid between the pore bodies must flow through pore throats, the pore throat size directly affects the seepage characteristics of the entire geological media

3. Coordination number (ζ) and its distribution: The pore coordination number represents the connectivity between pore bodies. For a geological media with high permeability, such as sand, one pore may be connected to multiple surrounding pores, and hence the coordination number is high (>6). For a geological media with low permeability, such as shale, the pore coordination number is relatively small (<4).

4. Porosity (n): The porosity represents the proportion of the void in the geological media. Here, the voids include pore bodies and pore throats, including dead pore bodies and corresponding pore throats.

5. Characteristic length (L): L is a concept introduced in an equivalent pore network representing the mesh length, which is the distance between adjacent pore bodies. L cannot be smaller than the average pore size of the two connecting pores.

6. Anisotropy parameter: Due to the different depositional factors of geo-materials, their hydraulic properties in different directions are different, which results in anisotropic permeability. The anisotropic parameter attempts to capture this hydraulic anisotropy.

The porosity is the ratio of the void volume to the total volume in the geological media. Here, the void volume includes the pore volume and the throat volume. Therefore, considering a single pore unit, the volume occupied by the pore body is:

$$V_{\mathrm{p}} = \frac{4}{3} \times \pi \times R_{\mathrm{p}}^3 \tag{4.1}$$

The pore throat is assumed as a cylinder in the model, so its throat radius and throat length determine its volume. It should be noted that the length of the throat should be the distance between the pore centers, and the volume of pore throat function should be as follow:

$$V_{\mathrm{th}} = \frac{\zeta}{2} \times \pi \times r_{\mathrm{th}}^2 \times (L - 2R_{\mathrm{p}}) \tag{4.2}$$

Where ζ is the coordination number, Rth is the throat radius, and L is the unit size. Therefore, porosity can be expressed as:

$$n = \frac{V_{\mathrm{p}} + V_{\mathrm{th}}}{L^3} = (\frac{4\pi R_{\mathrm{p}}^3}{3} + \pi R_{\mathrm{th}}^2 \times \left(\frac{L}{2} - R_{\mathrm{p}}\right) \times \zeta)/L^3 \tag{4.3}$$

The relationship between porosity, pore radius, throat radius, pore coordination number, and unit length is established from the above formula based on Figure 4.3. Among

the five parameters, the pore size Rp, the throat size Rth, the pore coordination number ζ, and the porosity n can be obtained directly from the experiments. Therefore, with the above parameters, one can construct the equivalent pore network.

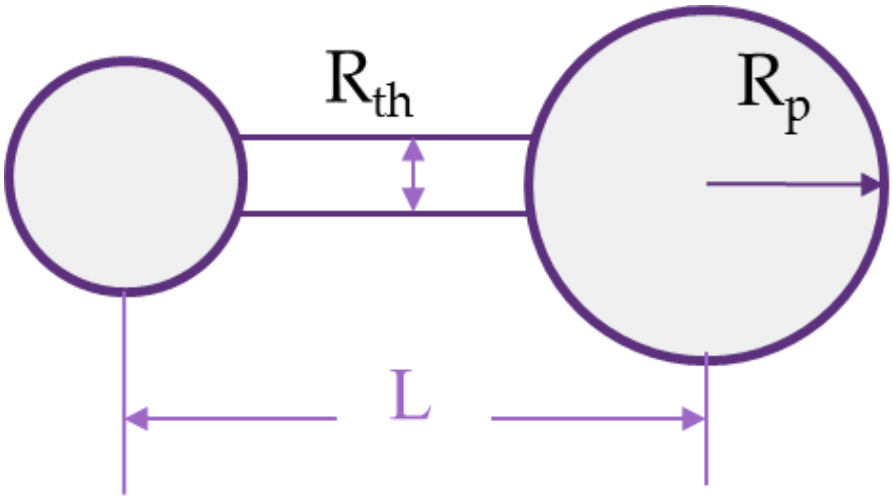

Figure 4.3 Pore connection in the pore network model

4.4 Nano Flow Simulation

The seepage rate can be calculated once the effective pore network is established. The most frequently used method is the iteration of flow calculations with appropriate boundary and initial conditions. For each iteration step, all the interconnected pores will be traversed to calculate the gas transport until the pressure distribution becomes stable. Following the typical gas permeability test, the model could be set as a constant pressure boundary on opposite sides and a no-flow boundary on other sides.

The relationship between the flow flux and permeability can be derived based on Equation (4.4) [100], where P_i and P_o represent the inlet and outlet pressure separately, Q_O is the volume flux at the outlet, L and A are the length the cross area of the sample.

$$k_g = 2P_o Q_o \mu L / A(P_i^2 - P_o^2) \quad (4.4)$$

Due to the size of flow channels of the seepage, the flow would be mainly dominated by slip flow and diffusion flow rather than Darcy flow when the pore size is considerably small. Knudsen number is used to evaluate different flow regimes, which is the ratio of mean free path of gas to pore channel size as shown in Equation (4.5), where λ is the mean free path of a specific type of gas molecule. Shown in Figure 4.4 and r is the pore channel radius [101].

$$K_n = \frac{\lambda}{r} \quad (4.5)$$

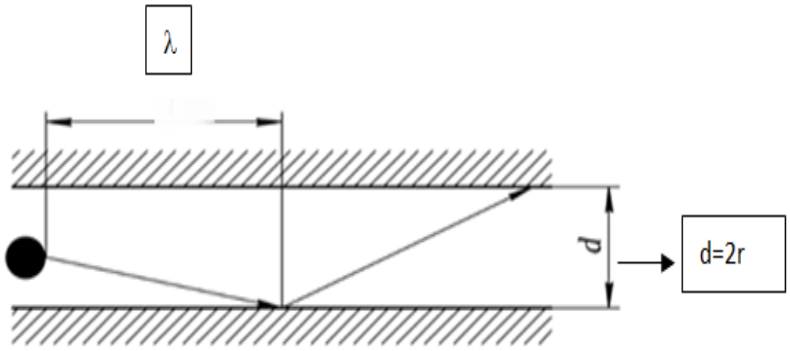

Figure 4.4 Demonstration of Knudsen number: mean free path of gas (λ) and pore channel diameter (d).

The variation of the Knudsen number varies during the dynamic gas flow, which will result in the change of flow regimes. Therefore, slip and transition flow are the typical gas flow in the shale matrix [102]. Therefore, the slippage impact and Knudsen diffusion in the

theoretical model must be combined using slippage theory and diffusion theory [103]. Considering the different flow regimes, Zhang et al. [41] proposed the following relationship between apparent permeability and Darcy permeability, as shown in Equation (4.6):

$$\frac{k_{app}}{k_0} = (1 + 4K_n) \cdot f + \frac{64}{3\pi} K_n \cdot (1 - f) \tag{4.6}$$

Where k_{app} is the apparent permeability, k_0 is the Darcy permeability, f is the coefficient of tube wall roughness.

For the slippage flow in the network, gas molecules slip along the wall, and a slippage correction factor (F) was introduced to account for this effect, as shown in Equation (4.7):

$$F = 1 + \frac{4c\lambda}{r} \tag{4.7}$$

Where c is a collision factor of 1 in this case, λ is the mean free path of gas, r is the pore channel size.

The transportation of gas is a dynamic process, and each pore needs to satisfy the law of conservation of mass. Taking pore i as a reference, pore i is connected to the surrounding four pores (Figure. 4.5). In the figure, s and e respectively represent the starting and ending pores of the pores connected to pore i. At each time step, the pressure in the throat is equal to the average pressure of pores linked in each step. From k to k+1 time step, the mass

change of the pore i is equal to the sum of mass flow rates of all neighboring linked pores. (Equation 4.8)

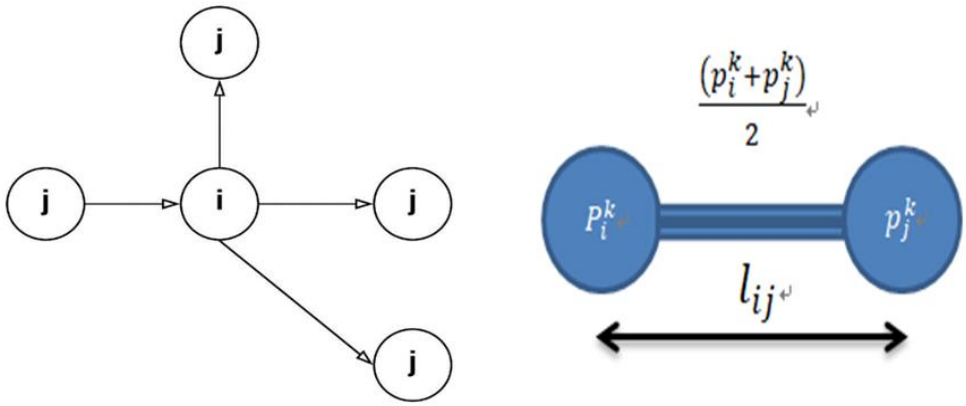

Figure 4.5 Schematic diagram of pore i connected pores.

$$m_i^k - m_i^{k+1} = \sum_{j=s}^{e} \frac{M}{RT}\left(F\frac{\pi r_{th}^4}{8\mu_g}\frac{\left(p_i^k + p_j^k\right)}{2} + \frac{2r_{th}}{3}\sqrt{\frac{8RT}{\pi M}}\right)\frac{p_i^k - p_j^k}{l_{ij}}\Delta t \qquad (4.8)$$

Where m is the mass of gas, M is the molar mass of gas molecules, R is ideal gas state constant, μ_g is gas (non-wetting phase) dynamic viscosity coefficient, F is the slippage correction factor, and T is the temperature.

In the ideal gas state, the mass of the gas stored in the pore i in the k time step is:

$$m_i^k = \frac{4}{3}\pi r_p^3 \frac{M}{RT} p_i^k \qquad (4.9)$$

Now replacing Equation (4.9) with Equation (4.10) produces:

$$p_i^{k+1} = p_i^k - \sum_{J=s}^{e} \left[\left(F \frac{\pi r_{th}^4}{8\mu_g} \frac{\left(p_i^k + p_j^k\right)}{2} + \frac{2r_{th}}{3} \sqrt{\frac{8RT}{\pi M}} \right) \frac{p_i^k - p_j^k}{l_{ij}} \right] \Delta t \Big/ \left[\frac{4}{3} \pi r_p^3 \right] \quad (4.10)$$

Equation (4.10) shows the dynamic pore pressure iterative process. Equation (4.10)account for the conservation mass for the entire pore network by applying different pressure to both inlet and outlet until there is a minimum pressure change in the pore network matrix (stable condition). During shale gas production, the outlet is in the atmosphere (0.1 MPa). Other side boundaries are no flow. When calculating, each connected pore will contribute to the conservation of the mass equation. When the time step is determined, the conservation of mass of each pore will be obtained for stable results. When the model is stable, the maximum pressure difference is less than the tolerance, defined as err=P_{outlet} /10^4, which is one to ten-thousandth of the boundary pressure below. The flow chart of this whole simulation is shown in Figure 4.6.

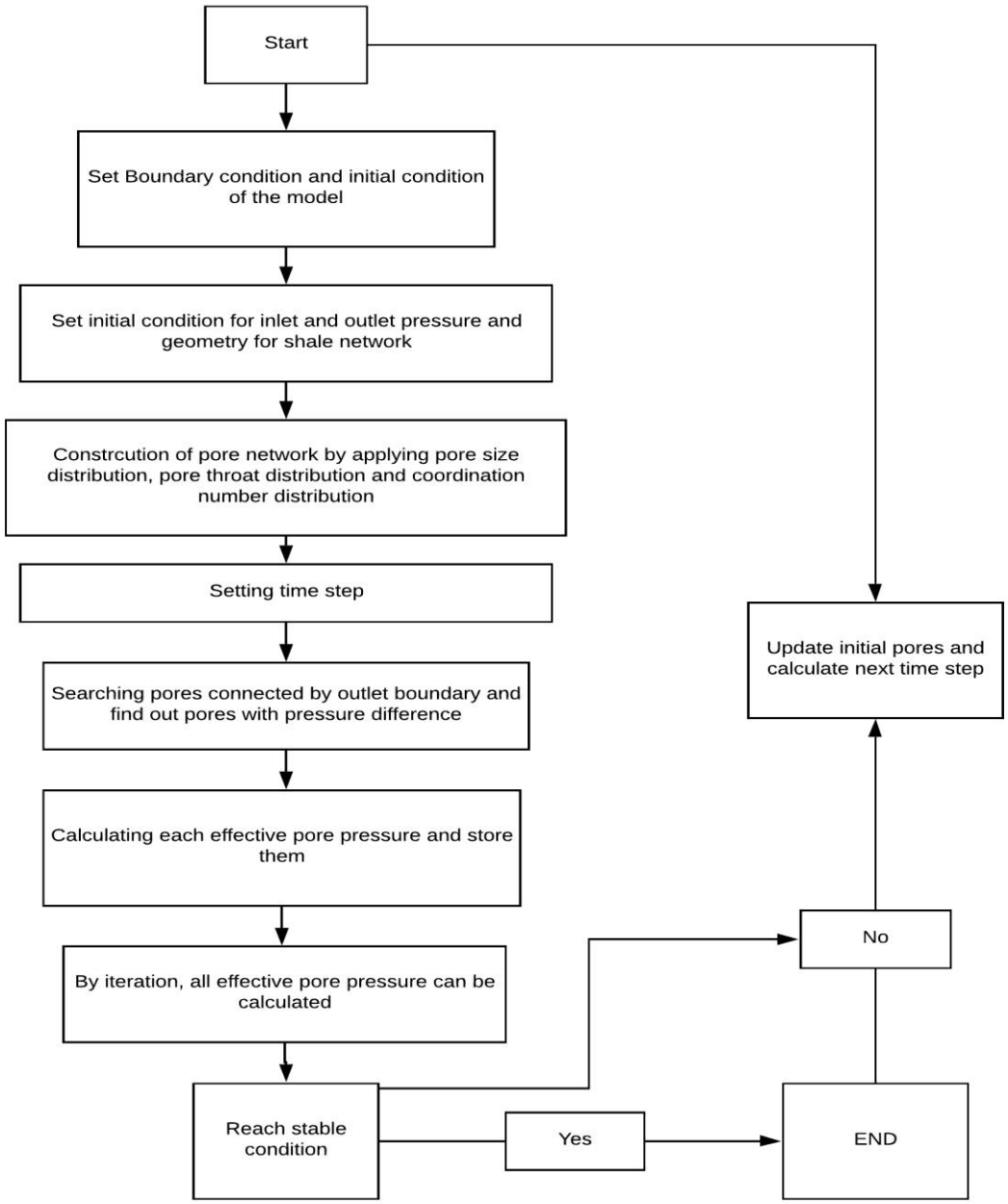

Figure 4.6 Calculation flow chart.

4.5 Construction of Pore Networks for Virgin and Treated Shale

The gas flow through the shale is directly linked to the geometry of the structural parameters required for the pore network. The pore network is a simplistic representation of the complicated pore geometry, which would enable the calculation of gas flow.

Therefore, by measuring the morphology of shale, it is possible to construct a realistic pore network and predict permeability.

The pore size distributions, pore throat, and coordination number within the pore network play a significant role in the hydraulic properties of shale. A pore network with such geometries is typically constructed with a network of comparatively large pore bodies linked to throats.

The pore network as a predictive instrument for permeability is a relatively new concept. The critical point here is how to build such a pore network with the geometric parameters of shale. The primary strategy is to obtain the pore morphology or geometric features directly using the methodologies outlined in Chapter 3. A comprehensive method will be described in this Chapter on how to construct a representative pore network using morphological parameters of both virgin and treated shale.

4.51 Quantification of Pore Structural Parameters

The following methods are used for the quantification of pore structural parameters and simple measurement of pore-size distribution. This research focuses on quantifying topological characteristics and incorporating such information into a pore network for both virgin and treated shale. To describe the complex shale pore system, several measuring techniques are required to characterize the surface area and distribution of pore size (BET, MIP), distribution of pore throat (SEM, CT), and total porosity (MIP).

The MIP is the standard technique used to determine pore size distribution in media varying in size from a micron to a nano-scale. The MIP test measures the amount of chemicals injected under pressure leading to a porosity measurement [104]. The porosity

is the main parameter impacting the permeability. For every shale sample, porosity will be measured.

Finney [105] proposed a calculation method for the spatial coordinate information of spherical particles in a random stacked spherical particle model. The spatial coordinates determined the geometrical information of the spherical particles and pores in the body. This has become a standard computer algorithm for randomly packed spherical particles. Bryant et al. [106] used the splitting method mentioned above to capture the pore structure according to the spherical particle packing model. The pore structure model can reflect irregular shapes of pore throats and the pore bodies. Bryant et al. [106] verified this by comparing the permeability with the measured results. Gao et al. [96] performed the microscopic seepage calculation by constructing the pore structure of sand. Gao et al. [96] included curved pore throats between pores. The mathematical function describing the curve between pore throats satisfies the Betis influence line, which is widely used in structural engineering, as shown in Figure 4.6. Several geological media of different porosity validated this method by comparing calculated and measured permeability values.

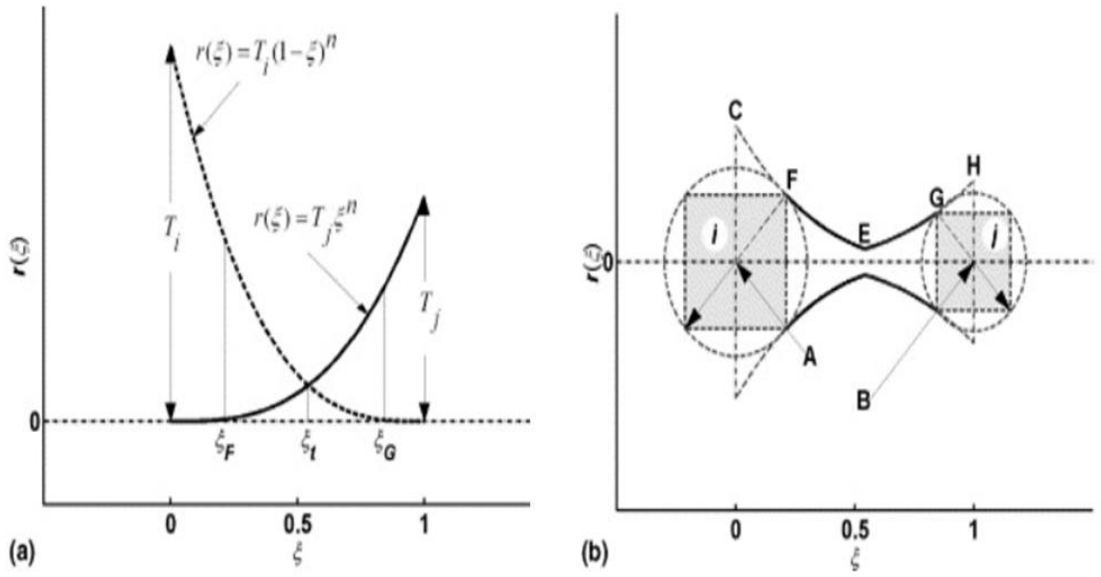

Figure 4.7 A: The influence lines as a function of coordination number. B: The outline of the bond connecting two-pore bodies.

Source: [107].

The three-dimensional reconstruction of the pore structure mainly relies on imaging technology to obtain its two-dimensional scanning slice and then extracts the pore structure based on the image. Wu et al. [108] obtained three-dimensional images of rock samples by scanning slices and then used the three-dimensional grid method, which considers spatial structure information (derived from 2D or 3D sample data, specifically thin-section data in the x, y, and z planes) identifying all the transition probabilities between the media's voids for a given local lattice [109]. Then the pore structure of rock samples was constructed by three-dimensional reconstruction and statistical analysis of the pore characteristics (Figure.4.8)

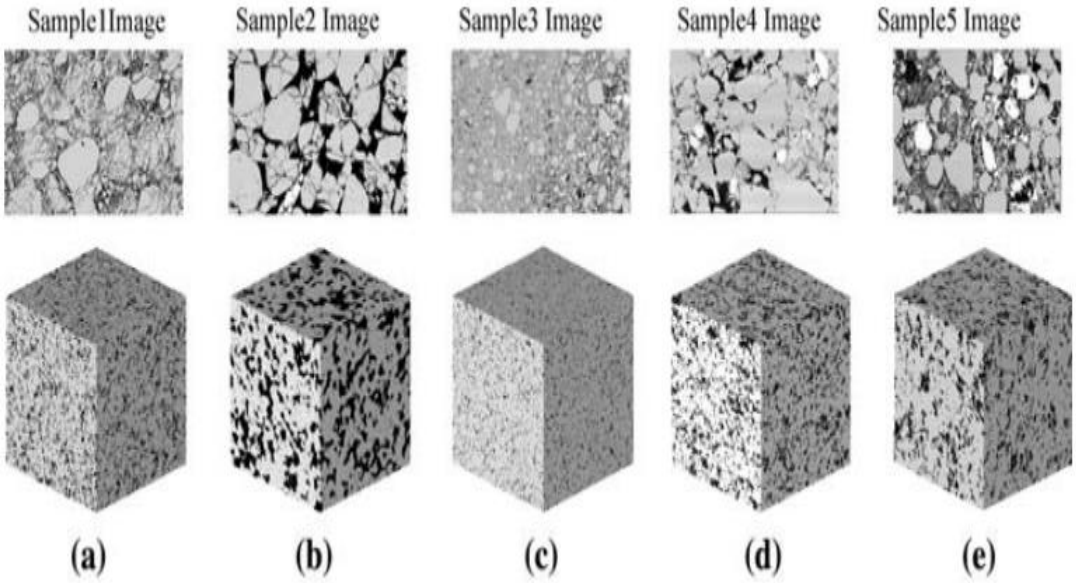

Figure 4.8 Reconstruction based on different shale slices.

Source: [108].

For the micro-nano pore-scale shale matrix, the pores in the two-dimensional scanning section are mostly isolated. Therefore, the connectivity of the pores in the actual shale matrix cannot be determined. Curtis et al. [110] performed SEM on nine typical shale samples as shown in Figure 4.9 to obtain two-dimensional slices of nano-scale pores and then reconstruction of three-dimensional pore structure of shale with low connectivity. Ma et al. [111] performed two-dimensional scanning electron microscopy imaging of shale samples, followed by three-dimensional reconstruction of three-dimensional scanning slices (Figure 4.10) and gas flow calculation analysis based on the extracted pore structure. Vega et al. [112] used X-ray imaging techniques to study the pore structure of Barnett, Eagle Ford, and Haynesville shale and obtained the porosity distribution of shale samples (See Figure 4.11).

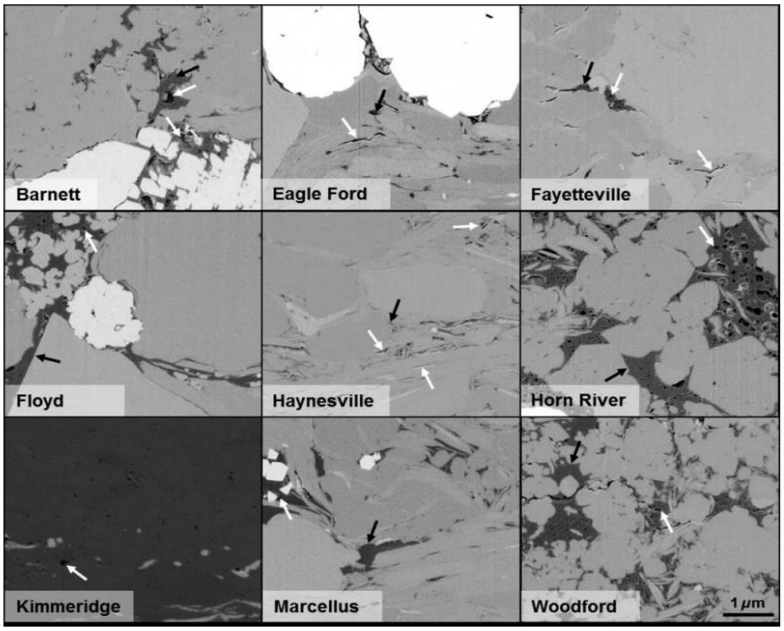

Figure 4.9 SEM of nine different shale samples cross-sectioned using focused ion beam milling.

Source: [110].

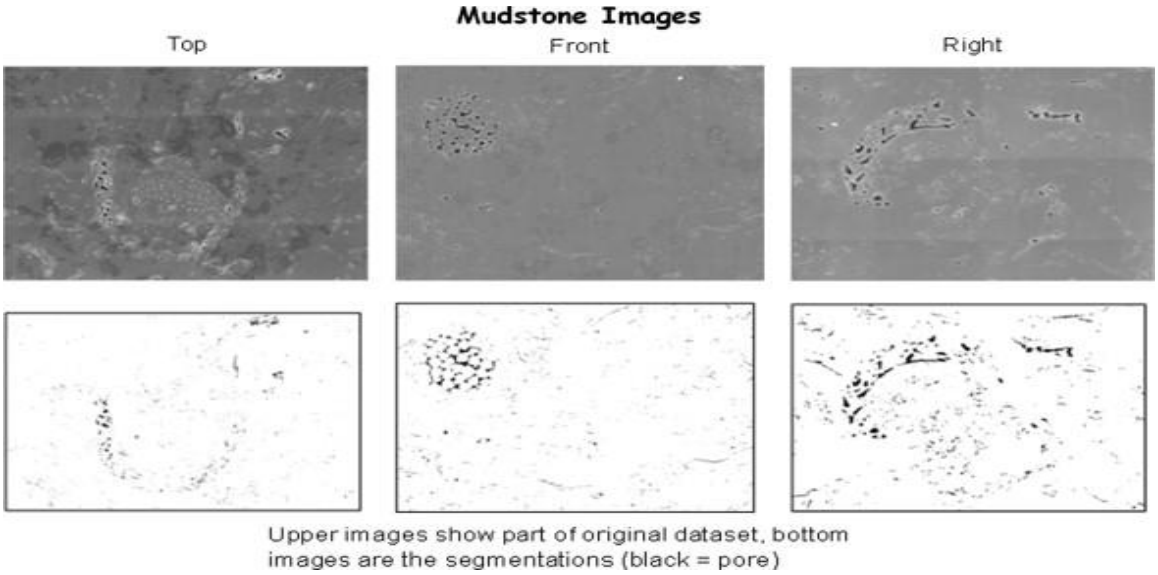

Figure 4.10 SEM scanning slices and binary images

Source: [111]**..**

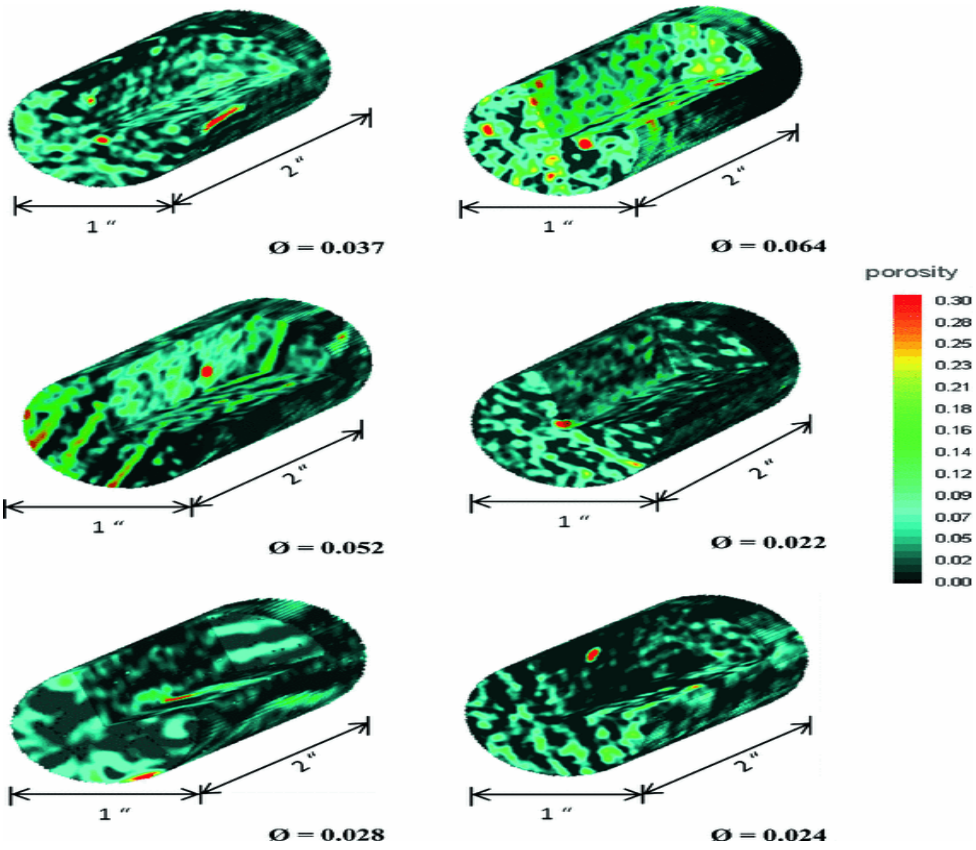

Figure 4.11 Three-dimensional porosity map reconstruction obtained for six additional Haynesville samples.

Source: [112].

The equivalent pore network model is a simple pore network based on the statistical results of the physical properties of geo-materials. It establishes pore structures that reflect its pore distribution and connectivity. The equivalent pore network model was first proposed by Fatt [37], where, based on the capillary model, a two-dimensional network model was proposed. Combined with the spherical particle accumulation model to reflect pore connectivity, a two-dimensional pore network that is a regular square network was proposed. Although the equivalent 3D pore network has more simplifications on the actual morphological structure of pores, it can better reflect the actual flow characteristics. The sample permeability calculated by the equivalent pore network model is basically of the

same order of magnitude as the actual measurements [113]. Now the equivalent pore network is ready to be constructed using the corresponding morphology represented by statistical pore parameters of shale. Figure 4.13 shows a flow chart of the proposed construction method of equivalent pore network of virgin and treated shale. The main steps are listed below:

1) The pore radius distribution is first generated and assigned to nodes and connections of a regular lattice, as shown in Fig 4-12. Figure 4-12 shows a 3x3x3 node lattice, but the size can be changed to match the desired accuracy.
2) The pore connection is generated. Randomly assign a target coordination number to each pore in the network for all phases. Inter-pore connections are randomly generated between adjacent pores using Equation (4-11).
3) If the throat size is directly specified, the unit size is solved using Equation (4-3); if the throat size is not specified, the test algorithm is used, and the unit sizes are solved by combining Equation (4-2) and Equation (4-3).
4) Eliminate isolated and dead-end pores in the network.

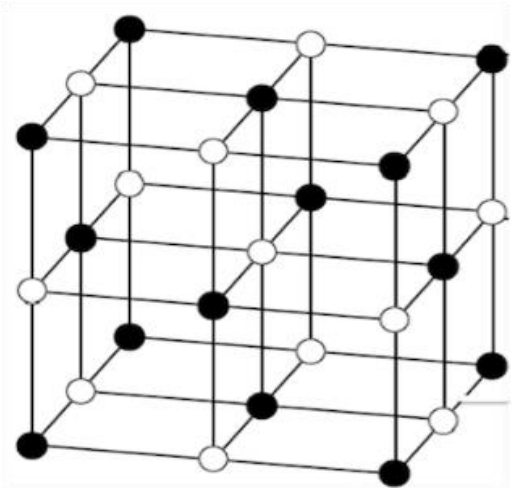

Figure 4.12 Regular lattices of the pore network.

4.52 Pore Size Distributions for Virgin and Treated Shale

The shale matrix is predominantly composed of pore throats (pores less than 2 nm diameter) and pore bodies (pores with 2-50 nm diameter). The shale matrix has both clay and carbonate minerals. Due to softening, two opposing observations are found: clay swelling

and carbonate dissolution. This should be appropriately accounted for in the constructed pore network of treated shale.

The pore-size distribution (PSD) is an essential aspect of a porous medium and affects most physical behaviors of porous media. Shales have a more complex pore structure than conventional reservoir rocks like sandstones and limestones. The most distinctive characteristic of shales is their multi-scale fabric linked to the microstructure of clay minerals. In shales, these clay aggregates form a locally aligned matrix with varying orientations, depending upon the depositional and stress history of the shale [114–116]. Hence, clay swelling would decrease the peaks of the pore size distribution for both pore throat and pore bodies. However, the acidity of fracturing fluid will dissolve carbonates in shale, creating many more macro-pores, which will shift the pore size distribution up due to the enlargement of pore throats and pore bodies.

Figure.4.13 shows the virgin pore size distribution. The conceptually expected pore size distributions after clay-swelling and acid-dissolution will be shown in Figure 4.14 and Figure.4.15, respectively. From the pore size distribution of the virgin sample, two peaks can be observed within the range of 0.3-160nm. The first peak shows the pore throats, and the second peak of the PSD shows the pore bodies.

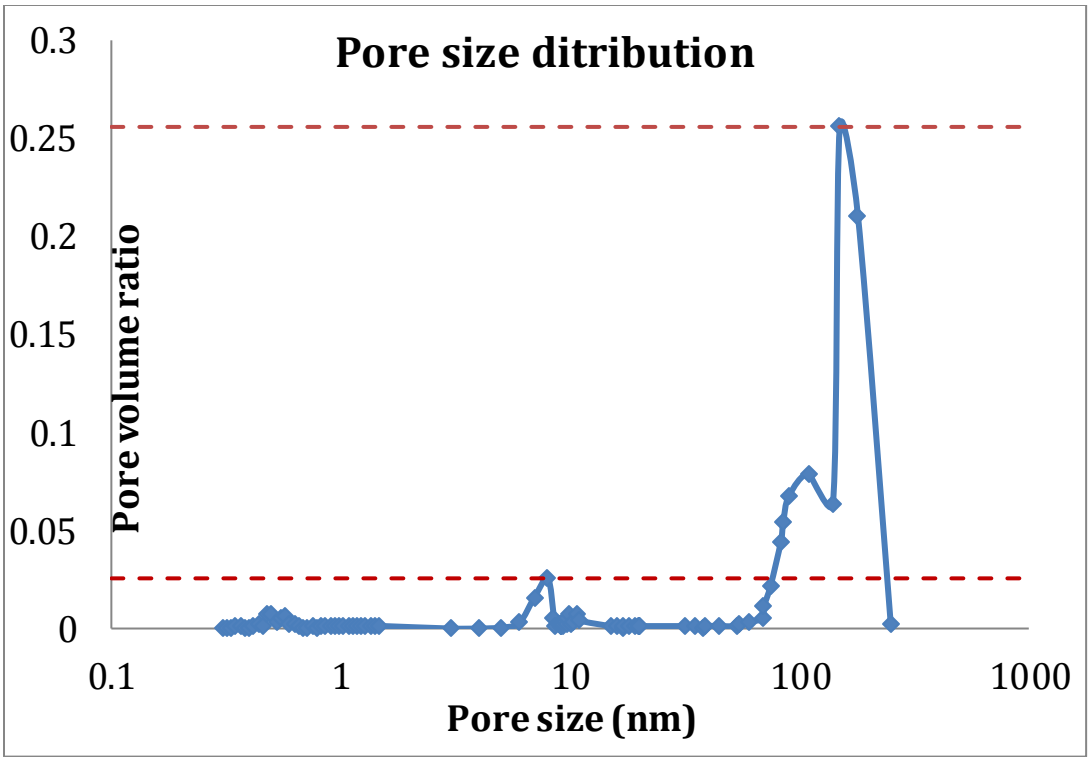

Figure 4.13 Pore size distribution of virgin shale sample of Longmaxi Shale[117].

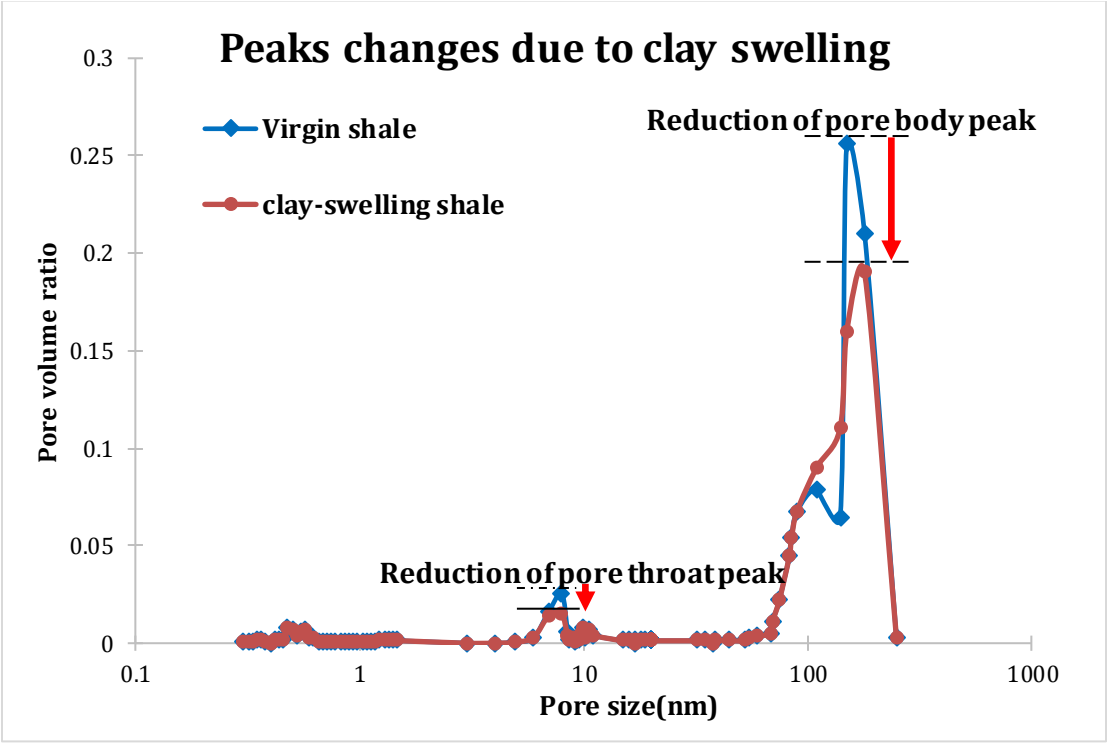

Figure 4.14 The changes in peaks due to clay-water reaction in Longmaxi Shale.

Figure 4.14 shows the conceptually expected PSD due to clay-swelling in shale after softening. The damage to the water-sensitive structure depends on the type of clay minerals, the distribution of clay minerals within the pore space, and the chemistry of the fracturing fluids. At the pore scale, clay-water interactions such as clay swelling will decrease pore throat and pore body volumes [118].On the contrary, the use of mild acid in the fracturing fluid can increase shale permeability. Mild acids will selectively dissolve carbonate minerals forming channels, which will create new pathways of the shale surface and even penetrate through to the bedding planes. Hence the well productivity will continue to benefit from the fluid pathways provided by the acid-carbonate reaction even after fracture closure. The clay-rich shale contains clay up to 60% of the total volume. Hence, such clays with carbonate dissolution and clay swelling will change the pore throat and pore body volume, as shown in Figure 4-16. Based on the treated shale PSD, pore throat and pore body size were determined, and the equivalent pore networks for both virgin and treated shale were constructed. Then the impact of fracturing fluid on shale was quantified in Chapter 5 by predicting the permeability of virgin and treated shale using the equivalent pore networks described.

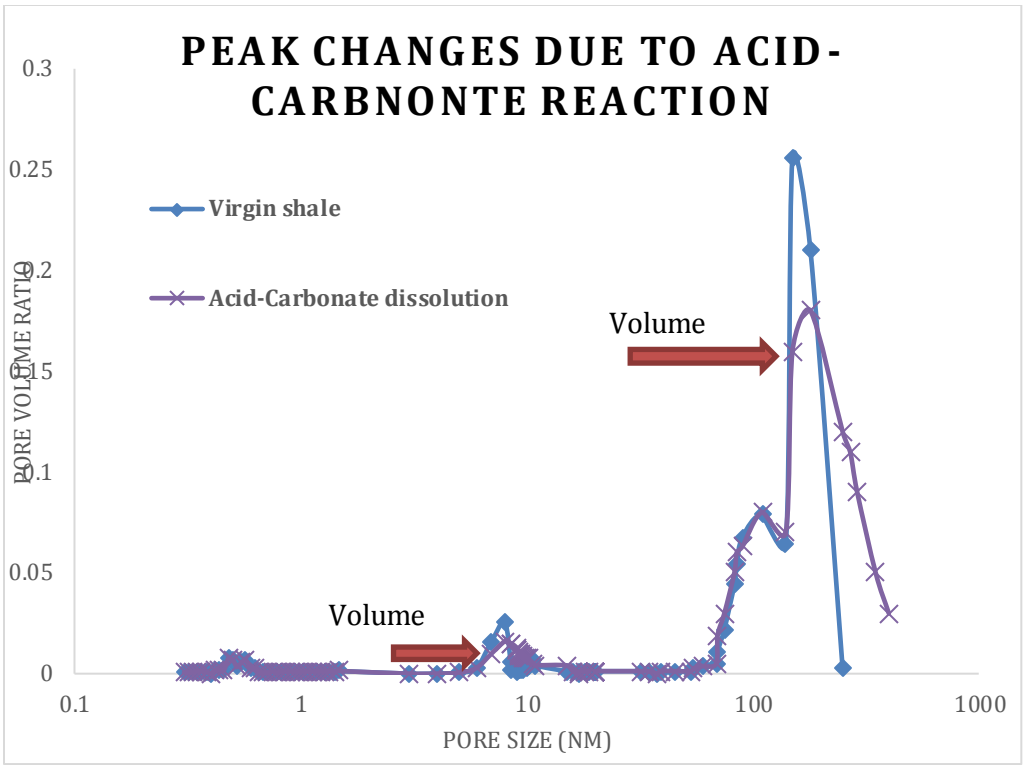

Figure 4. 15 Change in peaks due to acid-carbonate reaction in Longmaxi Shale.

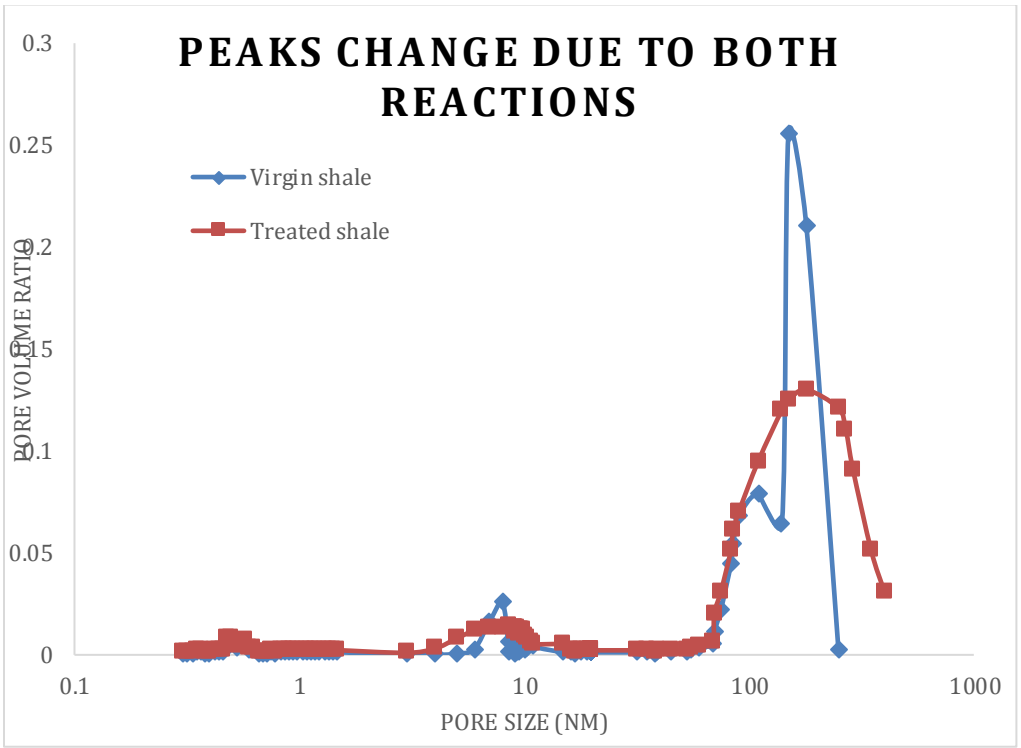

Figure 4.16 Peaks change due to both reactions in Longmaxi Shale.

4.6 Prediction of Permeability of Virgin and Treated Shale

Both the clay-swelling and carbonate-dissolution can be quantified based on PSDs. Hence the modeling parameters, porosity, pore size distribution, pore throat distribution, and coordination number can be determined. Based on the description in Chapter 3, once the pore networks were established for virgin and treated shale, the shale gas permeability can be predicted.

An important constraint in the calculation of the pore network is the network size. A smaller network can significantly improve the calculation efficiency, but the repeatability of calculations and stability becomes poor. If the network is too large, the stability of the calculations and the reliability of the model are high, but the calculation efficiency is low. Therefore, the determination of representative network size is the key to the application of the pore network.

The traditional pore network generally uses a grid size of 10×10×10, but such model size is only suitable for the cubic pore network model with a fixed coordination number. Gao et al. [96] used a computational model of 12×12×12, 15×15×15, and 20×20×20 to calculate the two-phase flow stability of the isotropic equivalent pore network. The results showed that the distribution of saturation and the calculation of relative permeability were consistent when the size of the equivalent pore model was 20×20×20.

To reflect the pore connectivity of different geological media, the coordination number in this research is not a fixed value. Still, it has a specific distribution, which makes the pore model produce isolated pores. Hence, such isolated pores need to be eliminated in the flow calculation as described in Chapter 4.

4.61 Permeability of Virgin Shale

Shale is a very dense, minimally connected geo-media [119,120]. The typical permeability of the shale matrix is 10^{-18} to 10^{-21} m^2 [121]. The pore size of the shale matrix is mainly distributed between several nm and several hundred nm, and the pore throat size is generally within 10 nm [41]. In addition, shale has significant anisotropy, as described before. Hence, a_x: a_y: a_z will be determined for the shale network to incorporate anisotropy.

The pore size and pore throat distributions for virgin shale have two peaks shown in Figure 4.17.

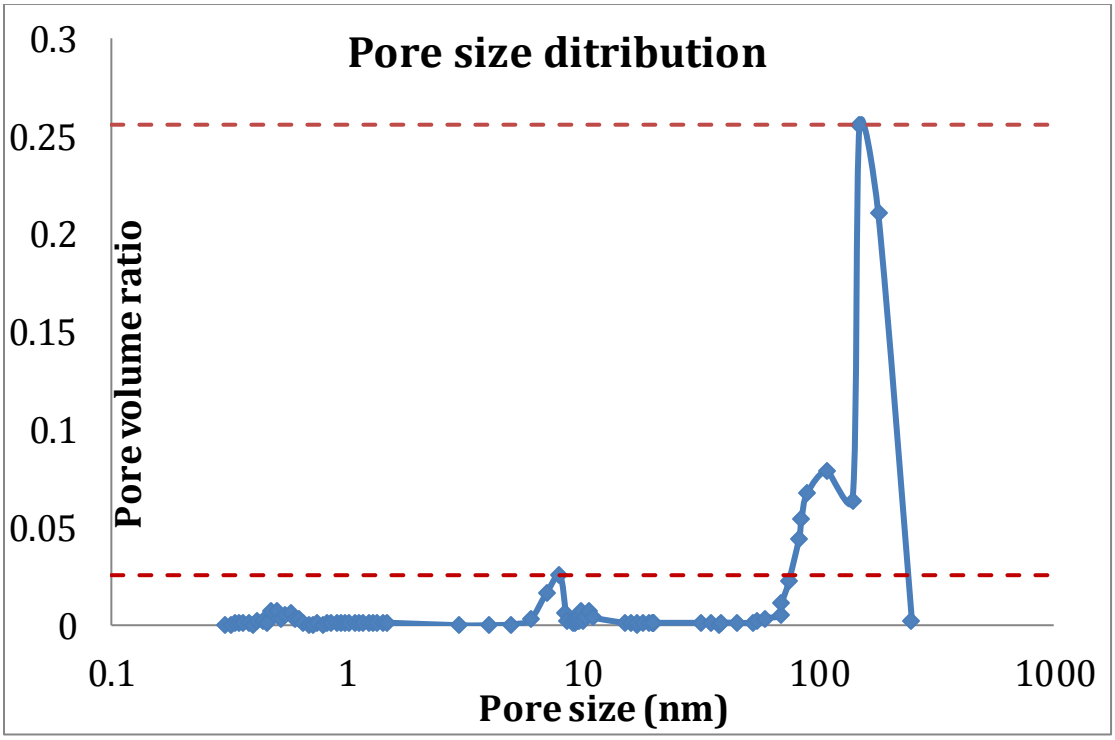

Figure 4.17 PSD for virgin shale of Longmaxi Shale.

Source:[117].

The pores are voids in the geological media, and various ways can obtain their size and distribution in the shale matrix. In this research, the random distribution of pores is artificially assigned to regular nodes in a lattice called an equivalent pore network. Hence,

all the pores are assigned to the network grid, so the total number of pores can be determined according to the model size. For example, a miniature model of 20 × 20 × 20 has 8000 pores, and the size of each pore is randomly generated based on the PSD, which obeys the normal distribution in the MATLAB program. Figures 4.18 and 4.19 show that the average pore body size is 150nm with a standard deviation of 20, and the average size of the pore throat is 16nm with a standard deviation of 2.

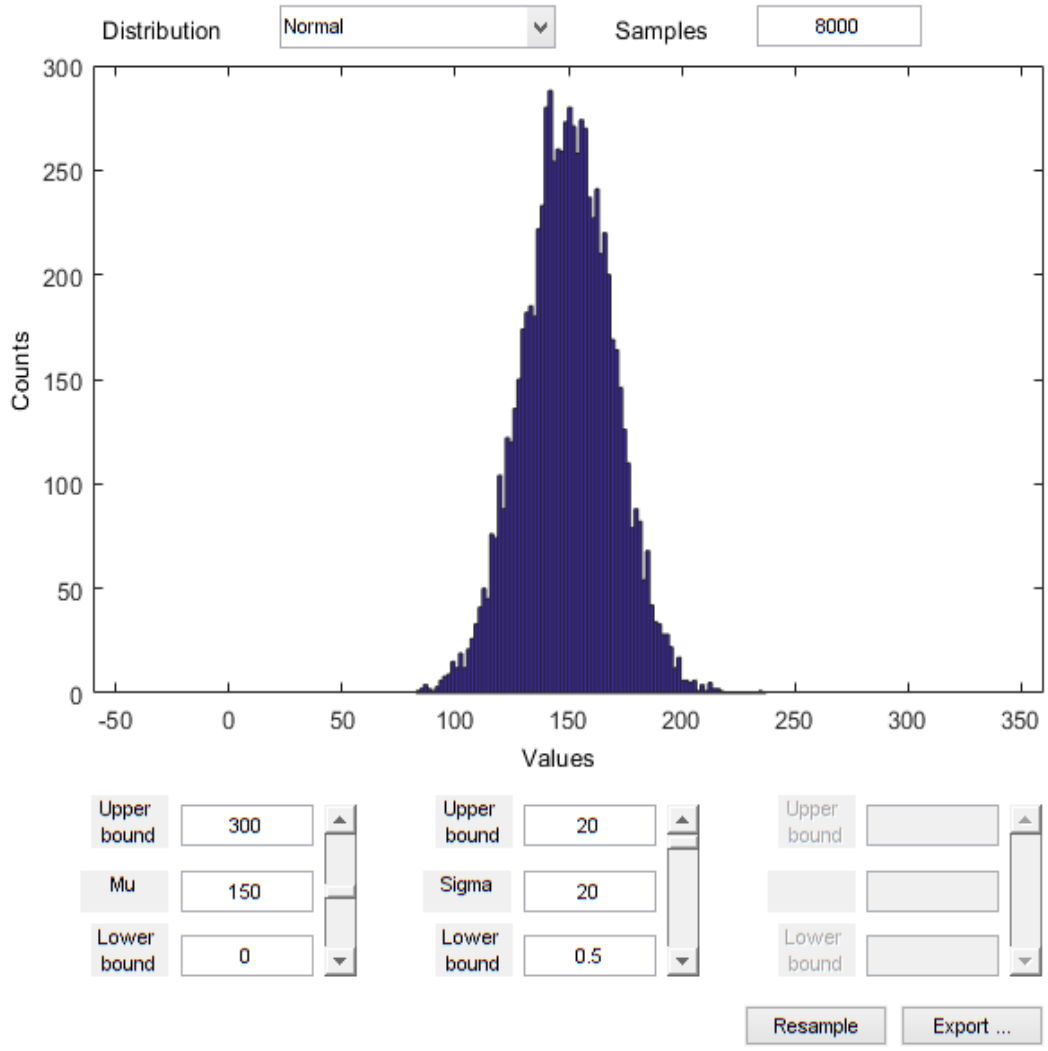

Figure 4.18 Virgin Pore body size distribution of Longmaxi Shale.

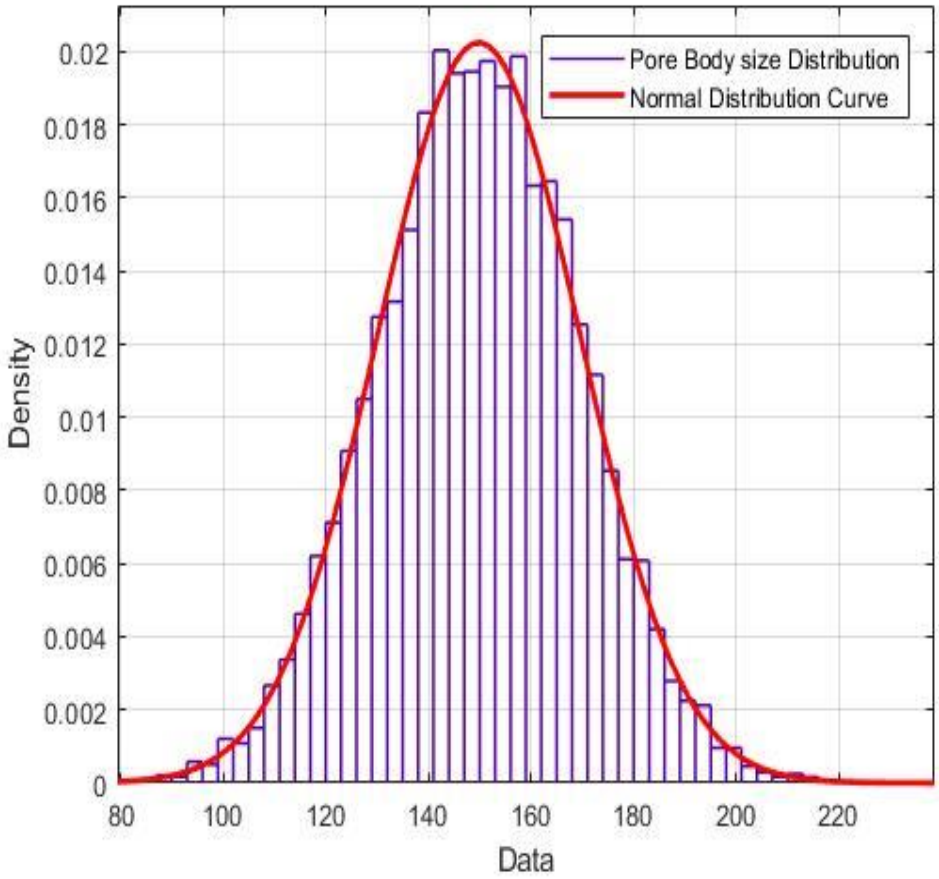

Figure 4.19 Fitted normal distribution curve of Longmaxi Shale.

The pore size and pore throat size satisfy the spatial correlation. That is, the size of two adjacent pores determines the size of each pore throat. The pore body size distribution can be extracted from the second or larger peak of the PSD shown in Figure 4.17 and can be fitted with a normal distribution of pores of virgin shale, as shown in Figure 4.19. Similarly, the pore throat size distribution can be fitted in a normal distribution of pore throats of virgin shale, as shown in Figure 4.21.

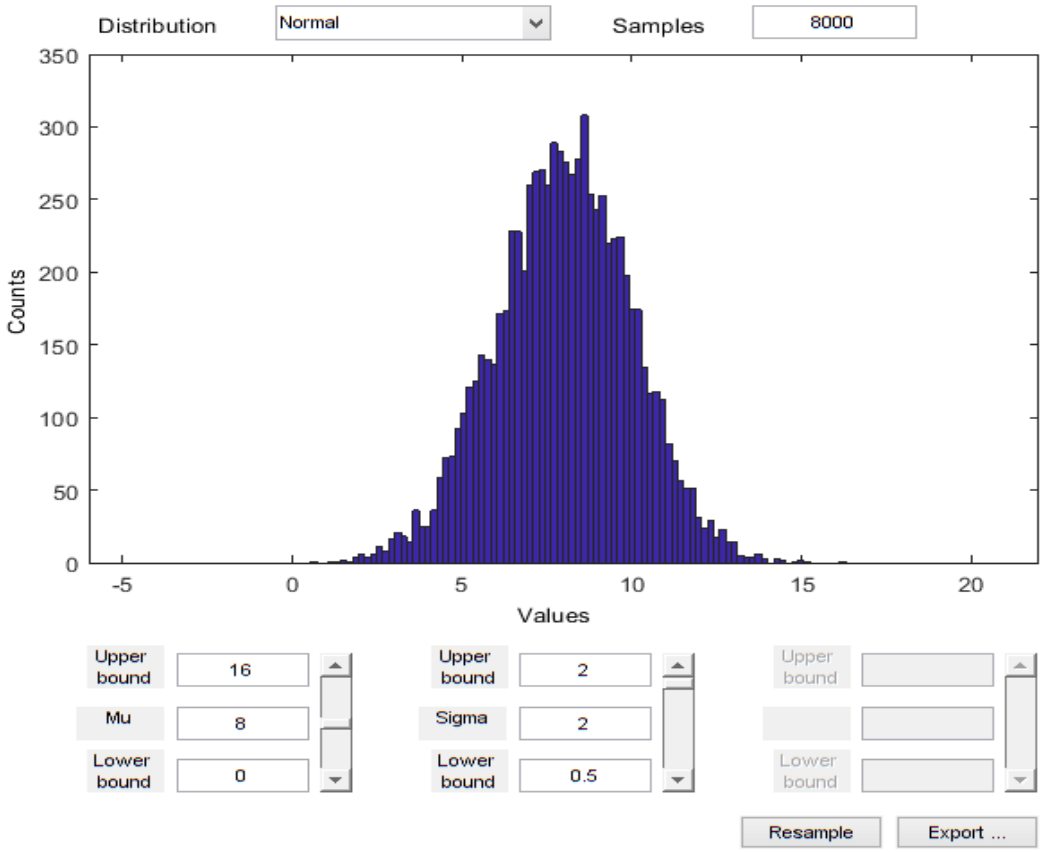

Figure 4.20 Virgin Pore throat size distribution of Longmaxi Shale.

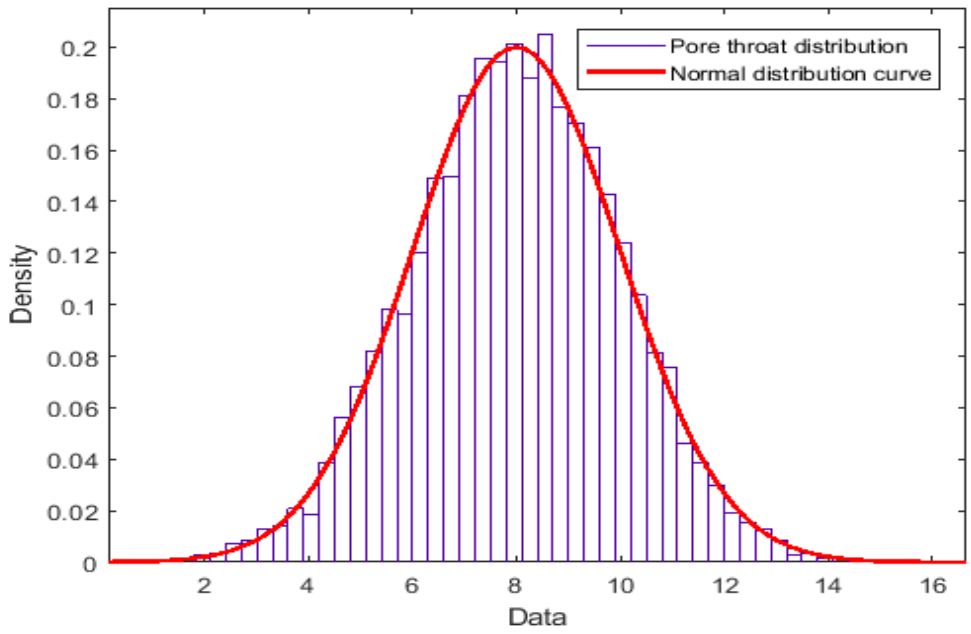

Figure 4.21 Fitted normal distribution curve of Longmaxi Shale.

The porosity of the shale is relatively low, generally lower than 10 %. The porosity of the geological media is positively correlated with the connectivity. Hence, with low porosity, the average coordination number for the shale matrix is typically 3 [41], whereas for well-graded sand is six.

To study the microscopic gas flow of shale, an equivalent pore network will be generated, and the typical network is shown in Figure 4.22. In this model, the X direction is the flow direction, where the upstream and downstream are kept at constant pressures. The upstream pressure is typically the reservoir pressure, and the downstream pressure is usually the atmosphere. The upstream pressure (p_{inlet}) is selected to vary from 4Mpa to 0.14Mpa to reflect the corresponding reduction in pressure with shale gas extraction. The remaining boundaries are zero flux boundaries. The permeability of virgin shale can then be calculated based on the parameters as described above and then shown in Figure 4.23.

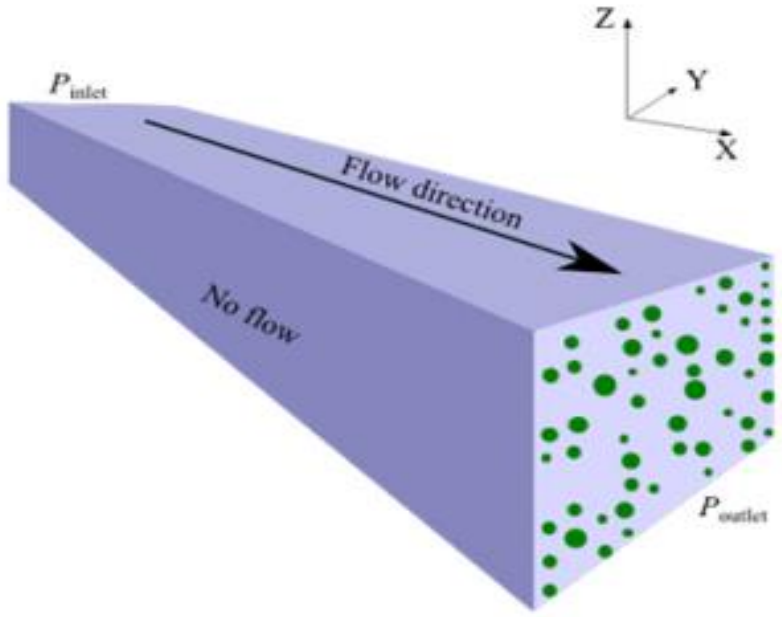

Figure 4.22 Flow direction and boundaries conditions.

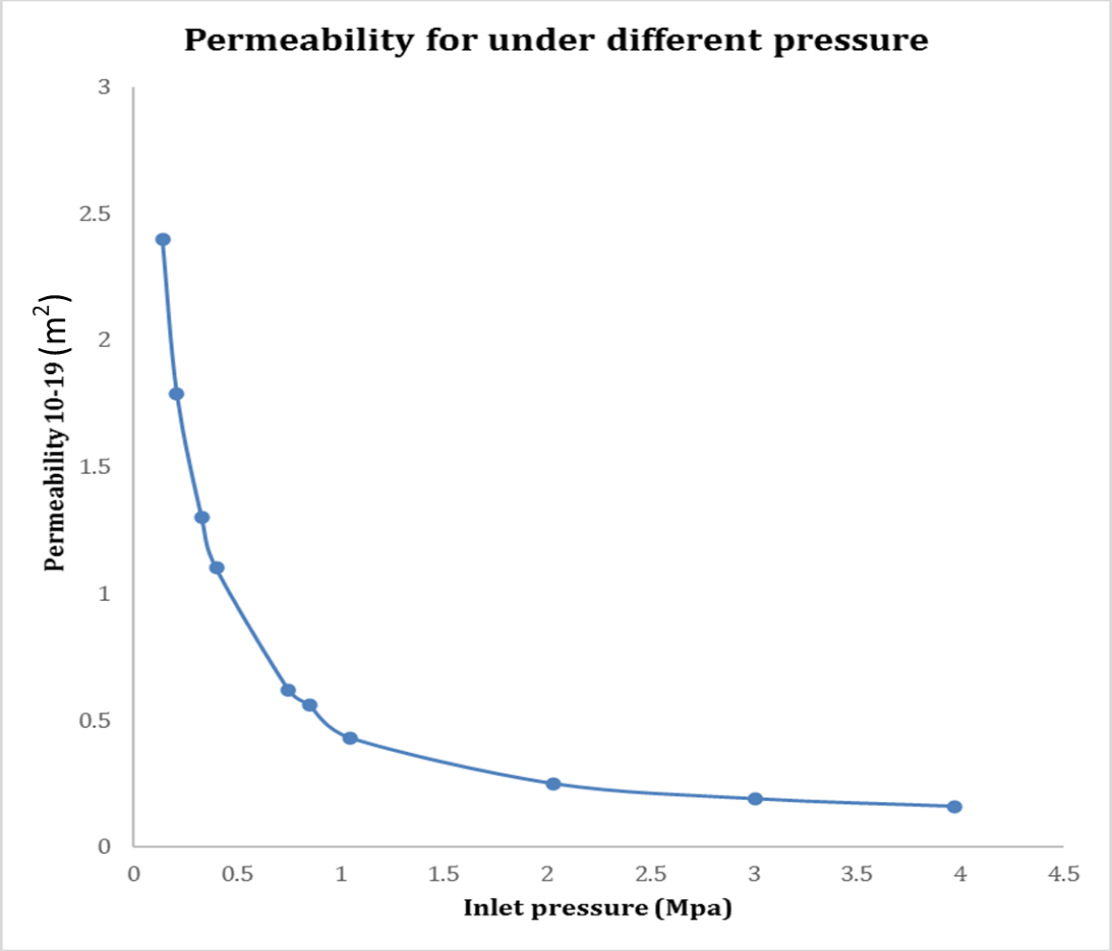

Figure 4.23 Predicted permeability of virgin shale of Longmaxi shale.

4.62 Permeability of Treated Shale

The PSD of treated shale can be represented as shown in Figure 4.24. There will be a reduction of the magnitude of two peaks of PSD. Therefore, average pore body size and average pore throat size tend to shift, resulting in smaller throat and pore sizes.

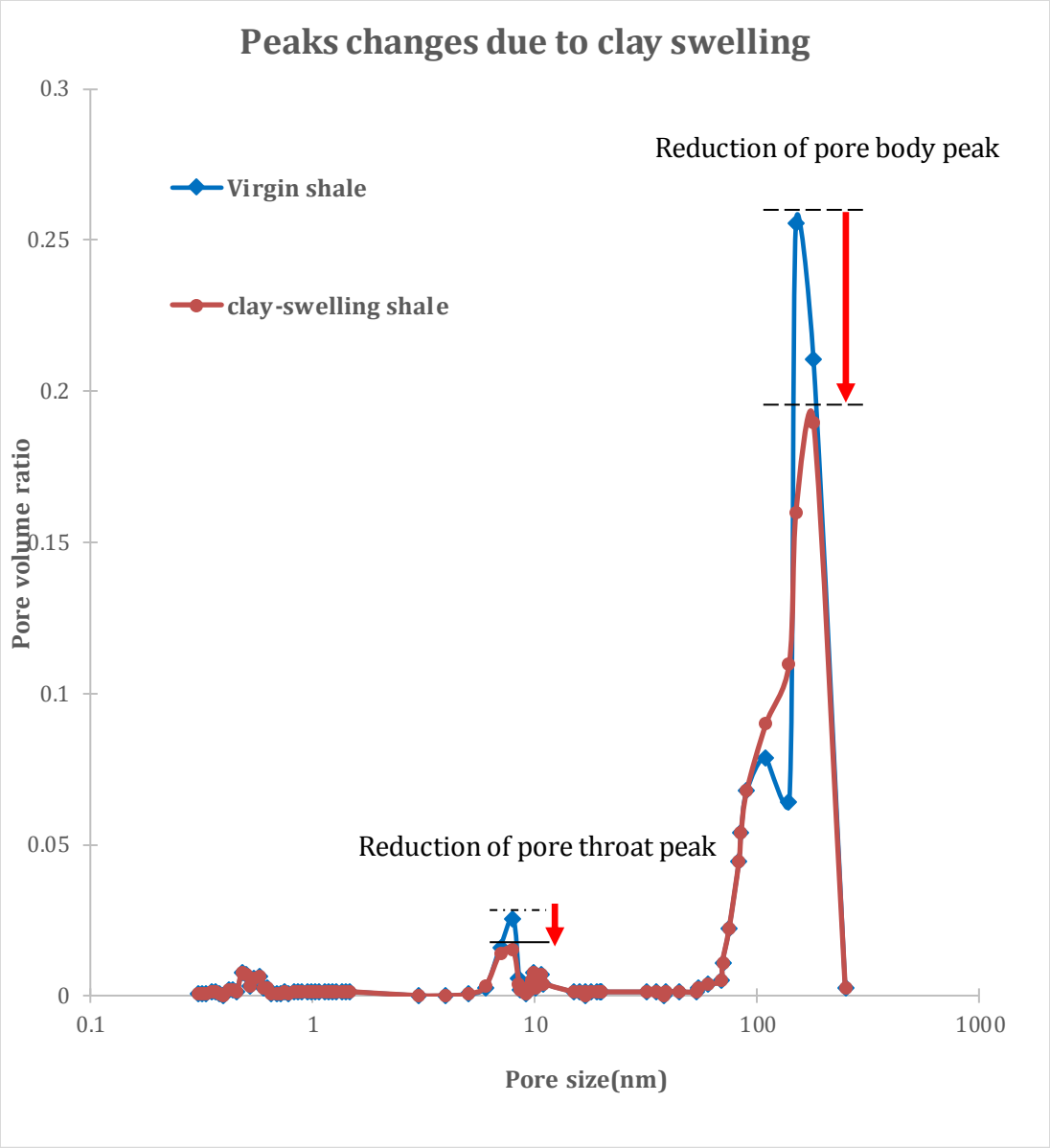

Figure 4.24 Peaks change due to softening in Longmaxi Shale.

Based on the PSD shown in Figure 4.24, the pore and throat distribution of treated shale can be extracted as shown in Figures 4.25 and 4.26.

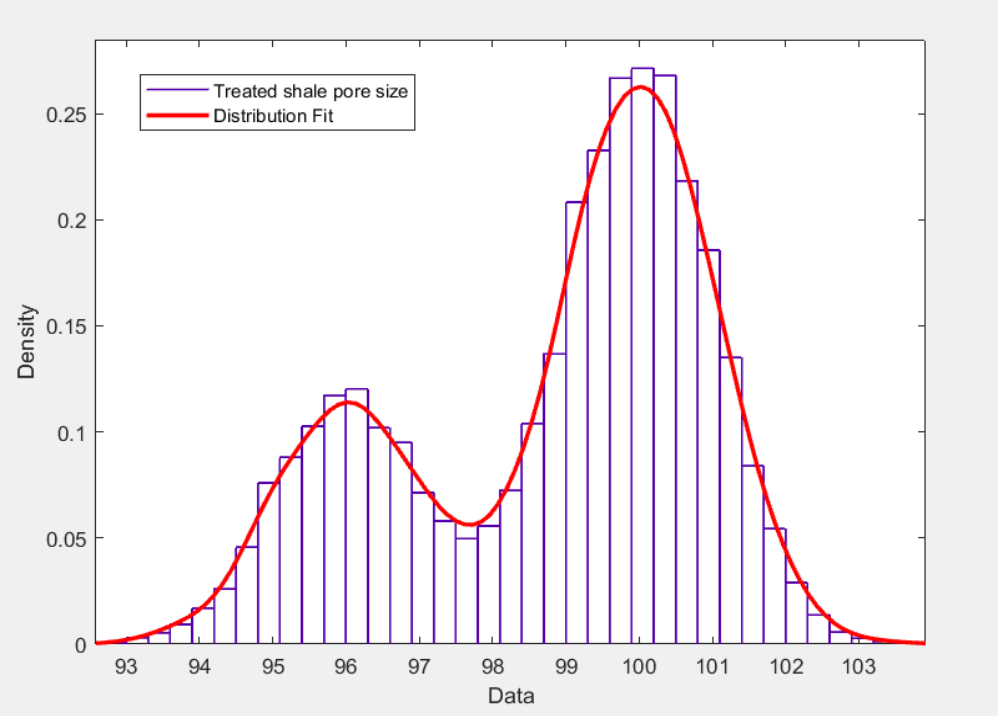

Figure 4.25 Treated shale pore size distribution of Longmaxi Shale.

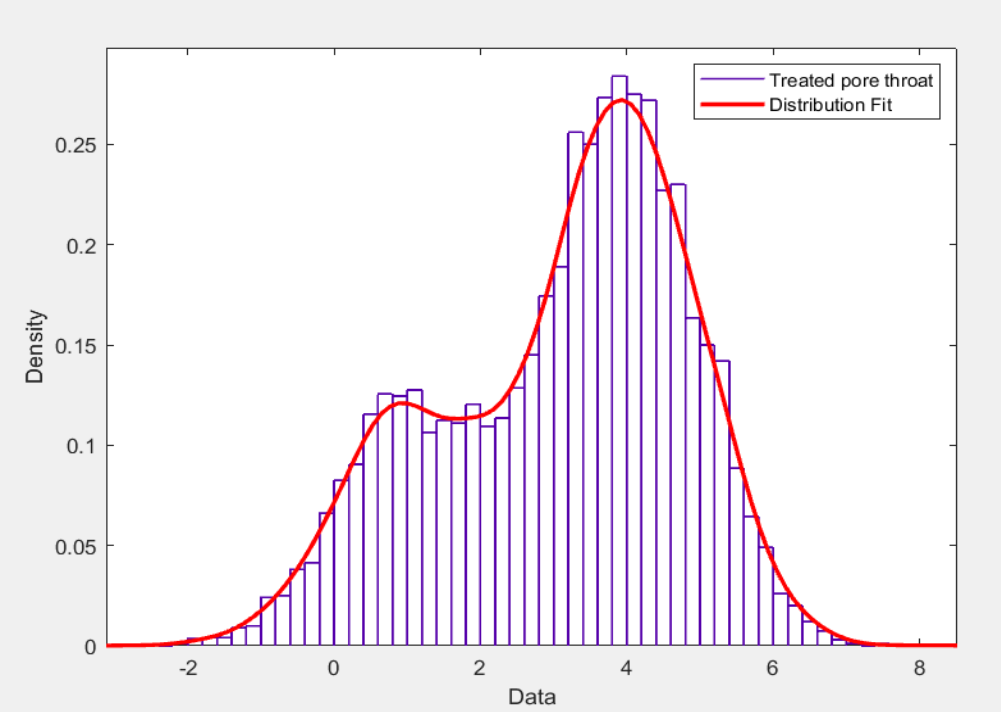

Figure 4.26 Treated shale pore throat distribution of Longmaxi Shale.

Based on the above information, an equivalent network for the treated shale can be developed. Both pore size and pore throat distributions are bimodal distributions in Longmaxi shale. However, to account for various ranges of pore size distributions for different shales, a universal distribution methodology (γ distribution) is used in this research. To simplify these bimodal distributions, γ distribution is used in the research [122]. The variation permeability of virgin and treated shale for various input pressures mimicking the depletion of shale gas in the pore is shown in Figure 4.27.

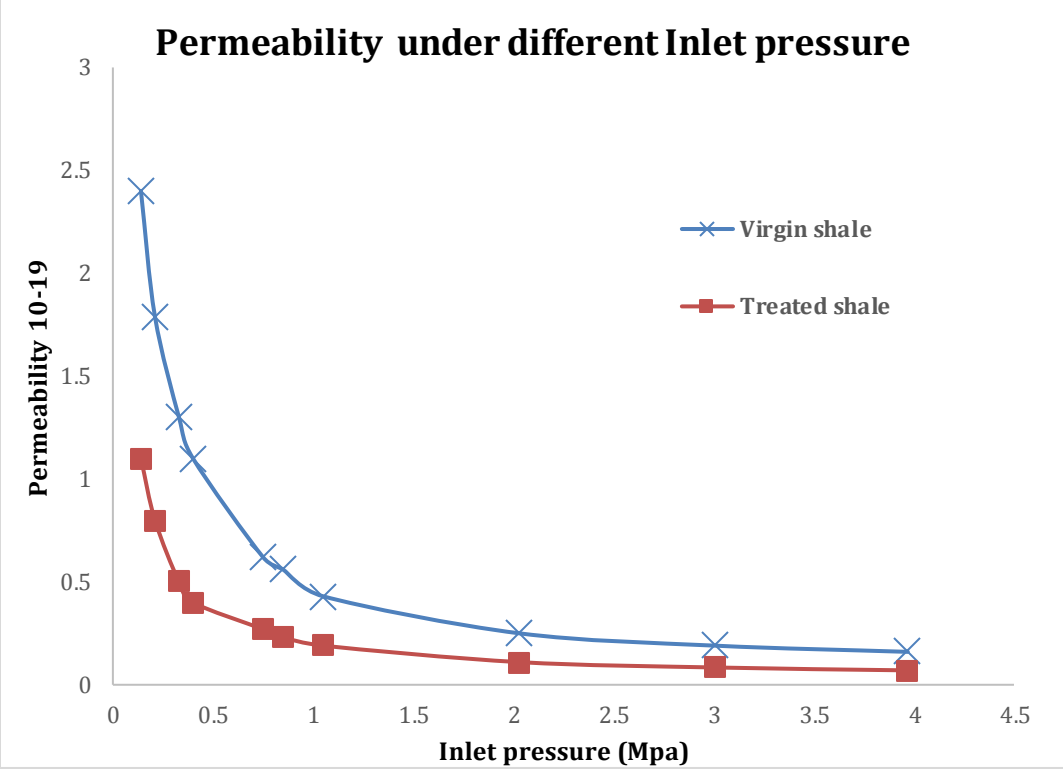

Figure 4.27 Predicted permeability of treated and virgin Longmaxi shale.

Figure 4.27 shows a significant reduction of permeability at low reservoir pressures of 0.14Mpa to 1.05Mpa. At the lowest inlet pressures, a 50% reduction in permeability occurred. The lower inlet reservoir pressures occur at the late stage of shale gas production,

and the apparent permeability will be significantly reduced at that stage due to the shale softening.

4.7 Impact of Shale Softening on Permeability

Using a pore network and coupling the porosity change measured in this study will provide insights into the changing permeability and help to quantify the damage due to shale softening. The permeability result is compared in this chapter based on the spatial structures and porosity of original and treated shale. Figure 4.28 shows a quarter of the 20*20*20 network used in the simulation to illustrate the pore bodies connected to pore throats where pore bodies are spheres, and the pore throats are cylindrical. Pore throats connect the pore bodies.

Based on several Longmaxi shale pore structure research [117,122]. The initial target shale of porosity (1.58%) was reconstructed. Furthermore, reduced porosity will be achieved by reducing the pore body and pore throat with a swell ratio of 0.69, as shown in Table 4.1.

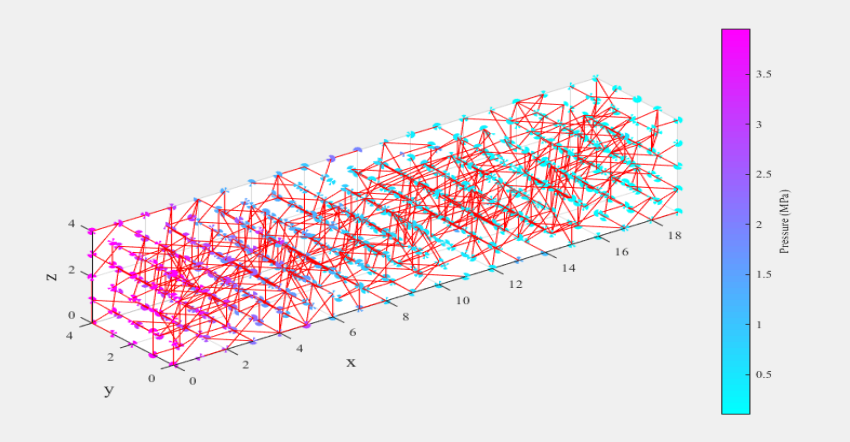

Figure 4.28 Illustration of a swelling pore network.

Table 4.1 Original Longmaxi shale PNW parameters

Porosity	Model size	Mean pore body diameter(nm)	Mean pore throat diameter(nm)	Coordination number	Swell ratio
Original (1.58%)	20*20*20	4.3	0.66	4	0
Treated (1.06%)	20*20*20	2.9	0.45	4	0.69

Several assumptions were made for the simulation as follows:

- Assumed that the swelling initializes from the first layer of the grid in contact with hydraulic fracturing.
- The pore body and the pore throat swell due to the clay-water reaction, but only the throat contributes to the matrix permeability
- As the softening progress gradually, the first layer swells first and then continues to the next layer until the entire model is swelled.

To demonstrate the swelling, Figure 4.29 shows an increase in swelling propagation through layers from no swell to swelling ratios of 0.35 and 0.69 for the layers in contact with hydraulic fracturing liquid, indicating swelling with the progress of fracturing. The outlet pressure and inlet pressure are fixed at 100000Pa and 200000Pa, respectively. The permeability of the original shale decreased dramatically as the swell ratio decreased. Figure 4.29 shows that the softening of shale is the main reason for the loss of permeability of the shale matrix.

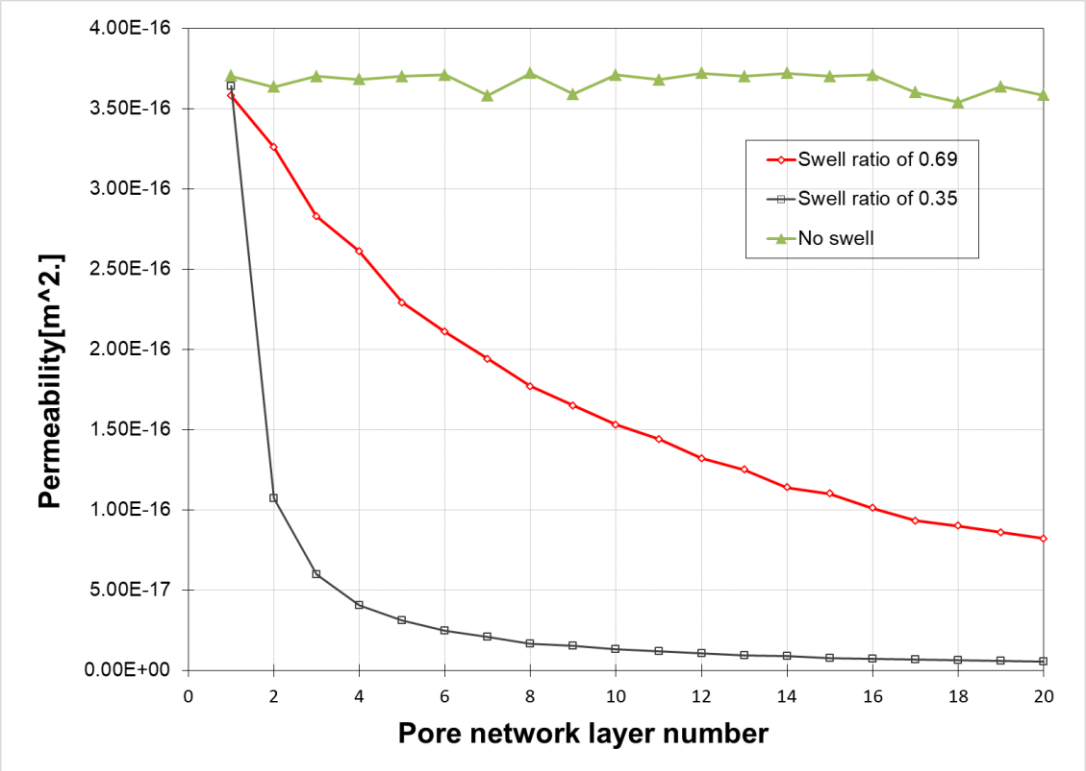

Figure 4.29 Impact of different swelling ratios on permeability of shale matrix.

It is reasonable to conclude that with the diffusion of moisture into the shale matrix, pore sizes in the whole grid decrease, hence the shale permeability. The permeability is substantially smaller than the original permeability in the extreme case when all layers swelled.

Four different simulations were performed to demonstrate further the stages of shale softening, which are situation 1 (no swelling, original shale), situation 2 (Layer one), situation 3 (half of the layers), and situation 4 (Treated shale), as shown in Figure 4.30. These stages represent hydraulic fracturing progress in which water seepage from the first layers to the entire grid. To understand the change of shale permeability during fracturing for different stages, swell ratio and layer number were assigned.

This simulation outlet pressure was fixed at 0.1 MPa, and the inlet pressure was gradually increased from 0.1MPa to 4MPa. The permeability decreases dramatically after half swelling to 0.39 of the initial permeability. In Longmaxi shale, even though the porosity reduces only by 0.5% of the original shale, the permeability reduced to 21% of the original. Both swelling layers and swelling ratio are used to indicate the stage of shale softening. Permeability changes can be calculated using the swelling pore network model.

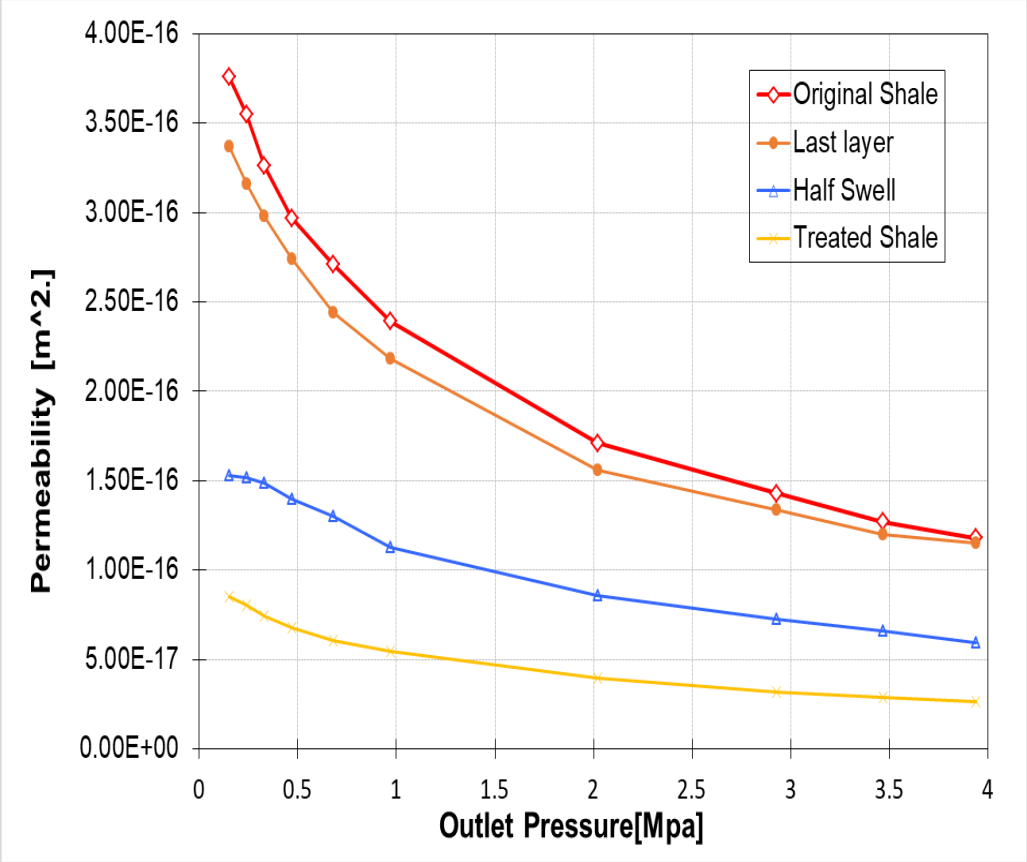

Figure 4.30 Permeability of different condition of shale.

CHAPTER 5

AN ANISOTROPIC PORE-NETWORK MODEL TO ESTIMATE THE SHALE GAS PERMEABILITY

5.1 Introduction

The extraction of natural gas from tight shale formations in the USA is one of the landmark events of the 21st century[123]. Horizontal drilling combined with hydraulic fracturing has allowed the extraction of large amounts of natural gas from low permeability tight shale formations previously considered impossible or uneconomical to exploit[124]. According to the U.S. Energy Information Administration, as of 2012, shale gas in the United States accounts for more than 40% of the total domestic natural gas production. Furthermore, it is expected to reach 50% by 2039[125].

The permeability of shale is a crucial design parameter for gas extraction [126]. Shale is a heterogeneous and anisotropic ultra-fine rock with low pore connectivity and extremely low intrinsic permeabilities of 10-18 to 10-21 (m2) [127–129]. The permeability test of shales using traditional laboratory techniques may not provide realistic values. This has to do with the measurement of in-situ permeability of nano-scale pores at high pressures. Core samples with stress-free fractures and atmospheric moisture plus Darcy flow interpretation for different flow regimes at diffident applied pressures may result in substantial deviation from in-situ values. Hence, it is important to understand the shale pore structure and develop a predictive tool for gas flow mechanisms using shale reservoir properties and shale pore structure.

At present, the research on pore-scale flow characteristics mainly focuses on typical geotechnical media such as sand and sandstone with millimeter or micrometer pores. As

geotechnical engineering seepage research gradually expands to rock formations and even shales with micro-nano scale pores, the traditional flow analysis cannot reasonably explain the fluid flow characteristics at the micro-nano pore scale. The seepage characteristics of tight shale formations can be studied from a microscopic perspective using a pore network model [129].

5.11 Previous Studies

A Pore network model can be used to investigate the micromechanics of seepage in porous media. Typical tight gas formations are usually porous media where nano-scale pores are randomly distributed within the shale matrix. Digital methods, including focused-ion-beam scanning-electron-microscopy (FIB-SEM) and computed tomography (C.T.), are used to obtain two-dimensional slices of the pore structure of the shale samples. Three-dimensional pore reconstruction models can be built based on slices. Previous works have reported different methods of pore reconstruction [111,129,130]. Vega et al. [112] studied the pore structure of Barnett, Eagle Ford, and Haynesville shale samples by using high X-ray contrast gas. Song et al. [131] reported a local-effective-viscosity multi-relaxation-time lattice Boltzmann model to simulate the gas transport in shale. All previous research provides essential information on shale structure and gas transport.

Direct simulation using pore reconstruction models can be computationally demanding due to the complicated boundary conditions for flow and gas transport in the shale pore structure. Alternatively, the equivalent pore network model is based on the statistical values of physical properties of rock and soil media to establish a simplified pore structure reflecting pore distributions and spatial connectivity. The equivalent pore network model was first proposed by Fatt [37]in 1956. He proposed a two-dimensional network model

based on capillary tubes, and combined the spherical pore accumulation model to account for the connectivity between pores, and proposed a two-dimensional regular grid network model. Nicholson and Petropoulos [132] 1971 established a three-dimensional equivalent pore network model and performed a quasi-static two-phase flow calculation. Since then, many scholars have studied the pore morphology of the pore network model. Dullien [133] 1979 simplified the connecting throats between pores into continuous capillary sections. Reeves and Celia[39] 1996 established a constant coordination number equivalent pore network model and further considered the linear change of pore throats. Although the equivalent pore network model simplifies the morphology and structure of the pores, it can better reflect the actual flow characteristics. The simulated permeability calculated based on the equivalent pore network model is the same order of magnitude based on actual test measurements[131–133]. Jerauld and Salter [97] in 1990 compared the equivalent three-dimensional pore network model with the pore reconstruction model and found that the permeability calculation results of the two are equivalent. These validations enabled the equivalent pore network model to be considered an established mathematical method to construct different rock and soil media pore structures based on flexibly based statistical pore parameters. However, unconventional shale geological conditions are very different; the solid phase usually consists of various mineral components in an intricate and anisotropic micro/nano pore structure [134][135]. Many shale gas formations have features such as heterogeneity, low matrix porosity, and low permeability, which is the critical factor that differentiates unconventional formations from those conventional formations.

An equivalent pore network is a simplified pore structure of the geo-media. It simplifies the complex flow paths (pore bodies, pore throats, etc.) in the geo-media into

regular geometric shapes, such as spheres and cylinders, as shown in Figure 5.1. This methodology gradually evolved from two-dimensional to three-dimensional and now developed into equivalent pore network models suitable for simulation of various geo-media. The pore bodies in an equivalent pore network represent the larger-sized cavities in the geo-media. The pores are connected by pore throats, smaller cavities, or nano-fractures for fluid migration. In an equivalent pore network, the size of pore radii varies, and they are regularly arranged on grid points. The distance between the centers of adjacent pores is a constant value to simplify calculations. The average number of surrounding pores varies depending on the geomaterial. The average number of active connections to a pore body is called the coordination number. By adjusting the size of the pore radius, pore throat radius, and coordination number, a pore network model can be developed to simulate the gas seepage within geo-media and conventional reservoir rocks [96].

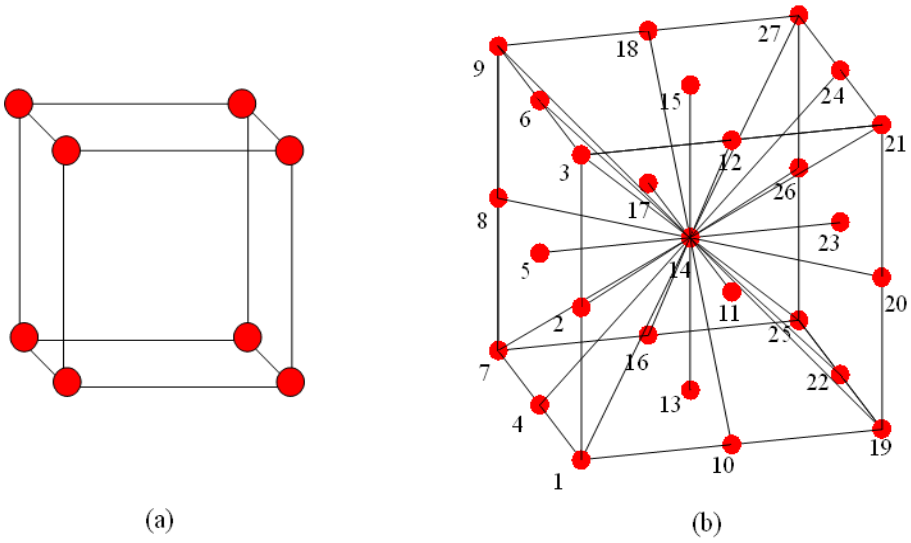

Figure 5.1 The geometry of the equivalent pore network (a) Cubic lattice with a constant coordination number of six (b) Cubic lattices with 26 pore coordination numbers.

Source: [39][38][40].

Zhang et al. [41] developed a nano-scale pore network model to describe the isotropic pore structure in shale formations based on a reduction factor for pore connections. This reduction factor depends on a dilution or a reduction algorithm. In this research, an anisotropic pore network model with an anisotropic ratio in three directions is developed by enhancing the model. This model is subsequently validated using measured permeability data.

5.12 Motivation and Importance of the Research

The use of pore network models to study the seepage characteristics of rock and soil media has been carried out to a large extent, but there are still certain shortcomings. The equivalent anisotropic pore network still needs to be further developed. Based on the equivalent pore network model, the relationship between the pore structure of shale and its seepage characteristics, especially anisotropic behavior, needs to be established. This manuscript presents the development of an equivalent anisotropic pore network model using pore body sizes, pore throat sizes, coordination numbers, and other pore structure parameters. This equivalent pore network can represent the average actual pore structure of shale to simulate the anisotropic permeability. Geological media behaving as underground reservoirs generally has extremely low pore connectivity [38]. Macro-scale gas flow simulations of such geological media usually ignore the impact of micro/nano-scale pore connectivity and flow regimes. The tight porosity and the complex connectivity of unconventional reservoirs make it challenging to account for the traditional macro/nano scale fluid flow. The establishment of a pore network model can account for complex geometric shapes and spatial connectivity of pores and provide an effective means to explain the fluid flow in tight formations such as shales with micro/nano pores.

The method of establishing an equivalent pore network model has dramatically improved calculation efficiency[136]. The model can also account for the heterogeneous characteristics of the shale. Still, the results of the equivalent pore network model often deviate from the actual pore network, and further research on the model construction method is needed. Multi-scale flow characteristics will have a significant impact in the case of low permeability. Many studies have paid attention to the flow regime transition at different scales and pressures. Therefore, considering the multi-scale flow characteristics, the pore network model can predict the permeability of geotechnical materials with low permeability and connectivity and obtained results that are more consistent with measured test results.

5.2 Construction of the Anisotropic Pore Network

When the average coordination number in the equivalent pore network model is low, then there may be cases where the coordination number of some pores may be less than 2, and hence becomes dead-end pores (ζ=1) or isolated pores (ζ=0). There may also be dead-end pore groups and isolated pore groups (multiple pores have less than two connections to the main percolation channels). These pores are in the actual pore structure. Still, they do not contribute to the flow, so they can be eliminated in the equivalent pore network model, thereby reducing computation time. To eliminate the pores that are not connected in the model, it is necessary first to define the isolated pores and the dead-end pores as follows:

1. The passage is connected to any downstream pores from any upstream pores through a non-repeating pore, called a seepage channel.
2. If any seepage channel contains a pore, it is called a seepage pore; otherwise, it is called a non-seepage pore.
3. For an interconnected non-seepage pore group, if a pore can be connected to any seepage channel, this pore group is defined as a dead-end pore group. Otherwise, it

becomes an isolated pore group.

According to the above definition, it can be seen that in the equivalent pore network shown in Figure 5.2, pore A is isolated, pore B is dead-end pore, pores C belongs to the isolated pore group, and pores D belong to the dead-end pore group. The dark region shows in Figure 5.2 shows the seepage pores and pore throats after the pretreatment of the pore structure.

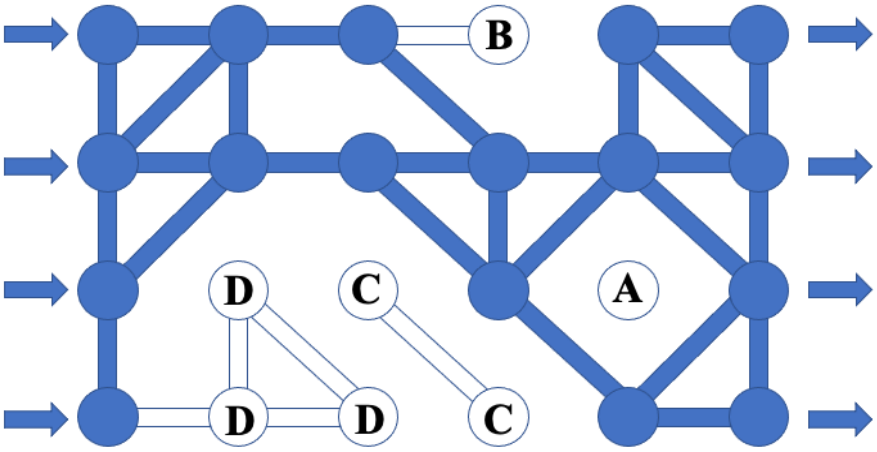

Figure 5.2 Schematic of pore types in the pore network.

Through the above discussion, a generation method for the pore network model can be summarized as:

1.Pore radii generation: Based on the distribution of pore body sizes, corresponding pore radii are randomly generated for each pore body in the network.

2.Pore connections: Randomly assign a target coordination number to each pore body in the network and randomly generate inter-pore connections between all adjacent pores.

3. Using the elimination method to exclude isolated and dead-end pores in the network.

5.3 The Anisotropy of Pore Network Model

Because shale is highly anisotropic with bedding, it is often less permeable in the vertical direction than in the horizontal direction [137]. The published permeability values vary by several orders of magnitude and are directly related to the applied effective stress (the difference between confining and pore pressure) and bedding orientation relative to the flow direction (parallel or normal to bedding). For different shale samples, including Mississippian Barnett Shale, Vermylen [138], Heller [139], and Heller et al.[140], showed that permeability values of shales are varying from 10^{-17} to 10^{-21}m^2. For Scandinavian Alum and Toarcian Shales, Ghanizadeh et al. [137] reported permeability between 10^{-17} and 10^{-22} m^2. In Western Canada for Woodford Shales, Pathi [126] reported three to four orders of magnitude differences in anisotropic permeability. Tinni et al. [141] found up to 100 times the anisotropy ratio for Devonian and Ordovician shale samples.

Due to geological deposition or layering structures in distinct directions, reservoir rocks for natural gas are often anisotropic. Because shale is highly anisotropic with bedding, permeability in the vertical direction is often much smaller than horizontal direction [137]. This anisotropy was incorporated into the pore network in this research.

Under normal circumstances, it is unlikely to connect all the pores. Therefore, by setting different coordination numbers of the model in each direction, anisotropy of geological media can be accounted for in the model. As for coordination number generation, the general practice was to delete the pore connections by using a dilute algorithm after generating the fully connected structure so that the pore connection is consistent with the actual shale.

Actual shale formations are anisotropic, and different directions often exhibit different permeabilities. In the process of model building, an anisotropic parameter can be used in

the equivalent pore network with different connection probabilities. Since the developed pore network model is three-dimensional, a new concept was introduced to consider the anisotropic permeabilities for three different planes of shale matrix: anisotropic ratio. It is defined as the ratio of the number of pore connections in the three directions of x, y, and z as (ax, ay, az); since the developed model is a regular lattice grid, the total number of connections for each plane is available after the construction also for the angels between connections to x, y, and z-axis, in this case (regular lattice cubic grid), angles between the space diagonal to each of the axis within a cubic would be 54.7° defined as α, β, and γ, respectively shown as Figure 5.3 when the certain shale media of given anisotropy ratio, the number of pore connections in the three directions of x, y and z are first guaranteed. To calculate the probability in other directions (α, β, and γ directions) other than x, y, and z directions, Equation (5.1) can be used, and connections to this lattice model are determined based on this connection probability.

$$\frac{\boldsymbol{p(\alpha,\beta,\gamma)}}{\boldsymbol{p(\zeta_i,\zeta_j)}} = \frac{\boldsymbol{a_x cos^2\alpha + a_y cos^2\beta + a_z cos^2\gamma}}{\boldsymbol{\bar{a}}} \qquad (5.1)$$

Where α, β, and γ are the angles between the connection direction and the *x*, *y*, and *z*-axis as shown in Figure 5.3(b), whereas Figure 5.3(a) shows traditional flow directions in direction and the *x*, *y*, and *z*-axis. The $\bar{a}$ is defined as the average connections of the whole pore network. This Equation describes the relationship between pore connection probability within a lattice grid and their spatial angles to *x*, *y*, and *z* directions. When the lattice grid was constructed, the pore connection could be calculated based on this theory.

As for the angles of α, β, and γ in the Equation, they can be calculated based on the basic lattice unit, as in this case: a cube with the same height, length, and width. In other cases, when the basic lattice unit is cuboid with different lengths, widths, and heights, this Equation can also be utilized to account for a more complicated connection.

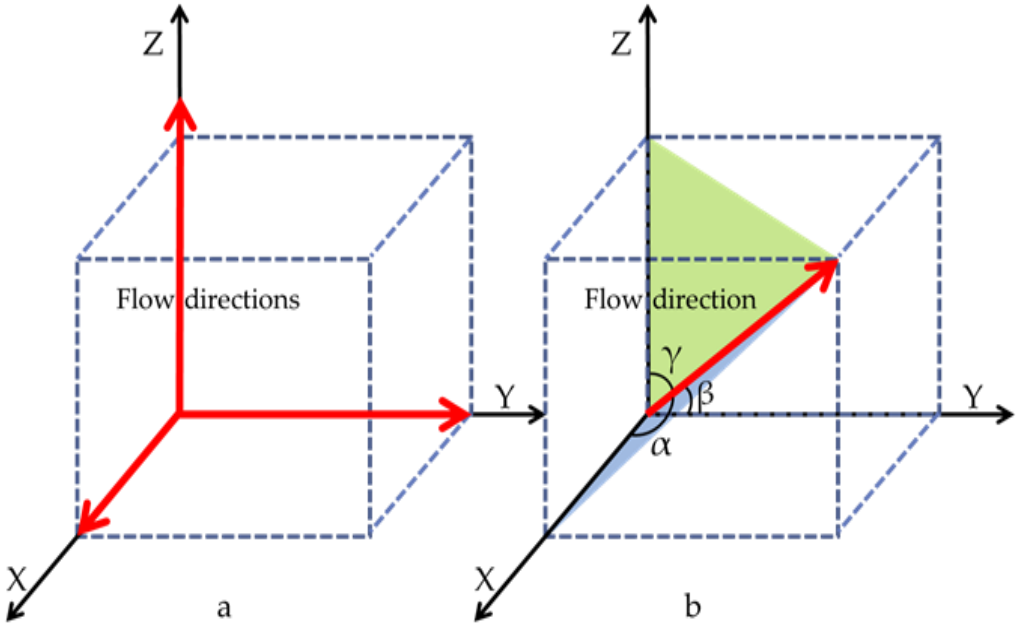

Figure 5.3 Space diagonal connection and angles schematic (a) Flow in x, y, and z directions (b) Flow in space.

The anisotropic equivalent pore network obtained by this method has a similar total number of connections to the isotropic network. However, the seepage behaviors of the three planes are different, which is validated by the anisotropic permeability experiments for shales.

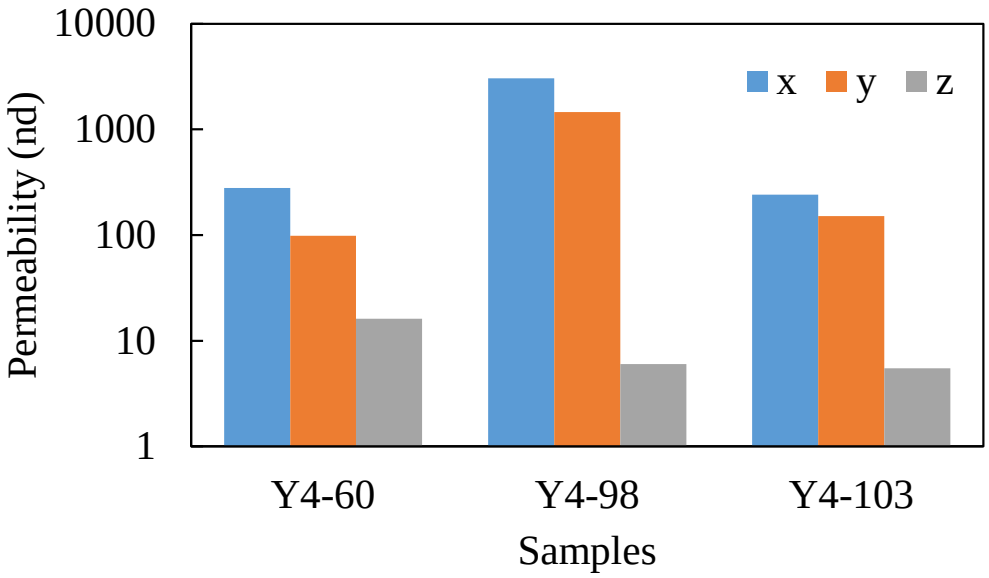

Figure 5.4 The anisotropic permeability of shale

Source: [142].

Figure 5.4 presents the average anisotropic permeability of three planes. Under normal circumstances, it is unlikely to connect all the pores. Therefore, by setting different coordination numbers of the model in each direction, the anisotropy of geological media can be accounted for. As for coordination number generation, the general practice was to delete the pore connections using a dilute algorithm after generating a fully connected structure [96] or using a reduction factor proposed by Zhang et al.

A. The pore connection is consistent with the actual shale. The sparse algorithm described above can generate pore connections, but the following problems still exist:
B. The reduction factor is not obtained from the pore structure of the accurate geotechnical medium but selected and hence has certain subjective randomness.

C. The reduction factor is not obtained from the pore structure of the accurate geotechnical medium but selected and hence has certain subjective randomness.

5.4 Probability-Based Anisotropy and Coordination Number Generation

A connection analysis reveals that although the pore connections are randomly and uniformly distributed throughout the model, for pores with different pore coordination numbers, the probability of their connections to the surrounding pores is different[143]. For example, for one pore with 26 coordination numbers, the probability of connection will be 100% [144,145] since the maximum connection number of a single pore of an equivalent pore network is 26. Here it is assumed that the probability of a connection between the pore bodies is only related to the coordination number of the two adjacent pores. It is essential to analyze the probability of connections of two pores within the pore network since this relationship will help build the anisotropic relationship in three directions.

For convenience, the two adjacent pores may be referred to as pore *i* and pore *j*, respectively. It is then assumed that pore *i* is connected to pore *j*, as shown in Figure 5.5. Below we calculate the probability of a case where the coordination number of the pore *i* is ζ_i, the coordination number of the pore *j* is ζ_j.

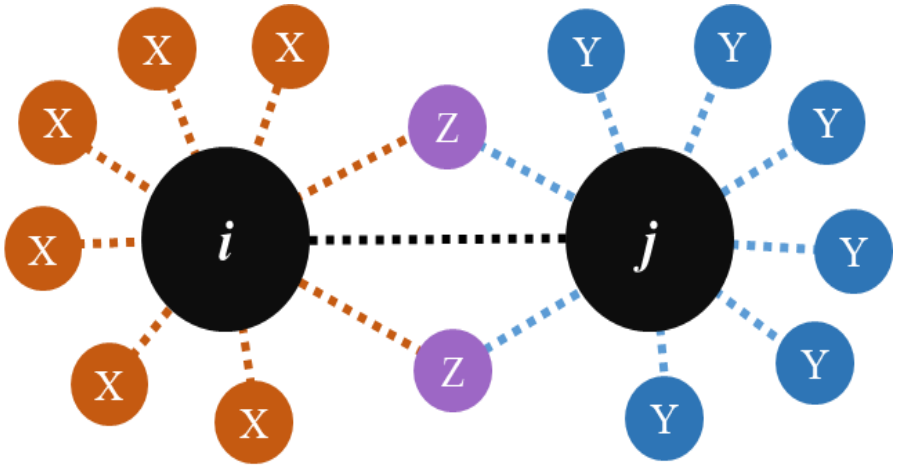

Figure 5. 5 Connection relationship between pore *i* and pore *j*.

For the pore *i*, the probability of generating ζ_i connections is p_1:

$$p_1(\zeta_i) = B(\zeta_i; 26, p_c) \tag{5.2}$$

where pc represents the average probability of the existence of the connection between pores, and B represents the probability distribution of the binomial distribution B(k; n, p), where it is defined as:

$$B(k; n, p) = \binom{n}{k} p^k (1-p)^{n-k} \tag{5.3}$$

In the generated pore network, the probability that the pores i and the pores j are connected is expressed as:

$$p_2(x) = p_1(\zeta_i) \cdot \frac{\zeta_i}{26} = B(\zeta_i; 26, p_c) \cdot \frac{\zeta_i}{26} \tag{5.4}$$

Since the pores *i* has been connected to the pores *j*, it is possible to randomly generate pores in the remaining 25 connections, whereby the probability of forming a connection between the two is p_3:

$$p_3(\zeta_i, \zeta_j) = p_2(\zeta_i) \cdot B(\zeta_j - 1; 25, p_c) = B(\zeta_i; 26, p_c) \cdot \frac{\zeta_i}{26} \cdot B(\zeta_j - 1; 25, p_c) \tag{5.5}$$

Equation (5.5) shows the probability of a connection between two pores. Similarly, the probability that there is no connection between the two pores can also be calculated. Therefore, the probability that no connection occurs between the two pores is $\overline{p_3}$:

$$\overline{p_3}(\zeta_{\mathrm{i}},\zeta_{\mathrm{j}}) = B(\zeta_{\mathrm{i}};26,p_{\mathrm{c}})\cdot(1-\frac{\zeta_{\mathrm{i}}}{26})\cdot B(\zeta_{\mathrm{j}};25,p_{\mathrm{c}}) \qquad (5.6)$$

In summary, given the two coordination numbers of these adjacent pores, the conditional probability of the connection between the pores is:

$$\boldsymbol{p(\zeta_i,\zeta_j) = \frac{p_3(\zeta_i,\zeta_j)}{p_3(\zeta_i,\zeta_j)+\overline{p_3}(\zeta_i,\zeta_j)} = \frac{\overline{\zeta_i}\,\overline{\zeta_J}}{p_c}/(\frac{\overline{\zeta_i}\,\overline{\zeta_J}}{p_c}+\frac{(1-\overline{\zeta_i})(1-\overline{\zeta_J})}{1-p_c})} \qquad (5.7)$$

Among them $\overline{\zeta_i}=\zeta_i/26$, $\overline{\zeta_j}=\zeta_j/26$ respectively, are called normalized coordination numbers of two pores.

It can be seen from Equation (5.7) that the probability of connection between pores is not only related to the coordination number of the two pores but also the average coordination number of the entire equivalent pore network model. Figure 5.6 shows the relationship between the probability of a connection between pores and the average coordination number of the network when the coordination number of the two pores is the same. Results show that when the average coordination number of the network is constant, the larger the pore coordination number, the greater the probability of connection between the pores. When the average coordination number of connected pores is constant, the larger the average coordination number of the network, the larger the probability of connection between the pores. The points on the straight dash line in Figure 5.6 show that the pore coordination number on each curve is equal to the average coordination number of the network, indicating that the coordination number of the two pores is the same as the average coordination number of the network.

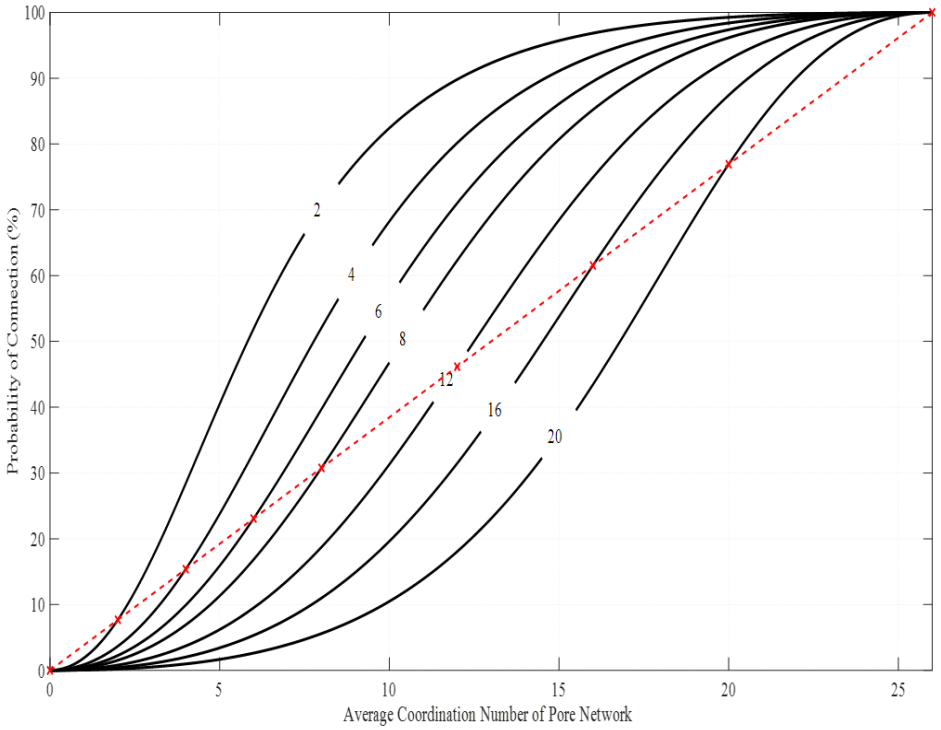

Figure 5.6 Relationship between the probability of connections and the average coordination number.

Based on the above, one can use the known coordination number distribution to generate the connection between the pores, using the following steps:

1. Randomly generate a series of matches according to a given distribution of coordination numbers and assign target coordination numbers to each pore. In coordination number assignment, a larger coordination number is assigned to the larger size pores to meet the actual statistical results. In our case, the coordination number has a general deviation of 0.1, which is relatively small.

2. For any two adjacent pores, based on the target coordination number assigned to the two pores, combined with the average coordination number of the entire model, the probability of the connection between the groups of pores is calculated by using Equation 5.7.

3. Make adjustments to all pores until the final pore network is generated.

The equivalent pore network model generated here avoids the decisive subjective reduction factor. The generated connection considers the distribution of coordination

numbers. Therefore, it can generate an equivalent pore network that is similar to the actual geo-material. Figure 5.7 and Table 5.2 show the connection of the equivalent pore network model with the target coordination number and the normal distribution and the gamma distribution using the above method where μ and α are the average numbers of normal distribution and gamma distribution, and σ and β are the standard deviations of both distributions respectively. The coordination number distribution and the target coordination number are close, with a mean error of less than 1%. However, gamma distribution has a lower error, and hence it was used in this research.

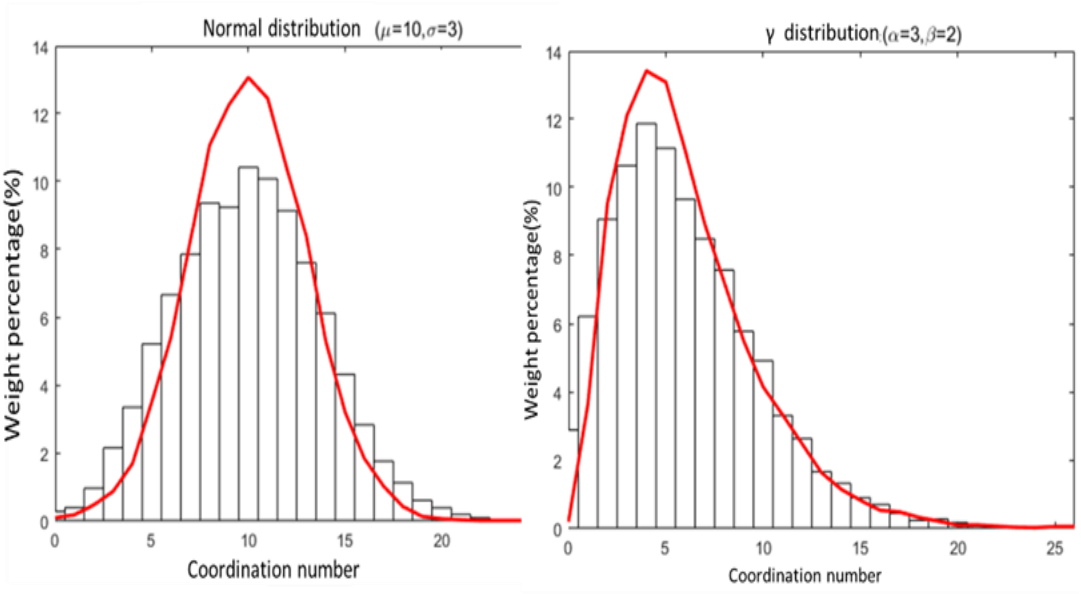

(a) (b)

Figure 5.7 Equivalent pore network model connection generation results (a) normal distribution (b) gamma distribution.

Table 5.1 Comparison between Two Distributions

Target distribution	Average coordination number			Standard deviation		
	Target	Actual	Error (%)	Target	Actual	Error (%)
Normal distribution（μ=10，σ=3）	9.99	9.97	-0.14	3.01	3.74	+24.23
γ distribution（α=3，β=2）	5.96	5.92	-0.82	3.43	3.74	+8.91

5.5 Calculation of Gas Permeability

5.51 Gas Movement in Pore Throats

In the pore network, the gas transfer through the pore throats is connected between pores. Therefore, the gas flux of the pore throat Qij can be determined as follows:

$$\boldsymbol{Q_{ij} = \alpha_{ij} K_{ij} \Delta p} \tag{5.8}$$

Where α_{ij} is a correction factor, K_{ij} is the liquid permeability of the pore throat, Δp is the pressure difference between the pores. The correction factor αij can be determined by the multi-flow regimes model, which includes the influence of slippage effect and Knudsen diffusion of gas in shale:

$$\boldsymbol{\alpha_{ij} = \frac{1 + 4K_n + \frac{32}{3\pi} K_n^{\,2}}{1 + 0.5K_n}} \tag{5.9}$$

where K_n is the Knudsen number [146], which can be expressed as:

$$K_n = \sqrt{\frac{\pi RT}{2M}}\frac{\mu}{p} \tag{5.10}$$

Where R is the universal gas constant, T is the absolute temperature, M is the molar mass, μ is the viscosity of the gas, p is the average gas pressure in the pore throat.The K_{ij} can be determined by Hagen-Poseuille equation [107]:

$$K_{ij} = \frac{\pi r_{ij}^{\,2}}{8\mu l_{ij}} \tag{5.11}$$

Where r_{ij} and l_{ij} are the radii and the length of the pore throat, due to the compressibility of the gas, the mass balance of a pore connected to several pore throats can be written as:

$$Q_{pore} = \sum \frac{2p_i}{p_i + p_j} Q_{ij} \tag{5.12}$$

Where Q_{pore} is the flux of the pore, p_i and p_j are the pressure at both ends of the pore throat. Based on Equations. (5.8-5.12) the gas transfer in the pore network can be solved. When αij is set as 1, the equations can calculate liquid transport in pore throats.

5.52 Macro permeability of the pore network

Considering one-dimensional seepage with constant pressure at the upstream and downstream boundaries, when the gas flow forms a stable field, and the density of the gas gradually changes with the pressure.

$$\frac{\mathrm{d}p}{\mathrm{d}L} = \frac{\mu}{\rho}\frac{Q_\mathrm{m}}{kA} = \frac{\mu}{p}\frac{RT}{M}\frac{Q_\mathrm{m}}{kA} \tag{5.13}$$

Where Q_m is the total mass flux of gas in the model, ρ is the density of the fluid, k is the macro gas permeability of the medium, A is the seepage area. After integration, Equation. (5.13) changes into:

$$p_\mathrm{u}^2 - p_\mathrm{d}^2 = \frac{\mu RT}{M}\frac{Q_\mathrm{m}}{kA}L \tag{5.14}$$

Where p_u and p_d are the constant pressure at the upstream and downstream boundaries of the model, L is the seepage distance of the model. Thus, the macro gas permeability of the entire equivalent pore network model can be calculated as shown below:

$$k = \frac{2\mu RT}{(p_\mathrm{u} + p_\mathrm{d})M}\frac{L}{A}\frac{Q_\mathrm{m}}{p_\mathrm{u} - p_\mathrm{d}} = \frac{\mu}{\bar{\rho}}\frac{L}{A}\frac{Q_\mathrm{m}}{p_\mathrm{u} - p_\mathrm{d}} \tag{5.15}$$

where $\bar{\rho}$ represents the average density of gas in the entire pore network. Please note that Equation. (5.15) can also be used to calculate the macro permeability of liquids by replacing average gas density with average liquid density in the pore network.

5.6 Results and Validation

5.61 Validation of the Anisotropic Model

The experimental results show that the permeability of Longmaxi formation shale in East Sichuan is in the order of 10^{-18} (in m^2)[142]. With the increase of the angle between the

shale and the bedding plane, the permeability of the shale decreases. The anisotropic permeability ratio of the Longmaxi shale along the bedding plane and the permeability of shale sampled on the vertical bedding plane varies from 3 to 10[142]. The permeability values of the shale samples in a different area of the bedding plane are relatively similar, but the permeability of different rock samples varies with the confining stress. As for the anisotropic pore network used in this research, the reasonable anisotropic ratio has to be adopted based on the previous research and the relationship between the anisotropic ratio, which refers to the connection number ratio in each plane as (ax: ay: az).

Based on the statistical study of this anisotropic pore network model, the initial results between the anisotropic permeability and the connection ratio for three flow planes, as shown in Table 5.2. The following are assumed for the calculations shown in Table 5.2: average pore body radius 0.1 μm and standard deviation 0.01; average coordination number 10 and standard deviation 0.1; average pore throat radius 0.1μm and standard deviation 0.01; and porosity 10 %. This table indicates that anisotropic permeability can be achieved using this connection ratio of three planes. Each of the factors has a different impact on permeability. The dominating flow plane (ax), which is the bedding plane, has a significant impact on permeability. When increasing the ratio of ax, the total permeability tends to increase, which means a higher connection number for the bedding plane will increase the permeability of the whole matrix.

On the contrary, the increase in the ratio of ay and az will decrease the total permeability. Therefore, it is reasonable that when increasing the vertical connections of shale, the permeability of the total formation will decrease. The isotropic pore network model could not predict the shale permeability when the pressure difference was low, as

shown in Figure 5.10. At the same time, the anisotropic model seems to predict the permeability for a wide range of input pressure values. Typically, when the pressure ranges from 0.1 MPa to 1 MPa, the isotropic model tends to predict a lower permeability value when compared to the measured values.

On the contrary, the permeability results of an anisotropic model, when adjusted to include the proper connection ratio, yielded similar values to those measured. Therefore, by applying and adjusting the connections ratio of each plane, one can use the anisotropic pore network model to represent the actual shale formation. For example, for Longmaxi shale, the typical anisotropic ratio is approximately 10.

Table 5.2 Impact of Connection Ratio on Permeability

(a_x:a_y:a_z)	1, 1, 1	1, 2, 1	1, 5, 1	1, 10, 1	1, 50, 1	1, 100, 1
Anisotropic permeability	4.11×10^{-18}	3.72×10^{-18}	3.32×10^{-18}	3.11×10^{-18}	2.89×10^{-18}	2.84×10^{-18}
(a_x:a_y:a_z)	1, 1, 1	2, 1, 1	5, 1, 1	10, 1, 1	50, 1, 1	100, 1, 1
Anisotropic permeability	4.11×10^{-18}	5.94×10^{-18}	8.13×10^{-18}	8.90×10^{-18}	9.28×10^{-18}	9.36×10^{-18}
(a_x:a_y:a_z)	1, 1, 1	1, 1, 2	1, 1, 5	1, 1, 10	1, 1, 50	1, 1, 100
Anisotropic permeability	4.11×10^{-18}	3.75×10^{-18}	3.38×10^{-18}	3.12×10^{-18}	2.90×10^{-18}	2.86×10^{-18}

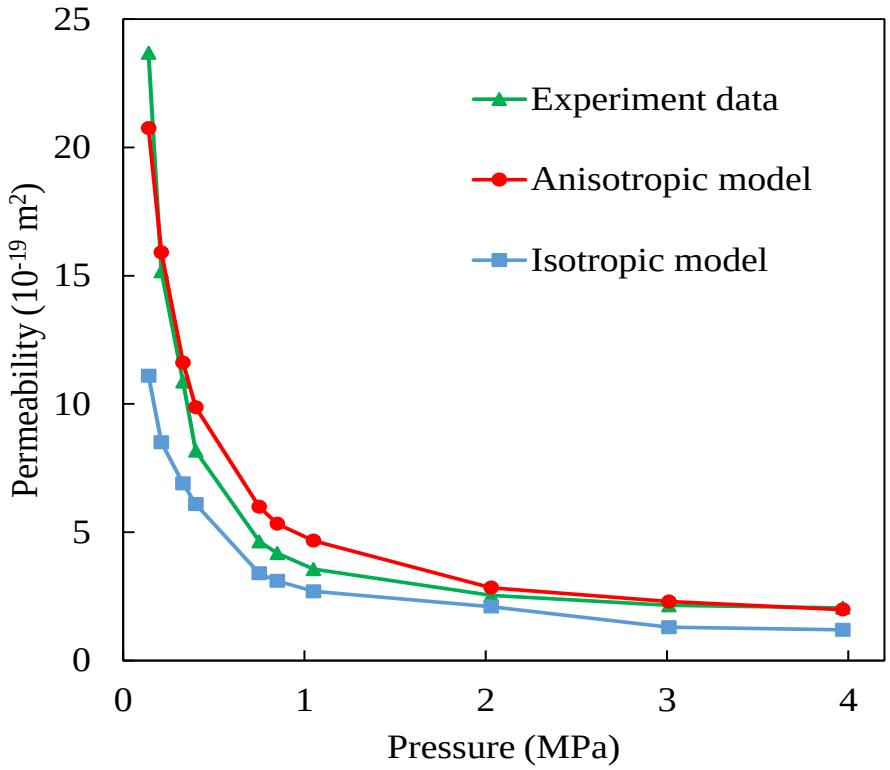

Figure.5.8 Comparison of permeability from experimental data and Isotropic/anisotropic pore-network model (Experiment data is Sample Z084, isotropic data and anisotropic data was compared).

5.62 Validation of the Model with Experimental data from Qaidam Basin Shale

Gao et al.[100,147] conducted a series of high-pressure gas permeability tests on four shale samples obtained from Longmaxi formation shale in East Sichuan. Several different types of shale samples were used for the test, and the representative sample parameters are shown in Table 5.2. For each sample, multiple sets of permeability tests under different pressures were performed. The outlet pressure of the test was fixed at 0.1 MPa, and the inlet pressure was gradually increased from 4 MPa to 0.1 MPa. By measuring the corresponding volumetric flow rate, the apparent permeability of the shale medium at the corresponding pressure was calculated, as shown in Figure 5.9.

Pores of Longmaxi shale are composed of organic and non-organic pores in the shale fabric and micro and macro cracks. These pores store shale gas, and their size directly determines the shale gas reservoir size and the feasibility of shale gas extraction. The anisotropic pore network was constructed based on the reported pore parameters of four different shales and shown in Table 5.3. Mercury injection capillary pressure test, N_2 absorption, and FIB-SEM technologies were used to obtain pore parameters of four Longmaxi shales under laboratory conditions[100].

The low-pressure absorption test supports the assumption of equivalent spherical and cylindrical pore shapes[146]. To simplify the understanding of the pore structure and facilitate the prediction of gas flow, the pore structure in the shale matrix was simplified to cylindrical capillaries[107,117,147]. Hence, the shale matrix pores consist of a large number of multi-diameter cylindrical pores connected spherical pore bodies in series and parallel.

Four anisotropic pore networks were developed for four shale samples obtained from the Longmaxi formation shale in East Sichuan using the steps described before. The size of each anisotropic pore network was 20×20×20. The pore diameters and porosity values were obtained from the experimental data reported in Gao et al.[100]. In that study, they conducted different tests, including CO_2 absorption, N_2 adsorption, and mercury intrusion, to obtain pore structures of four Longmaxi shales under laboratory conditions. Other parameters, including the pore throat diameters, coordination numbers, and anisotropic ratios, were based on our previous and current research on shale[96,100,148,149].

Then using those four anisotropic pore networks developed, the permeability of each shale was predicted. No flow boundary conditions were used, except for the inlet or

upstream and outlet or downstream boundaries. By setting the outlet pressure to 0.1 MPa, one can simulate gas flow results by changing the inlet pressure values and calculating the corresponding permeability. For each core sample, several simulations were performed corresponding to different inlet pressures of actual physical tests. Once the inlet and outlet pressures were applied, the simulation continued until a constant flow rate was reached.

Table 5.3 Shale Sample Parameters

Source:[41,117,148,149]

Sample	Pore diameter /standard deviation (nm)	Pore throat diameter/standard deviation (nm)	Coordination number/standard deviation	Anisotropic ratio (a_x:a_y;a_z)	Porosity (%)
C024	5.187, 0.4	0.51, 0.04	4, 0.3	17: 17: 1	5.98
C038	7.852, 0.4	0.81, 0.04	4, 0.3	22: 22: 1	5.34
C014	7.305, 0.4	0.87, 0.04	3, 0.3	25: 25: 1	2.55
Z084	4.333, 0.4	0.66, 0.04	3, 0.3	29: 29: 1	2.12

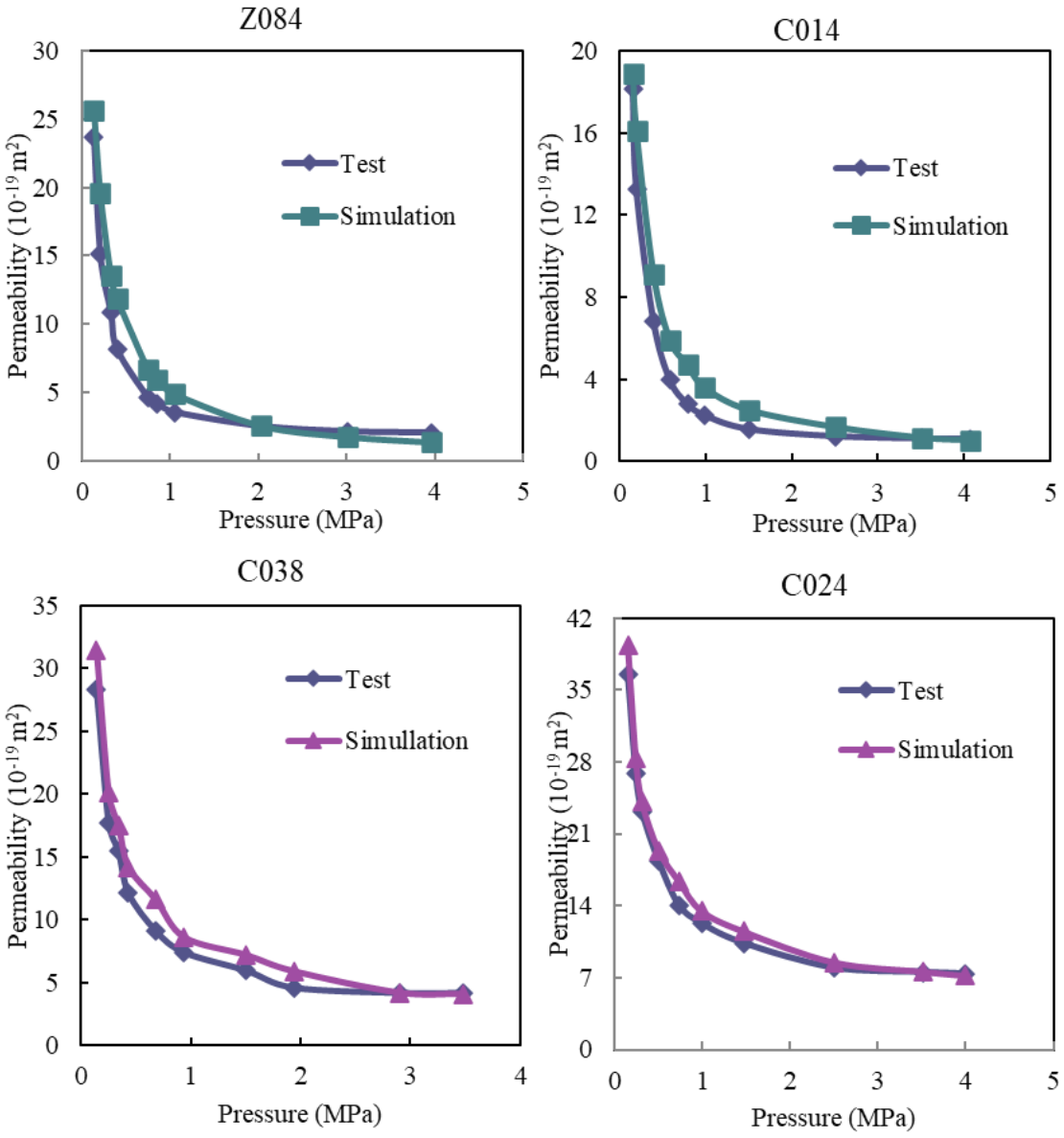

Figure 5. 9 Variation of the permeability with applied pressure for the four formations with the simulated results.

Based on the summary of the modeling parameters shown in Table 5.3, four permeability results of both actual test and simulation were compared in Figure 5.9. These simulations used the developed anisotropic pore network. Figure 5.9 shows the comparison between the experimental results and the results of the equivalent pore network model

simulation. It can be seen from Figure 5.9 that the simulation results of the pore-scale permeability calculation model are in good agreement, concluding that the proposed equivalent anisotropic pore network model can be used as a predictive tool.

For unconventional rock such as shale, porosity is usually less than 10%[150], pore-throat diameters are less than 1μm[110], and permeability is less than 1mD. Shale formations are strongly anisotropic due to their laminated surfaces, resulting in vast differences in mechanical properties along parallel and perpendicular lines to bedding planes[151–153]. Also, shale is highly anisotropic when compared to conventional rock. Shale nanopores are heterogeneous and contain organic (e.g., kerogen) and inorganic (e.g., clay and cementation) materials[154]. Hence at nano/micro-scale, the approach proposed by Song et al.[131] with pore structure obtained by scanning-electron-microscopy (FIB-SEM) and then using the local-effective-viscosity multi-relaxation-time lattice Boltzmann model to simulate the gas transport in shale would be preferable.

However, the gas trapped in shale is influenced by conditions that prevailed during reservoir-formation and subsequent environmental and seismic activities[155], which is a complex balancing operation, hence in the case of unconventional hydrocarbon resources, the gas content is affected by temperature and pressure in micro and nano scale-pores [127,151,152,156–158] To better estimate the potential for gaseous hydrocarbon recovery, it is essential to characterize these heterogeneous nanopores using pore-scale parameters, i.e., the pore body and throat distributions22. Hence, at the engineering scale for predicting potential shale gas extraction, the simplified pore structure of the geo-media using the equivalent pore network incorporating anisotropy may be preferred.

5.7 Summary and Conclusions

This manuscript describes the development of an improved pore-network model using a new algorithm for coordination numbers incorporating anisotropic ratio and the isolated pore elimination method. The model was validated by comparing simulated shale permeability with the measured data for four shales from the Longmaxi formation.

The construction of the equivalent anisotropic pore network model was first described in detail, especially the proposed coordination number generation method and the assignment of coordination numbers based on the connection probability of adjacent pores. The probability of connection was developed and found that the connection between two pores is not only related to the coordination number of two pores but also related to the average coordination number of the entire network. An anisotropic ratio (ax: ay: az) was then introduced to account for the anisotropic formation of gas-bearing shale. The three directional anisotropic ratios were defined as the ratio of pore connections in each direction to accurately represent the permeability behavior of different anisotropic formations such as soils, sandstones, or shale. For different formations, different anisotropic ratios were utilized to simulate different gas flow behaviors. A good agreement between predicted and measured permeability was obtained for four shale samples obtained from the Longmaxi formation in East Sichuan, showing that the anisotropic model is more representative than the conventional isotropic pore network model to represent pore connections in shale formations.

CHAPTER 6

NUMERICAL STUDY ON THE PRODUCTION RATE OF UNCONVENTIONAL GAS RESERVOIRS BASED ON PORE NETWORK MODEL

6.1 Introduction

The current booming shale gas production in the United States and the fast-growing global investment in shale gas exploration and construction are due to the combination of horizontal drilling and multistage hydraulic fracturing technology [159–161]. Multiple transverse hydraulic fractures are created when all wellbores are drilled in the minor horizontal tension direction. Therefore, maximizing the overall stimulated reservoir volume is critical in achieving a cost-effective gas supply [162,163]. Therefore, a nanoscale shale gas reservoir model is used in this research for gas transport, nano-flow, and geomechanics in a fractured horizontal well environment. Furthermore, this model is used to forecast shale gas output under various reservoir scenarios and investigate the factors that influence the declining trend of shale production rate over time. The findings and study discussed here enable a better understanding of gas production processes and depletion in a shale gas well under certain reservoir conditions. Shales are the most common sedimentary rocks in the crust of the earth. Recent activities in shale gas exploration have shown that shale gas will be the most significant portion of the future global energy supply as traditional reserves begin to decline [9,164,165]. Improved reservoir conditions, advancement in horizontal drilling, and hydraulic fracking technology make shale gas extraction commercially feasible successful [166]. However, in contrast to traditional reservoirs, shale gas reservoirs appear to be more costly to build and require specific technology to allow gas to be extracted at an economical pace due to its extremely low

matrix permeability and porosity [140,167,168]. Thus, it is essential to accurately model the shale gas output to determine how quickly the gas will be extracted and converted into revenue from each well and predict the economic feasibility of extracting natural gas.

Alterations in pore morphology can occur through a number of processes coupled with and interfering with fluid flow [169]. Chemical reactions or microbiological events, in this case, clay swelling, are examples of such processes. Although changes in pore surface properties and void space geometry arise at nano or even molecular scale, the engineering problem scales are usually much more significant. Therefore, the pore or nanoscale changes must be converted to engineering scale when modeling this engineering problem.

The contribution of shale morphology changes in the flow field is often characterized by effective hydraulic properties, which is also essential for computational viability [170,171]. One of these parameters is the permeability of a porous medium, which describes the resistance to fluid flux in the porous medium in a representative volume. The concept of permeability does not necessarily require a detailed description of the fluid-solid interface at the cost of losing details on the pore scale. However, the pore geometry cannot be ignored. The nanoscale parameters are the fundamental basis for the flow rate of a particular formation. In the model developed here, the nanoscale parameters are used to represent the actual shale matrix. A typical approach for integrating pore structure and morphology is to link changes in flow rate to porosity, another important shale matric parameter. This research aims to analyze porosity–flow rate relationship, outline their key characteristics and provide some guidelines for the shale matrix and its pore space alterations due to fracking.

6.2 Pore Network Model for the Nanoscale Flow

First, the representative unit of the equivalent pore network model is constructed for different shale formations to calculate and analyze their performance. After that, the representative unit is gradually expanded and correlated with the flow length to reach the engineering scale.

The pore network model application focuses on calculating and analyzing the complex low-connective anisotropic shale, focusing on the physical properties of the shale matrix itself. The specific process of constructing the pore-scale structure and analyzing the dynamic flow of shale gas at the pore-scale and sensitivity analysis of the main parameters affecting flow characteristics, including porosity and pore throat size, is described. Here the reservoir pressure and adsorption and desorption characteristics caused by organic matter distribution are considered to obtain the gas extraction rate.

6.21 Flow calculation between pores

When gas flows in nanoscale pores, the velocity of gas molecules at the sidewalls of the pores is not the same [172]. Therefore, Klinkenberg first studied the gas slip phenomenon in porous media and found that the slip effect significantly influenced gas permeation in porous media and gave the gas flow correction factor (F) expression considering the slip effect [173].

$$F = 1 + \frac{b_k}{p} = 1 + \frac{4\bar{\lambda}}{r} \tag{6.1}$$

Where b_k is the Klinkenberg slip factor, in this study, the Klinkenberg slip factor was introduced to modify Darcy's law to consider the gas slip effect, and the mass flow expression is:

$$Q_m = -F\frac{\rho k_0}{\mu_g}\nabla p = -F\frac{M}{RT}\frac{pk_0}{\mu_g}\nabla p \tag{6.2}$$

The diffusion of gas molecules in the nanotube is mainly caused by the violent collision with the sidewall of the pore. Knudsen diffusion is often used to describe this phenomenon. The mass flow rate (Q_d) of gas molecules produced by diffusion can be described by Fick's law:

$$Q_d = -D_i\frac{\delta c}{\delta x} \tag{6.3}$$

D_i is the gas diffusion coefficient in the micropores, and c is the mass fraction of gas. Gilron and Soffer proposed that the diffusion coefficient D_i is composed of the modified diffusion coefficient $D_{i,c}$ and the thermodynamic correction factor ψ(T,p), namely[174]:

$$D_i = D_{i,c}\Psi \tag{6.4}$$

Where $\Psi = \frac{\delta \ln p}{\delta c}$, Therefore, substituting Equation (6.4) into Equation (6.3) can obtain the diffusion mass flow rate. In Equation (6.4), replacing $D_{i,c}$ with the Knudsen diffusion coefficient can obtain the Knudsen diffusion mass flow rate. The Knudsen diffusion coefficient is:

$$D_{k,c} = \frac{2r}{3}\sqrt{\frac{8RT}{\pi M}} \tag{6.5}$$

The simultaneous combination of Equations (6.3), (6.4), (6.5) to obtain the mass flow rate of gas flow in a single tube due to Knudsen diffusion:

$$Q_k = -\frac{2r}{3}\sqrt{\frac{8RT}{\pi M}}\frac{M}{RT}\nabla p \tag{6.6}$$

Here the Klinkenberg slip flow and Knudsen diffusion terms are accounted to modify the mass flow expression to reflect the transition characteristics between flow regimes caused by the change of Knudsen number. The revised mass flow expression is as shown in Equation (6.7):

$$Q_m = -\left(F\frac{pr^2}{8\mu}f + \frac{2r}{3}\sqrt{\frac{8RT}{\pi M}}(1-f)\right)\frac{M}{RT}\nabla p \tag{6.7}$$

6.22 Gas transport between pores

The dynamic pore-scale flow calculation multiple flow mechanisms are converted into a single variable pore pressure function, which is convenient for the time and space discretization of the pressure term in the calculation. Therefore, the dynamic pore-scale flow calculation requires the pore-scale discretization of the continuum, including each

pore throat with its dominant flow mechanism. In addition, the dynamic flow model needs to consider the adsorption and desorption characteristics of the porous media based on the multi-fluid theory model.

The gas flow in the pore network model is a dynamic one, and each pore needs to satisfy the law of conservation of mass. Select pore i as a reference, and pore i is connected to the surrounding four pores (Figure 6.1). In the figure, s and e represent the starting and ending pores (numbered clockwise) of the pores connected to pore i, respectively. The pore information matrix needs to be stored in the calculation. The sequence connected to pore i is convenient for subsequent retrieval of node information. At each time step, the pressure of the pore throat is equal to the average pressure of the two adjacent pores (Figure 6.1). From time step k to time step k+1, the mass change of pore i is equal to the sum of the mass flow of all adjacent connected pores (Equation 6.8).

$$m_i^k - m_i^{k+1} = \sum_{j=s}^{e} \frac{M}{RT}\left(F\frac{\pi r_{th}^4}{8\mu_g}\frac{\left(p_i^k + p_j^k\right)}{2} + \frac{2r_{th}}{3}\sqrt{\frac{8RT}{\pi M}}\right)\frac{p_i^k - p_j^k}{l_{ij}}\Delta t \qquad (6.8)$$

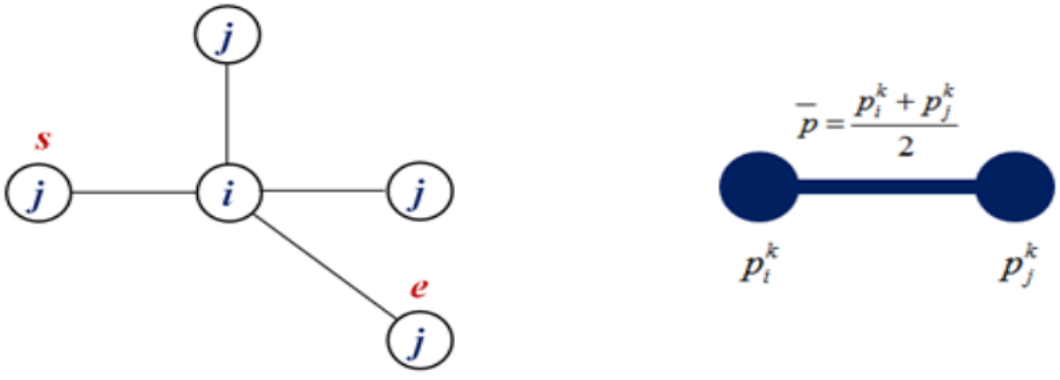

Figure 6.1 Pore i Schematic diagram of connected pores.

In an ideal gas state, the mass of gas stored in pore i in time step k is:

$$m_i^k = \frac{4}{3}\pi r_i^3 \frac{M}{RT} p_i^k \tag{6.9}$$

Substituting formula (6.9) into formula (6.8)

$$p_i^{k+1} = p_i^k - \sum_{j=s}^{e} \frac{M}{RT}\left(F\frac{\pi r_{th}^4}{8\mu_g}\frac{\left(p_i^k + p_j^k\right)}{2} + \frac{2r_{th}}{3}\sqrt{\frac{8RT}{\pi M}}\right)\frac{p_i^k - p_j^k}{l_{ij}}\Delta t / \frac{4}{3}\pi r_i^3 \tag{6.10}$$

Equation (6.10) shows the dynamic, iterative process of the pore pressure term. In the entire pore network solution domain, the initial pressure gradient only exists at the boundary. As the pressure gradually decreases, the flow covers the entire pore network. In the dynamic calculation, the time step is crucial for the stability of the explicit solution. The Courant number determines the time step dynamically. It accounts for the relationship between the time step and the space step where it should be less than 1 to ensure the stability of the calculation. In this pore network model, the definition of Courant number is expressed as formula (6.11):

$$\frac{v\Delta t}{\Delta l} = \frac{\frac{r_{th}^2}{8\mu_g}\frac{p_i^k - p_j^k}{l_{cb}}\Delta t}{l_{cb}} \leq 1 \tag{6.11}$$

In the formula, l_{cb} is the length of the coordination bond between two adjacent pores, and Δt is the time step for maintaining stable flow calculation between adjacent pores. Thus, the time step will be calculated for all pores in the entire pore network, and the minimum

value of the time steps for all pores is selected as the time step for the entire pore network model. In other words, in this calculation, the Courant number is kept less than 1 to ensure the stability of the iteration. Therefore, it is necessary to calculate the maximum time step allowed for all pores and take the smallest value for the simulation. Hence, the calculation steps are as follows:

(1) According to the initial calculated conditions, assign initial pore pressures to all pores.

(2) Adjust the pressure value for the pores at the boundary according to the calculated boundary conditions: for constant pressure boundary conditions, update the pore pressure to the set pressure value; for closed boundary conditions, keep the previous iteration result without processing.

(3) Calculate the Courant number of all pores and obtain the maximum allowable iteration time step under the condition that the Courant number is less than 1.

(4) According to the iteration time step, use formula (6.10) to calculate the pore pressure of the next iteration step for all pores.

(5) Repeat steps (2)-(4) until the iteration is completed or the convergence is reached.

In the above calculation, each pore and all other pores connected to it will form a unit for the mass conservation equation. When the time step is determined, the mass conservation equation composed of each unit will obtain a stable result. Hence in the model, the time is determined when the overall stability is reached. Then select the maximum value by searching the pressure difference between the k-th time step and the k+1 time step of each pore. The condition for the model to reach stability is that the maximum pressure difference is less than the allowable error. The allowable error is defined as $err = P_{outlet}/10^4$, one ten-thousandth of the lower boundary pressure.

6.2.3 Development of Pore Networks for Shale formations

Four anisotropic pore networks were developed for four shale formations studied in this research using the steps mentioned above. The size of each anisotropic pore network was

20×20×20. The pore diameters and porosity values were obtained from the experimental data reported before and repeated in Table 6.1. In that study, different tests, including CO_2 absorption, N_2 adsorption, and mercury intrusion, were conducted to obtain pore structures of four shale formations studied in this research under laboratory conditions. Other parameters, including the pore throats diameters, coordination numbers, and anisotropic ratios, were based on our previous and current research on shale. Then using those four anisotropic pore networks developed, the exit gas flow rate from the boundary exposed to atmospheric pressure with time was predicted. No flow boundary conditions were used, except for the inlet or upstream and outlet or downstream boundaries. For each core sample, several simulations were performed corresponding to different inlet pressures of actual physical tests. Once the inlet and outlet pressures were applied, the simulation continued until a constant flow rate was reached.

Table 6.1 Shale Sample Parameters

Sample	Pore diameter /standard deviation (nm)	Pore throat diameter/standard deviation (nm)	Coordination number/standard deviation	Anisotropic ratio (a_x:a_y;a_z)	Porosity (%)
Eagle Ford	8.5/0.4	2.9/0.2	4/0.1	22:22:1	4.41
Haynesville	5.4/0.3	1.6/0.1	4/0.1	22:22:1	2.94
Longmaxi	4.3/0.3	0.66/0.1	4/0.1	22:22:1	1.58
Opalinus	9.8/0.5	3.1/0.3	4/0.1	22:22:1	7.81

6.3 Sensitivity Studies of Flow Simulation

The different control factors of formation and gas exploration, such as intact shale gas pressure, clay content, and fracture spacing, determine the gas production rate. Therefore,

the ability of the pore network model to account for control factors needs to be investigated before actual gas production can be estimated based on the pore network model. However, there is little analysis of the variables of control factors of actual shale gas production because of the variability of unconventional shale gas deposits. Mayerhoffer used a numerical simulation of explicit fracture networks to predict reservoir volume [175]. According to the power-law exponential model, Mattar et al. [176] proposed a theory and methodological data processing. They showed the effect of the changing shutdown pressure distribution in the fracturing system on the volume flow rate of the well and the gas recovery. However, there is limited or no analysis of the nanoscale flow rate and decline in production rate with time.

A nanoscale shale gas reservoir simulator is designed to research the influence of different processes on shale gas production. The thoroughly combined physical method includes fluid movement through the formation matrix and cracks, shale gas adsorption and desorption, natural gas properties, and in-situ pressure that varies during the development process. This simulator enables us to combine nano flux mechanisms and geo-mechanical effects in fracture systems to assess which factors influence the global well production and ultimate rehabilitation of shale gas formations. Although the whole segment of a horizontal well can be simulated using the reservoir-scale simulator, with several transverse fractures, a unit volume can be simulated more effectively, and symmetrical boundary conditions can be applied along the borders so that overall gas output from the horizontal well can be calculated. Furthermore, constant output pressure on the wellbore is applied, and no flux conditions boundaries are applied.

This chapter lays out the motion equation and mathematical shale-gas transport model in the multi-scale medium in conjunction with the kinetic molecular principle and gas transport properties in the shale gas reservoir with nanoporous parameters. In addition, the radial flow pressure distribution formula and the control system for shale gas well control are obtained. Furthermore, the flow rate of gas well volume is analyzed, considering major control variables. Finally, the theoretical basis for effective shale gas extraction is provided.

6.31 The impact of the intact gas pressure on gas production rate

Shale gas reservoirs are rich organic formations that vary from one to another formation, including within the formation itself. The shale gas comprises largely free gas on the pore surface of the shale matrix and adsorbed gas onto the organic matter in the pore matrix [177,178]. As a result, shale gas reservoirs can yield significant free gas in the formation compared to conventional gas reservoirs [179]. Therefore, the intact gas pressure in the formation is an important contributing factor in gas recovery. Still, there is a minimal discussion on the influence of the gas pressure on gas output and may significantly impact the Arps decline curve analysis [180]. The intact gas pressure depends on the depth of the formation, clay content, and organic content.

To simulate the behavior of actual formations and to predict the amount of gas extraction using the pore network model, the correct intact gas pressure is needed. However, there was limited information on intact gas pressure, and it was decided to determine the impact of the intact gas pressure on the gas production rate. Therefore, four simulation pressures (20Mpa, 40Mpa, 60Mpa, and 80Mpa) were applied to each target shale. The regular 20*20*20 lattice grid was used to compare the impact of the intact gas pressure on the gas production rate. The simulation results are shown in Figures 6.2, 6.3, 6.4, and 6.5

for the four shale formations with a mathematical fit of a function flow rate $Q=A*t^{-B}$ as shown below.

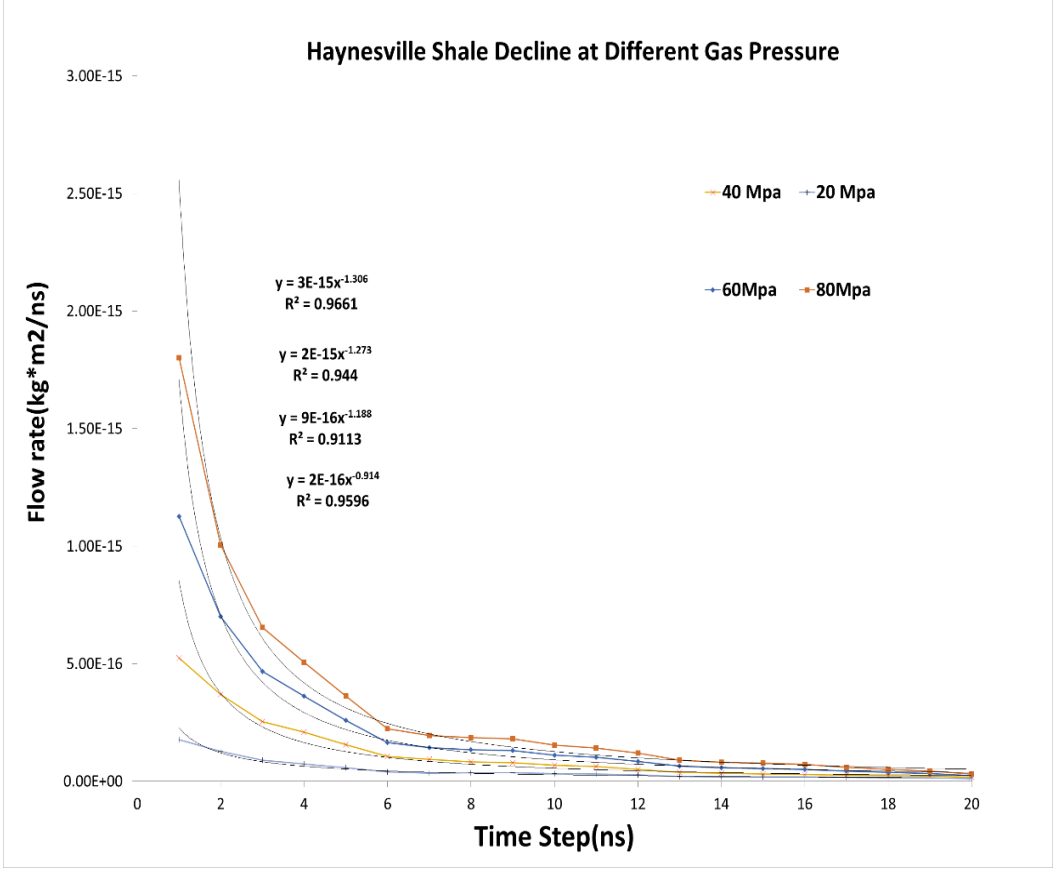

Figure 6.2 Haynesville shale flow production at different gas pressures.

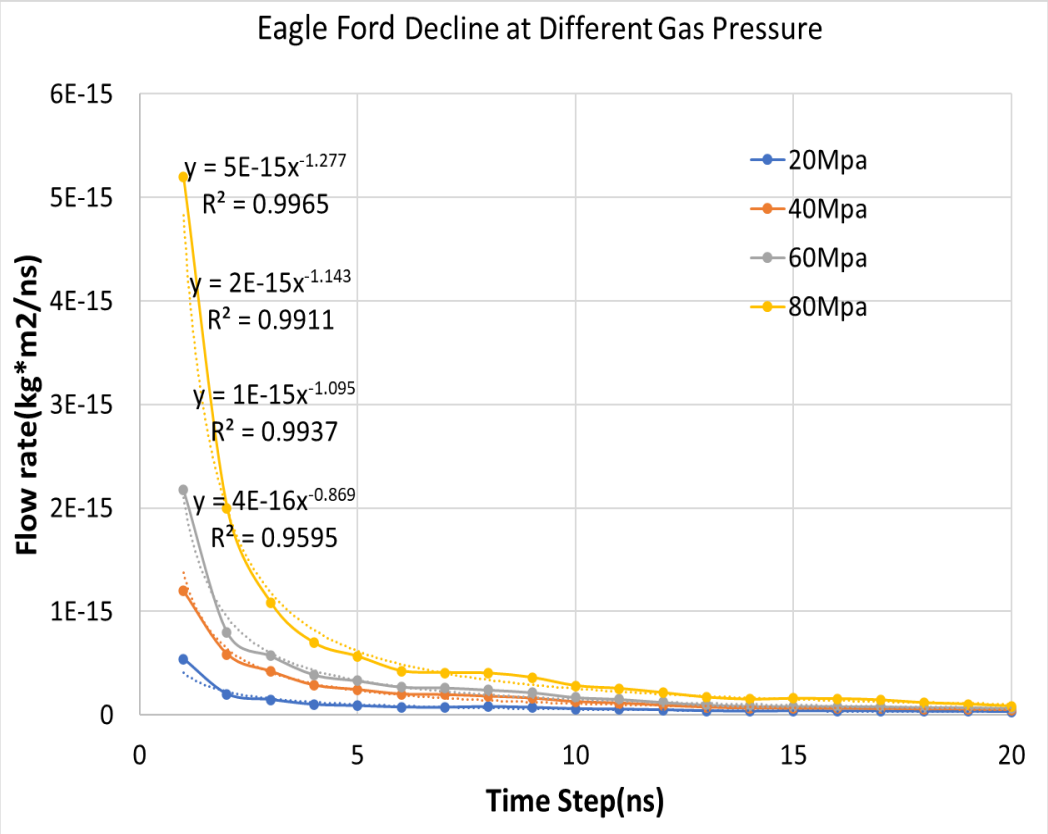

Figure 6.3 Eagle Ford shale flow production at different gas pressures.

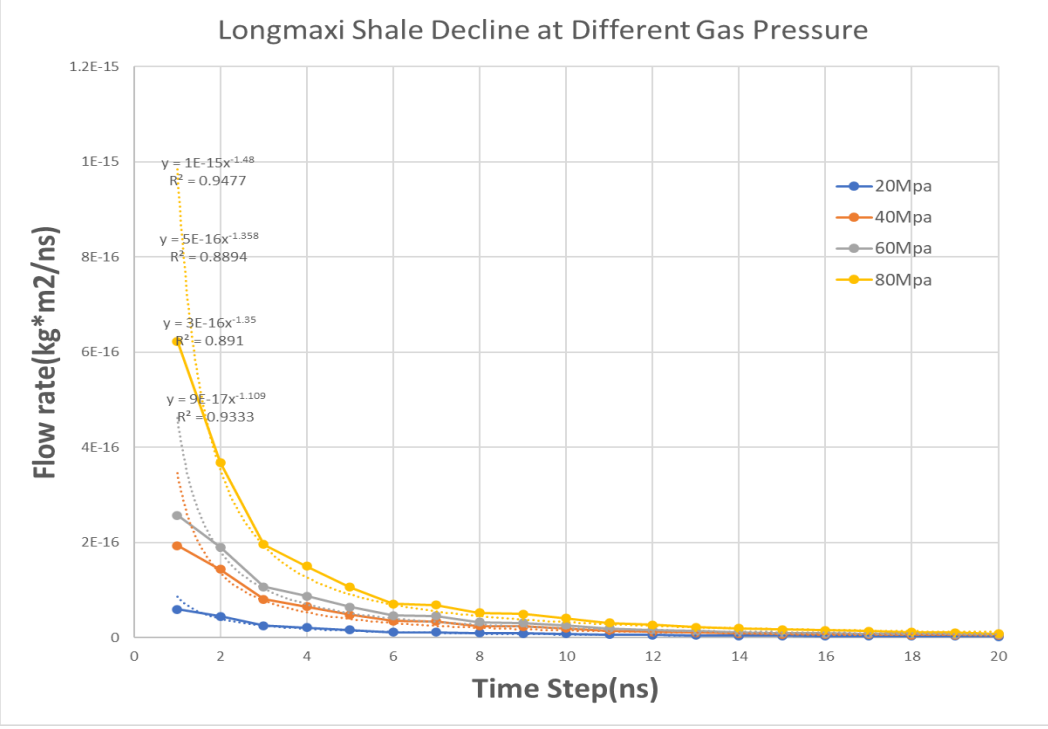

Figure 6.4 Longmaxi shale flow production at different gas pressures.

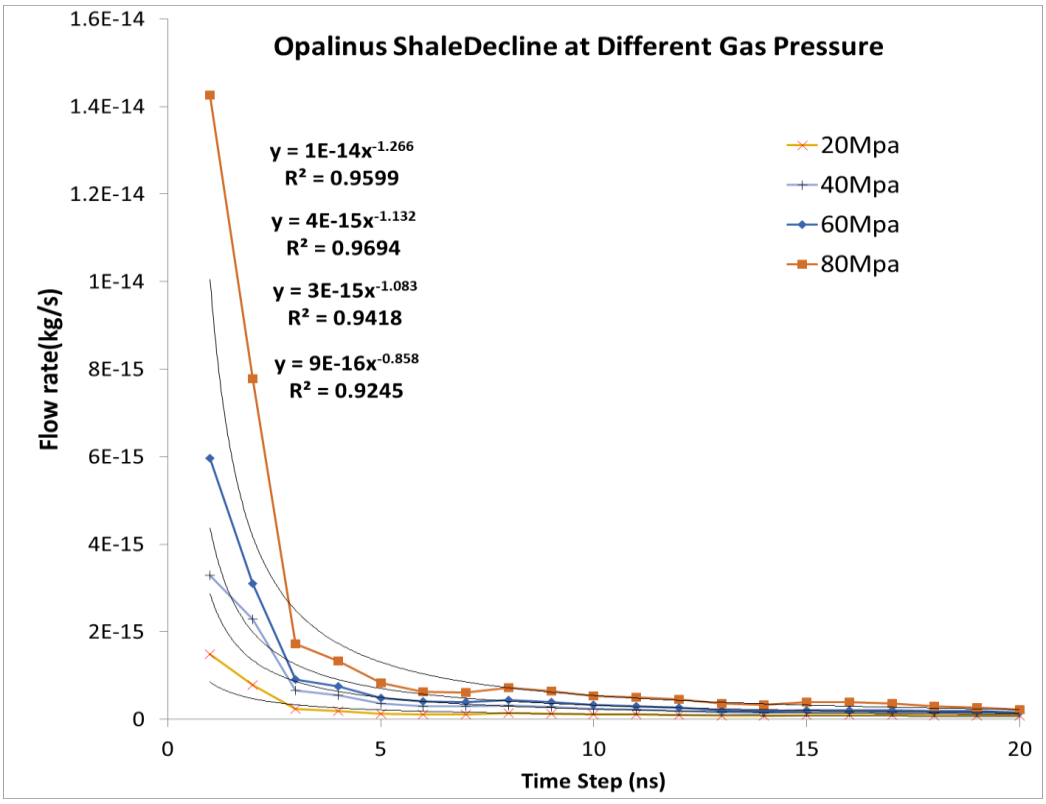

Figure 6.5 Opalinus shale flow production at different gas pressures.

Compared with the base case with the gas pressure of 20 Mpa, the decline rate of gas production decreases dramatically with the increasing initial gas pressure. However, the decline rate trend is similar. Comparing the impact of the intact gas pressure on the decline rate of gas production or the A and B values of fitted equation $Q=A*t^{-B}$ for shale formations are shown in Figures 6.6, 6.7, 6.8, and 6.9. They show the effect of gas pressure in controlling the decline slope. Furthermore, the power number of different gas pressure can be correlated for the 20*20*20 model for four selected shale formations. Correlations were found between gas pressure and decline curve slope for the four shale formations, as shown in Figure 6.6-6.9. Hence the nanoscale flow rate simulations can obtain actual production rate curves with different reservoir configurations based on this gas pressure sensitivity study.

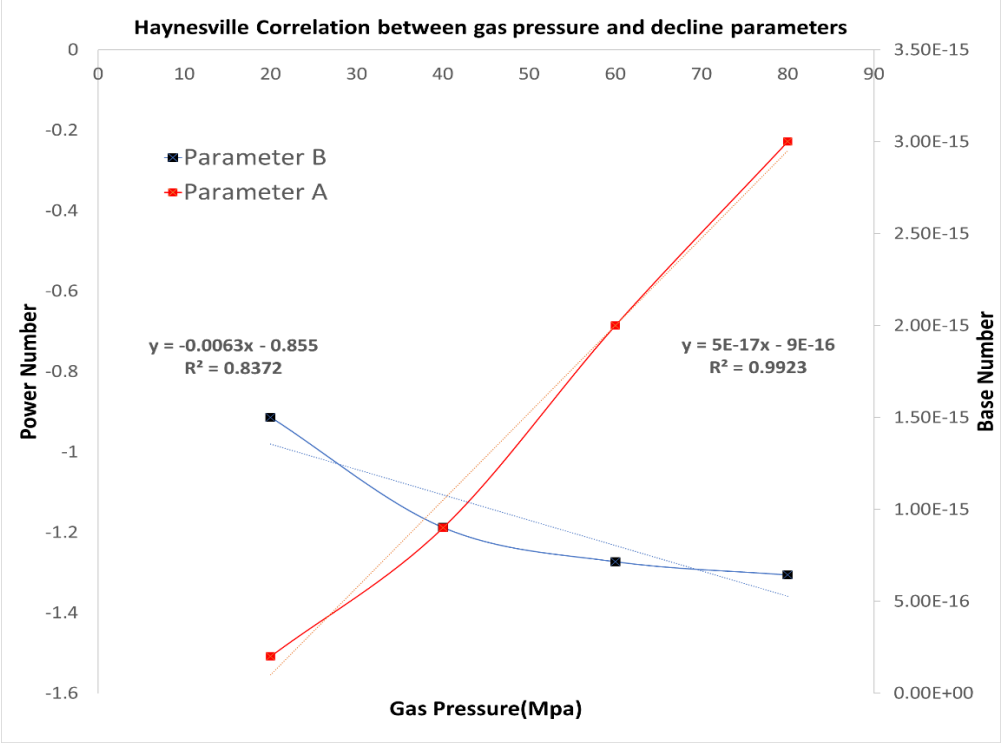

Figure 6.6 Decline parameters fittings with variation of gas pressure of Haynesville shale.

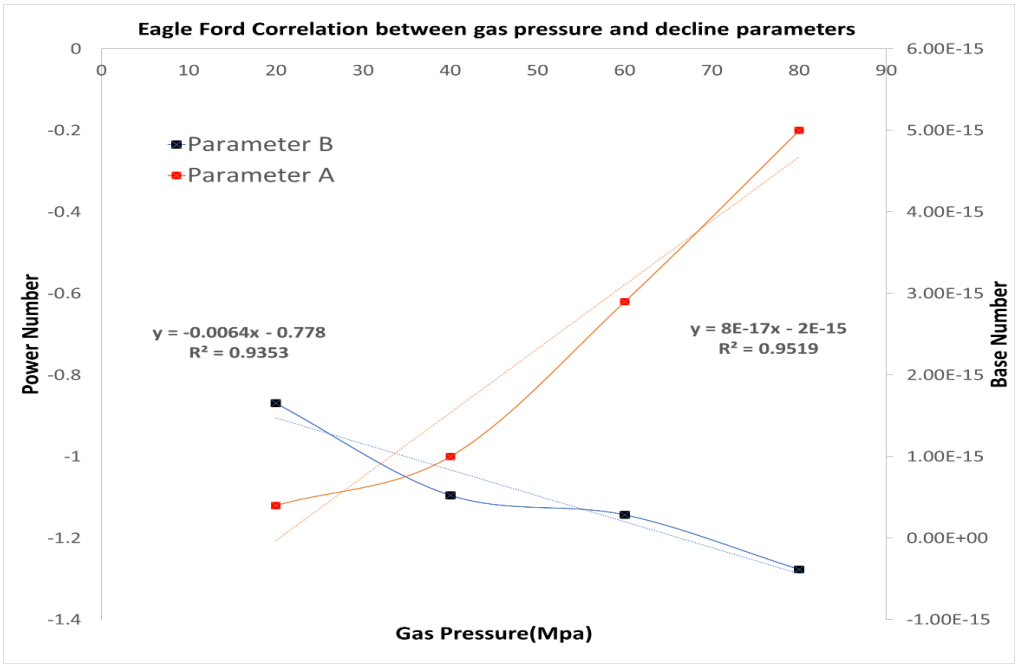

Figure 6.7 Decline parameters fittings with variation of gas pressure of Eagle Ford shale.

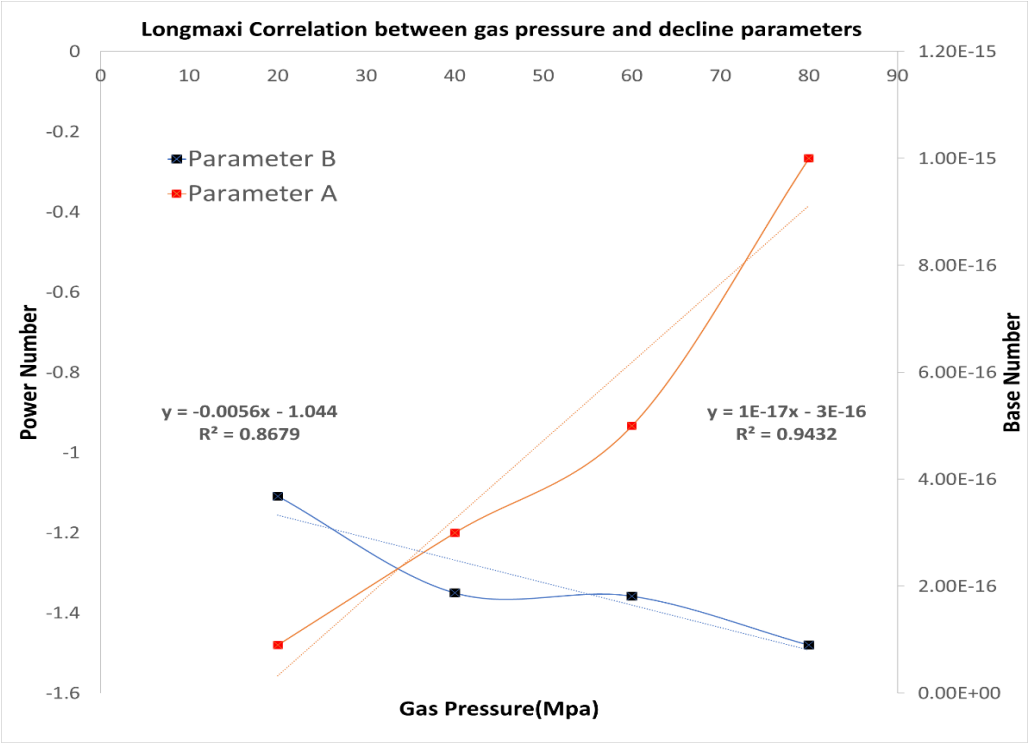

Figure 6.8 Variation of gas pressure correlation with power number of Longmaxi shale.

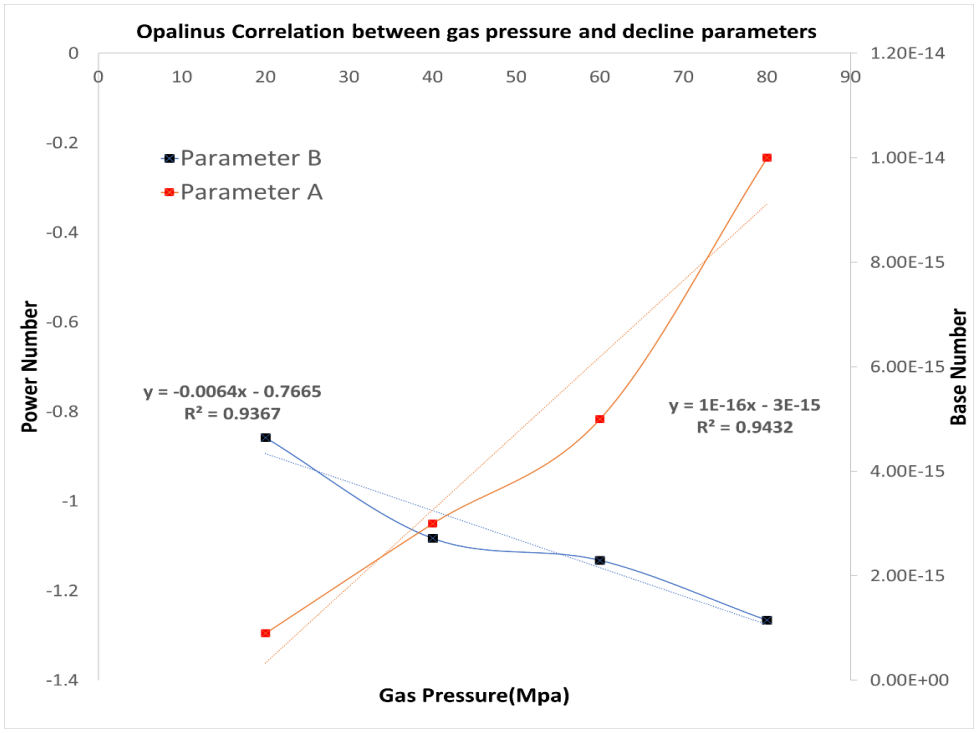

Figure 6.9 Variation of gas pressure correlation with power number of Opalinus shale.

6.32 The influence of the flow length

Figure 6.10 shows the 20*20*20 pore network model used in this research, where Figure 6.10 shows all 20 nodes in the lattice but only shows truncated to 4 nodes in Y and Z directions. If this nanopore network model to be applied for actual formation, then the length of the model in the X direction would be half of the fracture spacing shown in Figure 6.11b. This would require the number of pores in the X direction to be 1.5E9. Such simulation would require significant computational effort, and hence it is not feasible to use the pore network model used in this research to predict the actual shale gas production. Hence to obtain useful information from the pore network model used in this research, the grid size of the model was logically increased from 20*20*20 to 200*20*20,2000*20*20 and 20000*20*20 size grids and predicted the shale gas production rate with time for the four shale formations.

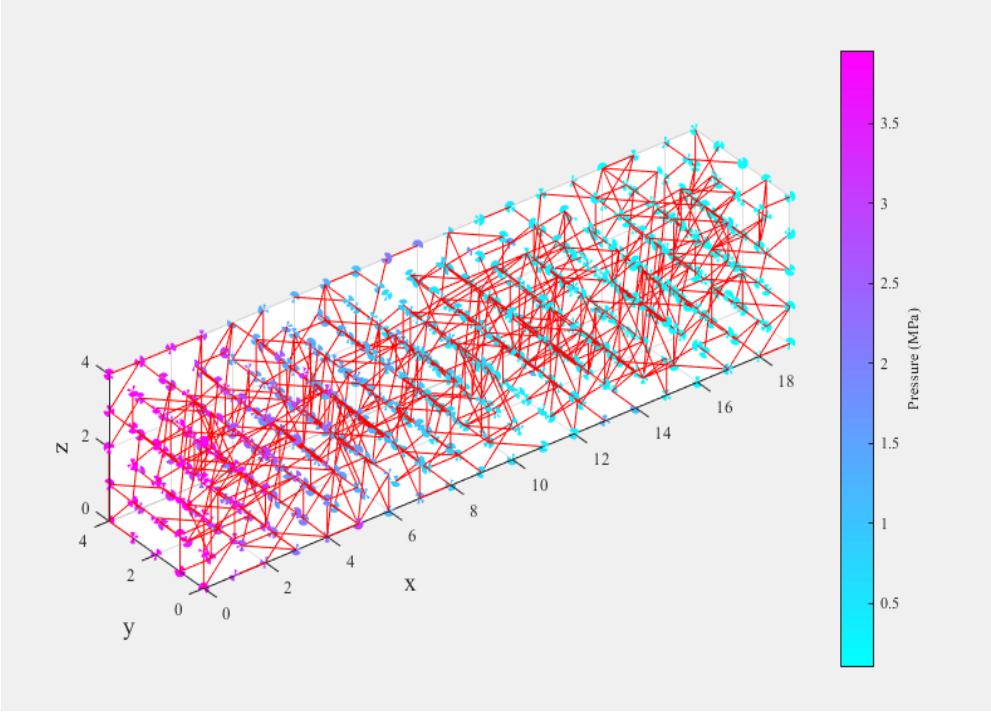

Figure 6.10 Illustration of the pore network.

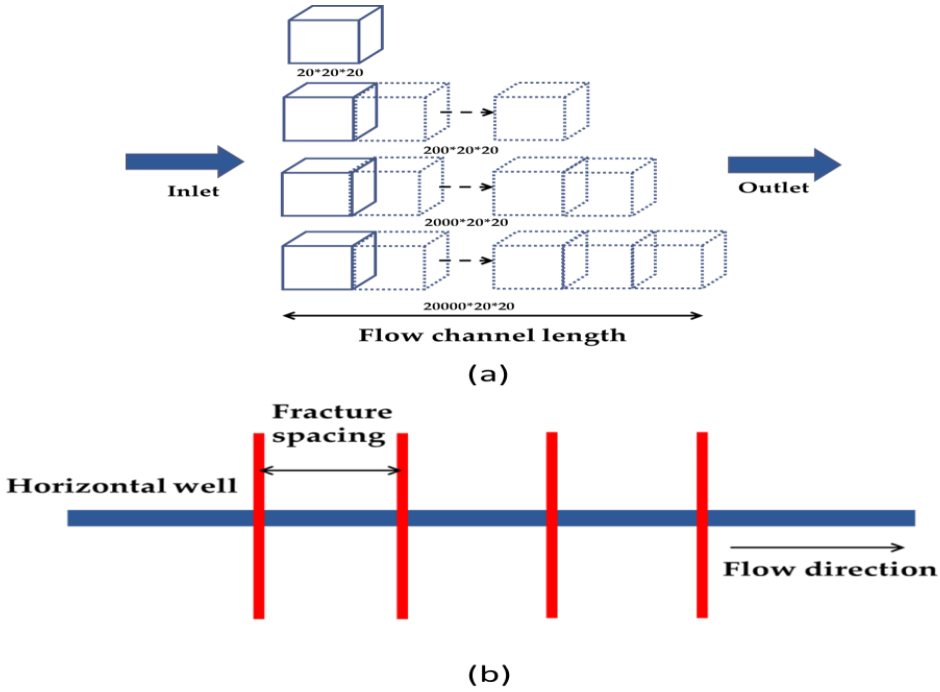

Figure 6.11 Nano-flow channel lengths and reservoir fracture spacing representation: (a) Schematic of Nano-scale grid. (b) Reservoir-scale fracture spacing.

Figure.6.11a shows the nanoscale 20*20*20, 200*20*20,2000*20*20, and 20000*20*20 pore network grids. Figures 6.12, 6.13, 6.14, and 6.15 show results of simulations with 20*20*20, 200*20*20, 2000*20*20, and 20000*20*20 grids for the selected four shale formations. Figures 6.12, 6.13, and 6.14 also show the fitted equation $Q=A*t^{-B}$ for shale formations for each grid size. Figures 6.12, 6.13, and 6.14 clearly show that the gas production rate sharply decreases during the initial steps and then slowly approaches zero. The methane gas production rate for all four grids decreases almost to zero within 20 nanoseconds. During the first few steps, the gas production rate dropped 20%-40% and, after the 15^{th} time steps, the production rate decreased and stabilized at around 5% per step. It is also noticeable that at the end of the 20-time steps, the production rate decreased by 90%.

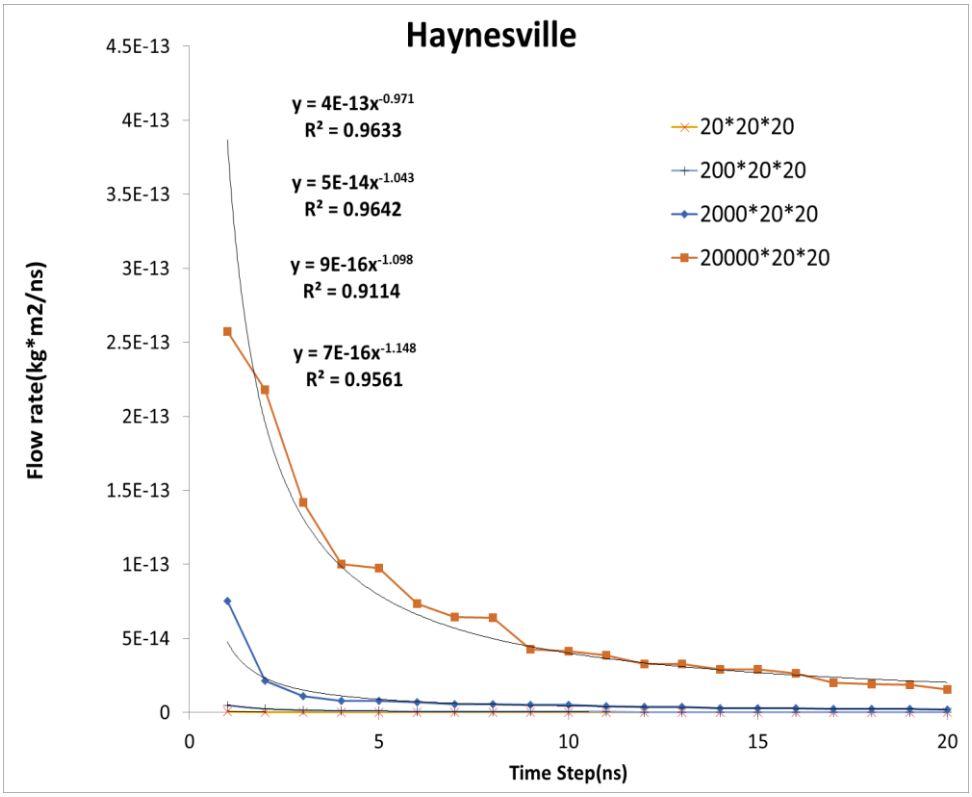

Figure 6.12 Four flow lengths simulation curves of Haynesville shale.

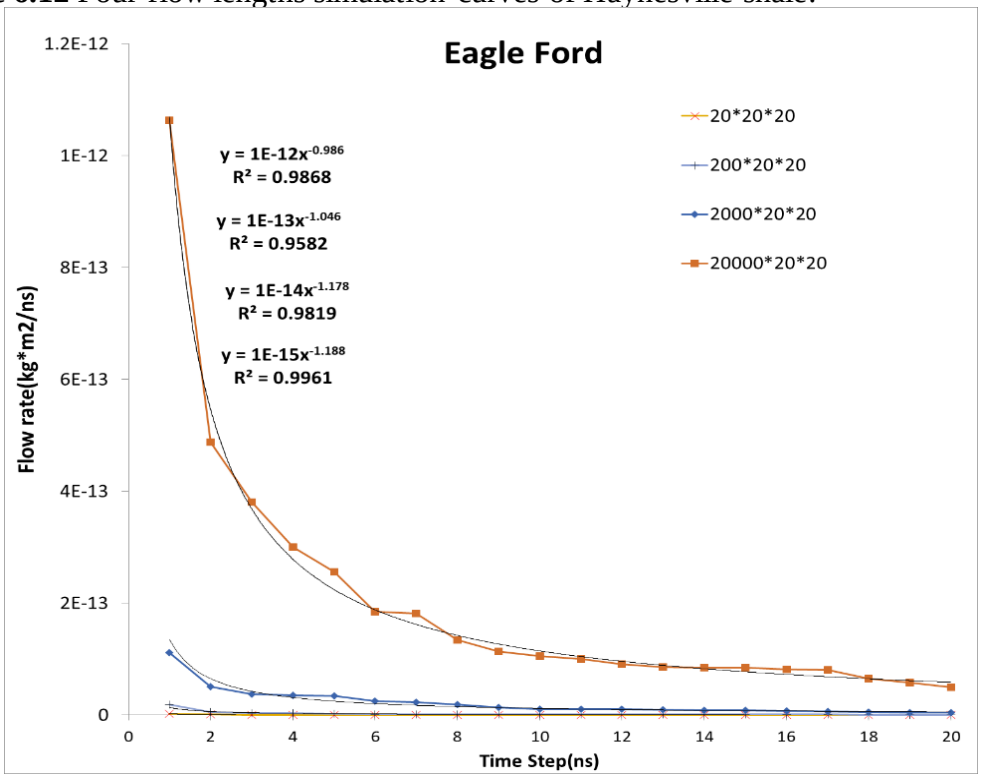

Figure 6.13 Four flow lengths simulation curves of Eagle Ford shale.

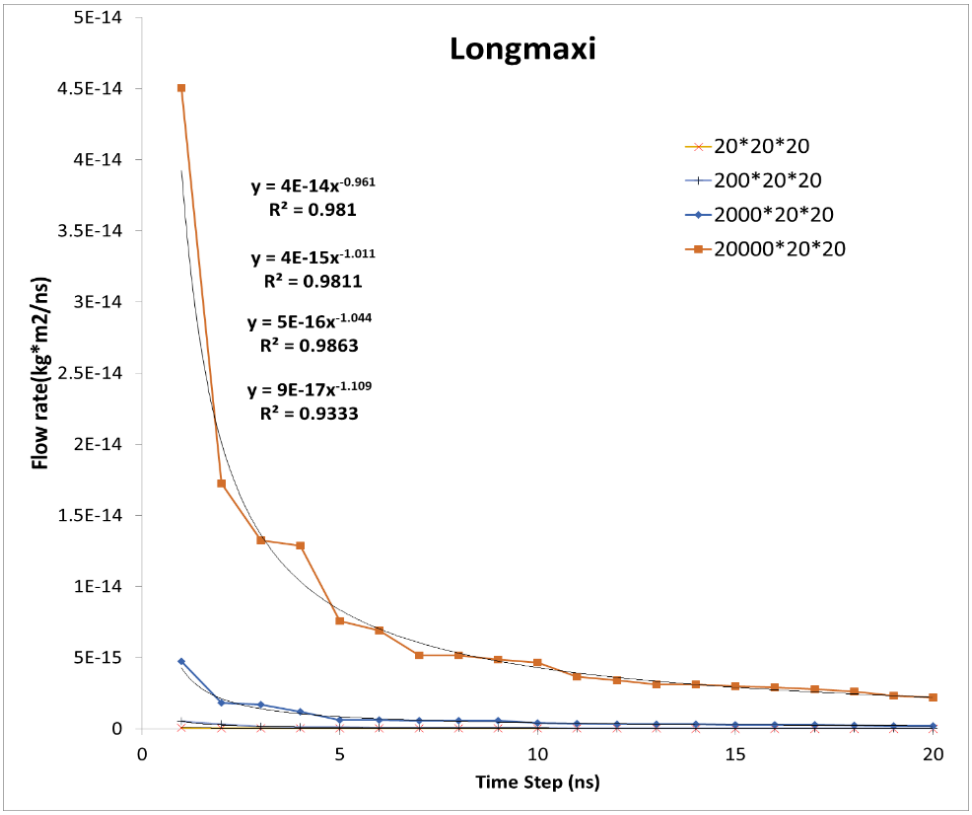

Figure 6.14 Four flow lengths simulation curves of Longmaix shale.

Correlations between fracture length and parameters A and B of the fitted equation $Q=A*t^{-B}$ for four shale formations are shown in Figures 6.15, 6.16, and 6.17. Good correlations were obtained for selected four shale formations indicating the ability to extrapolate to field scale with minimal computational efforts. As the flow seepage through the pore network, the different flow behaviors in this case: flow rate is reducing when the flow length is increasing.

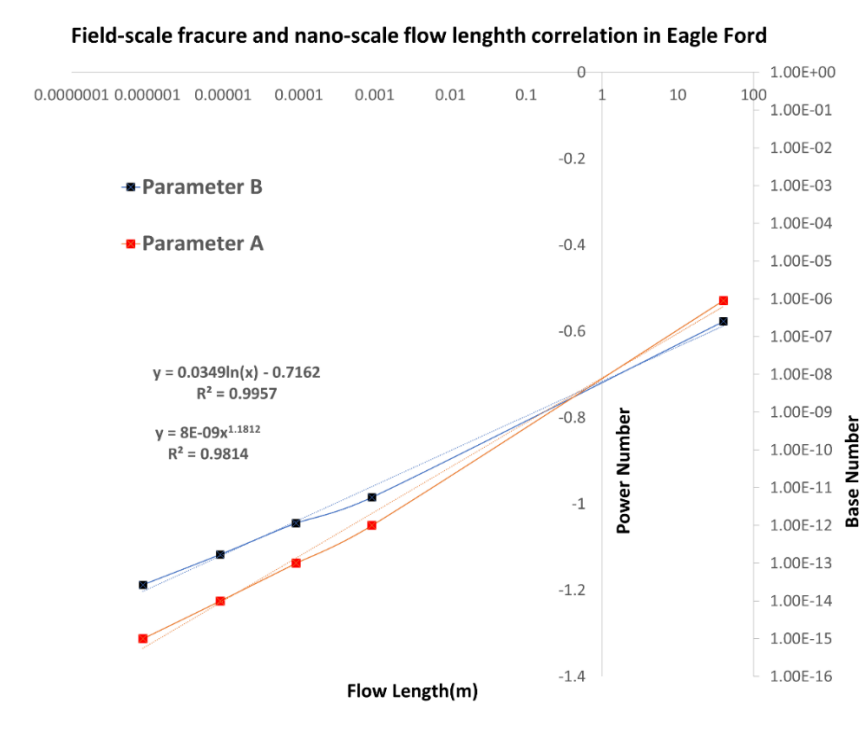

Figure 6.15 Correlations between flow length and decline power number for Eagle Ford.

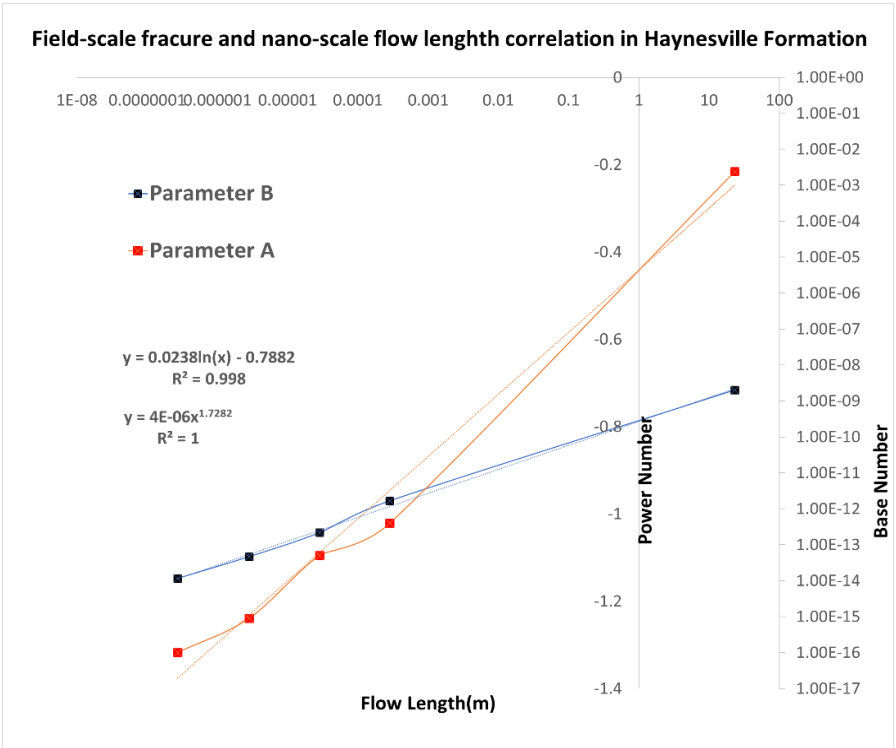

Figure 6.16 Correlations between flow length and decline power number for Haynesville.

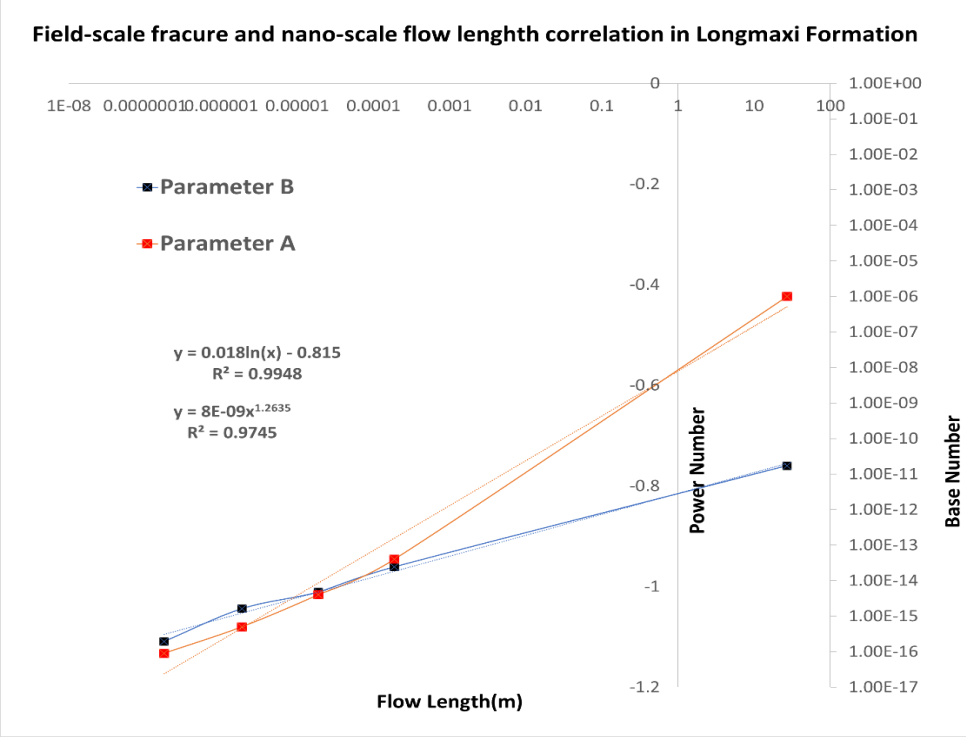

Figure 6.17 Correlations between flow length and decline power number for Longmaxi.

6.4 Impact of Shale Softening on Flow rate

Darcy's theory, which models pressure-driven viscous flow, is valid for reservoirs where the continuum principle holds and fluid velocity at the pore wall is believed to be zero. However, fluid continuum theory fails in shale reservoirs with pore throat radii in the nanometer range [181]. Gas molecules take a rather random path while still retaining a general flow trajectory governed by the pressure gradient. Instead of having zero speed, molecules bounce at pore walls and appear to slip. Many authors quantified the results by altering the slippage factor or determining apparent permeability as a function of the Knudsen number to suggest corrections for non-Darcy flow across various flow regions in nanopore space [182].

While several theoretical and analytical models for apparent enhancement of permeability in nanopore structures have been developed to account for gas slip behavior

effects, they neglect the alteration of the geometry of the pore structure caused by clay-swelling and the gas layer softening.

The pore micro/nanostructure would be influenced by the continuous decrease of pore gas pressures and seepage of fracking fluid. An extensive literature review on the evolution of matrix permeability during pressure degradation suggested a single model for matrix permeability, including the non-Darcy flow/gas slippage [183]. However, the impact of shale softening and porosity reduction through layers that affect the flow rate of the matrix at the nanoscale was not studied.

6.41 Progress of softening through layers.

Using a pore network model and coupling the porosity change measured in the laboratory study will provide insights into reducing the flow rate and help understand the damage due to shale softening. Based on spatial structures and porosity of original and treated shale, the flow rate result will be compared within changing flow length. Figures 6.18, 6.19, and 6.20 show a series of flow rate comparisons of the 20*20*20, 200*20*20,2000*20*20, and 20000*20*20 grids four selected shale formations. These Figures indicate the flow rate when the exit pore throat swelled for four formations with different flow lengths. The swelling effect was assumed to be occurring at the exit layer where the initial water injection occurred.

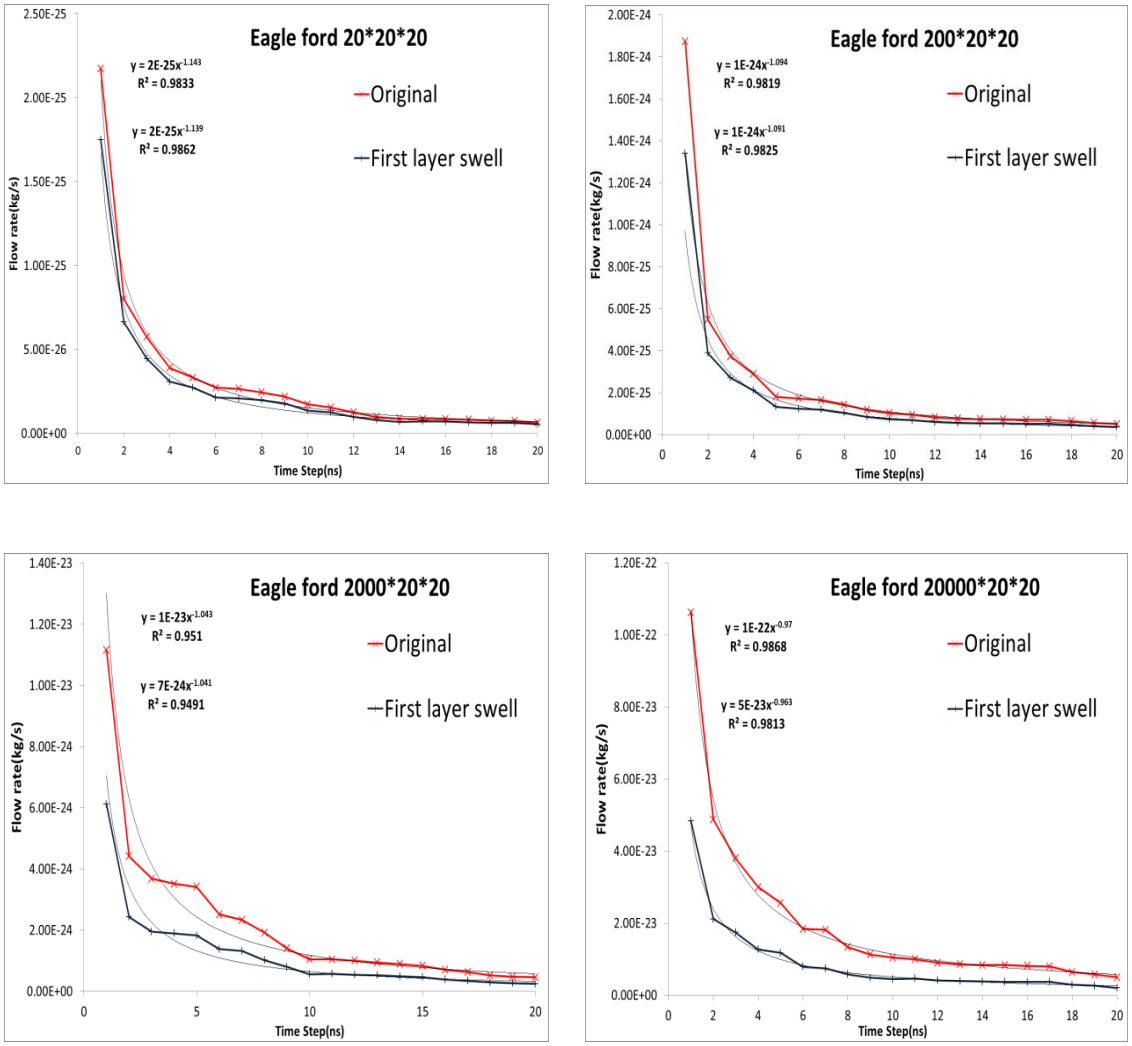

Figure 6.18 Flow length effect on initial reduction of flow rate for Eagle Ford.

As the flow lengths increase from the initial flow length of 8.64E-7 m to 9.15E-4 m for Eagle Ford, there is a gradual reduction for the initial flow rate when the flow channel is increasing potentially. The reduction rate of the initial flow rate is ranging from 7.89E-1 to 4.32E-1.

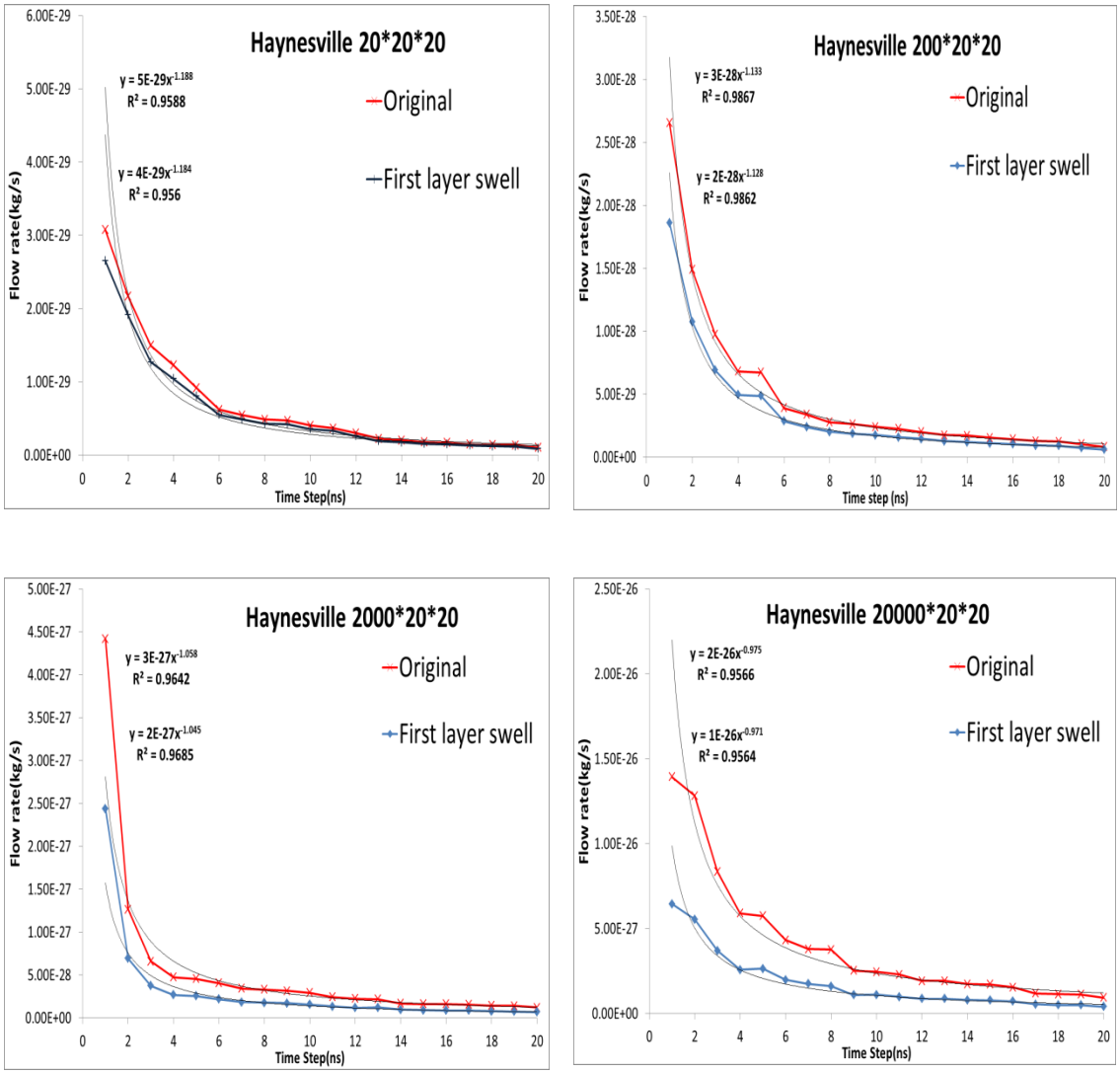

Figure 6.19 Flow length effect on initial reduction of flow rate for Haynesville shale.

A similar pattern was found using the parameters of Haynesville Shale. The initial flow rate reduction can be correlated to the flow channel length. From the initial 20*20*20 grid to 20000*20*20 grid, the initial flow rate reduced from 8.06E-1 to 4.56E-1.

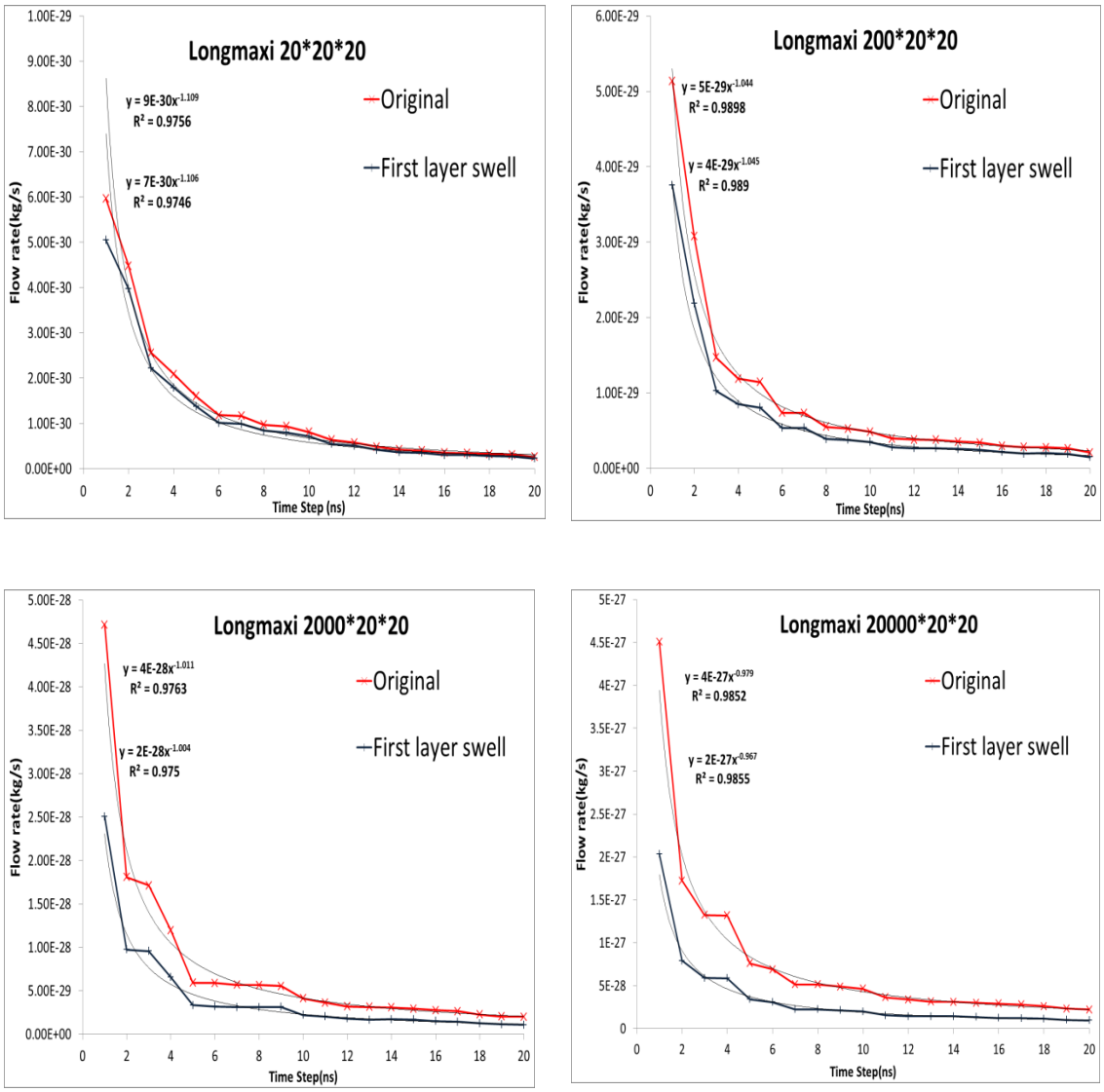

Figure 6.20 Flow length effect on initial reduction of flow rate for Longmaxi shale.

According to the above four sets of comparisons, the Nanoscale model can optimize the flow channel length and predict the flow behavior within the matrix. However, several assumptions were made for the simulation as follows:

- Assume that swelling initializes from the first layer of the grid in contact with hydraulic fracturing.

- The pore body and the pore throat both swell due to clay-water reaction, but only the throat contribute to the matrix flow rate
- As the softening progress gradually, the first the last layer swells and then continues to the next layer until the complete model is swelled.

As the shale softening continues, the progression of water intrusion will damage the whole matrix over time. Therefore, a representative 20*20*20 model was modified to study the shale softening effect. The outlet and inlet pressures are fixed at 5E6 Pa and 3.6E7 Pa. Figure 6.21 shows an increased level of swelling spread through the matrix from the initial-swell ratio of 0.9 to a severe condition of 0.1 swelling with fracturing progress for layers in contact with the hydraulic fractured liquid. As the swell ratio decreased, the flow rate of the original shale decreased.

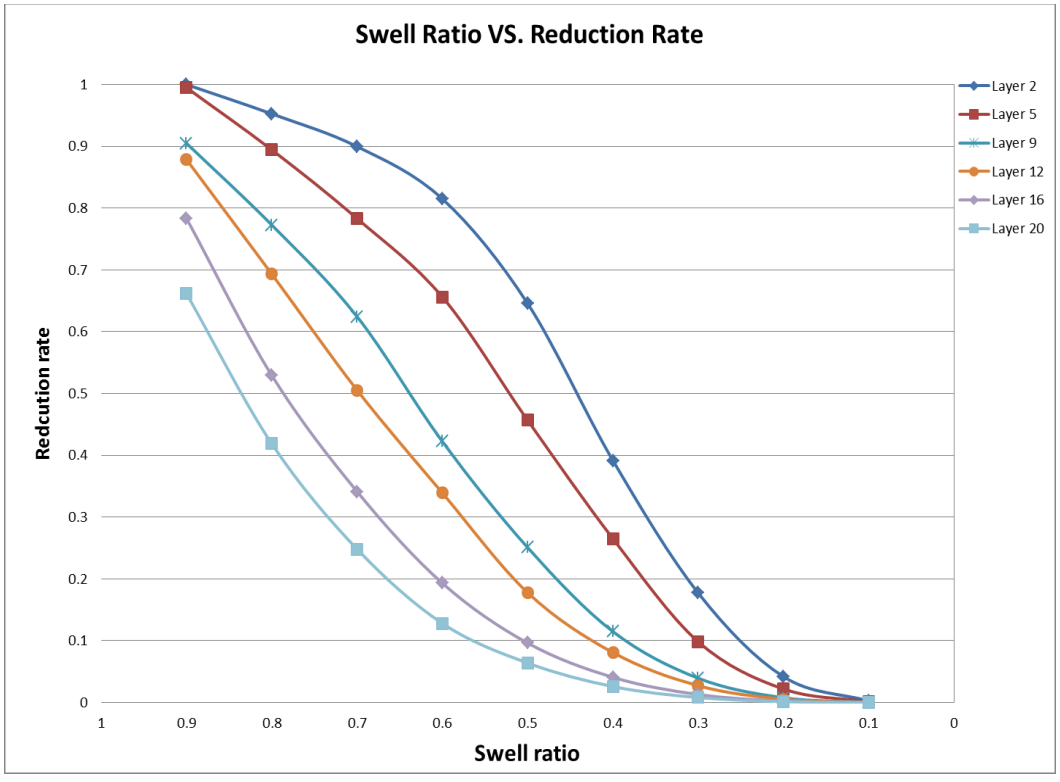

Figure 6.21 Impact of different swelling ratios on the flow rate of shale matrix.

It should be concluded that the spread of moisture into the shale matrix lowers the matrix flow rate across the grid. In the extreme case, the flow rate of the matrix is far less than the initial production rate if all layers swell.

With the advancement of fracturing water from the last layer into the entire grid, to understand the flow rate change of the shale matrix in several softening stages, the swell ratio and layer number were provided. After the half-swelling, the flow rate drops significantly to 0.62 of the first layer and 0.09 of the last layers. For Eagle Ford shale, even though the porosity of the original shale only decreases by 1.3%, the flow rate has been reduced by 99%. The progression of shale softening was demonstrated in different simulations, including layer 2, layer 5, layer 9, layer 12, layer 16, and layer 20, as shown in Figure 6.21. Both swelling layers and swelling ratio are used to indicate the stage of shale softening. Flow rate changes can be calculated using the swelling pore network model.

6.5 Nano Model to Field-scale Shale Gas Production

All the basic information for the four selected shale gas formations is listed in Table 6.2. Hydraulic fracturing data and gas production data are only available for Eagle Ford, Haynesville, and Longmaxi formations. In addition, several simulations including were performed using actual reservoir parameters. The input parameters for a simulation of base cases of Eagle Ford, which include reservoir conditions, nanostructure, fracturing, and valid gas properties, are presented in table 6.2.

All these input parameters are planned to represent the reservoir condition of the shale reservoir. For basic case simulation, the development of the matrix and softening is

discarded, with the results on the gas well output being studied separately in the following sections.

Table 6.2 Input Parameters for Three Major Shale

Source:[122,184–188]**.**

Input Parameter	Eagle Ford	Haynesville	Longmaxi	Opalinus
Initial reservoir pressure, Pin	49E6(Pa)	38E6(Pa)	19E6(Pa)	54E6(Pa)
Wellbore pressure, pout	1E5(pa)	1E5(pa)	1.5E5(pa)	1.5E5(pa)
Matrix porosity,	4.41(%)	2.94(%)	1.58(%)	7.81(%)
Fracture Length,	40(m)	23(m)	27(m)	40(m)
Grid length,	8.68E-7(m)	2.72E-7(m)	1.78E-7(m)	9.78E-7(m)
Gas type,	CH4	CH4	CH4	CH4
Reservoir temperature,	323.4K	350K	356K	356K
Molecular weight,	0.016(kg/mol)	0.016(kg/mol)	0.016(kg/mol)	0.016(kg/mol)
Universal gas constant,	8.314472 m^3*Pa/(K*mol)	8.314472 m^3*Pa/(K*mol)	8.314472 m^3*Pa/(K*mol)	8.314472 m^3*Pa/(K*mol)
Viscosity,	1.5E-6(pa*s)	1.5E-6(pa*s)	1.5E-6(pa*s)	1.5E-6(pa*s)
Distribution of pore body	8.5,0.4	5.4, 0.3	4.3,0.3	9.8,0.5
Distribution of pore throat	2.9,0.2	1.6,0.1	0.66, 0.1	3.1, 0.3
Coordination Distribution	4,0.1	4,0.1	4,0.1	4,0.1
Anisotropic ratio	22:22:01	22:22:01	22:22:01	22:22:01

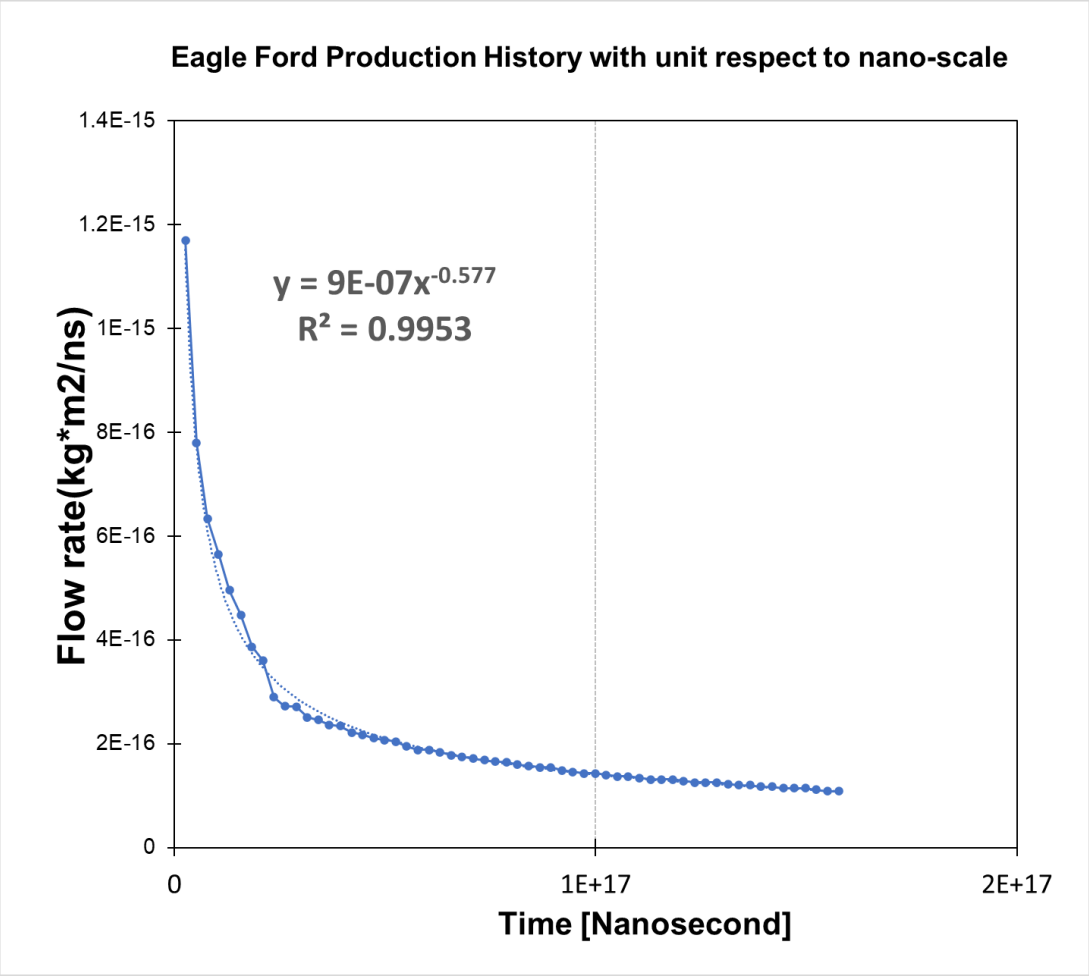

Figure 6.22 Eagle Ford historical production and simulation results.

Source: [186]

Dimmit, De Witt, La Salle, Live Oak, McMullen, Webb counties with 46 horizontal wells were chosen in this research to study the Eagle Ford Shale formation, which was reported in 2009. Like the Haynesville shale, the Eagle Ford shale formed at an average 5,000 ft long lateral, with the number of stages is currently 12 to 14 per stage. As shown in Figure 6.22, a fitting curve was discovered to be a power function: $Y=9E\text{-}77x^{-0.577}$.

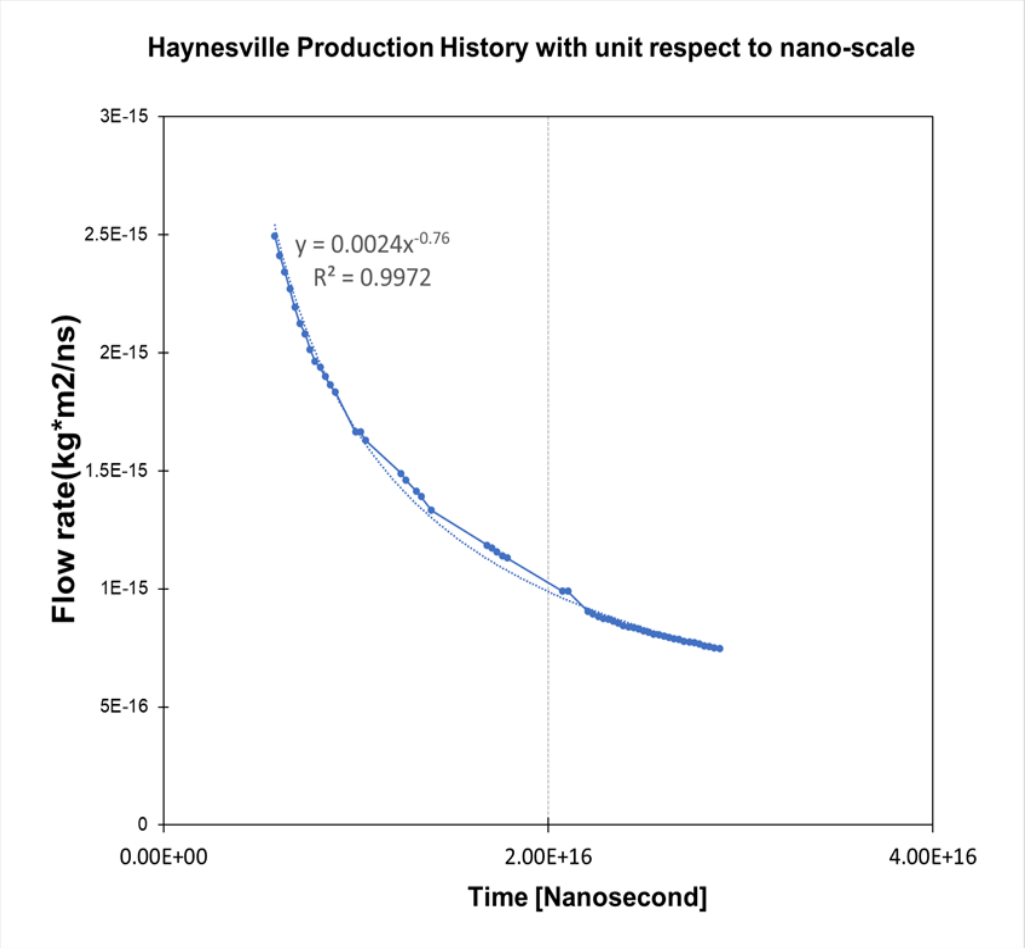

Figure 6.23 Haynesville historical production and simulation results.

Source: [184]

The central area for Haynesville Shale analysis was chosen in Bienville, Bossier, Caddo, De Soto, Red River, Sabine Parishes. In addition, typical production curves of Haynesville and Longmaxi shale were chosen here to study the decline characteristics individually, as presented in Figures 6.23 and 6.24.

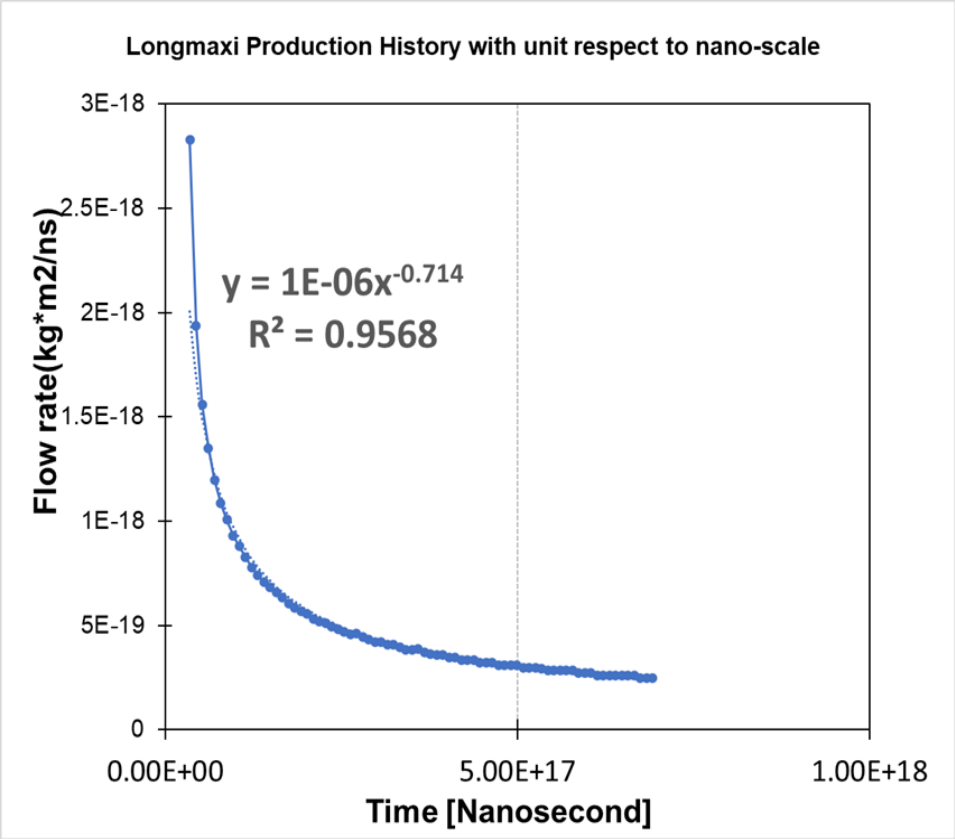

Figure 6.24 Longmaxi historical production and simulation results.

Source: [185,189].

The initial flow rates in Haynesville and Eagle Ford formations are higher than Longmaxi formations because their reservoir pressures are higher. The other reason for this may be that the hydraulic breakdown treatments were pumped in Haynesville and Eagle Ford formations. Operators drilled longer laterals with more phases and used more fluid or supporting quantities per step [8]. These two factors are more likely than variations in petrophysical properties between basins to affect the initial production discrepancy significantly. The gas production rate declines after the first few months of production. Each decline curve was fitted into power functions and the base number. The power number of each fitting was analyzed using nanoscale pore network simulation, as shown

in Figures 6.25, 6.26, and 6.27. For instance, as the flow length increases from 8.69647E-07 m to 9.1537E-04 m for Eagle Ford shale, the decline curve power was correlated as following:

$$\mathbf{y = 0.0349\ln(x) - 0.7162\ ,\ R^2 = 0.9957 \quad (Eagle\ Ford)}$$

$$\mathbf{y = 0.0238\ln(x) - 0.7906 \quad R^2 = 0.9986 \quad (Haynesville)}$$

$$\mathbf{y = 0.018\ln(x) - 0.815 \quad R^2 = 0.9948 \quad (Longmaxi)}$$

The three values of correlation coefficients are nearly one, which indicated good matches between these three formations.

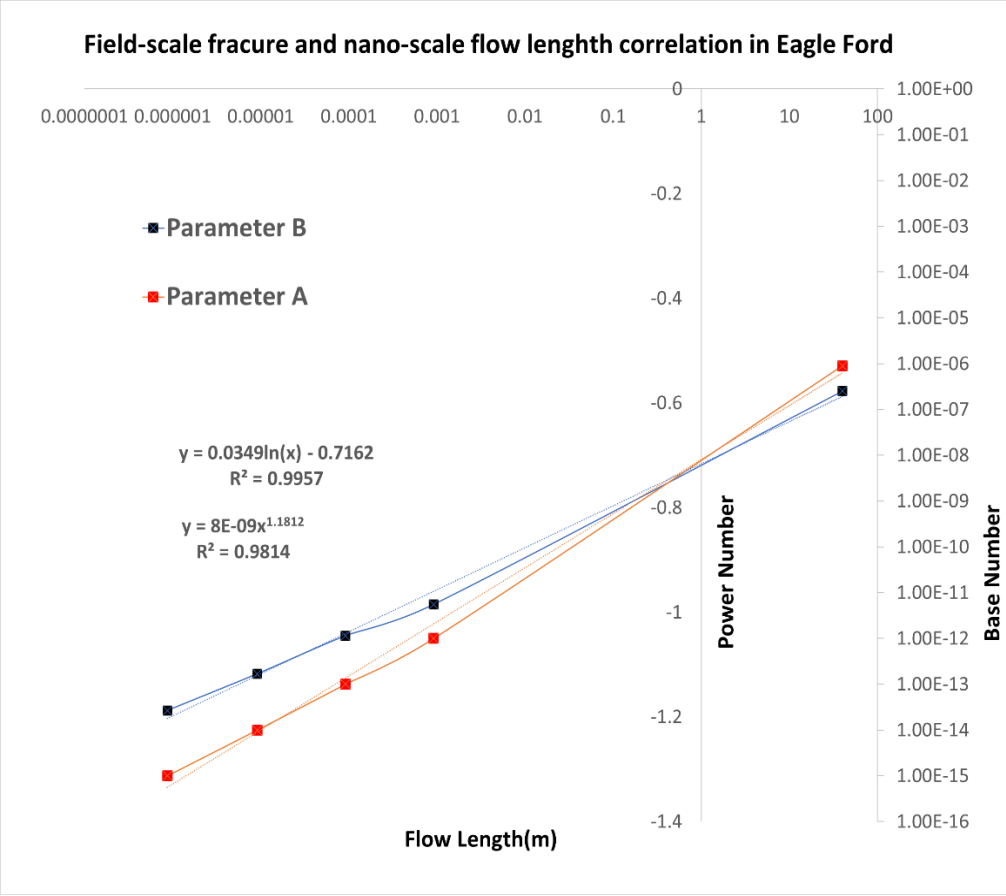

Figure 6.25 Field-scale fracture and nanoscale flow length correlation in Eagle Ford.

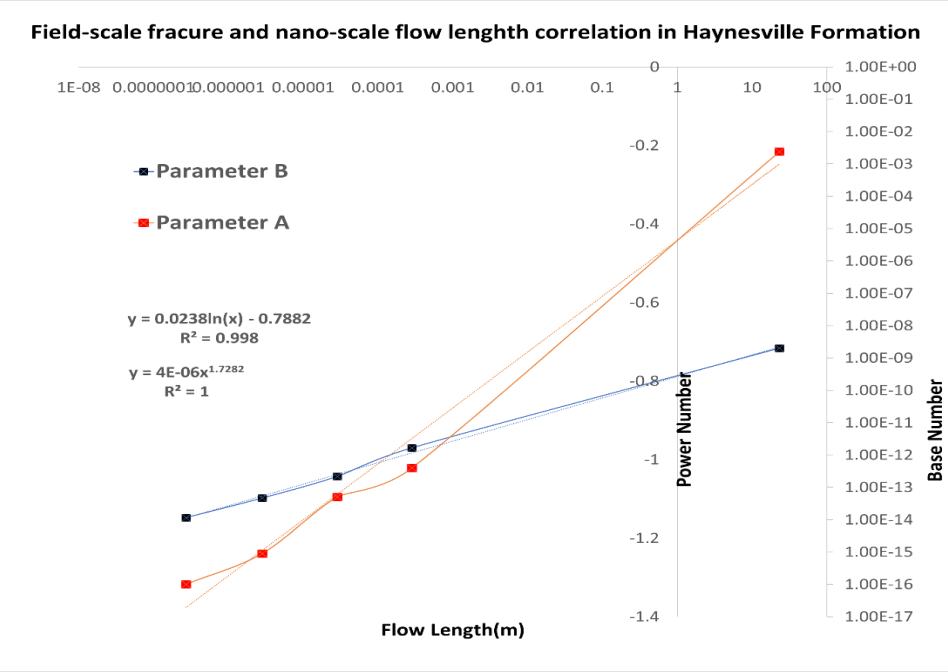

Figure 6.26 Field-scale fracture and nanoscale flow length correlation in Haynesville.

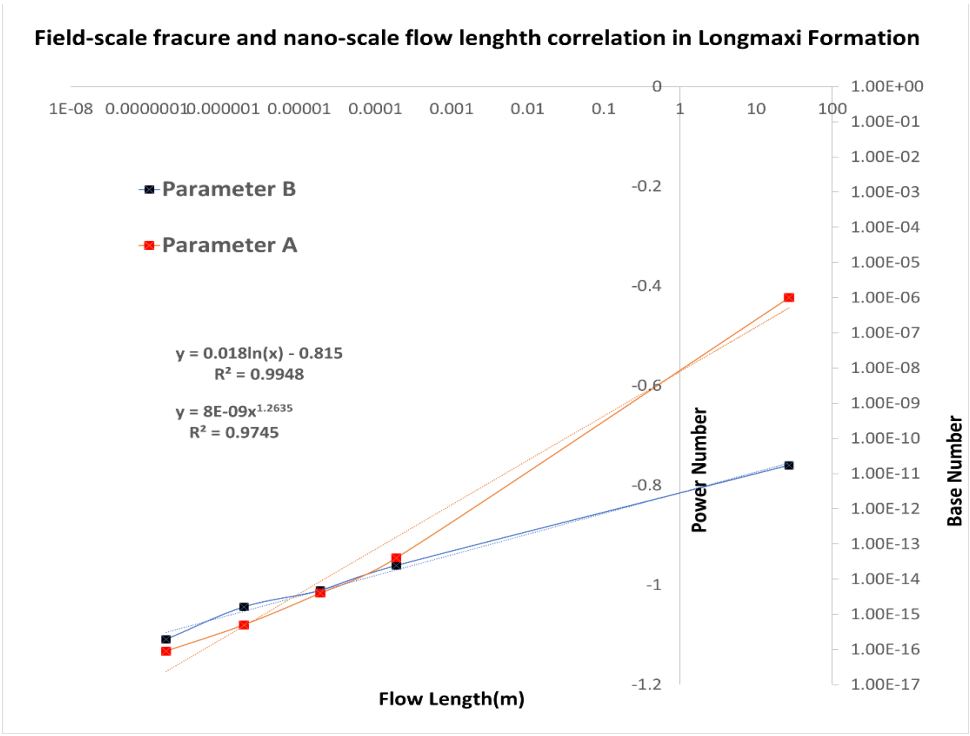

Figure 6.27 Field-scale fracture and nanoscale flow length correlation in Longmaxi shale.

6.6 Porosity-based Correlations and Prediction for Opalinus Shale Production

Correlations between the slope of variation of base and power number with the distance shown in Figures 6.25, 6.26, and 6.27 with formation porosity are shown in Figures 6.28 and 6.29.

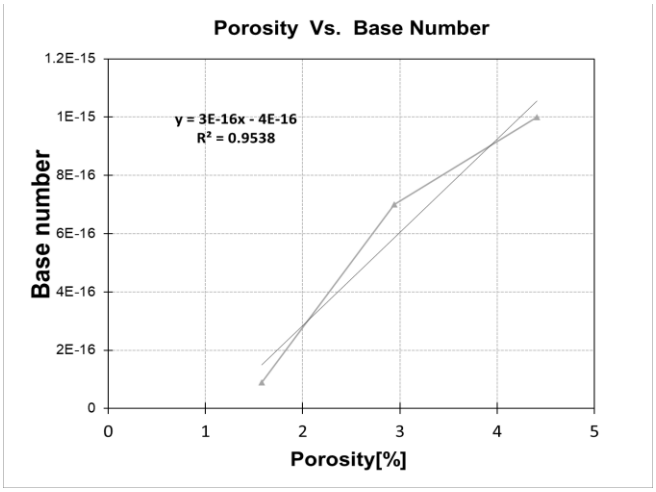

Figure 6.28 The relationship between the porosity of the shale formation and base number

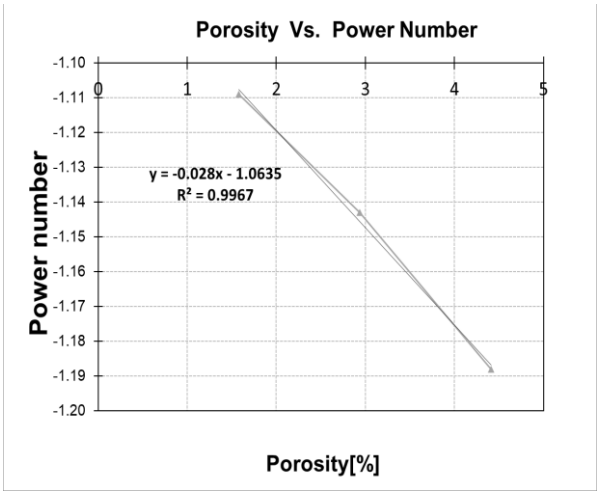

Figure 6.29 The relationship between the porosity of the shale formation and power number.

With the above two correlations and with known porosity, one can predict slopes of variation of the power equation $Q=A*t^{-B}$ (gas production rate with time) and the decline in gas production rate with time for an unknown formation. Hence, with the porosity of

7.8% for Opalinus shale gas production rate with time was constructed. Therefore, based on the above two correlations shown in Figures 14 and 15, fitted A and B values from nanoscale element of 20*20*20 nodes pore network model of Opalinus shale and assuming a fracture length of 40 meters for the Opalinus shale formation, which is a standard practice in unconventional extraction [192], the estimated the base and power numbers were 8E-8 and -1.282 respectively. Hence the initial raw gas production curve for Opalinus shale was constructed using the porosity-based curves and shown in Figure 6.30.

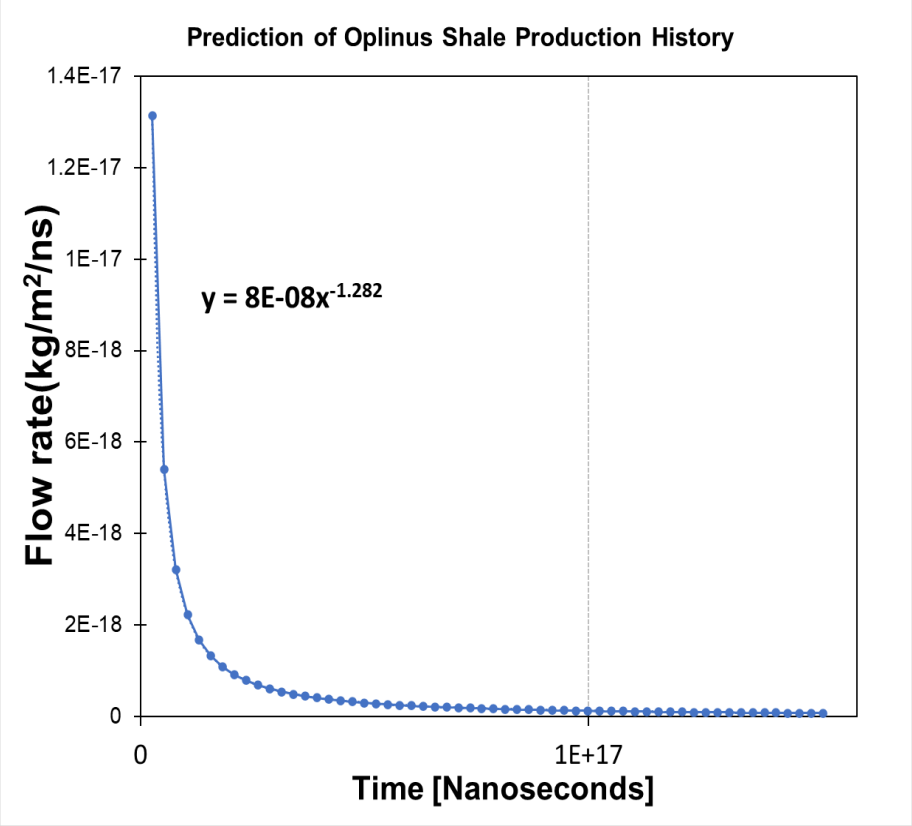

Figure 6.30 Predicted Opalinus shale production.

6.7 Discussions

These two relationships shown in Figures 6.25, 6.26, and 6.27 form the basis for how the fracture length or the flow length is related to the gas production rate for the unconventional

shale gas reservoirs. Moreover, they are logarithmic and power relationships for parameters B and A, respectively, with correlation coefficients of nearly one, indicating the flow length (model length) can be used with the model simulation of nano-size grid to predict the gas production rate for the unconventional shale gas reservoirs. Hence, the above demonstrate that the anisotropic pore network model can be used to predict the gas decline trend of gas production rate for the unconventional shale gas reservoirs.

The prediction of gas production rates with time of unknown formations with limited field geo-material information can be achieved using the pore network model. A flow chart for such is shown in Figure 6.31. The starting point of such prediction would be the simulation of the gas production rate with time for a nanoscale element of, say, 20*20*20 nodes using the pore network model. One would require the porosity and pore body and pore throat sizes and their distribution for such simulation. This can be obtained by analyzing a core sample from the formation. Also, for this simulation, trapped gas pressure should be known. If such information is not available, the sensitivity study used here with the formation depth may be used to estimate the trapped gas pressure. The two-liner equations shown in Figure 3 provide insight into how the gas pressure affects the decline trending for unconventional gas reservoirs. For example, with increasing the gas pressure, parameter A increases linearly; on the other hand, parameter B decreases linearly as the gas pressure increases. Once the gas production rate with time for a nanoscale element of say 20*20*20 nodes is performed, as shown in Figure 6. Then the resulting curves are fitted with a mathematical power function, Q=A*t-B. Then using the two correlations shown in Figures 6.28 and 6.29 with the porosity of the formation, the slopes of variation of A and B parameters of the power equation $Q=A*t^{-B}$ can be obtained. Now

with the flow length of the nanoscale element of say, 20*20*20 nodes and the slopes of variation of A and B parameters of the power equation $Q=A*t^{-B}$ as shown in Figure 6, the A and B parameter values of the power equation $Q=A*t^{-B}$ corresponding to half the hydraulic facture spacing can be obtained. With the estimated A and B values and using the power equation $Q=A*t^{-B}$, one can predict the gas production rate with time for an unknown formation with limited field geo-material information.

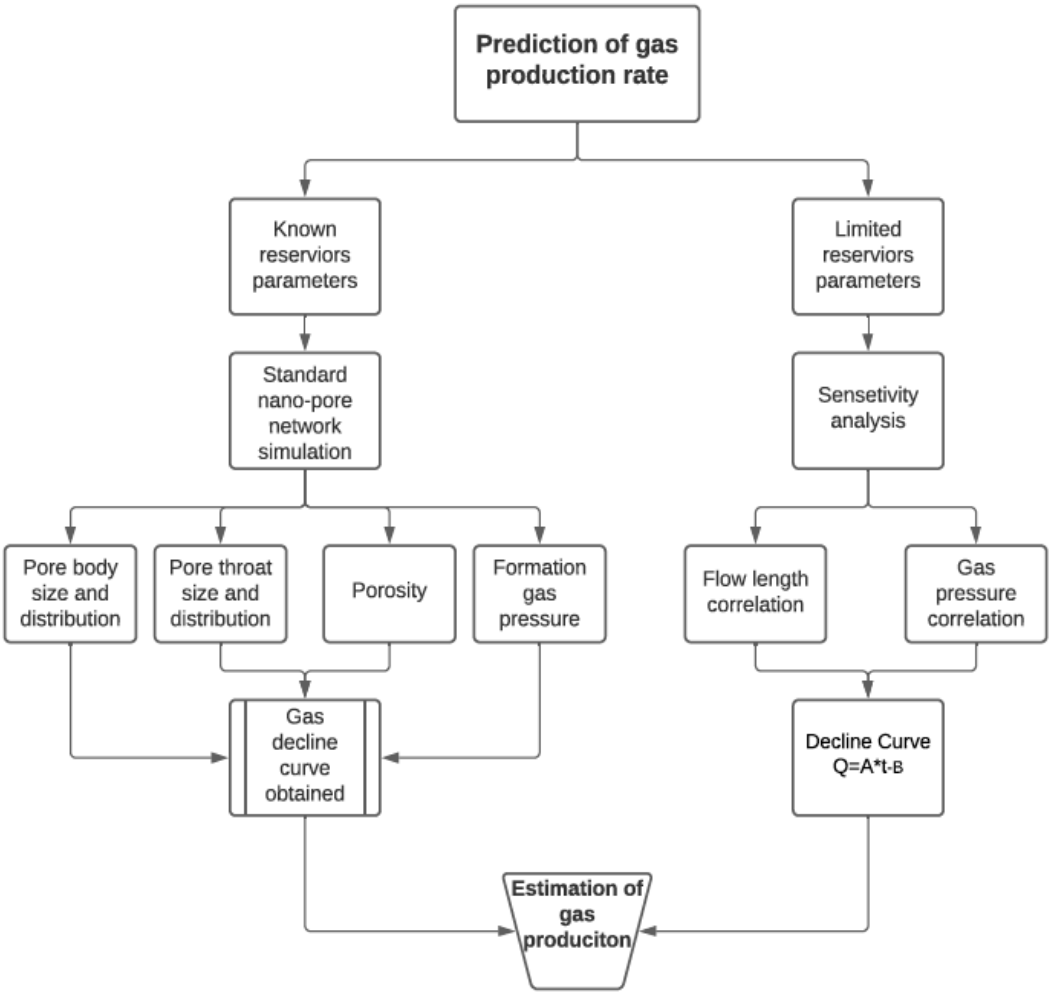

Figure 6.31 A flow chart for the methodology to predict gas production rate for new formations.

6.8 Summary and Conclusions

The prediction of gas production rates after fractures and their declining pattern for unknown shale reservoirs is important for the ultimate recovery and economic decision-making. This research first introduced the anisotropic pore network model to estimate the gas production and the decline trends for shale formations. Then using gas production data for three major shale formations, Eagle Ford shale, Haynesville shale, and Longmaxi shale, a methodology to predict the gas production rates and predicted the expected gas production rate for Opalinus shale formation. The major conclusion of this study are:

1. The anisotropic pore network model with nanoscale gas diffusion is appropriate to represent shale gas reservoir production. In addition, the decline curve of gas production based on a pore network model can be used to predict unknown reservoir gas production rates.

2. Flow length and trapped gas pressure remain the most dominating factors controlling gas flow declination when using the anisotropic pore network model. The decline in gas production decline was fitted to a power equation, $Q=A*t^{-B}$, where A is the base number and B is the power number. The variation of parameters A and B with flow length were fitted and yielded good R^2 values.

3. Two relationships between slopes of variation of parameters A and B with porosity were developed.

4. A methodology to predict the gas production rates with time for unknown formations with limited field geo-material.

5. This study lays the groundwork for scaling up the nano-scale pore network model to estimate engineering scale shale gas production.

CHAPTER 7

CONCLUSIONS

7.1 Summary

The seepage phenomenon of porous media is widespread in the field of geotechnical engineering. With the development of society and the economy, there are many new seepage problems in geotechnical media. The scope covered is a cross transition from traditional geotechnical engineering to environmental, energy, and other fields. The continuum model is based on Darcy's law, which simplifies the complex microscopic properties. As the pore size decreases, Darcy's law can no longer reasonably explain fluid motion in micro-nano-scale porous media. The pore structure model is based on the pore characteristics of the rock and soil medium, reflecting the characteristics of the pore size distribution, connectivity, and anisotropy of the rock and soil medium. The pore-scale seepage calculation can simulate the coexistence characteristics of actual multiple flow mechanisms and effectively reveal the microscopic flow mechanisms such as dynamic multiphase flow. Therefore, It is necessary to analyze the microscopic mechanism of porous media seepage from the pore scale.

The research work of this paper first considers that changes in the pore size of the rock and soil media will cause significant changes in the flow regime, especially for gases, due to the large molecular mean free path, as the rock and soil media change from millimeter-level pore sand to micron-level pore rock mass. When transitioning to the nano-porous shale matrix, the flow pattern of gas molecules changes. In response to the above phenomena, a theoretical model was developed; secondly, shale often exhibits a high anisotropic ratio with different pore scales, the pore structure characteristic parameters

were generalized, and the anisotropic ratio was proposed to further account for this unique characteristic, and an equivalent anisotropic pore network model was established; Thirdly, shale softening experiment was designed, and results were compared; the effect of shale softening was studied based on several experiments including XRD, BET, Density Analysis, and CT-Scanning. Finally, the theoretical gas production model was combined with the physical properties of the geotechnical medium; three historical gas production decline curves were analyzed, and simulation decline curves were correlated with the actual production data. This dissertation has mainly achieved the following research results:

A. The equivalent pore network models of different types of rock and soil media are established. Using pore size, pore throat size, throat size, coordination number, and other geotechnical media pore structure parameters, construct an equivalent pore network model that meets the requirements. This model uses a cubic pore unit as the basic unit and supports a maximum of 26 coordination numbers. The inter-pore throats are generated randomly. This dissertation further analyzes the probability of the connection between the pores using a fully random network. It proposes the generation method of the connection between the pores and considers the influence of anisotropic parameters on the connection of the pores.

B. The pore structure model of complex rock and soil media was established. Generalize the pore structure characteristics of different rock and soil media into basic physical parameters such as pore size distribution, pore throat size distribution, connectivity, porosity, etc., and construct a corresponding equivalent pore network model, which is reflected by setting thresholds for each coordination bond. Its existence probability reflects the pore connectivity of the medium. In addition, the proposed probability-based on anisotropic ratio reflects the multi-directional and anisotropic characteristics of the pore structure of rock and soil media. The size of the pore throat is determined by the connected pores and satisfies the spatial correlation of pores and pore throats. Based on the pore structure model, the representative unit body is calculated to reflect the stability of the model; the validity of the model is verified by comparing the permeability of the different rock and soil media with the test data. Based on effectiveness and stability, the pore structure model can provide hydraulic characteristic parameters for rock and soil media, especially for low-permeability media with low efficiency in obtaining test parameters.

C. A pore-scale single-phase gas flow calculation model based on the equivalent pore network model is established. Considering that the seepage material is in the gas or liquid phase, the fluid operating equations between the pores are analyzed, and the

dynamic seepage process and the steady seepage results are calculated using the time step iteration method and the Gauss-Seidel iteration method, respectively, and consider the influence of scale effect on seepage results is discussed. Using the calculation results of single-phase flow, the microscopic flow and the macroscopic seepage parameters were further combined to simulate permeability and mechanical dispersion coefficient values. At the same time, the influence of different pore network parameters on the macroscopic seepage parameters was analyzed. The comparison with the existing theoretical or experimental results shows that the model can calculate the hydraulic properties of the rock and soil media well.

D. The nano-scale pore network model can be used to predict the decline curves of three major shale plays. When the average pressure of the reservoir decreases to a certain level during boundary flows, gas flow declines over time at early transient flow phases. Moreover, the continued release of gas has a much lower impact on gas production at the late stage.

7.2 Future Research

The research work of this dissertation mainly focuses on the development of theoretical models and microscopic seepage mechanics calculation models. The establishment of the model is based on actual engineering problems as a physical background, abstracting the mathematical model, and the model has scientific significance for the reflection of microscopic flow phenomena and the revealing of the microscopic mechanism. However, since model calculations are mainly focused on the pore scale, there are still some limitations to practical engineering problems. Combined with the existing research work, this article believes that the following points are worth studying for further improving the microscopic seepage mechanics model and expanding its application:

1. Accurate extraction of pore structure of rock and soil media is needed for future work. The accuracy of pore structure parameters is the basis and prerequisite for correct subsequent simulation. Existing research mainly extracts pore structure based on pore body and throat distribution based on BET results, which is slightly insufficient for pore structures with cracks or complex shapes. Therefore, it is necessary to develop a pore structure extraction method suitable for special geotechnical media.

2. The interaction between rock and soil media and pore fluid. The mechanism of seepage and material migration at the pore scale is complex. In addition to the factors considered in this article, the adsorption, desorption, chemical reaction, and biodegradation of rock

and soil media will affect the flow of fluids and affect the rock and soil media. Influence, change the characteristic parameters of pores and throats. Furthermore, in fluid migration, the physical and chemical properties of the rock and soil media may also change, which further affects the movement of the fluid. Therefore, it is necessary to study the interaction between rock and soil media and pore fluid to simulate the phenomenon of microscopic pore seepage better.

3. Because of the multiscale variability in shale, current permeability models are unsuitable for field-scale investigations. The majority of shale gas flow model research has concentrated on predicting the microscale behavior of gas in shale, with just a few models focusing on the scale-up component. The PNW that should consider multiscale effect: from Micro-scale to Filed scale. More study on this topic is critical for the practical use of shale permeability models at the field scale.

REFERENCES

[1] U.S. EIA 2016 The International Energy Outlook 2016 *Int. Energy Outlook 2016*

[2] Zhiltsov S S and Zonn I S 2017 The evaluation of the world potential of shale gas reserves *Handbook of Environmental Chemistry* vol 52 (Springer Verlag) pp 17–24 Publisher: Springer

[3] Anon 2013 Tight gas: China's unsung unconventional energy revolution *Reuters July 8,2013*

[4] Lee B and Sohn I 2014 Review of Innovative Energy Savings Technology for the Electric Arc Furnace *Journal of the minerals,metals and Materials Society* **66** 1581–94

[5] Yingjie L, Xiaoyuan L, Yuelong W and Qingchun Y 2015 Effects of composition and pore structure on the reservoir gas capacity of Carboniferous shale from Qaidam Basin, China *Mar. Pet. Geol.* **62** 44–57

[6] EIA 2018 Where our natural gas comes from - U.S. Energy Information Administration (EIA),Washington,DC

[7] Anon *Categorical Review of Health Reports on Unconventional Oil and Gas Development; Impacts in Pennsylvania 2019* **78** 12-8

[8] Valkó P P and Lee W J 2010 A better way to forecast production from unconventional gas wells *Proceedings - SPE Annual Technical Conference and Exhibition* vol 3 (Society of Petroleum Engineers (SPE)) pp 1860–75

[9] Baihly J D, Malpani R, Altman R M R, Lindsay G and Clayton R 2015 Shale Gas Production Decline Trend Comparison Over Time and Basins Revisited *Society of Petroleum Engineers - Unconventional Resources Technology Conference, URTeC 2015* (American Association of Petroleum Geologists AAPG/Datapages)

[10] EIA 2014 New Eagle Ford wells continue to show higher production - Today in Energy - U.S. Energy Information Administration (EIA)

[11] Gale J F W, Reed R M and Holder J 2007 Natural fractures in the Barnett Shale and their importance for hydraulic fracture treatments *Am. Assoc. Pet. Geol. Bull.* **91** 603–22

[12] Howarth R W and Ingraffea A 2011 Natural gas: Should fracking stop? *Nature* **477** 271–3

[13] Bazan L W, Larkin S D, Lattibeaudiere M G and Palisch T T 2010 Improving production in the eagle ford shale with fracture modeling, increased conductivity

and optimized stage and cluster spacing along the horizontal wellbore *Society of Petroleum Engineers - SPE Tight Gas Completions Conference 2010* (OnePetro) pp 310–32

[14] Saputelli L, Lopez C, Chacon A and Soliman M 2014 Design optimization of horizontal wells with multiple hydraulic fractures in the bakken shale *Society of Petroleum Engineers - European Unconventional Resources Conference and Exhibition 2014: Unlocking European Potential* vol 2 (Society of Petroleum Engineers) pp 817–33

[15] Du J, Hu L, Meegoda J N and Zhang G 2018 Shale softening: Observations, phenomenological behavior, and mechanisms *Appl. Clay Sci.* **161** 290–300

[16] Akpan E U, Enyi G C, Nasr G, Yahaya A A, Ahmadu A A and Saidu B 2019 Water-based drilling fluids for high-temperature applications and water-sensitive and dispersible shale formations *J. Pet. Sci. Eng.* **175** 1028–38

[17] Gholami R, Elochukwu H, Fakhari N and Sarmadivaleh M 2018 A review on borehole instability in active shale formations: Interactions, mechanisms and inhibitors *Earth-Science Rev.* **177** 2–13

[18] van Oort E 2003 On the physical and chemical stability of shales *J. Pet. Sci. Eng.* **38** 213–35

[19] Caenn R, Darley H C H and Gray G R 2016 *Composition and Properties of Drilling and Completion Fluids: Seventh Edition*

[20] Gazaniol D, Forsans T, Boisson M J F and Piau J M 1995 Wellbore failure mechanisms in shales: prediction and prevention *JPT, J. Pet. Technol.* **47** 589–95

[21] Bates R L and Jackson J A 1984 Dictionary of Geological Terms: Third Edition (Rocks, Minerals and Gemstones), American Geological Institute. p. 392. ed J A J Robert L Bates

[22] Ground Water Protection Council and ALL Consulting 2009 Modern Shale Gas Development in the United States: A Primer *Mod. Shale Gas Dev. United States A Prim.* 116

[23] Allan Freeze R and Cherry J A *Groundwater*

[24] Roonwal G S 2018 Composition of the earth and mineral resources *Springer Geology* (Springer) pp 17–58

[25] Chermak J A and Schreiber M E 2014 Mineralogy and trace element geochemistry of gas shales in the United States: Environmental implications *Int. J. Coal Geol.* **126** 32–44

[26] Wu W and Sharma M M 2017 Acid fracturing in shales: Effect of dilute acid on properties and pore structure of shale *SPE Production and Operations* vol 32 (Society of Petroleum Engineers) pp 51–63

[27] DARLEY HCH 1969 LABORATORY INVESTIGATION OF BOREHOLE STABILITY *J Pet. Technol.* **21** 883–92

[28] Mojid M A and Cho H 2006 Estimating the fully developed diffuse double layer thickness from the bulk electrical conductivity in clay *Appl. Clay Sci.* **33** 278–86

[30] Lan Q, Xu M, Binazadeh M, Dehghanpour H and Wood J M 2015 A comparative investigation of shale wettability: The significance of pore connectivity *J. Nat. Gas Sci. Eng.* **27** 1174–88

[31] Groen J C, Peffer L A A and Pérez-Ramírez J 2003 Pore size determination in modified micro- and mesoporous materials. Pitfalls and limitations in gas adsorption data analysis *Microporous Mesoporous Mater.* **60** 1–17

[32] Eslinger E and Pevear D 1988 Clay minerals for petroleum geologists and engineers. *Clay Miner. Pet. Geol. Eng.* **126** 324–324

[33] Passey Q R, Bohacs K M, Esch W L, Klimentidis R and Sinha S 2010 From oil-prone source rock to gas-producing shale reservoir - Geologic and petrophysical characterization of unconventional shale-gas reservoirs *Society of Petroleum Engineers - International Oil and Gas Conference and Exhibition in China 2010, IOGCEC* vol 3 (Society of Petroleum Engineers) pp 1707–35

[34] Zhang J, Kamenov A, Zhu D and Hill A D 2015 Development of new testing procedures to measure propped fracture conductivity considering water damage in clay-rich shale reservoirs: An example of the Barnett Shale *J. Pet. Sci. Eng.* **135** 352–9

[35] Aderibigbe A A and Lane R H 2013 Rock/fluid chemistry impacts on shale fracture behavior *Proceedings - SPE International Symposium on Oilfield Chemistry* vol 2 (Society of Petroleum Engineers (SPE)) pp 680–9

[36] Sanaei A, Jamili A, Callard J and Mathur A 2014 Production modeling in the eagle ford gas condensate window: Integrating new relationships between core permeability, pore size, and confined PVT properties *Society of Petroleum Engineers Western North America and Rocky Mountain Joint Conference and Exhibition 2014* vol 1 (Society of Petroleum Engineers) pp 49–68

[38] Ioannidis M A and Chatzis I 1993 Network modelling of pore structure and transport properties of porous media *Chem. Eng. Sci.* **48** 951–72

[39] Reeves P C and Celia M A 1996 A functional relationship between capillary pressure, saturation, and interfacial area as revealed by a pore-scale network model *Water Resour. Res.* **32** 2345–58

[40] Raoof A, Hassanizadeh S M and Leijnse A 2010 Upscaling Transport of Adsorbing Solutes in Porous Media: Pore-Network Modeling *Vadose Zo. J.* **9** 624–36

[41] Zhang P, Hu L, Meegoda J N and Gao S 2015 Micro/Nano-pore Network Analysis of Gas Flow in Shale Matrix *Sci. Rep.* **5** 1–11

[42] You L, Xie B, Yang J, Kang Y, Han H, Wang L and Yang B 2019 Mechanism of fracture damage induced by fracturing fluid flowback in shale gas reservoirs *Nat. Gas Ind. B* **6** 366–73

[43] Johnston N and Beeson C M 1945 Water Permeability of Reservoir Sands *Trans. AIME* **160** 43–55

[44] Morris F C, Aune Q A and Gates G L 1959 Clay in Petroleum-Reservoir Rocks: Its Effect on Permeability, with Particular Reference to Tejon-Grapevine Area, Kern County, Calif.

[45] Goldenberg L C, Mandel S and Magaritz M 1986 Fluctuating, non-homogeneous changes of hydraulic conductivity in porous media. *Q. J. Eng. Geol.* **19** 183–90

[46] Fink D H, Rich C I and Thomas G W 1968 Determination of internal surface area, external water, and amount of montmorillonite in clay-water systems *Soil Sci.* **105** 71–7

[47] Krishna Mohan K, Reed M G and Scott Fogler H 1999 Formation damage in smectitic sandstones by high ionic strength brines *Colloids Surfaces A Physicochem. Eng. Asp.* **154** 249–57

[48] Norrish K 1954 The swelling of montmorillonite *Discuss. Faraday Soc.* **18** 120–34

[49] Zhang Z Z and Low P F 1989 Relation between the heat of immersion and the initial water content of Li-, Na-, and K-montmorillonite *J. Colloid Interface Sci.* **133** 461–72

[50] Wilson L, Wilson M J, Green J and Patey I 2014 The influence of clay mineralogy on formation damage in North Sea reservoir sandstones: A review with illustrative examples *Earth-Science Rev.* **134** 70–80

[51] Davy C A, Skoczylas F, Barnichon J D and Lebon P 2007 Permeability of macro-cracked argillite under confinement: Gas and water testing *Phys. Chem. Earth* **32** 667–80

[52] Barnaji M J, Pourafshary P and Rasaie M R 2016 Visual investigation of the effects of clay minerals on enhancement of oil recovery by low salinity water flooding *Fuel* **184** 826–35

[53] Baars C and Horak J 2018 Storage and conservation of geological collections—a research agenda *J. Inst. Conserv.* **41** 154–68

[54] Nitters G, Roodhart L, Jongma H, Yeager V, Buijse M, Fulton D, Dahl J and Jantz E 2000 Structured approach to advanced candidate selection and treatment design of stimulation treatments *SPE Reservoir Engineering (Society of Petroleum Engineers)* (Society of Petroleum Engineers (SPE)) pp 607–14

[55] Barbot E, Vidic N S, Gregory K B and Vidic R D 2013 Spatial and temporal correlation of water quality parameters of produced waters from Devonian-age shale following hydraulic fracturing *Environ. Sci. Technol.* **47** 2562–9

[56] Shaffer D L, Arias Chavez L H, Ben-Sasson M, Romero-Vargas Castrillón S, Yip N Y and Elimelech M 2013 Desalination and reuse of high-salinity shale gas produced water: Drivers, technologies, and future directions *Environ. Sci. Technol.* **47** 9569–83

[57] Estrada J M and Bhamidimarri R 2016 A review of the issues and treatment options for wastewater from shale gas extraction by hydraulic fracturing *Fuel* **182** 292–303

[58] Gasc-Barbier M and Tessier D 2007 Structural Modifications of a Hard Deep Clayey Rock due to Hygro-Mechanical Solicitations *Int. J. Geomech.* **7** 227–35

[59] Ferrari A, Favero V, Marschall P and Laloui L 2014 Experimental analysis of the water retention behaviour of shales *Int. J. Rock Mech. Min. Sci.* **72** 61–70

[60] Ewy R T 2015 Shale/claystone response to air and liquid exposure, and implications for handling, sampling and testing *Int. J. Rock Mech. Min. Sci.* **80** 388–401

[61] Sridharan A, Rao S M and Joshi S 1990 Classification of expansive soils by sediment volume method *Geotech. Test. J.* **13** 375–80

[62] Yilmaz I 2006 Indirect estimation of the swelling percent and a new classification of soils depending on liquid limit and cation exchange capacity *Eng. Geol.* **85** 295–301

[63] Lee J-M, Shackelford C D, Benson C H, Jo H-Y and Edil T B 2005 Correlating Index Properties and Hydraulic Conductivity of Geosynthetic Clay Liners *J. Geotech. Geoenvironmental Eng.* **131** 1319–29

[64] Mishra A K, Ohtsubo M, Li L and Higashi T 2005 Effect of salt concentrations on the permeability and compressibility of soil-bentonite mixtures *J. Fac. Agric. Kyushu Univ.* **50** 837–49

[65] Alawaji H A 1999 Swell and compressibility characteristics of sand-bentonite mixtures inundated with liquids *Appl. Clay Sci.* **15** 411–30

[66] Zolfaghari A, Dehghanpour H, Noel M and Bearinger D 2016 Laboratory and field analysis of flowback water from gas shales *J. Unconv. Oil Gas Resour.* **14** 113–27

[67] Friedman G M 2007 Classification of sediments and sedimentary rocks *Sedimentology* (Springer Netherlands) pp 202–16

[68] Chipera S J and Bish D L 2013 Fitting Full X-Ray Diffraction Patterns for Quantitative Analysis: A Method for Readily Quantifying Crystalline and Disordered Phases *Adv. Mater. Phys. Chem.* **03** 47–53

[69] Seiphoori A, Moradian Z, Einstein H H and Whittle A J 2016 Microstructural characterization of Opalinus shale *50th US Rock Mechanics / Geomechanics Symposium 2016* vol 4 (OnePetro) pp 2742–50

[70] Sun S, Liang F, Tang L, Wu J and Ma C 2017 Microstructural investigation of gas shale in Longmaxi Formation, Lower Silurian, NE Sichuan Basin, China *Energy Explor. Exploit.* **35** 406–29

[71] Banerjee S, Abdulsattar Z R, Agim K, Lane R H and Hascakir B 2017 Mechanism of polymer adsorption on shale surfaces: Effect of polymer type and presence of monovalent and divalent salts *Petroleum* **3** 384–90

[72] Ali M and Hascakir B 2017 Water/rock interaction for Eagle ford, marcellus, Green river, and Barnett shale samples and implications for hydraulic-fracturing-fluid engineering *SPE Journal* vol 22 (Society of Petroleum Engineers) pp 162–71

[73] Gutierrez M, Elston H, … D C-A E S and 2014 U Petrophysical Analysis of Eagle Ford Shale: A Preliminary Assessment *searchanddiscovery.com*

[74] Raheem Z 1979 Suggested methods for determining water content, porosity, density absorption and related properties and swelling and slake- durability index properties. *Int. J. Rock Mech. Min. Sci.* **16** 141–56

[75] Wang R, Zhang N, Liu X, Wu X, Chen J and Ma L 2015 Characteristics of pore volume distribution and methane adsorption on shales *Adsorpt. Sci. Technol.* **33** 915–38

[76] Kuila U and Prasad M 2013 Specific surface area and pore-size distribution in clays and shales *Geophys. Prospect.* **61** 341–62

[77] Li Y, Wang Z, Pan Z, Niu X, Yu Y and Meng S 2019 Pore structure and its fractal dimensions of transitional shale: A cross-section from east margin of the Ordos Basin, China *Fuel* **241** 417–31

[78] Hu J, Tang S and Zhang S 2016 Investigation of pore structure and fractal characteristics of the Lower Silurian Longmaxi shales in western Hunan and Hubei Provinces in China *J. Nat. Gas Sci. Eng.* **28** 522–35

[79] Gou Q, Xu S, Hao F, Yang F, Zhang B, Shu Z, Zhang A, Wang Y, Lu Y, Cheng X, Qing J and Gao M 2019 Full-scale pores and micro-fractures characterization using FE-SEM, gas adsorption, nano-CT and micro-CT: A case study of the Silurian Longmaxi Formation shale in the Fuling area, Sichuan Basin, China *Fuel* **253** 167–79

[80] Harrison A L, Jew A D, Dustin M K, Thomas D L, Joe-Wong C M, Bargar J R, Johnson N, Brown G E and Maher K 2017 Element release and reaction-induced porosity alteration during shale-hydraulic fracturing fluid interactions *Appl. Geochemistry* **82** 47–62

[81] Ji L, Zhang T, Milliken K L, Qu J and Zhang X 2012 Experimental investigation of main controls to methane adsorption in clay-rich rocks *Appl. Geochemistry* **27** 2533–45

[82] Milliken K L and Reed R M 2010 Multiple causes of diagenetic fabric anisotropy in weakly consolidated mud, Nankai accretionary prism, IODP Expedition 316 *J. Struct. Geol.* **32** 1887–98

[83] Donohue M D and Aranovich G L 1998 Classification of Gibbs adsorption isotherms *Adv. Colloid Interface Sci.* **76**–**77** 137–52

[84] Labani M M, Rezaee R, Saeedi A and Hinai A Al 2013 Evaluation of pore size spectrum of gas shale reservoirs using low pressure nitrogen adsorption, gas expansion and mercury porosimetry: A case study from the Perth and Canning Basins, Western Australia *J. Pet. Sci. Eng.* **112** 7–16

[85] Kuila U, McCarty D K, Derkowski A, Fischer T B, Topór T and Prasad M 2014 Nano-scale texture and porosity of organic matter and clay minerals in organic-rich mudrocks *Fuel* **135** 359–73

[86] Yang C, Zhang J, Han S, Wang X, Wang L, Yu W and Wang Z 2016 Compositional controls on pore-size distribution by nitrogen adsorption technique in the Lower Permian Shanxi Shales, Ordos Basin *J. Nat. Gas Sci. Eng.* **34** 1369–81

[87] Morrow C P, Yazaydin A Ö, Krishnan M, Bowers G M, Kalinichev A G and Kirkpatrick R J 2013 Structure, energetics, and dynamics of smectite clay interlayer

hydration: Molecular dynamics and metadynamics investigation of Na-hectorite *J. Phys. Chem. C* **117** 5172–87

[88] Kowalczyk P, Terzyk A P, Gauden P A, Leboda R, Szmechtig-Gauden E, Rychlicki G, Ryu Z and Rong H 2003 Estimation of the pore-size distribution function from the nitrogen adsorption isotherm. Comparison of density functional theory and the method of Do and co-workers *Carbon N. Y.* **41** 1113–25

[89] Anovitz L M and Cole D R 2015 Characterization and analysis of porosity and pore structures *Rev. Mineral. Geochemistry* **80** 61–164

[90] Dehghanpour H, Lan Q, Saeed Y, Fei H and Qi Z 2013 Spontaneous imbibition of brine and oil in gas shales: Effect of water adsorption and resulting microfractures *Energy and Fuels* **27** 3039–49

[91] Vengosh A, Jackson R B, Warner N, Darrah T H and Kondash A 2014 A critical review of the risks to water resources from unconventional shale gas development and hydraulic fracturing in the United States *Environ. Sci. Technol.* **48** 8334–48

[92] Adler P M 2013 *Porous Media: Geometry and Transports, Series in Chemical Engineering*

[93] Kovscek A R and Radke C J 1996 Gas bubble snap-off under pressure-driven flow in constricted noncircular capillaries *Colloids Surfaces A Physicochem. Eng. Asp.* **117** 55–76

[94] Xiong Q, Baychev T G and Jivkov A P 2016 Review of pore network modelling of porous media: Experimental characterisations, network constructions and applications to reactive transport *J. Contam. Hydrol.* **192** 101–17

[95] Raoof A, Nick H M, Hassanizadeh S M and Spiers C J 2013 PoreFlow: A complex pore-network model for simulation of reactive transport in variably saturated porous media *Comput. Geosci.* **61** 160–74

[96] Gao S, Meegoda J N and Hu L 2012 Two methods for pore network of porous media *Int. J. Numer. Anal. Methods Geomech.* **36** 1954–70

[97] Jerauld G R and Salter S J 1990 The effect of pore-structure on hysteresis in relative permeability and capillary pressure: Pore-level modeling *Transp. Porous Media* **5** 103–51

[98] Lerdahl T R, Oren P-E and Bakke S 2000 A Predictive Network Model for Three-Phase Flow in Porous Media (Society of Petroleum Engineers (SPE))

[99] Kanckstedt M A, Sheppard A P and Sahimi M 2001 Pore network modelling of two-phase flow in porous rock: The effect of correlated heterogeneity *Adv. Water Resour.* **24** 257–77

[100] Gao J, Yu Q and Lu X 2017 Apparent Permeability and Gas Flow Behavior in Carboniferous Shale from the Qaidam Basin, China: An Experimental Study *Transp. Porous Media* **116** 585–611

[101] Bhatnagar P L, Gross E P and Krook M 1954 A model for collision processes in gases. I. Small amplitude processes in charged and neutral one-component systems *Phys. Rev.* **94** 511–25

[102] Javadpour F 2009 Nanopores and apparent permeability of gas flow in mudrocks (shales and siltstone) *J. Can. Pet. Technol.* **48** 16–21

[103] Florence F A, Rushing J, Newsham K E and Blasingame T A 2007 Improved Permeability Prediction Relations for Low Permeability Sands (Society of Petroleum Engineers (SPE))

[104] Sondergeld C H, Ambrose R J, Rai C S and Moncrieff J . 2010 Micro-Structural Studies of Gas Shales (Society of Petroleum Engineers (SPE))

[105] Anon 1970 Random packings and the structure of simple liquids. I. The geometry of random close packing *Proc. R. Soc. London. A. Math. Phys. Sci.* **319** 479–93

[106] Bryant S L, King P R and Mellor D W 1993 Network model evaluation of permeability and spatial correlation in a real random sphere packing *Transp. Porous Media* **11** 53–70

[107] Acharya R C, van der Zee S E A T M and Leijnse A 2004 Porosity-permeability properties generated with a new 2-parameter 3D hydraulic pore-network model for consolidated and unconsolidated porous media *Adv. Water Resour.* **27** 707–23

[108] Wu K, Van Dijke M I J, Couples G D, Jiang Z, Ma J, Sorbie K S, Crawford J, Young I and Zhang X 2006 3D stochastic modelling of heterogeneous porous media - Applications to reservoir rocks *Transp. Porous Media* **65** 443–67

[109] Geman S and Geman D 1984 Stochastic Relaxation, Gibbs Distributions, and the Bayesian Restoration of Images *IEEE Trans. Pattern Anal. Mach. Intell.* **PAMI-6** 721–41

[110] Curtis M E, Sondergeld C H, Ambrose R J and Rai C S 2012 Microstructural investigation of gas shales in two and three dimensions using nanometer-scale resolution imaging *Am. Assoc. Pet. Geol. Bull.* **96** 665–77

[111] Ma J, Sanchez J P, Wu K, Couples G D and Jiang Z 2014 A pore network model for simulating non-ideal gas flow in micro- and nano-porous materials *Fuel* **116** 498–508

[112] Vega B, Dutta A and Kovscek A R 2014 CT Imaging of Low-Permeability, Dual-Porosity Systems Using High X-ray Contrast Gas *Transp. Porous Media* **101** 81–97

[113] Payatakes A C, Tien C and Turian R M 1973 A new model for granular porous media: Part I. Model formulation *AIChE J.* **19** 58–67

[114] Hornby B E, Schwartz L M and Hudson J A 1994 Anisotropic effective-medium modeling of the elastic properties of shales *Geophysics* **59** 1570–83

[115] Arns J Y, Robins V, Sheppard A P, Sok R M, Pinczewski W V. and Knackstedt M A 2004 Effect of network topology on relative permeability *Transp. Porous Media* **55** 21–46

[116] Sayers C M 2005 Seismic anisotropy of shales *Geophys. Prospect.* **53** 667–76

[117] Gao J, Xia L, Li Y and Yu Q 2016 Percolation characteristics of Carboniferous shale gas in Eastern Qaidam Basin *Earth Sci. Front.* **23** 103–12

[118] Aksu I, Bazilevskaya E and Karpyn Z T 2015 Swelling of clay minerals in unconsolidated porous media and its impact on permeability *GeoResJ* **7** 1–13

[119] Hu Q, Ewing R P and Dultz S 2012 Low pore connectivity in natural rock *J. Contam. Hydrol.* **133** 76–83

[120] Mehmani A and Prodanović M 2014 The effect of microporosity on transport properties in porous media *Adv. Water Resour.* **63** 104–19

[121] Amann-Hildenbrand A, Ghanizadeh A and Krooss B M 2012 Transport properties of unconventional gas systems *Mar. Pet. Geol.* **31** 90–9

[122] Zhang D, Zhang X, Guo H, Lin D, Meegoda J N and Hu L 2021 An anisotropic pore-network model to estimate the shale gas permeability *Sci. Rep.* **11** 7902

[123] Wang Q, Chen X, Jha A N and Rogers H 2014 Natural gas from shale formation - The evolution, evidences and challenges of shale gas revolution in United States *Renew. Sustain. Energy Rev.* **30** 1–28

[124] Anon 2016 Directional and Horizontal Drilling in Oil and Gas Wells *Alternative Energy and Shale Gas Encyclopedia* (John Wiley & Sons, Inc.) pp 695–6

[125] Gong B 2020 The Development and Implication of Crude Oil Market in the Context of the Shale Revolution *Shale Energy Revolution* (Springer Singapore) pp 37–52

[126] Creasey N H, Battensby J and Fletcher J A 2015 Factors Affecting the Permeability of Skin (University of British Columbia) pp 95–106

[127] Mehmani A, Prodanović M and Javadpour F 2013 Multiscale, Multiphysics Network Modeling of Shale Matrix Gas Flows *Transp. Porous Media* **99** 377–90

[128] Gao W L 2003 Effect of pore structure on the characteristics of percolation flow curves of Ansai low-permeability reservoir *Shiyou Kantan Yu Kaifa/Petroleum Explor. Dev.* **30** 79

[129] Blunt M J, Jackson M D, Piri M and Valvatne P H 2002 Detailed physics, predictive capabilities and macroscopic consequences for pore-network models of multiphase flow *Adv. Water Resour.* **25** 1069–89

[130] Zheng J, Ju Y and Wang M 2018 Pore-Scale Modeling of Spontaneous Imbibition Behavior in a Complex Shale Porous Structure by Pseudopotential Lattice Boltzmann Method *J. Geophys. Res. Solid Earth* **123** 9586–600

[131] Song W, Yin Y, Landry C J, Prodanovic M, Qu Z and Yao J 2021 A Local-Effective-Viscosity Multirelaxation-Time Lattice Boltzmann Pore-Network Coupling Model for Gas Transport in Complex Nanoporous Media *SPE J.* **26** 461–81

[132] Nicholson D and Petropoulos J H 1971 Capillary models for porous media: III. Two-phase flow in a three-dimensional network with Gaussian radius distribution. *J. Phys. D. Appl. Phys.* **4** 181–9

[133] Dullien F A L 1979 Porous media: fluid transport and pore structure.

[134] Du J, Whittle A J, Hu L, Divoux T and Meegoda J N 2021 Characterization of meso-scale mechanical properties of Longmaxi shale using grid microindentation experiments *J. Rock Mech. Geotech. Eng.* **13** 555–67

[135] Zhao Y P, Chen J, Yuan Q and Cheng C 2016 Microcrack connectivity in rocks: A real-space renormalization group approach for 3D anisotropic bond percolation *J. Stat. Mech. Theory Exp.* **2016**

[136] Abichou T, Benson C H and Edil T B 2004 Network model for hydraulic conductivity of sand-bentonite mixtures *Can. Geotech. J.* **41** 698–712

[137] Ghanizadeh A, Gasparik M, Amann-Hildenbrand A, Gensterblum Y and Krooss B M 2014 Experimental study of fluid transport processes in the matrix system of the European organic-rich shales: I. Scandinavian Alum Shale *Mar. Pet. Geol.* **51**

[138] Mackinlay J 1986 A Dissertation Submitted to the Department of Computer Science and the Committee on Graduate Studies of Stanford University in Partial Fulfillment

of the Requirements for the Degree of Doctor of Philosophy in Partial Fulfillment of the Requirements for th *Development*

[139] Heller R J, Vermylen J and Zoback M 2013 Multiscale investigation of fluid transport in gas shales *Am. Assoc. Pet. Geol. Bull.* **98** 975–95

[140] Heller R, Vermylen J and Zoback M 2014 Experimental investigation of matrix permeability of gas shales *Am. Assoc. Pet. Geol. Bull.* **98** 975–95

[141] Tinni A, Fathi E, Agarwal R, Sondergeld C, Akkutlu Y and Rai C 2012 Shale permeability measurements on plugs and crushed samples *Society of Petroleum Engineers - SPE Canadian Unconventional Resources Conference 2012, CURC 2012* vol 1 (OnePetro) pp 342–55

[142] Ma Y, Pan Z, Zhong N, Connell L D, Down D I, Lin W and Zhang Y 2016 Experimental study of anisotropic gas permeability and its relationship with fracture structure of Longmaxi Shales, Sichuan Basin, China *Fuel* **180** 106–15

[143] Hao L and Cheng P 2010 Pore-scale simulations on relative permeabilities of porous media by lattice Boltzmann method *Int. J. Heat Mass Transf.* **53** 1908–13

[144] Jivkov A P, Hollis C, Etiese F, McDonald S A and Withers P J 2013 A novel architecture for pore network modelling with applications to permeability of porous media *J. Hydrol.* **486** 246–58

[145] Raoof A and Majid Hassanizadeh S 2010 A new method for generating pore-network models of porous media *Transp. Porous Media* **81** 391–407

[146] Freeman C M, Moridis G J and Blasingame T A 2011 A Numerical Study of Microscale Flow Behavior in Tight Gas and Shale Gas Reservoir Systems *Transp. Porous Media* **90** 253–68

[147] GAO J, XIA L, LI Y, Frontiers Q Y-E S and 2016 undefined Percolation characteristics of Carboniferous shale gas in Eastern Qaidam Basin *en.cnki.com.cn*

[148] Zhang P, Hu L and Meegoda J N 2017 Pore-scale simulation and sensitivity analysis of apparent gas permeability in shale matrix *Materials (Basel).* **10** 104

[149] Zhang D, Meegoda J N, Goncalves Da Silva B M and Hu L *Impact of Hydraulic fracturing on Mineralogy on Change in Micro and Nano Porosity and Permeability of Shales*

[150] Dong T, Harris N B, Ayranci K, Twemlow C E and Nassichuk B R 2015 Porosity characteristics of the Devonian Horn River shale, Canada: Insights from lithofacies classification and shale composition *Int. J. Coal Geol.* **141**–**142** 74–90

[151] Khan S, Ansari S, Han H and Khosravi N 2011 Importance of shale anisotropy in estimating in-situ stresses and wellbore stability analysis in Horn River Basin *Society of Petroleum Engineers - Canadian Unconventional Resources Conference 2011, CURC 2011* vol 3 (Society of Petroleum Engineers) pp 2126–39

[152] Suarez-Rivera R, Green S J, McLennan J and Bai M 2006 Effect of Layered Heterogeneity on Fracture Initiation in Tight Gas Shales (Society of Petroleum Engineers (SPE))

[153] Kwon O, Kronenberg A K, Gangi A F, Johnson B and Herbert B E 2004 Permeability of illite-bearing shale: 1. Anisotropy and effects of clay content and loading *J. Geophys. Res. Solid Earth* **109** 10205

[154] Wang D, Yao J, Chen Z, Song W and Sun H 2020 Multiphase flow model from pores to cores in organic-rich shale *J. Pet. Sci. Eng.* **194**

[155] Wang L, Wang S, Zhang R, Wang C, Xiong Y, Zheng X, Li S, Jin K and Rui Z 2017 Review of multi-scale and multi-physical simulation technologies for shale and tight gas reservoirs *J. Nat. Gas Sci. Eng.* **37** 560–78

[156] Zhang P, Hu L, Wen Q and Meegoda J N 2015 A multi-flow regimes model for simulating gas transport in shale matrix *Géotechnique Lett.* **5** 231–5

[157] Wilkens R H 1997 Physical Properties of Rocks: Fundamentals and Principles of Petrophysics *Eos, Trans. Am. Geophys. Union* **78** 600

[158] LI Y, XUE H and TIAN S 2015 Talk about the Difference and Connection between Conventional and Unconventional Oil *Acta Geol. Sin. - English Ed.* **89** 261–2

[159] Energy Inofmration Administration 2013 *International Energy Outlook With projections to 2040 Washington*

[160] Anon Brooks, D. 2011. Shale gas revolution. The New York... - Google Scholar

[161] Haug M 2012 Shale gas and renewables: Divergence or win-win for transatlantic energy cooperation? *J. Transatl. Stud.* **10** 358–73

[162] Rafiee M, Soliman M Y and Pirayesh E 2012 Hydraulic fracturing design and optimization: A modification to zipper frac *Proceedings - SPE Annual Technical Conference and Exhibition* vol 4 pp 3359–74

[163] Aimene Y E and Ouenes A 2015 Geomechanical modeling of hydraulic fractures interacting with natural fractures - Validation with microseismic and tracer data from the Marcellus and Eagle Ford *Interpretation* **3** SU71–88

[164] Arps J J 1945 Analysis of Decline Curves *Trans. AIME* **160** 228–47

[165] Barree R D, Cox S A, Miskimins J L, Gilbert J V. and Conway M W 2015 Economic optimization of horizontal-well completions in unconventional reservoirs *SPE Production and Operations* vol 30 (Society of Petroleum Engineers) pp 293–311

[166] Orangi A, Nagarajan N R, Honarpour M M and Rosenzweig J 2011 Unconventional shale oil and gas-condensate reservoir production, impact of rock, fluid, and hydraulic fractures *Society of Petroleum Engineers - SPE Hydraulic Fracturing Technology Conference 2011* pp 676–90

[167] Cipolla C L, Lolon E P, Erdle J C and Rubin B 2010 Reservoir modeling in shale-gas reservoirs *SPE Reserv. Eval. Eng.* **13** 638–53

[168] Wang J Q, Zhao J F, Yang M J, Li Y H, Liu W G and Song Y C 2015 Permeability of laboratory-formed porous media containing methane hydrate: Observations using X-ray computed tomography and simulations with pore network models *Fuel* **145** 170–9

[169] Bernabé Y, Mok U and Evans B 2003 Permeability-porosity relationships in rocks subjected to various evolution processes *Pure Appl. Geophys.* **160** 937–60

[170] Al-Khulaifi Y, Lin Q, Blunt M J and Bijeljic B 2017 Reaction Rates in Chemically Heterogeneous Rock: Coupled Impact of Structure and Flow Properties Studied by X-ray Microtomography *Environ. Sci. Technol.* **51** 4108–16

[171] Battistelli A, Calore C and Pruess K *Analysis of salt effects on the depletion of fractured reservoir blocks Gas Systems View project Modeling of transient multiphase flow in CO2 injection wells with the wellbore-reservoir coupled simulator T2Well-ECO2M View project ANALYSIS OF SALT EFFECTS*

[172] Hadjiconstantinou N G 2006 The limits of Navier-Stokes theory and kinetic extensions for describing small-scale gaseous hydrodynamics *Phys. Fluids* **18**

[173] Klinkenberg L J 1941 The permeability of porous media to liquids and gases *Drilling and Production Practice 1941* pp 200–13

[174] Gilron J and Soffer A 2002 Knudsen diffusion in microporous carbon membranes with molecular sieving character *J. Memb. Sci.* **209** 339–52

[175] Mayerhofer M J, Lolon E P, Youngblood J E and Heinze J R 2006 Integration of microseismic fracture mapping results with numerical fracture network production modeling in the Barnett shale *Proceedings - SPE Annual Technical Conference and Exhibition* vol 2 pp 976–83

[176] Mattar L, Rushing J A and Anderson D M 2006 Production Data Analysis - Challenges, Pitfalls, Diagnostics *All Days* (SPE)

[177] Kok M V. and Merey S 2014 Shale Gas: Current Perspectives and Future Prospects in Turkey and the World *Energy Sources, Part A Recover. Util. Environ. Eff.* **36** 2492–501

[178] Kuila U and Prasad M 2013 Specific surface area and pore-size distribution in clays and shales *Geophys. Prospect.* **61** 341–62

[179] Boyer C, Kieschnick J, Suarez-Rivera R, Lewis R E and Waters G 2006 Producing gas from its source *Oilf. Rev.* **18** 36–49

[180] Arps J J 1945 Analysis of Decline Curves *Trans. AIME* **160** 228–47

[181] Sherman F S 1969 The Transition From Continuum to Molecular Flow *Annu. Rev. Fluid Mech.* **1** 317–40

[182] Civan F 2010 Effective correlation of apparent gas permeability in tight porous media *Transp. Porous Media* **82** 375–84

[183] Wang H and Marongiu-Porcu M 2015 Impact of shale-gas apparent Permeability on production: Combined effects of non-Darcy flow/gas slippage, desorption, and geomechanics *SPE Reservoir Evaluation and Engineering* vol 18 pp 495–507

[184] Baihly J D, Malpani R, Altman R, Lindsay G and Clayton R 2015 Shale gas production decline trend comparison over time and basins - Revisited *Society of Petroleum Engineers - Unconventional Resources Technology Conference, URTeC 2015*

[185] Weixu W, Chenggang X, Xing L, Heng W, Cheng N and Lizhi W 2017 Production controlling factors of the Longmaxi shale gas formation - A case study of Huangjingba shale Gas Field *Society of Petroleum Engineers - SPE/IATMI Asia Pacific Oil and Gas Conference and Exhibition 2017* vol 2017-Janua

[186] Gong X, Tian Y, McVay D A, Ayers W B and Lee W J 2013 Assessment of Eagle Ford shale oil and gas resources *Society of Petroleum Engineers - SPE Canadian Unconventional Resources Conference 2013 - Unconventional Becoming Conventional: Lessons Learned and New Innovations* vol 2 pp 1335–60

[187] Warren M N, Jayakumar S and Woodroof R A 2017 Haynesville shale horizontal well completions: What has been learned through post-stimulation completion diagnostics and how these learnings can be employed to make better wells *Proceedings - SPE Annual Technical Conference and Exhibition*

[188] Boulis A, Jayakumar R, Lalehrokh F and Lawal H 2012 Improved methodologies for more accurate shale gas assessments *Society of Petroleum Engineers - SPE Americas Unconventional Resources Conference 2012* pp 300–16

[189] Wei Y, Jia A, Wang J, Qi Y and Jia C 2018 Current Technologies and Prospects of Shale Gas Development in China *Shale Gas - New Aspects and Technologies* (InTech)

[190] Müller P J and Suess E 1979 Productivity, sedimentation rate, and sedimentary organic matter in the oceans-I. Organic carbon preservation *Deep Sea Res. Part A, Oceanogr. Res. Pap.* **26** 1347–62

[191] Zhang D, Meegoda J N, Goncalves Da Silva B M and Hu L 2021 *Impact of Hydraulic fracturing on Mineralogy on Change in Micro and Nano Porosity and Permeability of Shales*

[192] Li W, Jin C and Cusatis G 2016 Integrated Experimental and Computational Characterization of Shale at Multiple Length Scales *New Frontiers in Oil and Gas Exploration* (Springer International Publishing) pp 389–434